THE UNIVERSITY *of* EDINBURGH

PIXEL Analysis of Interactions in Organic and Inorganic Systems

Andrew Gerrard Patrick Maloney

Supervisor: Prof. Simon Parsons

PhD **University of Edinburgh** **2015**

Declaration

I declare that this Thesis has been written by me and that the work carried out is my own, or I have made a substantial contribution towards it except where specific reference is made to another. This work has not been submitted for another degree or professional qualification.

Andrew G. P. Maloney

Abstract

The PIXEL method has been used for several years to analyse intermolecular interactions in organic crystals. The simplicity and speed of the calculations, along with the breakdown of intermolecular energies into physical contributing terms, mean that it has had a massive influence on the way organic crystal structures are interpreted.

In the work done to date, the parameters required to perform a PIXEL calculation have been established for 1st, 2nd and 3rd row transition metals. Using these parameters, lattice energies of several transition metal complexes containing various chemical environments have been calculated and compared to experimental sublimation enthalpies. Straight line parameters for these results have been comparable to work by Gavezzotti, the author of the program, in testing the method for organic crystal structures.

In addition to lattice energies, PIXEL gives dimer interaction energies of molecules in a crystal structure. The values of these interactions have been compared to single point DFT energy calculations. PIXEL has shown good agreement with a range of different intermolecular interactions, along with a significant saving in computer time over the higher level calculations.

Aside from four empirical parameters, PIXEL requires only fundamental atomic properties such as ionisation potentials, electronegativities and van der Waals radii. For the most part, these values are obtained from standard reference tables and texts with the exception of atomic polarizabilities. This parameter is of great importance as it is used during the calculation of the dispersion term, an interaction which has a major influence on crystal packing. In previous work, atomic polarizabilities have been calculated using either the Slater-Kirkwood approximation or the Clausius-Mossotti relation. Both of these methods are rather simple, and do not account for possible changes in atomic polarizability resulting from differences in chemical environment. The Atoms in Molecules (AIM) approach has been used to attempt to obtain a range of polarizability values for atoms common to organic chemistry.

It is observed that in the series of straight chained primary monoamines, C_n-$H_{2n+3}N$, an alternation in melting points occurs between odd and even values of n. This alternation could be traced to differences in hydrogen-bonding and chain-packing that occur between odd and even-membered amines. Molecular interaction energy calculations were carried out using the PIXEL method, enabling quantitative energetic analysis of the packing differences. In this work, the crystal structures of the primary amines from ethylamine to decylamine were solved for the first time. All of these compounds are liquids at room temperature, so crystals were grown in situ by laser-assisted zone refinement at 10 K below their melting points. Diffraction data were then collected at 150 K. From propylamine to decylamine, all crystal structures are orthorhombic (or pseudo-orthorhomic) with the unit cell dimensions ~5 Å x ~7 Å x *c* Å, where c increases with

chain length. In the case of ethylamine, a phase characterised by single crystal diffraction at 180 K underwent a transition to a different phase on cooling to 150 K. The low-temperature phase was investigated using powder methods.

Publications

A. G. P. Maloney, P. A. Wood and S. Parsons, *CrystEngComm*, 2014, **16**, 3867-3882.

Acknowledgements

First of all, I would like to thank my supervisor, Prof. Simon Parsons, without whom none of this would ever have happened. From the start of my Masters project up until the end of my PhD you have been a fantastic, patient teacher and I've learned an incredible amount from you. Your vast knowledge of crystallography, and pretty much every other subject in existence, has never ceased to amaze me. In fact, I "canard-ly" believe how knowledgeable you are. Simon, it has been both a pleasure and a privilege.

Thanks to my second supervisor, Dr. Stephen Moggach. You've always been a great help with anything and everything I've had a problem with, and I truly appreciate everything you've done for me. Hopefully I've helped you pick up a few new stories over the years as well…

Thanks to Dr. Pete Wood, and indeed everyone else at the CCDC who has helped me throughout my PhD. Pete, your constant enthusiasm and helpfulness have always kept me on track. Thanks also to Dr. Carole Morrison, your patience and willingness to help with every (probably irritating) question I've had has been brilliant.

To all the members of the group that I've worked with over the years – Alex G., Nick, Pete, Alex P., Fraser, Chris C., Claire (my little sister), Giles, Charlie and Chris W. – you've all made my time here thoroughly enjoyable and it's always been fun coming into work as a result. Lastly, thanks to Scott, Jorge and Jack – these things are always easier when you work with some of your best friends.

Thanks to my friends, both in the department and beyond. Particular thanks to Emma, Peter, Jack, Patrick, Hubbard, Swav and Alex. You guys have always been there for me when I've needed you to be.

To my high school teachers – Dr. Oldershaw, Mr. Walsh and Dr. Sinclair – thank you for starting me off down this career path. Your infectious enthusiasm for your subjects really kindled my passion for science and always made me want to learn more.

To Iz, you've been my rock and my little ray of sunshine. Talking to you every night kept me going and I'm amazed you were able to put up with me at times. Here's to our next adventure!

Finally, to my parents. I couldn't have asked for a better pair. I would never have managed any of this without your constant love and support, particularly through the rough times, and your ability to put up with my grumpiness is nothing short of legendary. This is for you.

Contents

Chapter 1

Introduction

1.1 Introduction

Intermolecular interactions are of fundamental importance to our understanding of the solid state. They are responsible for phase stability and polymorphism, and are the driving forces of crystallisation itself. "Classical" investigation of these interactions relies on geometric analysis of a crystal structure to identify short intermolecular distances, which are defined by the distances between van der Waals surfaces, as calculated from the elemental van der Waals radii.[1] In reality, van der Waals radii are not constant, but are instead ellipsoidal,[2, 3] contracted with respect to the head-on contacts between atoms.[3] Van der Waals radii, and the corresponding surfaces, can also be altered by chemical environment. In organic cyano groups, the van der Waals radius needed to account for the shortest contacts between such functional groups is 1.60 Å,[3] while the same radius required for $[Ni(CN)_4]^{2-}$ ions is 1.25 Å,[3] over a 20% difference. Furthermore, whilst geometric analyses may indicate an interaction between molecules, they do not take the energy of the interactions into consideration. As such, taking a purely geometric approach can lead to important interactions being overlooked. For instance, in the crystal structure of cholest-5-en-3-ol dihydrocinnamate (CSD refcode CHOLOL), a cholesterol derivative, the strongest intermolecular interaction (-51 kJ mol^{-1}, with a dispersion contribution of -48 kJ mol^{-1})[4] occurs between molecules around 6 Å apart, and shows no discernible geometrical interaction (Figure 1.1).

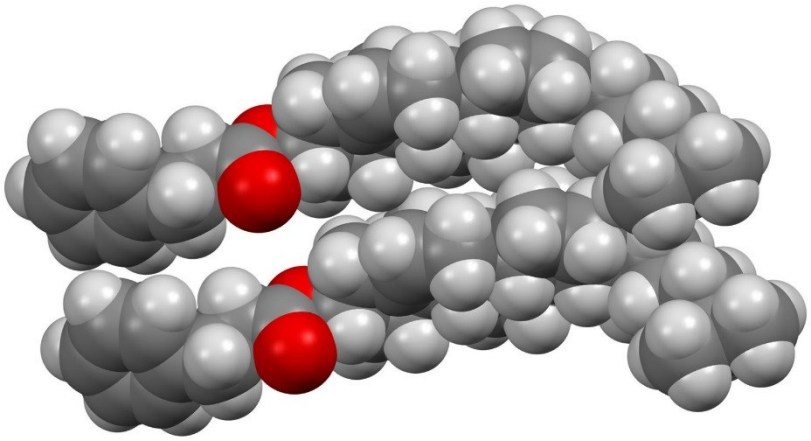

Figure 1.1: The strongest interaction in the crystal structure of a cholesterol derivative. Carbon atoms are dark grey, hydrogen light grey and oxygen red.

Similarly, in the phase I structure of *N*-methylimido-sulfuroxide difluoride,[5] the strongest interaction occurs at an S…N distance of 3.517 Å, 0.167 Å longer than the sum of the van der Waals radii of S and N (3.35 Å).

Serine monohydrate[6] is another example in which geometric analysis fails to give the full account of energetically important intermolecular interactions. The structure consists of layers of serine molecules with water molecules positioned between the layers (Figure 1.2). These result in a motif of short hydrogen bonds that, upon conventional geometric analysis based on hydrogen bonding criteria,[7] would seem to be the driving force behind the crystal packing.

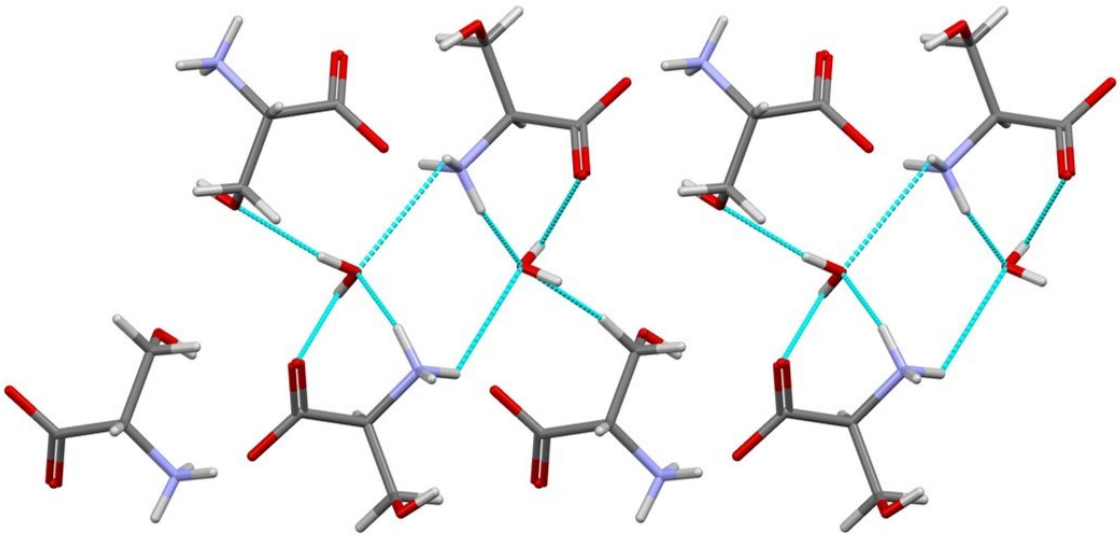

Figure 1.2: The serine monohydrate crystal structure showing the short hydrogen bonds (Taken from refcode LSERMH11). Carbon atoms are dark grey, hydrogen light grey, nitrogen blue and oxygen red.

Serine is a zwitterion, and there exists a significant electrostatic interaction between the layers. This is shown upon energetic analysis of the system, where one of the short hydrogen bonding interactions (1.922(7) Å, a distance normally indicative of a medium strength hydrogen bond), has an energy of -1.6 kJ mol^{-1} and is dwarfed by a long range (~6 Å) electrostatic interaction of -48.1 kJ mol^{-1} between the layers.

1.2 The PIXEL Method

The energetic analysis mentioned above was performed using PIXEL,[8] a method for evaluating intermolecular energies based on integrations over calculated electron densities of molecules. It allows for the total interaction energy to be separated into four principal contributing terms: Coulombic, polarisation, dispersion and repulsion. This separation of contributions allows for the character of an interaction to be inferred from the dominant term.

The calculations are based on a cube of electron density calculated by electronic structure methods from the atomic coordinates available from a crystal structure determination. This electron density is divided into a three dimensional grid, giving an array of pixels. Each of these pixels is then assigned to the atom in the molecule for which the nucleus – pixel distance is less than the atomic radius. Associating each pixel with a specific atom allows for the electron density to be ascribed different parameters based on its chemical environment. A cluster of molecules is built up around a central reference molecule using the space group symmetry of the crystal structure. The intermolecular energy between the central molecule and each molecule in the cluster is then evaluated by pair-wise evaluation of pixel-pixel energies between symmetry related molecules in the crystal structure (Figure 1.3).

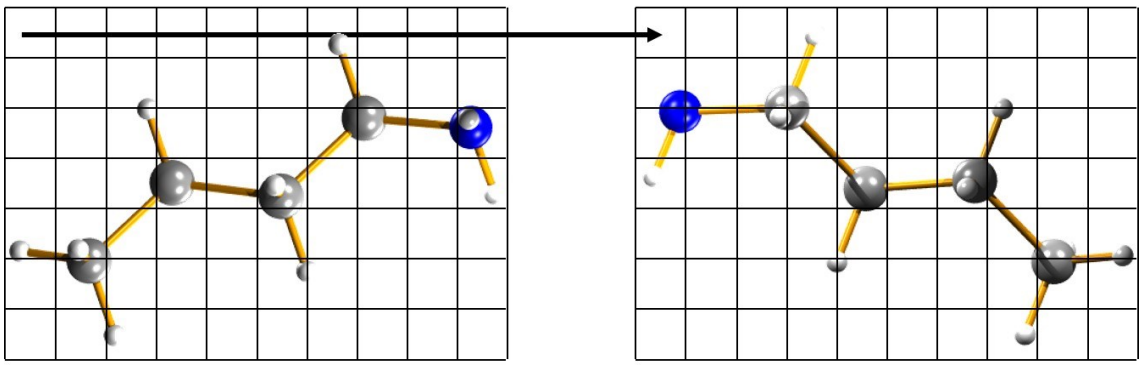

Figure 1.3: A representation of the PIXEL method. Cubes of electron density of a molecule are related to those of a symmetry related equivalent molecule. Distances between two pixels, represented by the arrow, are thus known from the crystal geometry. Carbon atoms are dark grey, hydrogen light grey, nitrogen blue.

1.3 PIXEL Interaction Terms

1.3.1 Coulombic Energy

The Coulombic interaction between a pair of molecules in the crystal structure is given by Coulomb's law. Consider two molecules, A and B, where A has nuclei of charge Z_j at positions $j = (x_j, y_j, z_j)$ and pixels of known charge q_k at positions $k = (x_k, y_k, z_k)$, and B has nuclei of charge Z_m at positions $m = (x_m, y_m, z_m)$ and pixels of known charge q_i at positions $i = (x_i, y_i, z_i)$. The electric potential generated by molecule A at point i of the charge density of molecule B is:

$$\Phi_i = \frac{1}{(4\pi\varepsilon_0)}\left[\sum_k \frac{q_k}{R_{ik}} + \sum_j \frac{Z_j}{R_{ij}}\right] \qquad (1.1)^9$$

Similarly, the electric potential generated by molecule A at nucleus *m* of molecule B is given by:

$$\Phi_m = \frac{1}{(4\pi\varepsilon_0)}\left[\sum_k \frac{q_k}{R_{km}} + \sum_j \frac{Z_j}{R_{jm}}\right] \qquad (1.2)^9$$

The total electrostatic energy is the sum of these electric potentials multiplied by the associated charges:

$$E_{Coul,AB} = \sum_i q_i \Phi_i + \sum_m Z_m \Phi_m \qquad (1.3)^9$$

1.3.2 Polarisation Energy

The polarisation energy is derived from the action of an applied electric field on a molecule which deforms the molecule's electron density. The resulting induced dipole moment μ is proportional to the electric field strength ε by a constant α, which is the molecular polarisability:

$$\mu = \alpha\varepsilon \qquad (1.4)^9$$

When the applied electric field is increased by *d*ε, the energy of the molecule will increase by –μ*d*ε. Consequently, on increasing the electric field from 0 to ε, the change in energy is given by:

$$\Delta E = -\int_0^{\varepsilon} \mu d\varepsilon \qquad (1.5)^9$$

which, when combined with Equation 1.4, gives:

$$\Delta E = -\int_0^{\varepsilon} \alpha\varepsilon d\varepsilon = -\frac{1}{2}\alpha\varepsilon^2 \qquad (1.6)^9$$

This result is incorporated into the PIXEL method by using atomic polarisabilities rather than molecular polarisabilities, so that $\alpha_i = (q_i/Z_{atom})\alpha_{atom}$, where α_i is the polarisability of pixel *i*, q_i is the charge of that pixel, and Z_{atom} and α_{atom} are the charge and polarisability of the associated atom respectively. The total polarisation energy of a molecule is given by the sum of the polarisation energies of the associated pixels.

1.3.3 Dispersion Energy

The PIXEL dispersion energy term is calculated by way of an extension of the Drude model[10] for calculating dispersion energy in three dimensions:

$$E_{disp} = \frac{-3\alpha_i \alpha_j h\nu}{4\left(4\pi\varepsilon^{\circ}\right)^2 \left(R_{ij}\right)^6} \qquad (1.7)^{10}$$

London proposed that since the energy term, $h\nu$, is related to the potential energy of an electron in the molecule, it can be approximated by the ionisation energy of the molecule. In the PIXEL method, each pixel is treated as a separate oscillating charge (as in the Drude model), and the term $h\nu$ is replaced by an "oscillator strength" E_{OS}. Each individual pixel i has its own ionisation potential I_i, and the oscillator strength between two pixels is given by:

$$E_{OS} = \left(I_i I_j\right)^{1/2} \qquad (1.8)^9$$

where I_i is a function of the ionisation potential I^o, and is given by:

$$I_i = I^{\circ} exp(-\beta R_i) \qquad (1.9)^9$$

where R_i is the distance between the pixel and the atomic nucleus and β is a parameter, which is dependent on the atom type, and which controls the rate at which the ionisation potential of a pixel falls away as the pixel is positioned further from the nucleus.

Repulsion Energy

In the PIXEL method, the repulsion energy is modelled as being proportional to the overlap between molecules. Given two molecules, A and B, this overlap, S_{AB}, is:

$$S_{AB} = \sum_{i,A} \sum_{j,B} \left[\rho_i(A)\rho_j(B)\right] V \qquad (1.10)^9$$

where ρ_i and ρ_j are the charge densities of molecules A and B and V is the pixel volume. This result is then split into contributions from pairs of atomic species, m and n, to give S_{mn}, by assigning each pixel to a specific atomic basin. The repulsion energy is then given by:

$$E_{rep,mn} = (K_1 - K_2 \Delta\chi_{mn}) S_{mn} \qquad (1.11)^9$$

where $\Delta\chi_{mn}$ is the difference in electronegativity between atomic species m and n, and K_1 and K_2 are empirical parameters. Since the origin of repulsion is quantum mechanical in nature, the overlap integral can be used as a semi-empirical approximation of the antisymmetrisation of the wavefunctions, which will increase as the molecules move closer together, with the corresponding increase in overlap. Since the PIXEL method uses undeformed electron densities, the term in the brackets in Equation 1.11

approximates the deformation of the electron densities as molecules come closer together in space.[9]

Gavezzotti initially proposed[11] an alternative method for the calculation of the repulsion energy:

$$E_{rep,AB} = K(S_{AB})^{\gamma} \qquad (1.12)$$

where S_{AB} is as Equation 1.10, and K and γ are empirical parameters different from K_1 and K_2 above. In the formulation of PIXEL used in this Thesis, the calculation of repulsion energies uses Equation 1.11.

Total Energy

The sum of the four terms (Coulombic, polarisation, dispersion and repulsion) gives the total intermolecular interaction energy. The result is a net energy of interactions between molecules in the solid state given along with a breakdown of how this energy is split between the various contributing terms. Furthermore, as the terms are calculated between symmetry equivalent molecules, use of a program such as Mercury[12], in tandem with the results of a PIXEL calculation, allows for interpretation of crystal packing from both geometric and energetic data. This facilitates the changing contributions of the four energy terms to be monitored along, for instance, a pressure study so that any possible changes in structure can be rationalised.

1.4 Practicalities of the PIXEL Method

The PIXEL method can only be applied to ordered crystal structures, and crystal symmetry must be lowered if necessary to ensure that no atoms in the structure sit on special positions so as to ensure there are only whole molecules in the asymmetric unit. The number of molecules in the asymmetric unit must be two or less. The original pixels formed from the electron density (0.04 x 0.04 x 0.04 Å) are too numerous to be practical for a quick calculation on a desktop computer. They are therefore combined according to a user-defined "condensation number" n into larger "super-pixels," commonly of 0.12 x 0.12 x 0.12 Å (n = 3) or 0.16 x 0.16 x 0.16 Å (n = 4) to use for the energy calculations. A smaller pixel size will result in a more accurate determination of the energies, but will increase the computing time four-fold for every step in n, since the computing times scale as the square of the number of pixels.[9]

A cluster of molecules is built up around a central reference molecule, and the size of this cluster is specified in the calculation, although it is typically 10 – 20 Å for molecular species and 40 – 50 Å or larger for charged species.[13] A larger cluster size is used when the Coulombic energy term, which is a long-range interaction, will continue to make a significant contribution to the total energy at long distances.

Certain measures are taken to compensate for the overlap of pixels that occurs when molecules are in close proximity. In the calculation of the Coulombic term, overlapping densities may lead to singularities due to the R^{-1} dependence in Equations 1.1 and 1.2, and to counter this pixel-pixel distances that are less than half the size of one of the dimensions of the super-pixels referred to above are reset to half of this distance in what is known as the "collision avoidance" procedure.

Similarly, in the calculation of the polarisation term, short pixel-pixel distances can lead to very high electric fields greater than 10^{13} V m^{-1}, which are physically unreasonable in molecular crystals. To compensate for this the collision avoidance procedure is applied before a damping term d_i is added to Equation 1.6 to calculate the polarisation energy at pixel *i*:

$$\Delta E_{POL,i} = -\frac{1}{2}\alpha_i[\varepsilon_i d_i]^2 \qquad \text{for } \varepsilon < \varepsilon_{max},\ d_i = \exp - (\varepsilon_i/(\varepsilon_{max} - \varepsilon_i)) \quad (1.13)^9$$

and $E_{POL,I} = 0$ for $\varepsilon > \varepsilon_{max}$. ε_{max} is an empirical parameter in the formulation and is normally set at 150 x 10^{10} V m^{-1}.

For the dispersion term, once again short pixel-pixel distances can lead to singularities due to the R^{-6} dependence of Equation 1.7. Consequently, the dispersion energy between two molecules A and B is given by:

$$\Delta E_{DISP,AB} = -\frac{3}{4}\sum_{i,A}\sum_{j,B} E_{OS} f(R)\alpha_i\alpha_j \,/\left[(4\pi\varepsilon_0)^2 (R_{ij})^6\right] \quad (1.14)^9$$

where $f(R) = \exp[-(D/R_{ij} - 1)^2]$ for $R_{ij} < D$, and D is an adjustable empirical parameter normally given the value 3.50 Å.

Finally, the standard value for the empirical parameter β in Equation 1.9 is 0.4 and those of K_1 and K_2 in Equation 1.11 are 4800 and 1200 respectively.

1.5 *Performance of the PIXEL Method*

Since the development of the PIXEL method by Gavezzotti in 2005, it has been used extensively to model intermolecular interactions in crystal structures, to rationalise phase transitions, and to investigate polymorphism. The performance of the PIXEL method in the calculation of both lattice energies and dimer interactions has been investigated in various studies. What follows is a review of work performed to date using the PIXEL method.

1.5.1 Validation of the PIXEL Method with Experimental Sublimation Enthalpies

The performance of the PIXEL method has been validated by Gavezzotti several times since its inception by comparing the lattice energies calculated by the method to experimental sublimation enthalpies.[8, 9, 14, 15] In more recent work,[16] PIXEL lattice energies for 154 organic compounds were compared to experimental sublimation enthalpies (Figure 1.4).

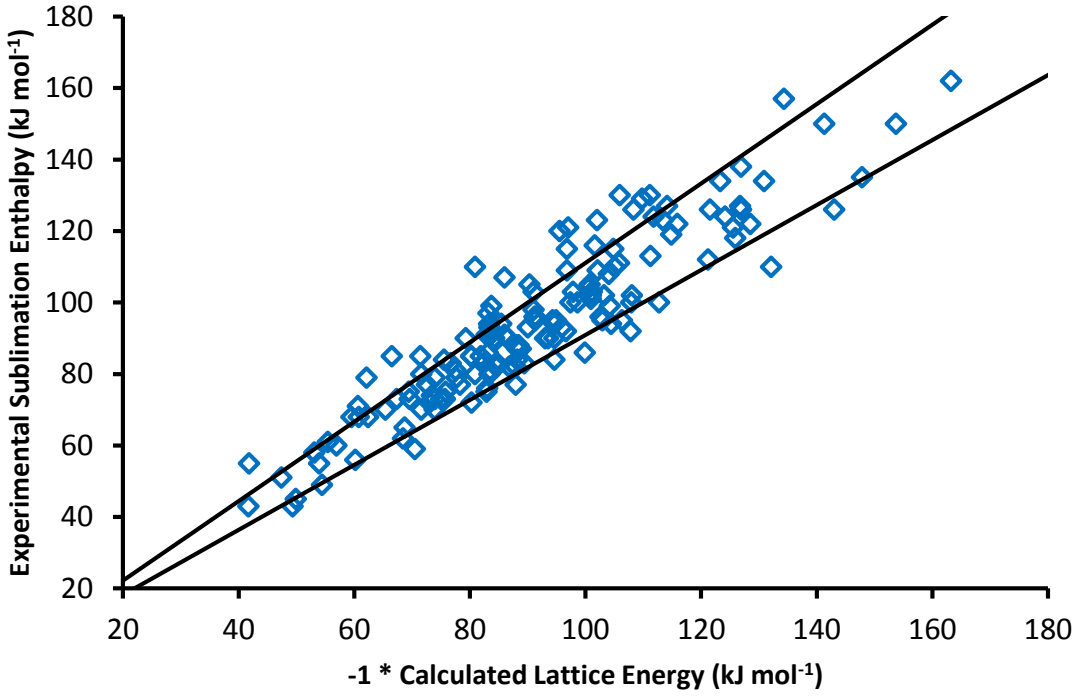

Figure 1.4: Calculated lattice energies compared to experimental sublimation enthalpies for 154 organic compounds. The black lines are ±10% of the experimental values. Reproduced from data in ref. 16.

The least squares parameters for the data in Figure 1.4 are $y = 1.03(1)\,x$ (where y are experimental sublimation enthalpies and x are PIXEL calculated lattice energies)

and R = 0.92. Surov *et al*. have also shown good agreement between PIXEL lattice energies and experimental sublimation enthalpies for a range of *N*-(3-thia-1-azabicyclo[3.3.1]non-2-ylidene)aniline derivatives, where the maximum deviation between PIXEL energies and experimental sublimation enthalpies was 11.9 kJ mol^{-1}.[17] Additionally, the calculated lattice energies showed the same trend in stability for the three derivatives studied as was obtained experimentally.

However, the PIXEL method does not take any conformational changes upon sublimation into account, and this can result in poor agreement with experimental sublimation enthalpies, as evidenced in work on oxalic acid by Raabe[18] and in a study of 1,2,4-thiadiazole derivatives by Surov and co-workers,[19] indicating that additional care should be taken when investigating flexible molecules, and in cases such as amino acids where proton transfer occurs upon sublimation[13]. Additionally, Aldridge *et al*.[20] have shown that PIXEL tends to overestimate lattice energies in boron-containing compounds by around 10%, although the correlation coefficient for their data was 0.95, indicating that the systematic overestimation for boron compounds may be the result of incorrect atomic parameterisation in the PIXEL method.

1.5.2 Comparison of PIXEL Energies with Higher Level Computational Methods

A comparison between the lattice energies calculated using the PIXEL method compared to those obtained through dispersion corrected periodic DFT and *ab initio* methods was performed by Maschio *et al*.[21] In this study, the results of which are shown in Figure 1.5, PIXEL lattice energies for a set of 60 organic compounds containing a range of different functional groups were compared to DFT-D calculated lattice energies at the B3LYP-D*/6-31G** level (where B3LYP-D* is a modified version of B3LYP-D).[22] Additionally, the performance of the LMP2/6-31G** (with an augmented basis set for H, C, N and O) and B97-D/6-31G** methods were compared for a subset of seven compounds.

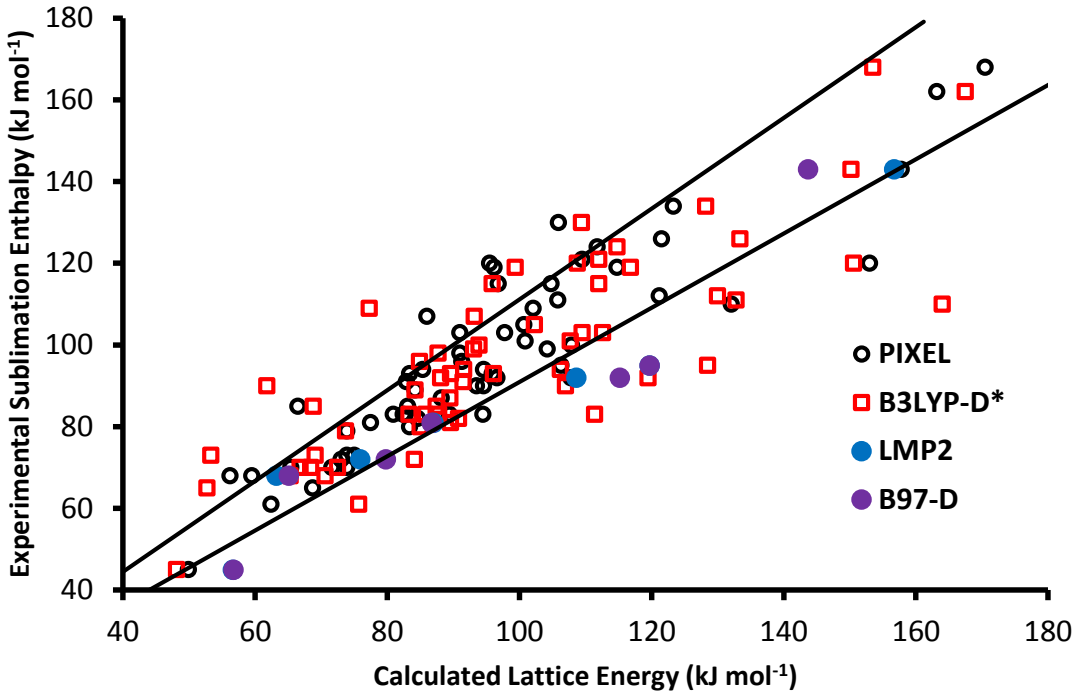

Figure 1.5: PIXEL calculated lattice energies and those from higher level computational methods compared to experimental sublimation enthalpies. The solid lines are ±10% of the experimental values. Reproduced from data in ref 21.

The least squares parameters for the lines of best fit $y = mx$ that can be drawn through the data points are shown in Table 1.1 for Set 1 (the full set of 60 compounds) and Set 2 (the subset of 7 compounds).

Set	m_{PIX}	R_{PIX}	$m_{B3LYP\text{-}D*}$	$R_{B3LYP\text{-}D*}$	m_{LMP2}	R_{LMP2}	$m_{B97\text{-}D}$	$R_{B97\text{-}D}$
1	1.01(1)	0.89	0.97(2)	0.77	–	–	–	–
2	0.93(3)	0.96	–	–	0.89(3)	0.97	0.89(4)	0.94

Table 1.1: The straight line parameters for the data points shown in Figure 1.5.

As the straight line parameters in Table 1.1 show, out of all four methods tested, PIXEL gives the best fit to experimental data. Additionally, Zhang *et al*. have reported agreement between lattice energies calculated using PIXEL and those from periodic DFT calculations (Wb97xd functional, no basis set details provided), where additionally experimental trends in sublimation enthalpies were reproduced by both methods.[23]

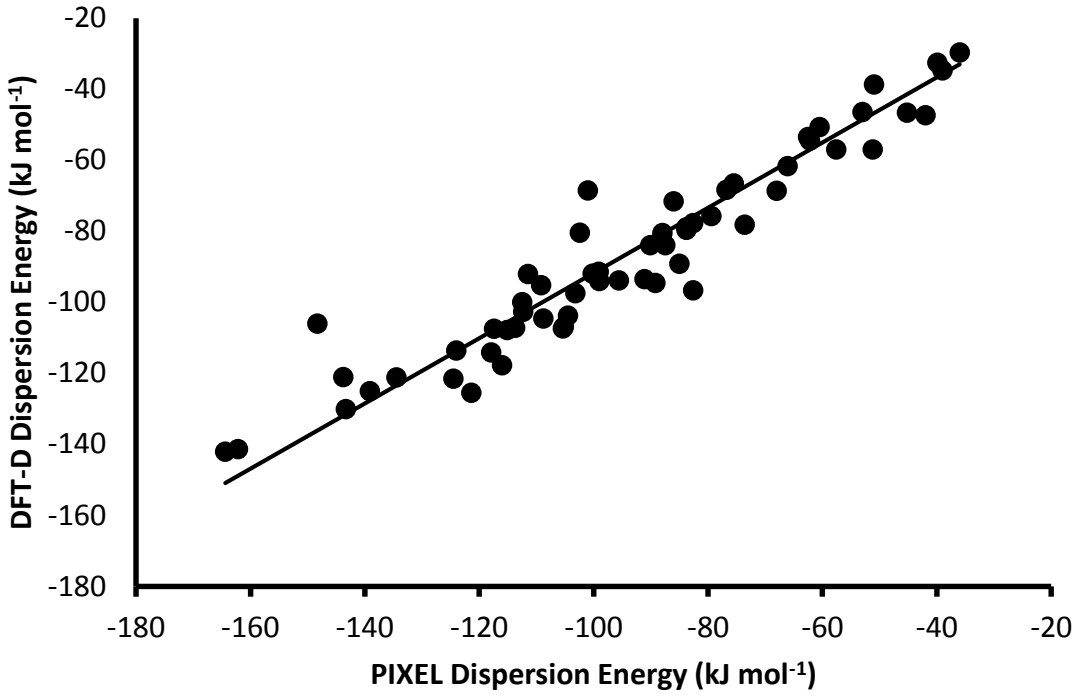

Figure 1.6: The PIXEL and DFT-D dispersion energies for 60 organic compounds. The black line is the least-squares straight line. Reproduced from ref. 21.

In the study by Maschio *et al*.[21] the total dispersion energies for each of the 60 organic complexes calculated by PIXEL were compared to those obtained at the B3LYP-D* level (Figure 1.6). The agreement between the PIXEL dispersion energies and those calculated with higher level DFT-D methods is given by the straight line $y = 0.92(1)\,x$ with a correlation coefficient $R = 0.95$ (black line in Figure 1.6), indicating the reliability of the London type method of calculating the dispersion energy used in PIXEL calculations.

In addition to lattice energies, the dimer interaction energies produced by PIXEL can be compared to those obtained from higher level computational methods. Work by Schweizer and Dunitz to investigate the interaction energies between dimers in the crystal structure of benzene[24] showed that, while the PIXEL calculated dimer energies were lower than those obtained at the MP2/6-31+G* and MP2/6-311++G** levels (with and without counterpoise corrections), the overall lattice energy estimated from these interactions, -43.8 kJ mol^{-1}, was closer to the literature sublimation enthalpy of -44.4 kJ mol^{-1} than those obtained from the MP2 calculations. Additionally, in calculations on a selection of fluorobenzene dimers, Schweizer and Dunitz demonstrated that PIXEL energies showed a similar trend in the order of dimer stability to energies calculated at

the MP2/6-311++G** level,[25] as did their study of alloxan.[26] PIXEL energies for two parallel displaced fluorobenzene dimers were not well reproduced (-12.5 and -9.4 kJ mol^{-1} from PIXEL calculations compared to -15.2 and -15.1 kJ mol^{-1} from MP2).

Volkov and Coppens have shown qualitative agreement for electrostatic interaction energies in six glycine dimers calculated using PIXEL with those calculated from the Morokuma-Ziegler scheme, and from Buckingham expressions utilising moments obtained through Hirshfeld "Stockholder" and AIM analysis (Figure1.7).[27]

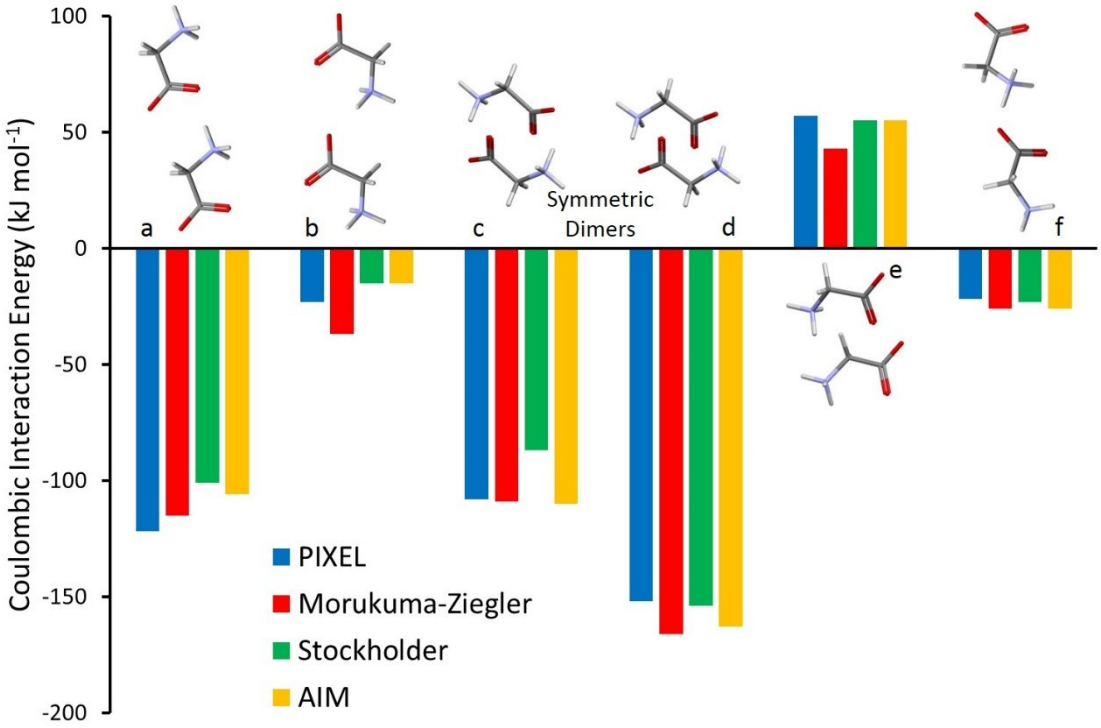

Figure 1.7: Coulombic energies between selected dimer interactions a – f. Dimers c and d are symmetrically related. Reproduced from data in ref. 27. Dimer models were generated from refcode GLYCIN19. Carbon atoms are dark grey, hydrogen light grey, nitrogen blue and oxygen red.

PIXEL dimer energies were found to be consistent with those obtained at the B3LYP/6-31G** level for a series of fluorinated 1,4-phenylenediboronic acids by Durka and co-workers (fitting of the PIXEL energies versus DFT gives straight line parameters $y = 1.02(1)x$ and $R = 0.98$).[28]

Kamiński *et al*. have shown deviations from the total energies calculated with PIXEL to those obtained from periodic DFT calculations at the B3LYP/pVTZ level, although the sum of the PIXEL electrostatic and polarisation energies showed the same trend in the strength of interactions as obtained from experimental values.[29]

1.5.3 Comparison of PIXEL Energies with Force Field Methods

The lattice and dimer energies calculated using the PIXEL method have been compared to those obtained using force field methods,[30-33] where the more detailed breakdown of intermolecular interaction energies into chemically meaningful terms afforded by the PIXEL method was found to be particularly advantageous. Additionally, in an early study by Dunitz and Gavezzotti,[34] electrostatic energies calculated by the PIXEL method were compared to those obtained from the UNI force field[35] for three polymorphs of 1,4-dichlorobenzene. The trends were found to be very different for the two methods, where PIXEL energies were much larger and sometimes of the opposite sign to those obtained from point-charges, highlighting the advantages of the treatment of Coulombic interactions by the PIXEL method over more traditional point charge methods.

Gavezzotti has compared the performance of the PIXEL method to that of the AA-CLP force field method for the calculation of the lattice energies of 154 organic compounds (Figure 1.8).[16]

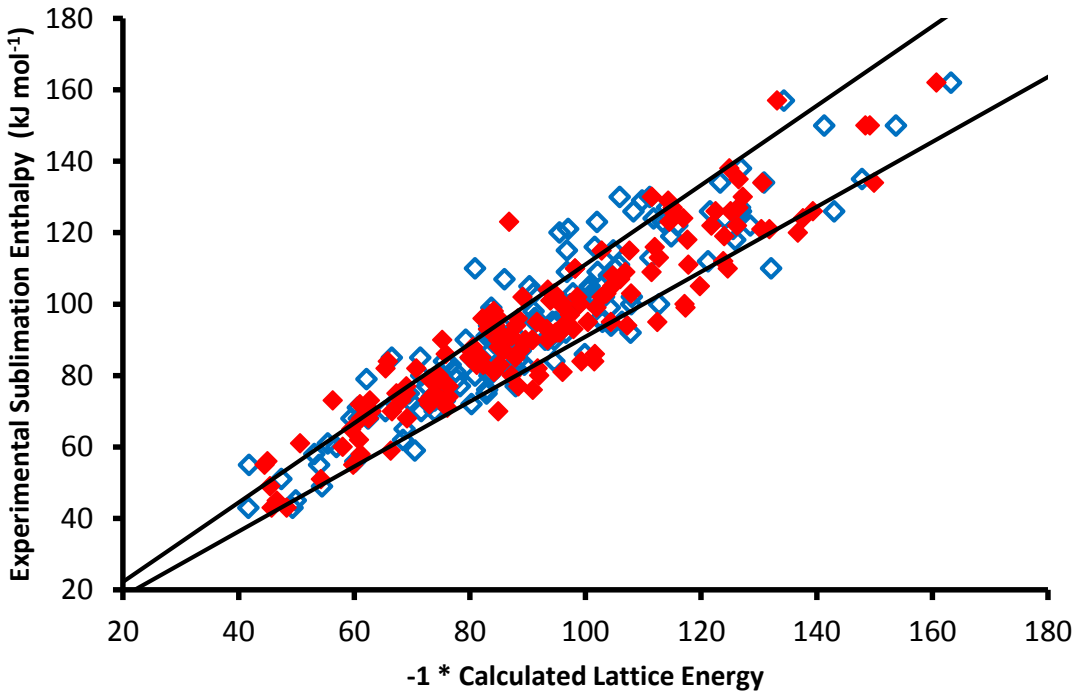

Figure 1.8: Lattice energies calculated with the PIXEL method (open blue diamonds) and with the AA-CLP force field method (closed red diamonds) compared to experimental sublimation enthalpies for 154 organic compounds. The black lines are ±10% for the experimental values. Reproduced with data from ref. 16.

The least squares parameters for these data are $y = 0.97x$ and $R = 0.845$ for the PIXEL energies, and $y = 1.02x$ and $R = 0.849$ for the AA-CLP energies, indicating that the two methods produce very similar results for calculated lattice energies compared to experimental values. However, significant differences exist between the component energy terms (Figure 1.9)

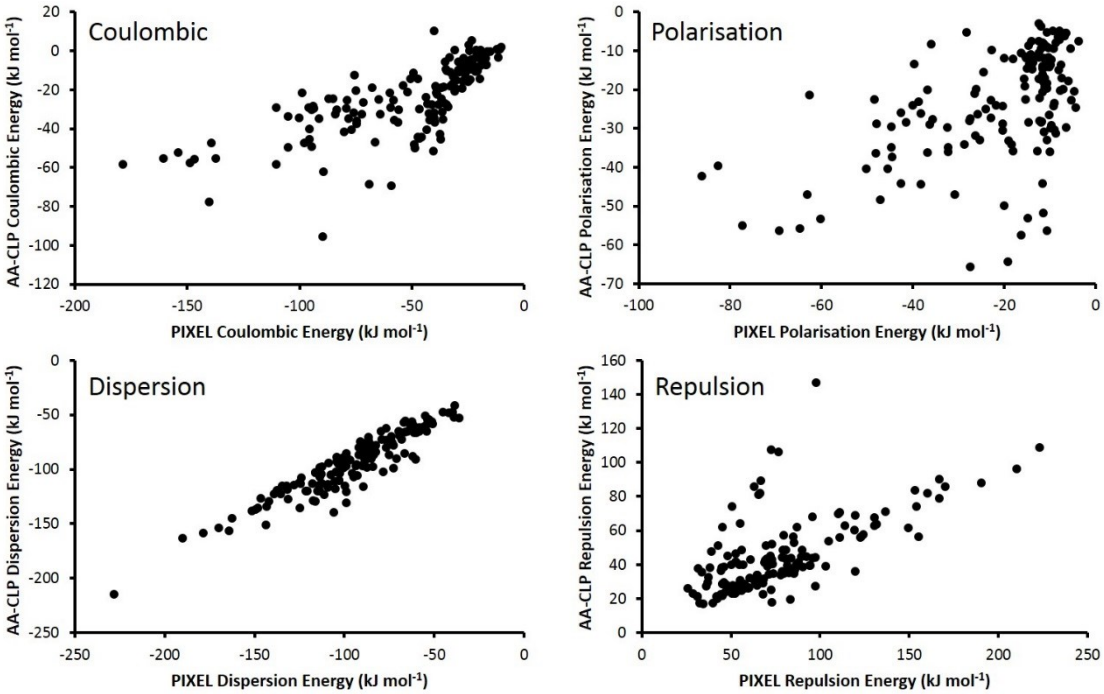

Figure 1.9: PIXEL component energies of the lattice calculations for 154 organic compounds compared to those obtained from the AA-CLP force field method. Reproduced with data from ref. 16.

While the dispersion terms for the two methods are very similar (due to the methods used in each process being somewhat alike), the correlation between the other terms is very poor. While the rapid nature of the AA-CLP force field calculations means that they are highly suited to the reproduction of experimental lattice energies, the modelling of the component energy terms indicates that the use of such methods as a tool for analysis of specific interactions where dispersion energies do not dominate should be treated with caution. The PIXEL method, at a reasonable increase in computing time, affords energy terms that, considering the agreement with other computational methods are a significant improvement on those obtained through force field methods.

1.6 Uses of the PIXEL Method

1.6.1 Using PIXEL to Rationalise Packing Effects

Since the PIXEL method produces interaction energies broken down into Coulombic, dispersion, repulsion and polarisation terms, the chemical nature of an interaction between molecules in a crystal can be inferred and used to rationalise packing effects that are difficult to understand through a purely geometric analysis.[4] This is highlighted by an investigation of nitrobenzene derivatives, where stacking interactions were found to be energetically dominant, with interactions of around 50 kJ mol^{-1}, compared to short hydrogen bonding interactions of around 10 kJ mol^{-1}.[36] Early PIXEL studies on organic fluorine compounds[30, 37] revealed why aliphatic hydrocarbons and fluorocarbons do not readily mix but aromatic species do (Table 1.2).

Dimer	E_{Coul}	E_{pol}	E_{disp}	E_{rep}	E_{tot}
B:B	-0.8	-4.0	-32.3	23.5	-13.6
HFB:HFB	-0.8	-4.2	-36.0	19.4	-19.9
B:HFB	-12.7	-4.7	-33.8	21.6	-29.7
H:H	-8.5	-3.8	-37.4	27.8	-22.0
P:P	-0.8	-0.1	-12.2	3.9	-9.1
H:P	-1.0	-0.4	-11.9	4.7	-8.5

Table 1.2: PIXEL total energies and component terms for the most stable dimer interactions between a selection of fluorinated and non-fluorinated organic compounds. B = benzene, HFB = hexafluorobenzene, H = hexane, P = perfluorohexane. Values are in kJ mol^{-1}. Reproduced from data in ref. 37.

Table 1.2 shows that, while the dispersion interactions are similar between all of the aromatic dimers, the significant increase in the Coulombic interaction between the benzene:hexafluorobenzene heterodimer makes it more stable than either of the homodimers. In the case of aliphatic compounds, the lower dispersion interaction of the heterodimer leads to the weakest total interaction of the three systems shown. Furthermore, the lower interactions between perfluorohexane dimers compared to hexane dimers sheds some light on why perfluorohexane has the lower boiling point (333 K compared to 341 K). This analysis was expanded on in an investigation of arene-perfluoroarene stacking interactions, where stacking energies of 20 – 25 kJ mol^{-1} were calculated, comparable to medium strength hydrogen bonds,[38] with similar interactions between dimers of benzene and its derivatives.[39]

Studies of a 1:1 complex of acetylene and benzene highlighted the importance of polarisation energies, where the magnitude of the polarisation energy (around 15 kJ mol^{-1}) was equal to the Coulombic contribution for the C-H…π interaction, and is the driving force of the formation of the T-shaped dimer observed in the crystal structure.[40] Gavezzotti has probed the energies of crystals with two molecules in the asymmetric unit,[41] demonstrating that the most energetic dimer interaction in $Z' = 2$ structures is on average more strongly interacting than when $Z' = 1$. However, the energy of this most tightly bound dimer can lie anywhere from 10% to 70% of the total lattice energy, highlighting that in many cases the asymmetry occurs between weakly interacting molecules.

Gavezzotti has also applied the PIXEL method to the nature of halogen bonding, noting that while short halogen-oxygen and halogen-nitrogen contacts do form in many crystal structures, these interactions are not always the most energetically stabilising.[42] For instance, in the crystal structure of the co-crystal of 1,2-bis(4-pyridyl)ethene and 1,4-dibromo-2,3,5,6-tetrafluorobenzene (refcode IKUHUR03), the short Br…N contact (2.81 Å) with an energy of 10 kJ mol^{-1} is lower than the surrounding stacking interactions, which sum to 62 kJ mol^{-1} (Figure1.10)

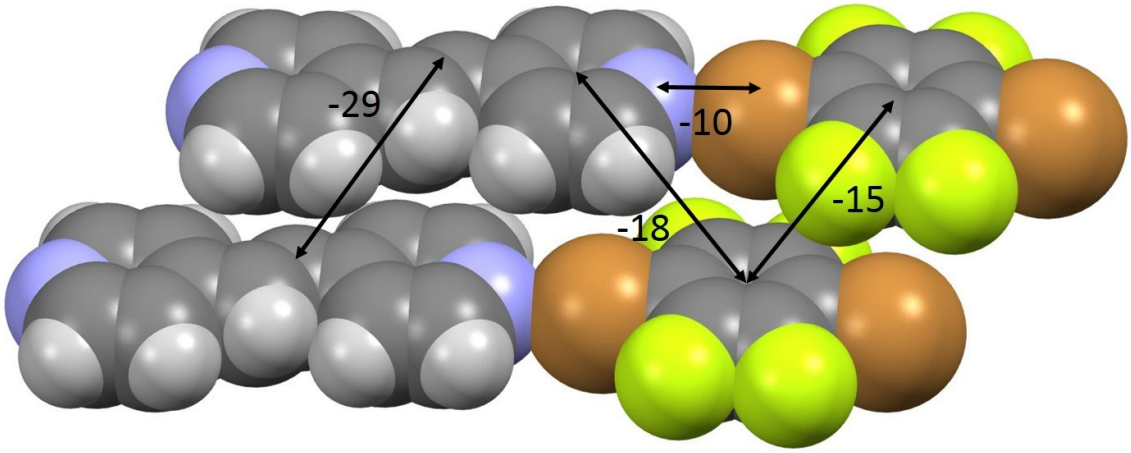

Figure 1.10: The Br…N interaction is lower than all of the surrounding stacking interactions. Values are in kJ mol^{-1}. Reproduced from data in ref. 42 and refcode IKUHUR03. Carbon atoms are dark grey, hydrogen light grey, nitrogen blue, fluorine light green and bromine brown.

Kaźmierczak and Katrusiak have used the breakdown of energy terms to rationalise the interactions in "loose" crystals where the closest contacts are greater than the sum of the van der Waals radii.[43] In the crystal structure of *bis*(trichlorosilyl)acetylene (refcode WILWUJ), the loosest structure in the CSD, a

dispersion interaction of -24.2 kJ mol^{-1} occurs between the two closest molecules, even though the closest contact (Cl…Cl) is 0.256 Å longer than the sum of the van der Waals radii of the two chlorine atoms (3.5 Å).

PIXEL analysis is becoming a common step in the analysis of novel crystals, co-crystals and solvates,[44-49] and several studies have investigated the differences in intermolecular interactions and packing effects over families of related compounds, isomers and tautomers.[50-71] In the 2:1 sulfamethazine-theophylline co-crystal, both tautomers of sulfamethazine are present (Figure 1.11).[52]

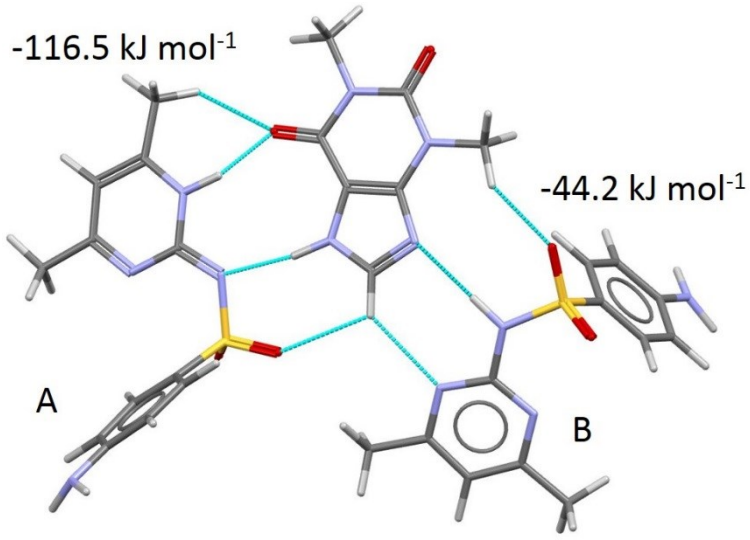

Figure 1.11: The two tautomers of sulfamethazine in the 2:1 cocrystal with theophylline. Reproduced from refcode AWIJEW and data from ref. 52. Carbon atoms are dark grey, hydrogen light grey, nitrogen blue, oxygen red and sulphur yellow.

The presence of both tautomers of sulfamethazine is surprising, as the form protonated at the nitrogen atom of the aromatic ring (molecule A in Figure 1.11) is found (through DFT calculations, B3LYP/6-311++G**) to be 33.2 kJ mol^{-1} less stable than when the nitrogen atom in the chain is protonated (molecule B), and, to date, no crystal structures exist of the higher energy form. PIXEL analysis of the intermolecular energies, however, shows that the strong interaction of -116.5 kJ mol^{-1} between theophylline and sulfamethazine A more than compensates for the destabilisation of this tautomer, and made it possible for it to be observed in the solid state for the first time.

Abboud *et al*. have rationalised the conformational disorder in a benzaldehyde derivative through the analysis of specific intermolecular interactions,[72] where the interaction energies of one conformer were found to be 13.2 kJ mol^{-1} more favourable than the other, a result consistent with an experimentally higher observed occupancy

(0.740(5)). Khorasani and Fernandes have used PIXEL lattice and dimer interaction energies to study the solid state Diels-Alder reaction of 9-methylanthracene with bis(*N*-cyclobutylimino)-1,4-dithiin, where the formation of an unfavourable (+ 34.3 kJ mol^{-1}) interaction between methyl groups in neighbouring molecules resulting from one interaction pathway affects the reaction mechanism.[73]

Concerted geometric and PIXEL energetic analysis have been used to investigate trends in hydrogen bonding in cyclic dimers of carboxylic acids,[74] and the breakdown of PIXEL interaction energies into Coulombic and dispersion components makes it an ideal method to investigate the interplay between hydrogen bonding and other interactions in crystal structures, as evidenced by various studies.[75-78] An analysis of the competing interactions in the crystal structures of the primary amines[79] is presented in Chapter 6 of this thesis.

In the crystal structures of tetrafluoronaphthoic acid and tetrafluoronaphthamide,[75] competition exists between hydrogen bonding and arene stacking interactions similar to those described in Table 1.2, which are both present in these molecules. Figure 1.12 shows the intralayer and interlayer hydrogen bonding motifs present in the crystal structure of tetrafluoronaphthamide.

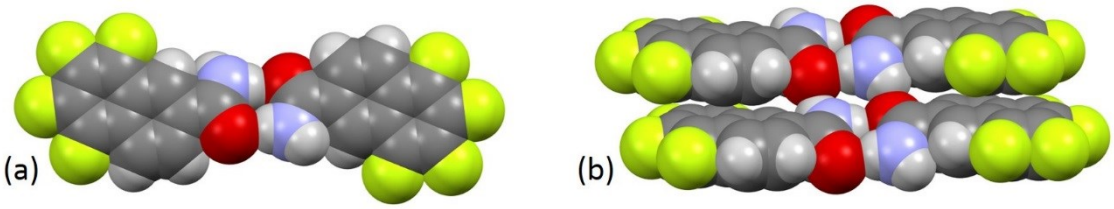

Figure 1.12: The intralayer hydrogen bonding (a) and interlayer hydrogen bonding (b) in the crystal structure of tetrafluoronaphthamide (refcode VUHQUL). Carbon atoms are dark grey, hydrogen light grey, nitrogen blue, oxygen red and fluorine light green.

The intralayer cyclic hydrogen bond (Figure 1.12a) has a total energy of -57 kJ mol^{-1}, with a large Coulombic component of -73 kJ mol^{-1}, and is the strongest interaction in the structure. The interlayer hydrogen bond (Figure 1.12b) has a total interaction energy of -44 kJ mol^{-1}, and consists of a Coulombic term of -35 kJ mol^{-1}, with a complementary dispersion term of -38 kJ mol^{-1} due to the stacking interaction of the aromatic rings. While the most favourable interactions between fluorinated (Ar^F) and non-fluorinated (Ar^H) arene systems described above (Table 1.2) occur between heterodimers (Ar^F – Ar^H interaction) with no ring offset (i.e. the aromatic rings lie directly above one another), in the tetrafluoronaphthamide crystal the ring offset is as

large as 2.91 Å due to the geometry of the interlayer hydrogen bonding interaction. In tetrafluoronaphthoic acid a similar offset occurs, but it is smaller at 2.57 Å. Due to the positions of the molecules with respect to this offset, the more favourable Ar^F – Ar^H interactions are replaced by less favourable Ar^F – Ar^F and Ar^H – Ar^H interactions, and as such the strongest possible stacking interactions in these structures are sacrificed in the interest of a stronger hydrogen bonding network.

Gibson *et al.* used the results of PIXEL calculations on the structures of 4-benzylalanine, which displays an absence of hydrogen bonding, and 4-benzylalanine hydrochloride, which exhibits a number of hydrogen bonds, to rationalise the different solubilities of these compounds in chlorobenzene,[80] while similar work was performed in a study of the hydrochlorination of 4,4'-methylenedianiline.[81] Panini and Chopra have used PIXEL energies to explore short C-H…F contacts,[82] citing their results, which show significant Coulombic character, as evidence of hydrogen bonding.

In polymorphic systems, it was shown that slight differences in Coulombic energies leads to the yellow polymorph of ROY (5-methyl-2[(2-nitrophenyl)amino]-3-thiophenecarbonitrile) being the most thermodynamically stable.[32] Similar studies have explored the differences in polymorphs of *D*-mannitol, aflatoxin and aspirin,[83] while PIXEL calculations showed differences between Coulombic, polarisation and dispersion contributions to two polymorphs of a Asn-Asn-Gln-Gln tetrapeptide.[84] Several other studies have used the PIXEL method to investigate polymorphism, where although total lattice energies were found to only vary by a few kJ mol^{-1}, the breakdown of component energy terms and analysis of specific intermolecular interactions have highlighted subtle differences between structures.[5, 85-94] In a study of two polymorphs of *N*-[2-(hydroxymethyl)phenyl]benzamide,[85] the total PIXEL lattice energies of polymorphs I and II were found to differ by only 2.7 kJ mol^{-1} (-129.7 and -127.0 kJ mol^{-1} respectively). However, the nature of the intermolecular interactions were very different in the two polymorphs (Figure 1.13).

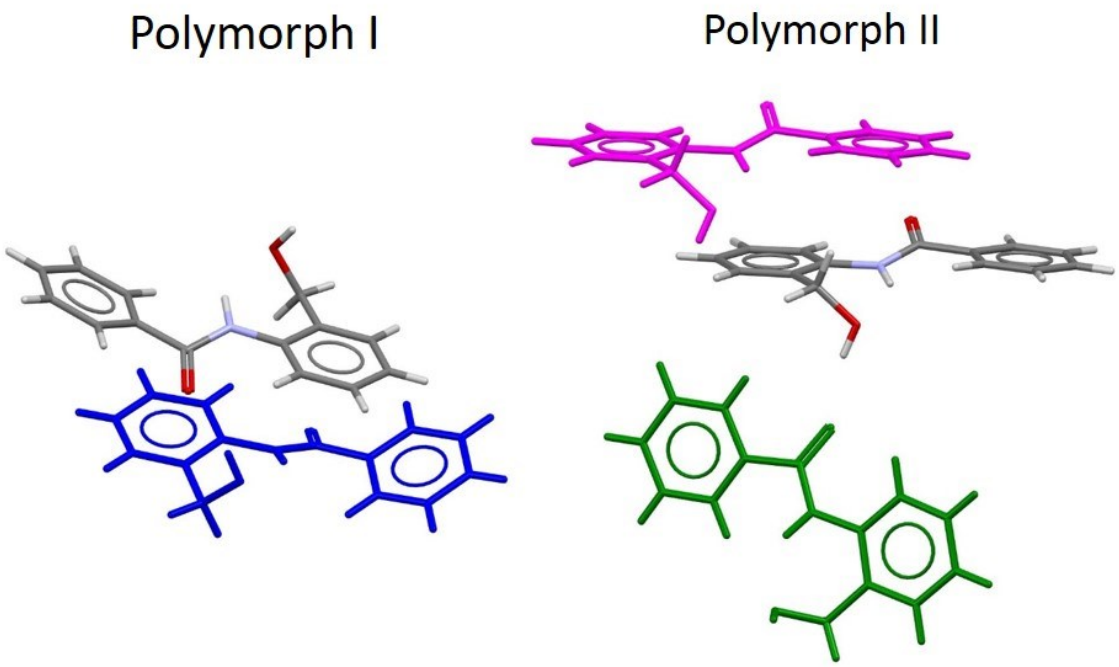

Figure 1.13: The principal intermolecular interactions in the two polymorphs of *N*-[2-(hydroxymethyl)phenyl]benzamide. Reproduced from refcodes AWEWAB and AWEWAB01. Carbon atoms are dark grey, hydrogen light grey, nitrogen blue and oxygen red.

In polymorph I, the most favourable interaction (blue in Figure 1.13) consists of both an O-H…O=C hydrogen bond and a stacking interaction with an interaction energy of -62.7 kJ mol^{-1}, making up almost half of the total lattice energy. In polymorph II, this interaction seems to be split over two different molecules. While a similar hydrogen bonding interaction is still the strongest (-38.2 kJ mol^{-1}, green molecule), the stability is retained through a different stacking arrangement between a different molecule (-27.9 kJ mol^{-1}, magenta in Figure 1.13). The total energy of these two interactions is therefore -66.1 kJ mol^{-1}, comparable to the single strong interaction in polymorph I, and an indicator of how different combinations of intermolecular interactions in different polymorphs can lead to similar total lattice energies.

The analysis of PIXEL calculated intermolecular interactions in crystals has been recently facilitated by the development of Bond's processPIXEL program.[95] This takes the results of a PIXEL calculation and generates energy-vectors[96, 97] to represent the individual interactions. These vectors can be viewed through Mercury superimposed on the crystal structure, allowing the most important interactions, along with the major contributing terms, to be viewed easily (Figure 1.14)

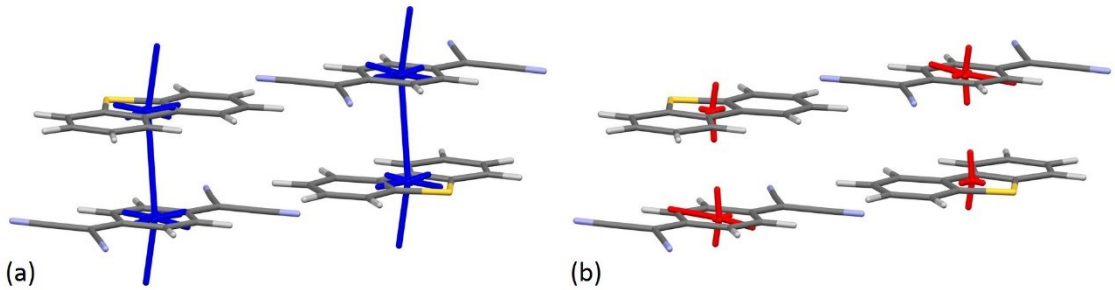

Figure 1.14: The differences in the dispersion component (a) and the Coulombic component (b) in the stacking interaction of the co-crystal of dibenzothiophene and 7,7,8,8-tetracyanoquinodimethane visualised using processPIXEL. Reproduced from ref. 95. Carbon atoms are dark grey, hydrogen light grey, nitrogen blue and sulphur yellow.

Figure 1.14 shows the visualisation produced by processPIXEL of the dispersion and Coulombic terms for the stacking interaction in the co-crystal of dibenzothiophene and 7,7,8,8-tetracyanoquinodimethane. It is clear from the figure that the dispersion term dominates this interaction, and visualisation of interaction energies in this way will facilitate the analysis of crystal packing and clarify which interactions dominate a crystal structure.

1.6.2 Using the PIXEL Method to Investigate Structures Under Pressure

In addition to the example of serine monohydrate cited above in Section 1.1, the PIXEL method has been used extensively to study the ways in which intermolecular interactions are changed by the effects of pressure, and to rationalise how such changes can lead to phase transitions. In other high pressure studies, energetic analysis of the structures of L-serine[13] and aniline[98, 99] showed that rather than as a consequence of interactions becoming more repulsive in these cases, intermolecular energies remained relatively constant upon application of pressure. Phase changes in these structures were subsequently found to be the result of a need to reduce volume, a result contrary to that deduced from geometric analysis alone in the case of L-serine, where the phase transition was originally ascribed to the avoidance of short H…O contacts.[100, 101] Similar energetic studies were carried out on α-glycine, although no phase transition is observed in this structure.[102]

The crystal structure of salicylaldoxime-I[103] consists of pairs of molecules interacting through oximic OH…O hydrogen bonds to form dimers, which in turn interact through π…π stacking contacts. It was found that the total lattice energy

becomes more positive upon application of pressure up to 5.28 GPa due to an increase in the repulsion term caused by the molecules being forced closer together, a result common to substituted salicylaldoximes.[104] A phase transition between 5.28 GPa and 5.93 GPa results in a small change in unit cell (estimated at -0.4 $Å^3$) volume with a corresponding energy change of -1.4 kJ mol^{-1}, but PIXEL calculations showed an estimated increase in stability of around 25 kJ mol^{-1} for the new form II over form I. Salicylaldoxime is therefore an unusual example of a high pressure phase transition being driven by intermolecular interactions rather than simply the need to minimise volume. Analysis of the individual interactions in salicylaldoxime-I shows that there are seven principal intermolecular interactions (> 2.5 kJ mol^{-1}) the strongest of which is the oximic hydrogen bond (-25.0 kJ mol^{-1} at ambient conditions, Figure 1.15a), with two stacking interactions with energies of -8.7 and -8.1 kJ mol^{-1} at ambient conditions the next strongest (Figure 1.15b).

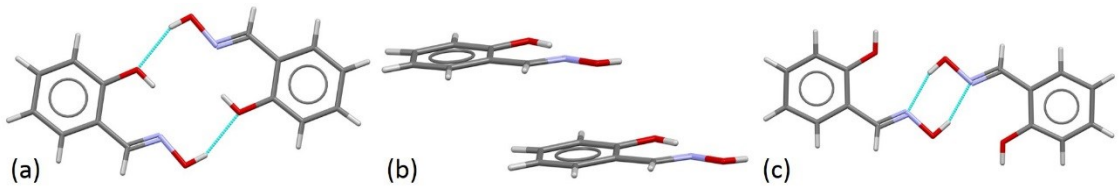

Figure 1.15: (a) The oximic hydrogen bonded dimer at ambient conditions, (b) the stacking interaction that is strongly affected by pressure and (c) the O-H…N hydrogen bond formed in phase II. Structures obtained from CSD refcodes SALOXM03 and SALOXM09. Carbon atoms are dark grey, hydrogen light grey, nitrogen blue and oxygen red.

After the phase transition, a new O-H…N hydrogen bond is formed which has an energy of -16.0 kJ mol^{-1} (Figure 1.15c). This is comparable to the energy of the original oximic hydrogen bond at 5.28 GPa (-17.6 kJ mol^{-1}), which ceases to be an attractive interaction after the phase transition. PIXEL analysis along the pressure series from ambient up to 5.28 GPa shows that the energies of the oximic hydrogen bond and one of the stacking interactions are strongly affected by pressure (Figure 1.16), and that the phase transition occurs in order to avoid the increasing repulsion caused by further shortening of these interactions.

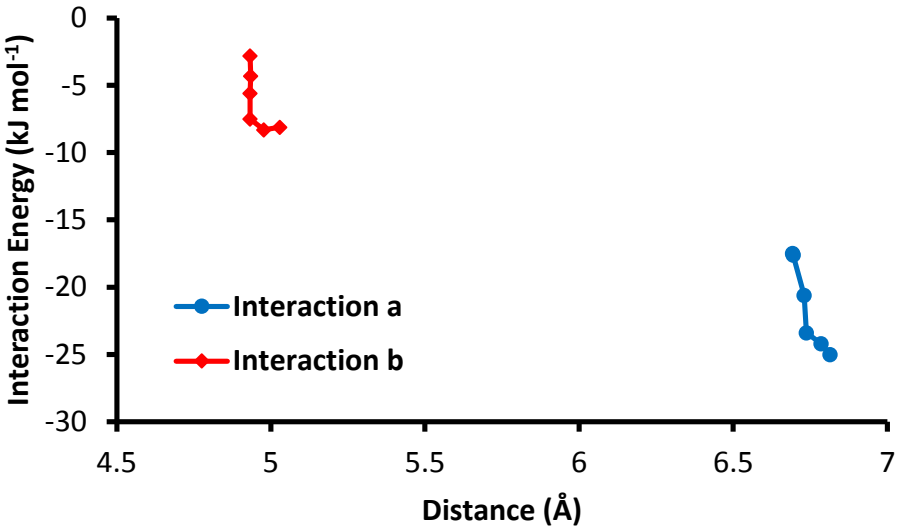

Figure 1.16: The change in the energies of interactions (a) and (b) (Figure 1.15) as the distances between centres of mass are reduced upon the application of pressure up to 5.28 GPa. Reproduced from data in ref. 103.

The analysis of how the energies of specific intermolecular interactions change upon application of pressure has also been used to analyse the structure of 3-aza-bicyclo(3.3.1)nonane-2,4-dione, where it was predicted that a phase transition might occur at pressures higher than 7 GPa due to increasing repulsion interactions between principal intermolecular contacts,[105] and in bianthrone where the increasing instability of the main intermolecular interactions is likely the cause of the observed phase transition and accompanying colour change in this compound at high pressures.[106] Similar analysis has been performed during pressure studies of the crystal structures of rubrene,[107] acrylic acid,[108] (2-fluoro-3-pyridyl)(4-iodophenyl)borinic 8-oxyquinolinate,[109] betaine monohydrate,[110] L-cysteic acid monohydrate,[110] *S*-4-sulfo-L-phenylalanine monohydrate[110] and 1,2-bis(2-methylbenzothiophen-3-yl)perfluorocyclopentene.[111]

In a high pressure study of salicylamide, Johnstone *et al.*[112] reported that the ambient phase structure, salicylamide-I, was stable up to 5.1 GPa. This structure was found to be different to two previously reported structures of salicylamide,[113, 114] where PIXEL analysis found that short H…H contacts in these structures were highly destabilising, indicating that the original structures were incorrect, using the wrong origin for the reported coordinates. In the work by Johnstone, a new phase, salicylamide-II, was obtained through *in situ* crystal growth at 0.2 GPa and PIXEL

calculations, along with DFT calculated vibrational frequencies, were used to rationalise the differences between the two structures. Comparison of calculated lattice energies found that phase-I was around 2 kJ mol^{-1} more favourable than phase-II at 0.2 GPa, and that phase-I was dominated by Coulombic and polarisation terms while phase-II is favoured by dispersion and lower repulsion energies. The differences in the Coulombic terms were a result of a more favourable hydrogen bonding network in phase-I, where individual interactions were almost double those observed in phase-II, although this loss in hydrogen bonding is compensated for in phase-II by more numerous stacking and C-H…π interactions. Vibrational frequency calculations showed that it was these differences in hydrogen bonding and dispersion interactions that led to the formation of salicylamide-II at 0.2 GPa as a result of more a more favourable zero point energy and higher entropy.

The PIXEL method has been used to investigate several other new polymorphs of compounds obtained through *in situ* high pressure crystallisation, such as imidazole,[115] D,L-mandelic acid,[116] aniline[117] and propionamide,[118] where differences in lattice energies and intermolecular interaction energies have been used to rationalise the differences between polymorphs. Additionally, Fabbiani *et al.*[119] used PIXEL calculations to investigate crystals of γ-amino butyric acid obtained from a seed crystal grown at high pressure.

As these examples show, since the PIXEL method gives a breakdown of the individual interaction energies in a crystal into chemically meaningful terms in addition to the total lattice energy of the structure, it is ideally suited to aiding the analysis of the changes in crystal structures at increasing pressures.

1.6.3 Crystal Structure Prediction and Crystal Energy Landscapes

Over the last decade, the PIXEL method has been applied to crystal structure prediction (CSP). It has performed successfully in Cambridge Crystallographic Data Centre blind tests,[120, 121] where the energies of crystal structures generated through the Zip-Promet procedure[122] and minimised with the UNI force field were calculated with PIXEL. However, since no change in the molecular conformation is possible during PIXEL calculations, it has not been used in the generation of energy minimised crystal structures during CSP studies, although it has been used to rationalise the outcomes of

such investigations. Since the PIXEL method gives a breakdown of intermolecular interaction energies into chemically meaningful terms such as Coulombic and dispersion forces, calculations of dimer energies can be utilised to ascertain which interactions are dominant in the formation of different crystal structures. This is exemplified in a study by Cruz Cabeza *et al.*[123] where PIXEL calculations on the results of the crystal structure prediction of carbamazepine (CBZ) and its derivatives (carbamazepine 10,11-epoxide (ECBZ), oxcarbazepine (OXCBZ) and 10,11-dihydrocarbamazepine (DHCBZ)) were used to understand why hydrogen bonded chains are favoured in some derivatives but not others.

Interaction	Molecule	Crystal Structure	E_{Coul}	E_{pol}	E_{disp}	E_{rep}	E_{total}
anti-dimers	CBZ	exp. form III	-32.7	-11.3	-6.0	25.2	-24.8
	ECBZ	hyp. rank 1	-29.2	-9.6	-6.1	21.8	-23.0
	DHCBZ	hyp. rank 8	-35.1	-11.6	-6.4	28.8	-24.2
	OXCBZ	hyp. rank 6	-27.2	-8.0	-5.8	17.8	-23.1
syn-dimers	ECBZ	exp. *Pbcn*	-17.8	-5.2	-5.5	9.4	-19.0
chains	CBZ	hyp. rank 2	-21.5	-9.8	-15.5	22.2	-24.7
	DHCBZ	exp. $P2_1/c$	-25.8	-11.7	-16.4	25.4	-28.6
	OXCBZ	exp. $P2_1/c$	-25.5	-10.9	-16.4	23.8	-28.9

Table 1.3: Interaction energies per molecule for the most stable (experimental or hypothetical) dimers and chains in the structures calculated using the PIXEL method for carbamazepine and its derivatives. Energies are in kJ mol^{-1}. *Syn* and *anti* refer to the relative orientations of the carbamazepine rings. Reproduced from ref. 123.

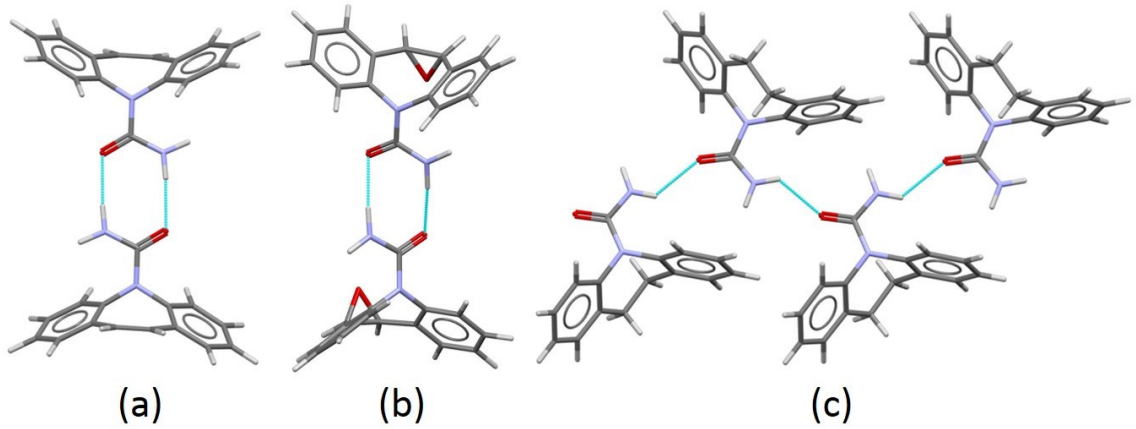

Figure 1.17: The three types of interactions investigated in carbamazepine derivatives: (a) *anti*-dimer; (b) *syn*-dimer; (c) chain. Produced from refcodes CBMZPN02, ZIPTEX and VACTAU01. Carbon atoms are dark grey, hydrogen light grey, nitrogen blue and oxygen red.

Table 1.3 shows the interaction energies between pairs of carbamazepine and carbamazepine derivative molecules (Figure 1.17) calculated using the PIXEL method from the study of Cruz Cabeza. The Coulombic terms are clearly stronger for the dimer interactions rather than the chains in all cases, leading to CBZ favouring such an interaction experimentally. However, it can be seen that the loss in Coulombic energy upon formation of chains is compensated for by a significant increase in the dispersion term, and this results in the chain motif being favoured by 4.4 and 5.8 kJ mol^{-1} in DHCBZ and OXCBZ respectively. In the case of ECBZ, while chains are not formed, it is clear that the Coulombic energy for the *anti*-dimer conformation is significantly greater than for the experimentally observed *syn*-dimer, indicating that polymorphism could be expected for this compound. The breakdown of interaction energies into component terms provides valuable insight into the relative energetic benefits of different packing motifs, and is therefore a useful tool in the analysis of the results of crystal structure prediction, further examples of which include the study of chlorothiazide,[124] cocrystals of *cis*-carboxamides and carboxylic acids,[125] hydantoins, dihydrouracils and uracils,[126] creatine,[127] and the drug molecules 3-(4-(benzo[d]isoxazole-3-yl)piperazin-1-yl)-2,2-dimethylpropanoic acid and 3-(4-dibenzo[b,f][1,4]oxepin-11-yl-piperazin-1-yl)-2,2-dimethylpropanoic acid.[128] Additionally, PIXEL calculated lattice energies were used to investigate the experimental and predicted structures of Pigment Red 168 and other dihalogenated anthanthrones,[129] and Bhardwaj *et al*. used both lattice energies and dimer energies to investigate different experimental and predicted forms of olanzapine.[130]

The nature of the crystal energy landscapes of molecular compounds, that is to say the feasible crystal structures generated by computational methods, can be thoroughly investigated with the PIXEL method. In work performed by Gavezzotti[131] the Zip-Promet procedure was used to generate crystal energy landscapes for three organic compounds: naphthalene, naphthoquinone and 1,2-dichlorobenzene. Additionally, the energy landscapes of 2,3-dimethylbenzoic acid, parabanic acid and pyridine were investigated with PIXEL, where the crystal structures were obtained from previous analyses.[132-134] For naphthalene and naphthoquinone the experimental structures were reproduced as the most stable, as well as that of pyridine form II (form I could not be investigated as it has $Z' = 4$). For 2,3-dimethylbenzoic acid the

experimental structure was ranked second, while for 1,2-dichlorobenzene the experimental structure was the third most favourable. In all of these cases, the PIXEL method performed as well as or better than calculations with the UNI force field or distributed multipole analysis. However, PIXEL was unable to reproduce the experimental structure of parabanic acid as the most stable, although it was postulated that this was a result of the complicated hydrogen bonding network in this crystal structure, and the minimisation procedure using the UNI force field described above may not have generated a suitable model.

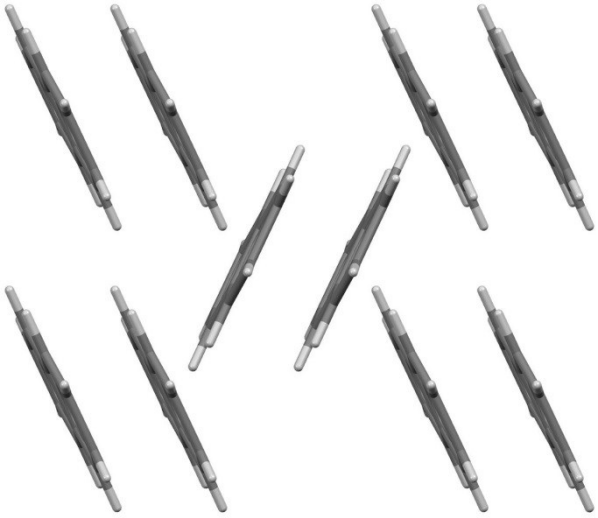

Figure 1.18: The crystal structure of naphthalene is a compromise between a stacking interaction and that achieved through a herringbone motif. Carbon atoms are dark grey and hydrogen light grey.

The breakdown of PIXEL energies into chemically meaningful terms was used in the above study to rationalise how different packing motifs achieve a balance of favourable intermolecular interactions. As such, the forces that determine the structure that is observed experimentally can often result from a compromise between several types of interaction. For instance, in the experimental crystal structure of naphthalene (Figure 1.18), the arrangement of molecules where the interplanar angle is 47° seems to be a combination of two thermodynamically favourable motifs where the molecules are stacked parallel and perpendicular. A similar study was performed on caffeine and some other methylxanthines,[135] where the results were able to rationalise why anhydrous caffeine does not form an ordered crystal upon dehydration due to the thermodynamically unfavourable rearrangement required to generate a stable structure.

Additionally, Braun *et al.* used PIXEL calculated lattice and dimer energies to investigate the crystal energy landscape of pyrogallol anhydrate.[136]

Expanding on previous work investigating short oxygen-oxygen contacts in nitro compounds,[137] Gavezzotti used the PIXEL calculated dimer energies to classify the interactions in a sample of 1177 organic crystals, and to estimate the forces acting between the molecules based on energy differences as the distances between the dimers were varied.[138] It was found that, in many crystal structures, destabilising contacts can often occur between nearby molecules, such as in the case of 3-methyl-3-pyrazolin-5-one (Figure 1.19).

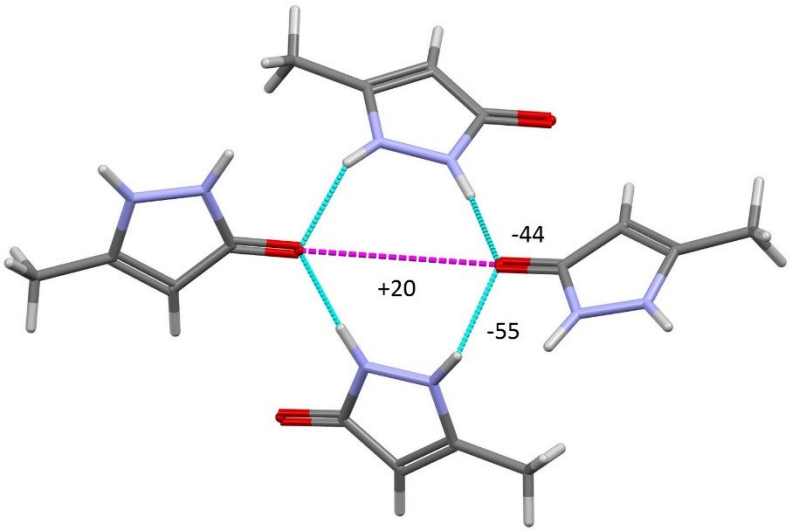

Figure 1.19: A destabilising interaction (magenta line) occurs in near neighbours of the crystal structure of 3-methyl-3-pyrazolin-5-one (CSD refcode MPYAZO11), compensated for by hydrogen bonding interactions (blue lines). Energies are in kJ mol^{-1}. Reproduced from ref. 138. Carbon atoms are dark grey, hydrogen light grey, nitrogen blue and oxygen red.

The strong hydrogen bonding interactions in the structure of 3-methyl-3-pyrazolin-5-one result in the formation of a tetramer, where a destabilising interaction occurs between the carbonyl oxygen atoms (separated by a distance of 3.11 Å). Additionally, the interaction between the N-H groups across the hydrogen bond ring is also destabilising (+8 kJ mol^{-1}). As Gavezzotti comments, the presence of such interactions are likely to be a contributing factor to the difficulties of crystal structure prediction. In a similar fashion to that described above, PIXEL dimer energies have been used to rank the interaction energies of supramolecular synthons,[139] and as part of a wider study to investigate the instability of furocoumarin.[140]

1.7 Concluding Remarks

As this review has shown, the PIXEL method yields energies that are comparable to both experimental data and the results of higher level computational methods. The approximations made in the PIXEL formulation allow for a set of fully transferable parameters that are applicable to almost any system, indicated by the great variety of work that has taken advantage of this conceptually simple method of calculating interaction energies. On an average desktop computer, a lattice energy calculation for a simple organic compound takes around half an hour, while a dimer interaction energy is achieved in around thirty seconds, and it is the speed and simplicity that makes the PIXEL method particularly appealing for energetic studies in the solid state.

1.8 References

1. A. Bondi, *Journal of Physical Chemistry*, 1964, **68**, 441-451.
2. S. S. Batsanov, *Structural Chemistry*, 2000, **11**, 177-183.
3. S. C. Nyburg and C. H. Faerman, *Acta Crystallographica Section B - Structural Science*, 1985, **41**, 274-279.
4. A. Gavezzotti, *CrystEngComm*, 2013, **15**, 4027-4035.
5. R. Mews and S. Parsons, *Zeitschrift für Kristallographie*, 2014, **229**, 649-660.
6. R. D. L. Johnstone, D. Francis, A. R. Lennie, W. G. Marshall, S. A. Moggach, S. Parsons, E. Pidcock and J. E. Warren, *CrystEngComm*, 2008, **10**, 1758-1769.
7. P. A. Wood, F. H. Allen and E. Pidcock, *CrystEngComm*, 2009, **11**, 1563-1571.
8. A. Gavezzotti, *Zeitschrift für Kristallographie*, 2005, **220**, 499-510.
9. A. Gavezzotti, *Molecular Aggregation - Structure Analysis and Molecular Simulation of Crystals and Liquids*, 1st edn., Oxford University Press, New York, 2007.
10. M. Rigby, E. B. Smith, W. A. Wakeham and G. C. Maitland, *The Forces Between Molecules*, Clarendon Press, Oxford, 1986.
11. A. Gavezzotti, *Journal of Physical Chemistry B*, 2003, **107**, 2344-2353.
12. C. F. Macrae, I. J. Bruno, J. A. Chisholm, P. R. Edgington, P. McCabe, E. Pidcock, L. Rodriguez-Monge, R. Taylor, J. van de Streek and P. A. Wood, *Journal of Applied Crystallography*, 2008, **41**, 466-470.
13. P. A. Wood, D. Francis, W. G. Marshall, S. A. Moggach, S. Parsons, E. Pidcock and A. L. Rohl, *CrystEngComm*, 2008, **10**, 1154-1166.
14. A. Gavezzotti, *Journal of Chemical Theory and Computation*, 2005, **1**, 834-840.
15. A. Gavezzotti, *CrystEngComm*, 2003, **5**, 429-438.
16. A. Gavezzotti, *New Journal of Chemistry*, 2011, **35**, 1360-1368.
17. A. O. Surov, A. N. Proshin and G. L. Perlovich, *Acta Crystallographica Section B - Structural Science*, 2014, **70**, 47-53.
18. G. Raabe, *Zeitschrift für Naturforschung Section A - A Journal of Physical Sciences*, 2002, **57**, 961-966.
19. A. O. Surov, B. Cong Trinh, A. N. Proshin, P. Roussel, A. Idrissi and G. L. Perlovich, *Journal of Physical Chemistry B*, 2013, **117**, 10414-10429.
20. S. Aldridge, A. J. Downs, C. Y. Tang, S. Parsons, M. C. Clarke, R. D. L. Johnstone, H. E. Robertson, D. W. H. Rankin and D. A. Wann, *Journal of the American Chemical Society*, 2009, **131**, 2231-2243.
21. L. Maschio, B. Civalleri, P. Ugliengo and A. Gavezzotti, *Journal of Physical Chemistry A*, 2011, **115**, 11179-11186.
22. B. Civalleri, C. M. Zicovich-Wilson, L. Valenzano and P. Ugliengo, *CrystEngComm*, 2008, **10**, 405-410.
23. C. Zhang, X. Xue, Y. Cao, J. Zhou, A. Zhang, H. Li, Y. Zhou, R. Xu and T. Gao, *CrystEngComm*, 2014, **16**, 5905-5916.
24. W. B. Schweizer and J. D. Dunitz, *Journal of Chemical Theory and Computation*, 2006, **2**, 288-291.
25. J. D. Dunitz and W. B. Schweizer, *Chemistry - A European Journal*, 2006, **12**, 6804-6815.
26. J. D. Dunitz and W. B. Schweizer, *CrystEngComm*, 2007, **9**, 266-269.
27. A. Volkov and P. Coppens, *Journal of Computational Chemistry*, 2004, **25**, 921-934.
28. K. Durka, K. N. Jarzembska, R. Kaminski, S. Lulinski, J. Serwatowski and K. Wozniak, *Crystal Growth & Design*, 2012, **12**, 3720-3734.
29. R. Kaminski, S. Domagala, K. N. Jarzembska, A. A. Hoser, W. F. Sanjuan-Szklarz, M. J. Gutmann, A. Makal, M. Malinska, J. M. Bak and K. Wozniak, *Acta Crystallographica Section A - Foundations and Advances*, 2014, **70**, 72-91.
30. J. D. Dunitz, A. Gavezzotti and W. B. Schweizer, *Helvetica Chimica Acta*, 2003, **86**, 4073-4092.
31. A. Gavezzotti, *Structural Chemistry*, 2005, **16**, 177-185.
32. J. D. Dunitz and A. Gavezzotti, *Crystal Growth & Design*, 2005, **5**, 2180-2189.
33. A. Gavezzotti, *Advanced X-Ray Crystallography*, 2012, **315**, 1-32.
34. J. D. Dunitz and A. Gavezzotti, *Helvetica Chimica Acta*, 2002, **85**, 3949-3964.
35. A. Gavezzotti and G. Filippini, *Journal of Physical Chemistry*, 1994, **98**, 4831-4837.
36. F. Demartin, G. Filippini, A. Gavezzotti and S. Rizzato, *Acta Crystallographica Section B - Structural Science*, 2004, **60**, 609-620.

37. J. D. Dunitz, *ChemBioChem*, 2004, **5**, 614-621.
38. S. Bacchi, M. Benaglia, F. Cozzi, F. Demartin, G. Filippini and A. Gavezzotti, *Chemistry - A European Journal*, 2006, **12**, 3538-3546.
39. J. D. Dunitz and A. Gavezzotti, *Angewandte Chemie - International Edition*, 2005, **44**, 1766-1787.
40. R. Boese, T. Clark and A. Gavezzotti, *Helvetica Chimica Acta*, 2003, **86**, 1085-1100.
41. A. Gavezzotti, *CrystEngComm*, 2008, **10**, 389-398.
42. A. Gavezzotti, *Molecular Physics*, 2008, **106**, 1473-1485.
43. M. Kazmierczak and A. Katrusiak, *Journal of Physical Chemistry C*, 2013, **117**, 1441-1446.
44. M. Abboud, V. Mamane and E. Aubert, *Acta Crystallographica Section C - Crystal Structure Communications*, 2013, **69**, 56-60.
45. S. Saouane, G. Buth and F. P. A. Fabbiani, *Acta Crystallographica Section C - Crystal Structure Communications*, 2013, **69**, 1238-1242.
46. K. Durka, S. Lulinski and J. Serwatowski, *Acta Crystallographica Section E - Structure Reports Online*, 2013, **69**, O1818-O1818.
47. A. O. Surov, A. P. Voronin, A. N. Manin, N. G. Manin, L. G. Kuzmina, A. V. Churakov and G. L. Perlovich, *Molecular Pharmaceutics*, 2014, **11**, 3707-3715.
48. A. Berzins, E. Skarbulis, T. Rekis and A. Actins, *Crystal Growth & Design*, 2014, **14**, 2654-2664.
49. P. Panini, R. Shukla, T. P. Mohan, B. Vishalakshi and D. Chopra, *Journal of Chemical Sciences*, 2014, **126**, 1337-1345.
50. R. S. Forgan, B. D. Roach, P. A. Wood, F. J. White, J. Campbell, D. K. Henderson, E. Kamenetzky, F. E. McAllister, S. Parsons, E. Pidcock, P. Richardson, R. M. Swart and P. A. Tasker, *Inorganic Chemistry*, 2011, **50**, 4515-4522.
51. K. A. Solanko and A. D. Bond, *Acta Crystallographica Section B - Structural Science*, 2011, **67**, 437-445.
52. J. Lu, A. J. Cruz-Cabeza, S. Rohani and M. C. Jennings, *Acta Crystallographica Section C - Crystal Structure Communications*, 2011, **67**, O306-O309.
53. T. Gelbrich, T. L. Threlfall and M. B. Hursthouse, *CrystEngComm*, 2012, **14**, 5454-5464.
54. G. Kaur, P. Panini, D. Chopra and A. R. Choudhury, *Crystal Growth & Design*, 2012, **12**, 5096-5110.
55. C. M. L. Vande Velde, M. Zeller and V. A. Azov, *Journal of Molecular Structure*, 2012, **1016**, 109-117.
56. J. D. Dunitz and A. Gavezzotti, *Journal of Physical Chemistry B*, 2012, **116**, 6740-6750.
57. M. Karanam and A. R. Choudhury, *Crystal Growth & Design*, 2013, **13**, 4803-4814.
58. P. Panini and D. Chopra, *CrystEngComm*, 2013, **15**, 3711-3733.
59. P. Panini, T. P. Mohan, U. Gangwar, R. Sankolli and D. Chopra, *CrystEngComm*, 2013, **15**, 4549-4564.
60. G. Wesela-Bauman, P. Ciecwierz, K. Durka, S. Lulinski, J. Serwatowski and K. Wozniak, *Inorganic Chemistry*, 2013, **52**, 10846-10859.
61. A. O. Surov, K. A. Solanko, A. D. Bond, A. Bauer-Brandl and G. L. Perlovich, *CrystEngComm*, 2013, **15**, 6054-6061.
62. D. Dey, V. Prakash, D. Chopra, Vasu and M. Srinivas, *Journal of Chemical Crystallography*, 2014, **44**, 450-458.
63. P. Panini, K. N. Venugopala, B. Odhav and D. Chopra, *Proceedings of the National Academy of Sciences India Section A - Physical Sciences*, 2014, **84**, 281-295.
64. R. Shukla, T. P. Mohan, B. Vishalakshi and D. Chopra, *CrystEngComm*, 2014, **16**, 1702-1713.
65. A. Elahi and R. Kant, *European Chemical Bulletin*, 2014, **3**, 763-769.
66. D. Dey, T. P. Mohan, B. Vishalakshi and D. Chopra, *Crystal Growth & Design*, 2014, **14**, 5881-5896.
67. K. N. Jarzembska, A. A. Hoser, R. Kaminski, A. O. Madsen, K. Durka and K. Wozniak, *Crystal Growth & Design*, 2014, **14**, 3453-3465.
68. A. Gavezzotti and S. Rizzato, *Journal of Organic Chemistry*, 2014, **79**, 4809-4816.
69. J. D. Dunitz, A. Gavezzotti and S. Rizzato, *Crystal Growth & Design*, 2014, **14**, 357-366.
70. P. Venkatesan, S. Thamotharan, R. G. Kumar and A. Ilangovan, *CrystEngComm*, 2015, **17**, 904-915.
71. A. Berzins and A. Actins, *CrystEngComm*, 2014, **16**, 3926-3934.

72. M. Abboud, A. Kadimi, V. Mamane and E. Aubert, *Acta Crystallographica Section C - Crystal Structure Communications*, 2010, **66**, O381-O384.
73. S. Khorasani and M. A. Fernandes, *Crystal Growth & Design*, 2013, **13**, 5499-5505.
74. A. Gavezzotti, *Acta Crystallographica Section B - Structural Science*, 2008, **64**, 401-403.
75. F. Cozzi, S. Bacchi, G. Filippini, T. Pilati and A. Gavezzotti, *CrystEngComm*, 2009, **11**, 1122-1127.
76. S. L. Childs, P. A. Wood, N. Rodriguez-Hornedo, L. S. Reddy and K. I. Hardcastle, *Crystal Growth & Design*, 2009, **9**, 1869-1888.
77. I. Mata, E. Molins, M. Amat, N. Llor and B. Checa, *Acta Crystallographica Section C - Crystal Structure Communications*, 2012, **68**, O114-O118.
78. K. Durka, S. Lulinski, K. N. Jarzembska, J. Smetek, J. Serwatowski and K. Wozniak, *Acta Crystallographica Section B - Structural Science*, 2014, **70**, 157-171.
79. A. G. P. Maloney, P. A. Wood and S. Parsons, *CrystEngComm*, 2014, **16**, 3867-3882.
80. E. K. Gibson, J. M. Winfield, K. W. Muir, R. H. Carr, A. Eaglesham, A. Gavezzotti, S. F. Parker and D. Lennon, *Physical Chemistry Chemical Physics*, 2009, **11**, 288-297.
81. E. K. Gibson, J. M. Winfield, K. W. Muir, R. H. Carr, A. Eaglesham, A. Gavezzotti and D. Lennon, *Physical Chemistry Chemical Physics*, 2010, **12**, 3824-3833.
82. P. Panini and D. Chopra, *Crystal Growth & Design*, 2014, **14**, 3155-3168.
83. A. Gavezzotti, *Journal of Pharmaceutical Sciences*, 2007, **96**, 2232-2241.
84. A. Gavezzotti, *Acta Crystallographica Section D - Biological Crystallography*, 2008, **64**, 905-908.
85. C. F. Zipp, M. A. Fernandes, H. M. Marques, J. P. Michael and C. B. Perry, *Crystal Growth & Design*, 2011, **11**, 1431-1436.
86. K. Durka, A. A. Hoser, R. Kaminski, S. Lulinski, J. Serwatowski, W. Kozminski and K. Wozniak, *Crystal Growth & Design*, 2011, **11**, 1835-1845.
87. S. Varughese, M. S. R. N. Kiran, K. A. Solanko, A. D. Bond, U. Ramamurty and G. R. Desiraju, *Chemical Science*, 2011, **2**, 2236-2242.
88. A. Gavezzotti, F. Demartin, C. Castellano and I. Campostrini, *Physics and Chemistry of Minerals*, 2013, **40**, 175-182.
89. C. F. Zipp, H. W. Dirr, M. A. Fernandes, H. M. Marques and J. P. Michael, *Crystal Growth & Design*, 2013, **13**, 3463-3474.
90. A. A. Hoser, D. M. Kaminski, A. Matwijczuk, A. Niewiadomy, M. Gagos and K. Wozniak, *CrystEngComm*, 2013, **15**, 1978-1988.
91. P. Panini, K. N. Venugopala, B. Odhav and D. Chopra, *Acta Crystallographica Section B - Structural Science, Crystal Engineering and Materials*, 2014, **70**, 681-696.
92. K. Krukle-Berzina and A. Actins, *International Journal of Pharmaceutics*, 2014, **469**, 40-49.
93. I. Sovago, M. J. Gutmann, J. G. Hill, H. M. Senn, L. H. Thomas, C. C. Wilson and L. J. Farrugia, *Crystal Growth & Design*, 2014, **14**, 1227-1239.
94. G. Wesela-Bauman, S. Lulinski, J. Serwatowski and K. Wozniak, *Physical Chemistry Chemical Physics*, 2014, **16**, 22762-22774.
95. A. D. Bond, *Journal of Applied Crystallography*, 2014, **47**, 1777-1780.
96. O. V. Shishkin, V. V. Dyakonenko and A. V. Maleev, *CrystEngComm*, 2012, **14**, 1795-1804.
97. O. V. Shishkin, V. V. Medvediev, R. I. Zubatyuk, O. O. Shyshkina, N. V. Kovalenko and J. M. Volovenko, *CrystEngComm*, 2012, **14**, 8698-8707.
98. N. P. Funnell, A. Dawson, D. Francis, A. R. Lennie, W. G. Marshall, S. A. Moggach, J. E. Warren and S. Parsons, *CrystEngComm*, 2010, **12**, 2573-2583.
99. N. P. Funnell, W. G. Marshall and S. Parsons, *CrystEngComm*, 2011, **13**, 5841-5848.
100. S. A. Moggach, D. R. Allan, C. A. Morrison, S. Parsons and L. Sawyer, *Acta Crystallographica Section B - Structural Science*, 2005, **61**, 58-68.
101. S. A. Moggach, W. G. Marshall and S. Parsons, *Acta Crystallographica Section B - Structural Science*, 2006, **62**, 815-825.
102. S. A. Moggach, S. Parsons and P. A. Wood, *Crystallography Reviews*, 2008, **14**, 143-183.
103. P. A. Wood, R. S. Forgan, D. Henderson, S. Parsons, E. Pidcock, P. A. Tasker and J. E. Warren, *Acta Crystallographica Section B - Structural Science*, 2006, **62**, 1099-1111.
104. P. A. Wood, R. S. Forgan, A. R. Lennie, S. Parsons, E. Pidcock, P. A. Tasker and J. E. Warren, *CrystEngComm*, 2008, **10**, 239-251.
105. P. A. Wood, D. A. Haynes, A. R. Lennie, W. D. S. Motherwell, S. Parsons, E. Pidcock and J. E. Warrens, *Crystal Growth & Design*, 2008, **8**, 549-558.

106. R. D. L. Johnstone, D. Allan, A. Lennie, E. Pidcock, R. Valiente, F. Rodriguez, J. Gonzalez, J. Warren and S. Parsons, *Acta Crystallographica Section B - Structural Science*, 2011, **67**, 226-237.
107. S. Bergantin, M. Moret, G. Buth and F. P. A. Fabbiani, *Journal of Physical Chemistry C*, 2014, **118**, 13476-13483.
108. B. F. Johnston, W. G. Marshall, S. Parsons, A. J. Urquhart and I. D. H. Oswald, *Journal of Physical Chemistry B*, 2014, **118**, 4044-4051.
109. G. Wesela-Bauman, S. Parsons, J. Serwatowski and K. Wozniak, *CrystEngComm*, 2014, **16**, 10780-10790.
110. R. D. L. Johnstone, A. R. Lennie, S. Parsons, E. Pidcock and J. E. Warren, *Acta Crystallographica Section B - Structural Science*, 2009, **65**, 731-748.
111. C. H. Woodall, S. K. Brayshaw, S. Schiffers, D. R. Allan, S. Parsons, R. Valiente and P. R. Raithby, *CrystEngComm*, 2014, **16**, 2119-2128.
112. R. D. L. Johnstone, A. R. Lennie, S. F. Parker, S. Parsons, E. Pidcock, P. R. Richardson, J. E. Warren and P. A. Wood, *CrystEngComm*, 2010, **12**, 1065-1078.
113. Y. Sasada, T. Takano and M. Kakudo, *Bulletin of the Chemical Society of Japan*, 1964, **37**, 940-946.
114. F. Pertlik, *Monatshefte für Chemie*, 1990, **121**, 129-139.
115. D. Paliwoda, K. F. Dziubek and A. Katrusiak, *Crystal Growth & Design*, 2012, **12**, 4302-4305.
116. W. Cai, J. Marciniak, M. Andrzejewski and A. Katrusiak, *Journal of Physical Chemistry C*, 2013, **117**, 7279-7285.
117. N. P. Funnell, A. Dawson, W. G. Marshall and S. Parsons, *CrystEngComm*, 2013, **15**, 1047-1060.
118. F. P. A. Fabbiani, C. R. Pulham and J. E. Warren, *Zeitschrift für Kristallographie*, 2014, **229**, 667-675.
119. F. P. A. Fabbiani, G. Buth, D. C. Levendis and A. J. Cruz-Cabez, *Chemical Communications*, 2014, **50**, 1817-1819.
120. G. M. Day, W. D. S. Motherwell, H. L. Ammon, S. X. M. Boerrigter, R. G. Della Valle, E. Venuti, A. Dzyabchenko, J. D. Dunitz, B. Schweizer, B. P. van Eijck, P. Erk, J. C. Facelli, V. E. Bazterra, M. B. Ferraro, D. W. M. Hofmann, F. J. J. Leusen, C. Liang, C. C. Pantelides, P. G. Karamertzanis, S. L. Price, T. C. Lewis, H. Nowell, A. Torrisi, H. A. Scheraga, Y. A. Arnautova, M. U. Schmidt and P. Verwer, *Acta Crystallographica Section B - Structural Science*, 2005, **61**, 511-527.
121. G. M. Day, T. G. Cooper, A. J. Cruz-Cabeza, K. E. Hejczyk, H. L. Ammon, S. X. M. Boerrigter, J. S. Tan, R. G. Della Valle, E. Venuti, J. Jose, S. R. Gadre, G. R. Desiraju, T. S. Thakur, B. P. van Eijck, J. C. Facelli, V. E. Bazterra, M. B. Ferraro, D. W. M. Hofmann, M. A. Neumann, F. J. J. Leusen, J. Kendrick, S. L. Price, A. J. Misquitta, P. G. Karamertzanis, G. W. A. Welch, H. A. Scheraga, Y. A. Arnautova, M. U. Schmidt, J. van de Streek, A. K. Wolf and B. Schweizer, *Acta Crystallographica Section B - Structural Science*, 2009, **65**, 107-125.
122. A. Gavezzotti, *Zip-Promet*, (1999-2000) University of Milano, Milan.
123. A. J. Cruz Cabeza, G. M. Day, W. D. S. Motherwell and W. Jones, *Crystal Growth & Design*, 2007, **7**, 100-107.
124. A. Johnston, J. Bardin, B. F. Johnston, P. Fernandes, A. R. Kennedy, S. L. Price and A. J. Florence, *Crystal Growth & Design*, 2011, **11**, 405-413.
125. A. M. Moragues-Bartolome, W. Jones and A. J. Cruz-Cabeza, *CrystEngComm*, 2012, **14**, 2552-2559.
126. A. J. Cruz-Cabeza and C. H. Schwalbe, *New Journal of Chemistry*, 2012, **36**, 1347-1354.
127. D. E. Braun, M. Orlova and U. J. Griesser, *Crystal Growth & Design*, 2014, **14**, 4895-4900.
128. D. E. Braun, J. A. McMahon, L. H. Koztecki, S. L. Price and S. M. Reutzel-Edens, *Crystal Growth & Design*, 2014, **14**, 2056-2072.
129. M. U. Schmidt, E. F. Paulus, N. Rademacher and G. M. Day, *Acta Crystallographica Section B - Structural Science*, 2010, **66**, 515-526.
130. R. M. Bhardwaj, L. S. Price, S. L. Price, S. M. Reutzel-Edens, G. J. Miller, I. D. H. Oswald, B. F. Johnston and A. J. Florence, *Crystal Growth & Design*, 2013, **13**, 1602-1617.
131. A. Gavezzotti, *CrystEngComm*, 2003, **5**, 439-446.
132. R. Boese, M. T. Kirchner, J. D. Dunitz, G. Filippini and A. Gavezzotti, *Helvetica Chimica Acta*, 2001, **84**, 1561-1577.
133. T. C. Lewis, D. A. Tocher, G. M. Day and S. L. Price, *CrystEngComm*, 2003, **5**, 3-9.

134. A. T. Anghel, G. M. Day and S. L. Price, *CrystEngComm*, 2002, **4**, 348-355.
135. L. Carlucci and A. Gavezzotti, *Chemistry - A European Journal*, 2005, **11**, 271-279.
136. D. E. Braun, R. M. Bhardwaj, J.-B. Arlin, A. J. Florence, V. Kahlenberg, U. J. Griesser, D. A. Tocher and S. L. Price, *Crystal Growth & Design*, 2013, **13**, 4071-4083.
137. C. J. Eckhardt and A. Gavezzotti, *Journal of Physical Chemistry B*, 2007, **111**, 3430-3437.
138. A. Gavezzotti, *Acta Crystallographica Section B - Structural Science*, 2010, **66**, 396-406.
139. J. D. Dunitz and A. Gavezzotti, *Crystal Growth & Design*, 2012, **12**, 5873-5877.
140. A. Gavezzotti, *Crystal Growth & Design*, 2013, **13**, 3801-3815.

Chapter 2

Application of the PIXEL Method to Transition Metal Complexes

2.1 Synopsis

Parameters required to perform a PIXEL energy calculation have been obtained for the 1st, 2nd and 3rd row transition metals. Using these parameters, lattice energies of thirty-two 1st row, five 2nd row and six 3rd row transition metal complexes have been calculated and compared to experimental values giving straight line parameters of $y = 0.99(1)x$ (where y are the experimental sublimation enthalpies and x are the calculated lattice energies, both in kJ mol^{-1}) and a correlation coefficient $R = 0.92$ for 1st row species, and $y = 1.02(3)x$ and $R = 0.92$ for 2nd row and 3rd row species. These results are comparable to results obtained by Gavezzotti in testing the method for organic crystal structures. Additionally, energies of interactions including chromium hexacarbonyl, stacking interactions in *bis*(acetylacetonato)-oxo-vanadium(IV), intermolecular embraces and dihydrogen bonding have been calculated using PIXEL and compared to higher level computational methods.

2.2 Introduction

The development of PIXEL,[1, 2] a method for evaluating intermolecular interactions based on integrations over calculated electron densities of molecules, has allowed energetic analysis in crystal structures to be carried out quickly with an accuracy comparable to high level quantum mechanical methods. PIXEL gives the total interaction energy separated into four principal contributing terms: Coulombic, polarization, dispersion and repulsion. This separation of contributions allows for the character of an interaction to be inferred from the dominant term.

Prior work [3-6] has demonstrated that the PIXEL method is widely applicable to chemical species that are made up of the elements common in organic chemistry. The presence of a metal centre in a transition metal complex will significantly influence the interaction energies compared to a similar organic system. The ability to calculate intermolecular energies in metal complexes is an extremely exciting prospect as it will reveal how metals can be used to modify “organic” interactions. Some examples of this are known already; for instance Orpen and co-workers have shown that H-bond acceptors based on metal halides and oxalates can be used to form much more reliable and reproducible supramolecular building blocks than those based on purely organic ligands.[7, 8] The ability to model metal-metal intermolecular interactions is of great use in

the study of supramolecular assembly, as is shown by the investigation of Pt(II) interactions by Pérez Pas *et al.* in a TD/DFT study.[9] While such metal-metal interactions are less well studied than interactions such as hydrogen bonding in supramolecular chemistry, many systems have received a great deal of attention, particularly the interactions between Au(I) centres in the phenomenon known as aurophilicity.[10, 11]

Beyond crystal engineering, calculations of intermolecular interactions that involve metal containing species play an extremely important role in a wide variety of different areas of chemistry. Di Tomasso *et al*. have used DFT to study the different intermolecular energies of possible interaction pathways to better understand the factors controlling Ru(II) hydrogenation catalysis,[12-14] while more recently Li *et al.* performed calculations to investigate the performance of cobalt and copper analogues of a pre-existing nickel catalyst for olefin purification.[15]

Transition metal species exist in many proteins, and a great deal of computational effort is invested in the study of the binding affinities and selectivities of protein-ligand interactions in these systems,[16-18] and the desire to find more efficient methods of drug design means that efficient computational analysis of metal-based pharmaceuticals is an ever expanding field,[19] such as the analysis of the interactions of zinc ions with several anti-inflammatory drugs.[20]

Metal-organic frameworks, large porous structures consisting of metal oxides linked by organic ligands, are increasingly being studied as potential gas storage and separation materials, and a variety of computational methods are used to study the adsorption of small molecules in these systems.[21-23]

With this wide variety of different aspects of chemistry all being enhanced by the study of interactions between metal containing species, the PIXEL method, with its conceptual simplicity and computational efficiency, presents a potentially powerful addition to the toolkit of computational techniques.

The PIXEL formulation requires a range of different atomic properties to calculate the intermolecular energy terms. While these are established for many non-metal atomic species, no parameters are defined for transitions metals. The parameters involved are for the most part simple properties such as ionisation potentials, and so are easily obtained from various standard data sources. One of the greatest appeals of the

original PIXEL method is its transferability across many different chemical systems, and as such the parameters derived for transition metal species must be such that they are able to preserve this quality.

In this work, we expand the PIXEL method to include 1st, 2nd and 3rd row transition metal atoms before investigating a range of dimer interactions in various transition metal complexes including dihydrogen bonding and intermolecular embraces.

2.3 Adaptation of the PIXEL Method to Transition Metal Species

2.3.1 Definition of Metal Parameters

The four energy terms which are evaluated during a PIXEL calculation depend on a small number of fundamental atomic parameters. Values of these parameters for atoms common in organic chemistry are embedded in the PIXEL code, but new values for transition metals were defined for the present work and validated against experimental sublimation enthalpies. The names used to refer to the parameters in the following sections are those used in the PIXEL program manual and Gavezzotti's publications, where full details of their definition, use and significance can be found.[2, 24, 25]

Definition of some parameters is straightforward. ***ZTOT*** and ***ZVAL*** are the total number of electrons and the number of valence electrons in the neutral atom; ***POTIO*** is the first ionisation energy (in atomic units)[26] and ***WEIGHT*** is the atomic weight.[27] For other parameters a choice among several possibilities needs to be made. Unless otherwise specified, values used for non-metallic elements forming the ligands were the program defaults.

Dispersion energies are calculated in a London-type expression in which the ionisation energy of a pixel is used to approximate the pixel 'oscillator strength'. ***DIFA*** (also given the symbol $\boldsymbol{\beta}$ in Gavezzotti's papers) is a "variable ionisation" parameter which controls the reduction of the ionisation energy of a pixel as the distance to the nucleus increases.[2] Gavezzotti's recommended value of 0.4 $Å^{-1}$ is used throughout the work described below. Variation of ***DIFA*** between 0.1 and 1.0 $Å^{-1}$ yielded values of the lattice energy of $TiCl_4$ between -46.4 and -57.7 $kJmol^{-1}$. A value of -53.0 $kJmol^{-1}$ was

obtained with the standard value 0.4 $Å^{-1}$, compared to the experimental value of -51.9 $kJmol^{-1}$. [28] *

The covalent radii of atoms, ***RINTER*****,** are used in PIXEL to check for short internuclear distances, and not used to calculate energies. Values were taken from Ref. 27.

RAVDW, the van der Waals radius is used to assign pixels of electron density to atomic basins. The sets of values reported by Nag *et al.*[29] and Batsanov[30] were tested.

The atomic polarisability, ***POLZE*** or α in $Å^3$, appears in the calculation of both the polarization and dispersion terms. Variation of α(Ti) between 3.5 and 5.0 $Å^3$ yielded values of the $TiCl_4$ lattice energy between -45.9 and -57.1 $kJmol^{-1}$.

For non-metallic species the PIXEL method makes use of the Slater-Kirkwood approximation to estimate α according to Equation 2.1,

$$\alpha = \frac{1}{a_0}\left(\frac{R_{vdW}}{1.05\sqrt{3}}\right)^4 \qquad (2.1)$$

where a_0 is the Bohr radius and R_{vdW} is the van der Waals radius. The Nag and Batsanov radii were tested.

The Clausius-Mossotti relation (Equation 2.2) is another simple method for estimating atomic polarisabilities:

$$\alpha = \frac{\varepsilon-\varepsilon_0}{\varepsilon+2\varepsilon_0}\frac{3V_m}{4\pi} \qquad (2.2)$$

where V_m is the atomic volume, ε is the dielectric constant of the species and ε_0 is the permittivity of free space. For metals, the dielectric constant $\varepsilon \rightarrow \infty$, so that the first term of this equation tends to unity, giving $\alpha = 3V_m/4\pi$. Atomic volumes were obtained from the crystal structures of the elemental metals at room temperature and pressure.

The electronegativity, ***ELNEG***, is used in the calculation of the repulsion energy. Both Pauling and Allred-Rochow values[27] were investigated.

2.3.2 PIXEL Calculations and the Treatment of Ligand Parameters

For each structure OH, NH and CH distances were changed to 0.993, 1.015 and 1.089 Å, respectively. This 'normalisation' procedure involves moving H positions to values typically obtained by neutron diffraction and corrects approximately for the

* All of these test calculations were performed using Parameter Set 5 (see below, Table 2.4)

effects of asphericity of H-atom electron densities which lead to systematic shortening of distances involving hydrogen atoms when determined by X-ray diffraction. The electron density was obtained in a single-point calculation with a B3LYP functional and a 6-31G** basis set (Gaussian 09)[31] for main group elements and first-row transition metals. Second-row transition metal species were treated with the LanL2DZ basis set, and third-row metals used the LanL2DZ basis set with corresponding pseudopotentials to model the core orbitals of the metal atom. The "cube" format electron density files were then used in PIXEL calculations using the PIXELc module from the OPiX package[32] which had been modified to read a table of transition metal parameters described in Section 2.3.1. Unless otherwise specified, the pixel size for all calculations was 0.16 x 0.16 x 0.16 Å (corresponding to 'condensation level' 4 in the program).[2]

While atomic parameters in PIXEL calculations are intended to be transferable between different compounds, values of atomic polarisabilities may be varied depending on chemical bonding. For instance, three different atomic polarisabilities are used for carbon, depending on whether it is aliphatic, aromatic or bridging aromatic as in naphthalene. While such differences might ideally be taken into account for other species (e.g. carbonyl and ether oxygen atoms), the dominance of carbon in organic compounds means that it is much more important to account for variation in its different chemical environments than it is for less abundant atomic species. While in practice only α(C) is usually varied, modification of the atomic polarisabilities of other species has been performed previously by Gavezzotti,[33] for example for chloride ions in ionic organic crystals.

Though carbon is a common constituent of many ligands, it may be necessary to consider alternative values of polarisabilities of non-carbon atoms in cases such as homoleptic carbonyl complexes, where the molecular surface is composed of exposed oxygen atoms. PIXEL analysis of molecular carbon monoxide, using the default parameters in the program, yields a lattice energy of -7.875 kJ mol^{-1}. This compares favourably with the experimentally determined value of 7.9(2) kJ mol^{-1} (average value from three determinations). However, when carbon monoxide is acting as a ligand, PIXEL results were found to be around 20 kJ mol^{-1} lower than the literature value when the default value of α(O) (0.75$Å^3$) was used (e.g. $Cr(CO)_6$, literature sublimation enthalpy 69.6 kJ mol^{-1}, calculated lattice energy 47.8 kJ mol^{-1}). Carbonyl oxygen

therefore, like carbon, seems to require its own value of α(O) depending on whether the CO is ligating or not. By testing different values of atomic polarisability of O, a value of α(O) = 1.0 Å^3 was chosen for this species when carbon monoxide is acting as a ligand, yielding a lattice energy of 70.5 kJ mol^{-1}. Table 2.1 shows the atomic polarisabilities used for ligand atoms in all calculations.

Atom	Atomic Polarisability
H	0.39
C aliphatic	1.05
C aromatic	1.35
C aromatic bridge	1.90
N	0.95
O	0.75
O carbonyl	1.00
F	0.50
Cl	2.30
S	3.00
S ligating	3.60

Table 2.1: Atomic polarisabilities for non-metal atoms used in all calculations.

Support for these adjustments was obtained by calculation of atomic polarisabilities in CO and $Cr(CO)_6$ by the Atoms In Molecules method[34] as described by Keith[35] using structures optimised at the B3LYP/6-31G** level. The values of α(O) obtained for CO and $Cr(CO)_6$ were 0.57 and 0.86 Å^3, respectively, a similar relative increase to the one proposed above.

2.3.3 Selection of Experimental Sublimation Enthalpies for Validation

A compilation of experimental sublimation enthalpies[28] was cross-referenced with the Cambridge Structural Database[36] to obtain a set of transition metal complexes for which both crystal structure and experimental sublimation data are available. Sublimation enthalpies are notoriously difficult to measure, and different determinations may yield wildly disparate results: for example two different measurements of the sublimation enthalpy of ferrocene give values of 64.6 kJ mol^{-1} [37] and 84.0 kJ mol^{-1}.[38] For this reason, only compounds with a minimum of two independent sublimation enthalpy determinations were used for validation. The enthalpy values were arithmetically averaged with no weighting after elimination of any obvious outliers. The full validation data set, which contains 43 different compounds, is given in Table 2.2,

and chemical structures are given in the supplementary data. Also listed in Table 2.2 are the CSD refcodes, along with average experimental sublimation enthalpies and PIXEL calculated lattice energies. All complexes investigated had centrosymmetric crystal structures, and as such, no polarisation correction was necessary.

Compound Number	CSD Refcode	Transition Metal	Experimental Sublimation Enthalpy	PIXEL Calculated Lattice Energy
1	ACACCR07	Cr	119.5 ± 8.7	124.5
2	ACACCS	Cr	120.4 ± 13.3	118.1
3	ACACCU02	Cu	118.7 ± 9.9	113.4
4	ACACMN21	Mn	119.3 ± 6.0	126.7
5	ACACVO12	V	140.6 ± 0.4	143.7
6	BZCRCO14	Cr	94.6 ± 4.7	93.8
7	CCRTOL01	Cr	94.0 ± 1.4	97.7
8	CDCPTI04	Ti	122.5 ± 3.0	131.8
9	CEHPIO01	Ti	94.6 ± 9.0	93.5
10	COACAC10	Co	138.7 ± 4.0	136.2
11	CPNDYV07	V	58.2 ± 1.1	76.8
12	CUBEAC01	Cu	156.6 ± 4.0	157.0
13	CUQUIN05	Cu	166.3 ± 5.3	159.6
14	DBENCR11	Cr	83.6 ± 6.1	93.7
15	DCYPCO04	Co	71.1 ± 1.5	75.8
16	DERNOD05	Cu	124.9 ± 2.9	129.5
17	DMTCCU	Cu	150.8 ± 4.6	170.9
18	DURHEE	Ni	120.4 ± 11.5	99.2
19	FEACAC03	Fe	121.92 ± 9.0	120.0
20	FEROCE27	Fe	73.6 ± 4.2	71.5
21	FOHCOU02	Cr	69.6 ± 1.9	70.5
22	IGAGEC	Cr	117.5 ± 7.8	81.6
23	IPEZOS	Cu	129.0 ± 1.9	124.0
24	IPTCNI10	Ni	145.5 ± 3.5	152.8
25	LIYLIO	Co	132.6 ± 15.3	134.2
26	MACACU10	Cu	133.0 ± 2.5	124.7
27	NCKLCN01	Ni	71.2 ± 1.0	74.1
28	NIDCAR06	Ni	153.7 ± 2.9	151.6
29	NISALO01	Ni	109.5 ± 3.5	115.4
31	QQQBWP03	Cu	113.5 ± 2.4	115.6
32	TCBMNI	Ni	146.0 ± 8.5	148.8
33	ACACPD01	Pd	128.1 ± 4.0	138.6
34	CYCPRU06	Ru	78.8 ± 3.4	83.0
35	FUBYIK01	Mo	72.6 ± 3.5	65.7
36	HCYPMO02	Mo	87.0 ± 7.8	82.9
37	HQUIPD	Pd	163.3 ± 6.7	154.4
38	KOKPEF	Hf	104.4 ± 4.9	94.9
39	KOVSOD02	W	74.9 ± 2.9	55.9
40	QQQCXJ02	Ir	112.0 ± 21.6	115.3
41	REGSAY	Hf	127.2 ± 3.5	109.1
42	REPKIH	W	90.4 ± 8.2	101.2
43	SINWER	Os	76.2 ± 3.9	84.6

Table 2.2: The 43 compounds used for validation and parameterisation. Compound numbers correspond to a scheme contained within the supplementary information. PIXEL calculated energies shown here use Parameter Set 5.

2.3.4 Calculations of Individual Intermolecular Interactions

Dimers displaying various types of intermolecular interactions were selected to compare the PIXEL results with those of higher level computational methods. A range of interactions were investigated involving chromium hexacarbonyl, vanadyl stacking, metal hydrides participating in dihydrogen and halogen bonding[39-41] and the intermolecular embrace of a pair of $Ru(bipy)_3$ complexes.[42]

A combination of Mercury and Materials Studio[43] was used to obtain models which were then optimised using Gaussian09 at the same level of theory and basis set as used in the literature studies. These optimised structures were then used for PIXEL calculations as described above. Further analysis was performed with CrystalExplorer,[44] where the required wavefunctions were calculated with the program TONTO[45] at the HF/STO-3G level.

2.4 Results and Discussion

2.4.1 Parameter Set Selection and Reproduction of Experimental Sublimation Enthalpy Data

Five different parameter sets were constructed using different combinations of methods for estimation of the van der Waals radii, polarisability and electronegativity, as defined in Section 2.3. The different combinations are given in Table 2.3, with values for each parameter set being listed explicitly in the Supplementary Information. We follow Gavezzotti[46] in quantifying the performance of the sets using the gradients and correlation coefficients of straight-line fits of the experimental sublimation energies of Table 2.2 to the calculated energies. The results are also listed in Table 2.3; the straight-line fits used unit weights and were constrained to intercept at the origin.

Set	RAVDW	POLZE	ELNEG	m_{all}	R_{all}	m_{1st}	$R_{1st\ row}$	$m_{2nd/3rd}$	$R_{2nd/3rd}$
1	Batsanov	CM	Pauling	1.01(1)	0.92	1.00(2)	0.92	1.06(3)	0.92
2	Batsanov	SK	Pauling	1.01(2)	0.92	0.99(2)	0.92	1.09(3)	0.93
3	Nag	SK	Pauling	1.02(2)	0.92	1.01(2)	0.92	1.06(4)	0.91
4	Nag	CM	Pauling	1.01(1)	0.92	0.99(1)	0.92	1.06(3)	0.93
5	Batsanov	CM	Allred-Rochow	0.99(1)	0.92	0.99(2)	0.92	1.02(3)	0.92

Table 2.3: The changes made to each data set during optimisation. References are given in the text above. Regarding the *POLZE* column, CM sands for Claussius Mossotti and SK stands for Slater-Kirkwood. *m* and *R* are gradients and correlation coefficients of the straight-line fits for all, 1st row only and 2nd/3rd row only transition metal complexes.

The data in Table 2.3 show that there is little difference between the performances of the different parameter sets, demonstrating the robustness of the PIXEL method to different choices of reasonable parameters. Set 5, the parameters of which are shown in Table 2.4, was chosen for further analyses because the volume (and therefore polarisability) of an elemental metal and the Allred-Rochow electronegativities are more unambiguously defined in terms of readily accessible experimental data than the quantities used to define parameters in other sets. Furthermore, the gradient and correlation coefficient for 2nd and 3rd row transition metals for set 5 are better than the other sets.

Atom	*DIFA*	*RAVDW*	*RINTER*	*ZTOT*	*ZVAL*	*POLZE*	*ELNEG*	*POTIO*	*WEIGHT*
Ti	0.4	2.15	1.32	22	4	4.18	1.32	0.251	47.88
V	0.4	2.05	1.22	23	5	3.31	1.45	0.248	50.94
Cr	0.4	2.05	1.17	24	6	2.86	1.56	0.249	52.00
Mn	0.4	2.05	1.17	25	7	2.93	1.60	0.273	54.94
Fe	0.4	2.05	1.16	26	8	2.81	1.64	0.289	55.85
Co	0.4	2.00	1.16	27	9	2.62	1.70	0.289	58.93
Ni	0.4	2.00	1.15	28	10	2.61	1.75	0.281	58.69
Cu	0.4	2.00	1.35	29	11	2.81	1.75	0.284	63.55
Zn	0.4	2.10	1.31	30	12	3.63	1.66	0.345	65.38
Zr	0.4	2.30	1.45	40	12	5.56	1.33	0.251	91.22
Nb	0.4	2.15	1.34	41	13	4.30	1.60	0.253	92.91
Mo	0.4	2.10	1.29	42	14	3.72	2.16	0.261	95.94
Tc	0.4	2.05	1.23	43	15	3.41	1.90	0.267	98.91
Ru	0.4	2.05	1.24	44	16	3.23	2.20	0.271	101.07
Rh	0.4	2.00	1.25	45	17	3.29	2.28	0.274	102.91
Pd	0.4	2.05	1.28	46	18	3.51	2.20	0.307	106.42
Ag	0.4	2.10	1.34	47	19	4.07	1.93	0.278	107.87
Cd	0.4	2.20	1.41	48	20	5.15	1.69	0.330	112.41
Hf	0.4	2.35	1.44	72	12	5.32	1.23	0.251	178.49
Ta	0.4	2.20	1.34	73	13	4.31	1.33	0.277	180.95
W	0.4	2.10	1.30	74	14	3.78	1.40	0.289	183.85
Re	0.4	2.05	1.28	75	15	3.51	1.46	0.288	186.21
Os	0.4	2.00	1.26	76	16	3.34	1.52	0.310	190.20
Ir	0.4	2.00	1.26	77	17	3.40	1.55	0.330	192.22
Pt	0.4	2.05	1.29	78	18	3.61	1.44	0.329	195.08
Au	0.4	2.10	1.34	79	19	4.04	1.42	0.339	196.97
Hg	0.4	2.05	1.44	80	20	5.87	1.44	0.384	200.59

Table 2.4: Transition metal parameters for set 5. Abbreviations and units are described in Section 2.3.1.

For set 5 the gradient of the straight line fit was 0.99(1) with a correlation coefficient of 0.92 (Figure 2.1). These data compare favourably with respective values of 0.96 and 0.89 obtained by Gavezzotti for 172 organic crystal structures.[2]

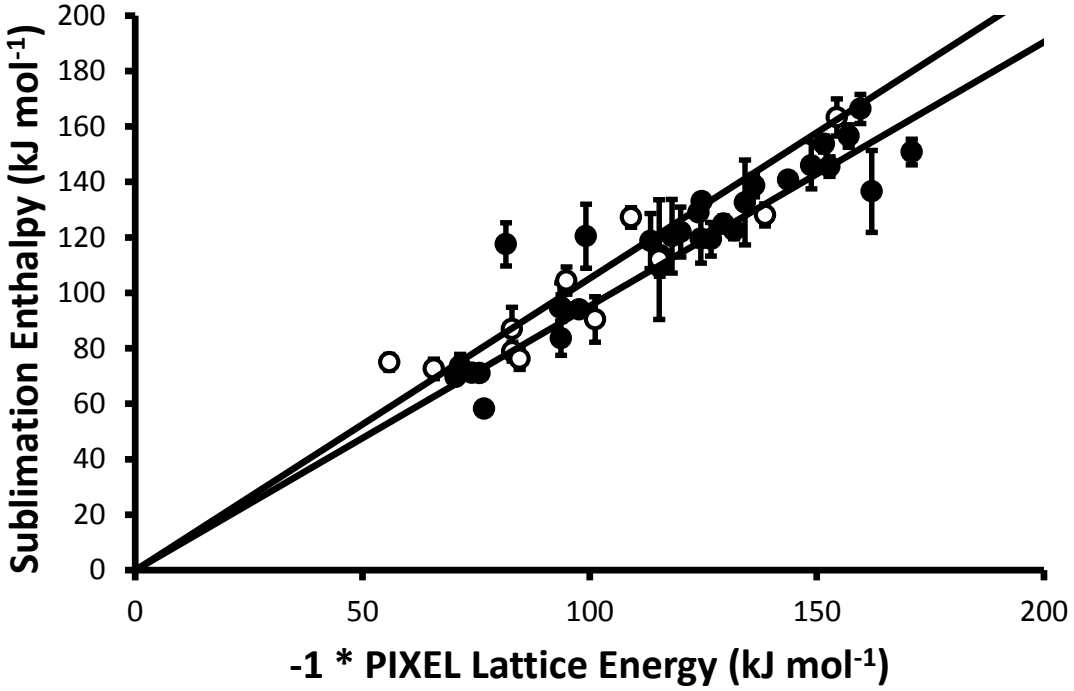

Figure 2.1: Comparison of experimental sublimation enthalpies with values calculated by PIXEL (parameter set 5) for 1st row (closed circles) and 2nd and 3rd row (open circles) transition metal complexes for which the sublimation enthalpy has been determined multiple times. The black lines are ±5% of the experimental sublimation enthalpy.

The improvement over organic materials apparently obtained for the metal complexes is ascribable to limitation of the validation data-set to compounds for which multiple sublimation energies determinations are available. If all available data (105 complexes) are used the gradient and correlation coefficient are 0.96(2) and 0.69, respectively (Figure 2.2).

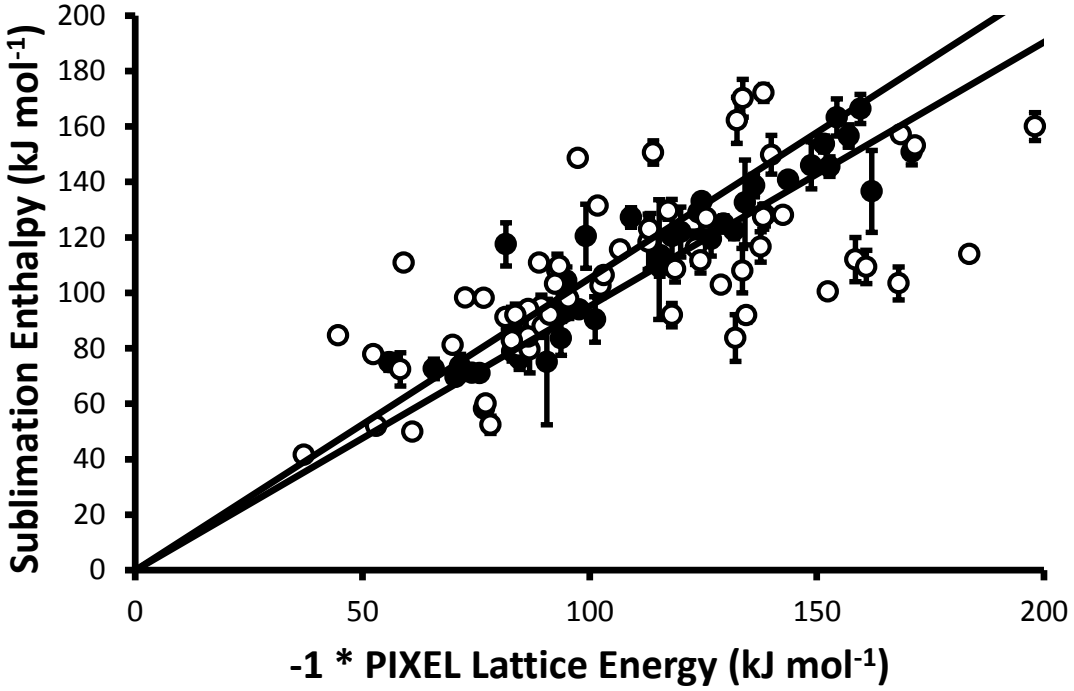

Figure 2.2: A similar comparison to that shown in Figure 2.1 but including complexes (shown as open circles) for which the sublimation enthalpy has been determined only once. All points from Figure 2.1 are shown as closed circles.

The data presented in Figure 2.1 are dominated by first-row transition metal complexes, these data alone yielding a gradient and correlation coefficient equal to 0.99(1) and 0.92, respectively. The data for second and third row complexes are more limited, and the fitting statistics are 1.02(3) and 0.92. Some elements, such as technetium and gold, are not represented at all.

Overall, while the data presented above indicate that the PIXEL method can be applied with some confidence to first-row metal complexes, more data are needed to establish that the same is true for compounds containing heavier metals. In the absence of a large body of experimental data, the following sections aim to compare the results of PIXEL calculations with energies obtained for chromium hexacarbonyl, stacking interactions in *bis*(acetylacetonato)-oxo-vanadium(IV), dihydrogen bonding in 2nd and 3rd row transition metal complexes and for intermolecular interactions between ruthenium complexes to those calculated by quantum mechanical methods.

2.5 Analysis of Intermolecular Interactions Using the New Parameters

Since PIXEL gives a breakdown not only of the total energy but also the individual intermolecular energies into chemically meaningful terms, it can be used to infer the nature of the interaction between two molecules. The structures of two first row transition metal complexes, chromium hexacarbonyl and *bis*(acetylacetonato)-oxo-vanadium(IV), serve as illustrations of how PIXEL can be used to rationalise the strongest interactions in crystal structures. Bond's processPIXEL program,[47] a method of visualising the PIXEL output by displaying vectors scaled to the magnitude of each interaction, and CrystalExplorer[44] are used for further analysis.

2.5.1 The Structure of Chromium Hexacarbonyl

Chromium hexacarbonyl (CSD refcode FOHCOU02) is a molecular solid held together by van der Waals interactions.[48] The space group of chromium hexacarbonyl is *Pnma*, and the molecules form layers in the crystal structure situated on the mirror planes at y = ¼ and y = ¾. The literature sublimation enthalpy of chromium hexacarbonyl is 69.6(19) kJ mol^{-1} (an average of twelve determinations[28]), and the PIXEL calculated lattice energy is 70.5 kJ mol^{-1}, a result which lies within the error bounds of the experimental value. Analysis with processPIXEL shows that there are three principal interactions for each $Cr(CO)_6$ molecule, shown molecules A, B and C relative to the reference molecule (in green) in Figure 2.3. Table 2.5 shows the breakdown of the component energy terms from the PIXEL calculation, as well as the Cr…Cr distances of these three interactions.

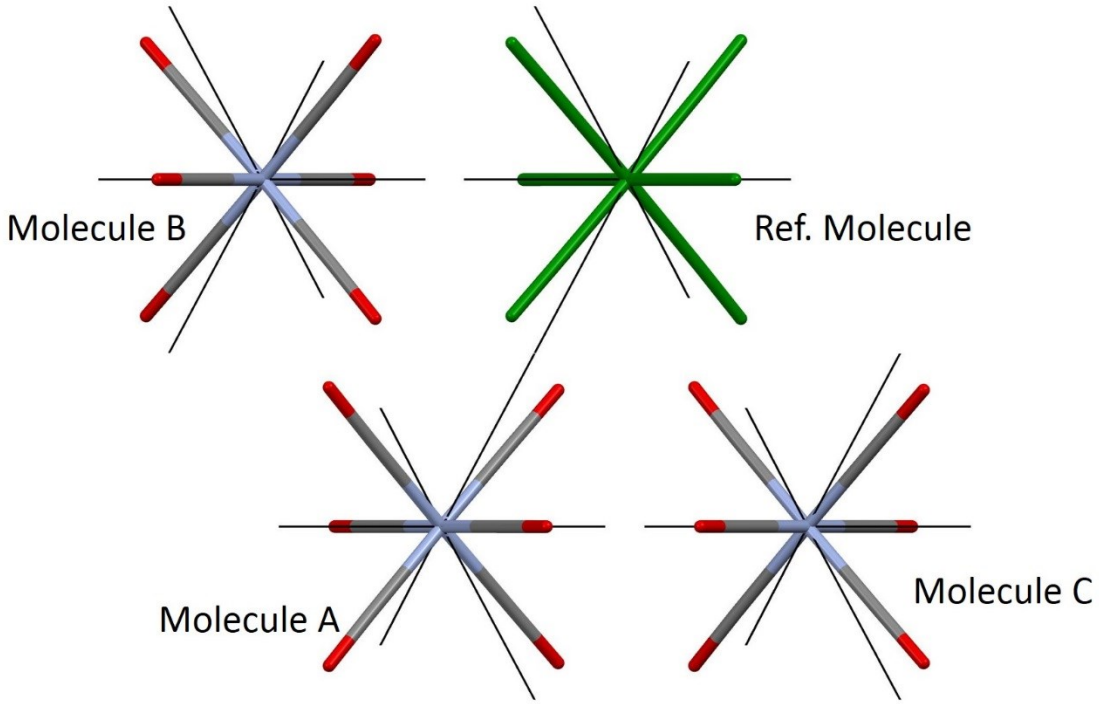

Figure 2.3: processPIXEL output for the total intermolecular energies of chromium hexacarbonyl as viewed down the crystallographic *c*-axis. The energy vectors show the interaction energies scaled to that of the strongest interaction. The reference molecule is shown in green, and the strongest interaction is between this and molecule A. The interaction to molecule B is the second strongest, and that to molecule C is the weakest.

Interacting Molecule	E_{coul}	E_{disp}	E_{pol}	E_{rep}	E_{tot}	Cr…Cr (Å)
A	-5.8	-18.7	-1.8	13.0	-13.3	6.236
B	-2.6	-16.9	-1.2	8.9	-11.9	6.213
C	-4.3	-11.2	-1.1	7.4	-9.1	6.888

Table 2.5: PIXEL component terms and Cr…Cr distances for the three principal intermolecular interactions in $Cr(CO)_6$. Values are in kJ mol^{-1} unless otherwise indicated.

PIXEL analysis shows that the interactions are predominantly dispersion based. The dispersion interaction for two sets of three similarly arranged CO molecules to those in the strongest dimer interaction A (carried out by performing a separate PIXEL calculation on a $Cr(CO)_6$ dimer while making the atomic polarisabilities 0.0001 $Å^3$ for all other atoms, effectively "turning off" their dispersion contribution) is calculated at -11.6 kJ mol^{-1}. The increase in the dispersion term for this interaction in $Cr(CO)_6$ (-18.7 kJ mol^{-1}) is a result of the higher polarisability upon ligation of the carbonyl. AIM calculations, carried out on wavefunctions calculated at the B3LYP/6-31G** level, show that there is an increase from 1.41 $Å^3$ to 1.96 $Å^3$ per CO fragment (calculated as

the sum of α(C) + α(O)) upon ligation, and this greater polarisability results in the stronger dispersion terms.

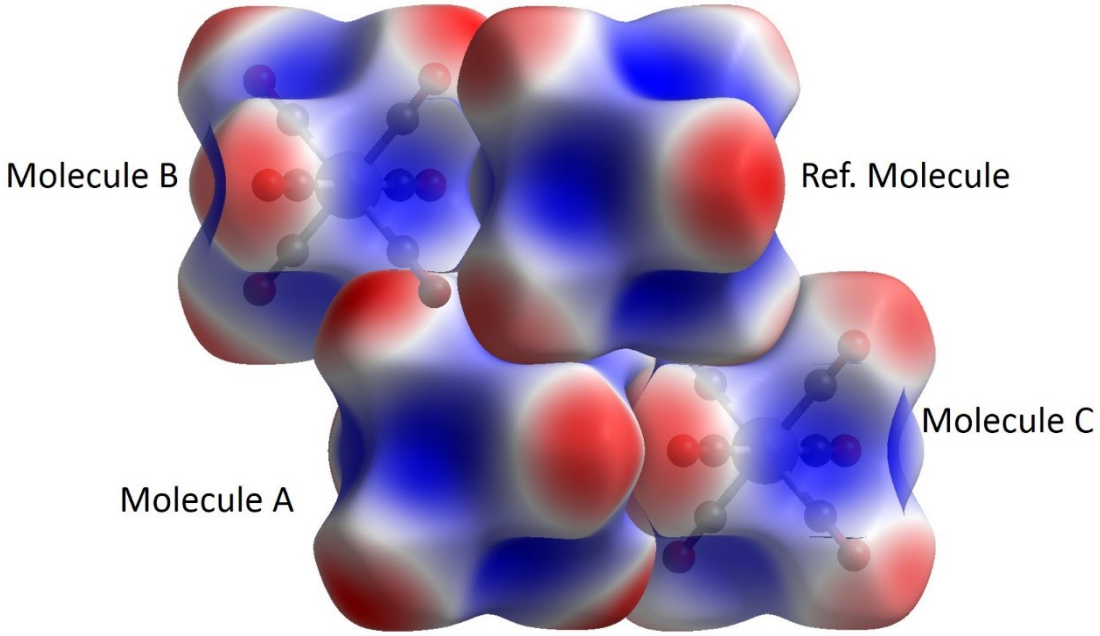

Figure 2.4: An illustration of the Coulombic interactions in $Cr(CO)_6$ using the electrostatic potential (ESP) mapped onto Hirshfeld surfaces. The weaker Coulombic interactions are shown as transparent. The surface is mapped from -0.036 au (red) to 0.047 au (blue). Wavefunctions were obtained at the HF/STO-3G level.

The greater Coulombic energies for interactions A and C are due to a more favourable overlap of the electrostatic potentials between the molecules involved in these interactions. Figure 2.4 shows the Crystal Explorer output for the electrostatic potential mapped onto the Hirshfeld surface of each molecule in the unit cell. Favourable overlap occurs when the red regions of one molecule are in contact with the blue regions of a neighbouring molecule, and the white lines separating these regions are contiguous. While this is the case for interactions A and C, Figure 2.4 shows that in the interaction with molecule B there is some overlap between the red regions of the ESPs, indicating the reason for the weaker Coulombic term in this case.

2.5.2 The Structure of Bis(Acetylacetonato)-Oxo-Vanadium(IV)

In the crystal structure of *bis*(acetylacetonato)-oxo-vanadium(IV) (CSD refcode ACACVO12),[49] the molecules are arranged in an offset stacking arrangement located around inversion centres. The literature sublimation enthalpy of 140.6(4) kJ mol^{-1} (the average of two measurements)[28] is reproduced successfully by PIXEL with a calculated

lattice energy of 143.7 kJ mol^{-1}. Use of processPIXEL shows that the strongest interaction arises from the stacking of two molecules (Figure 2.5) where the distance between the molecules is 4.531 Å, a motif which is prevalent among other vanadyl containing structures.[50-52]

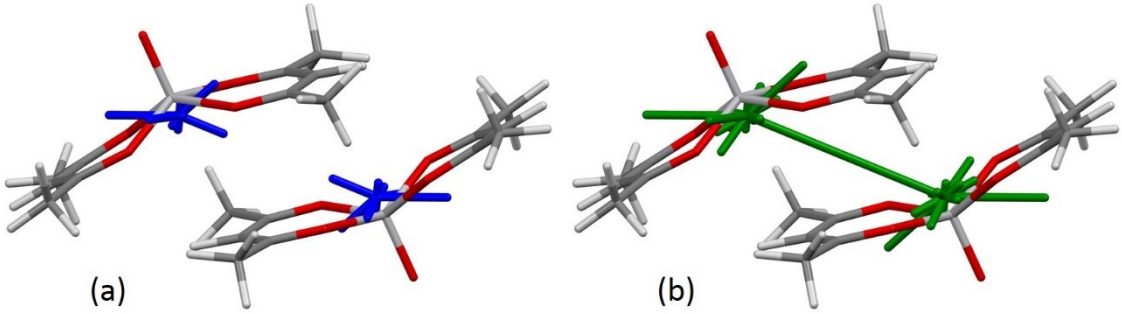

Figure 2.5: processPIXEL output for the Coulombic (a) and dispersion (b) components of the stacking interaction between *bis*(acetylacetonato)-oxo-vanadium(IV) molecules.

PIXEL calculates the energy of this stacking interaction as -65.0 kJ mol^{-1}, a surprisingly high value, but higher level calculations agree with this magnitude (B3LYP-D/6-31G*: -65.9 kJ mol^{-1}; B2PLYP-D/6-31G*: -52.9; MO5-2X/6-311++G**: -53.5; SCS MP2: -67.7 kJ mol^{-1}).† This is an extremely strong stacking interaction; for instance, it is ten times as strong as a similar stacking interaction between two benzene molecules (-7 kJ mol^{-1}).[5] Table 2.6 shows the breakdown of the PIXEL energy into its component terms.

Term	E_{Coul}	E_{disp}	E_{pol}	E_{rep}	E_{tot}
Energy (kJ mol^{-1})	-28.8	-67.9	-9.8	41.5	-65.0

Table 2.6: PIXEL component terms of the stacking interaction between *bis*(acetylacetonato)-oxo-vanadium(IV) molecules.

Table 2.6 show that the dispersion term dominates this interaction, but there is also substantial electrostatic character. A CrystalExplorer plot of the electrostatic potential shows that the magnitude of the Coulombic term results from the efficient dipole-dipole overlap in the stacking interaction (Figure 2.6).

† MO5-2X performed with Gaussian09, B3LYP-D & B2PLYP-D performed with ORCA. SCS MP2 calculations were performed using ORCA by Tanja van Mourik at St. Andrews University, for which she is gratefully acknowledged.

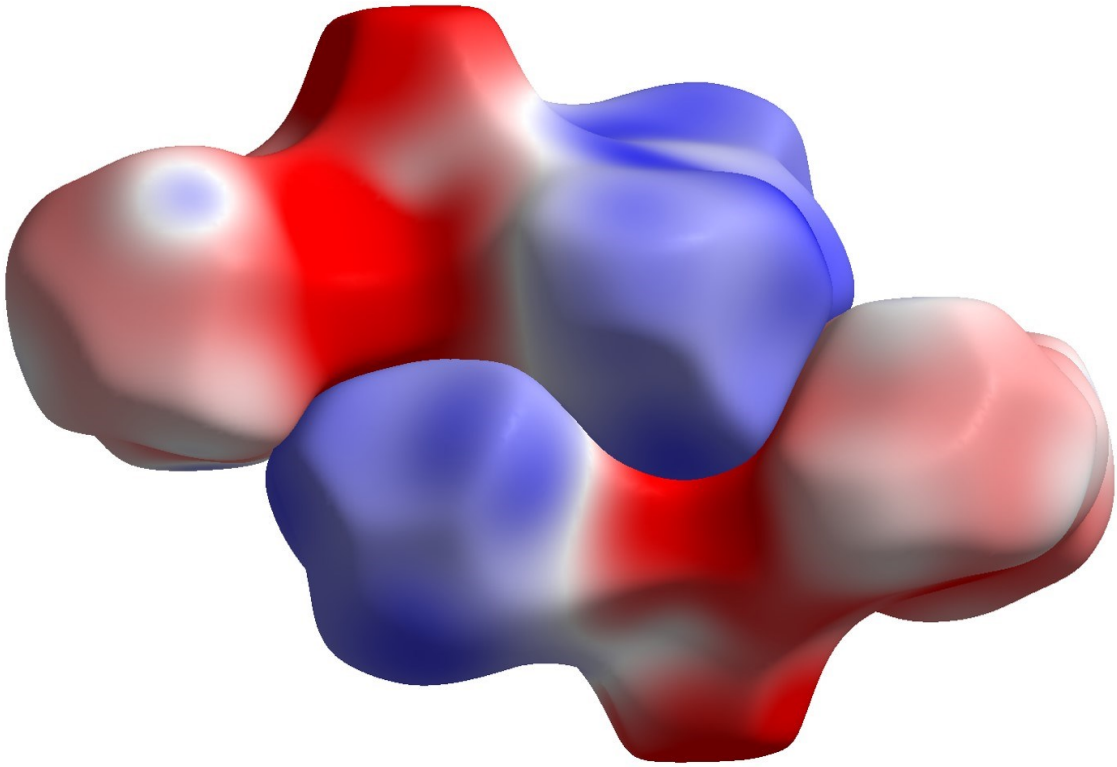

Figure 2.6: The stacking interaction in *bis*(acetylacetonato)-oxo-vanadium(IV) shown using the electrostatic potential mapped onto Hirshfeld surfaces. The surface is mapped from -0.036 au (red) to 0.047 au (blue). Wavefunctions were obtained at the HF/STO-3G level.

The magnitude of the dispersion interaction arises from the presence of the vanadium. The dispersion term for the interaction of only the acetylacetonato ligands (calculated in a similar method as described above for $Cr(CO)_6$, setting the atomic polarisabilities of the oxo-vanadium moiety to 0.0001 $Å^3$) is -51.5 kJ mol^{-1}. The high atomic polarisability of vanadium (3.31 $Å^3$) results in the increase of 16.4 kJ mol^{-1} in the dispersion term observed for the stacking interaction of the transition metal complexes.

2.5.3 Dihydrogen Bonding

When a hydrogen atom is bound directly to a transition metal centre, the electron density of the hydrogen atom can be altered sufficiently that it can display acidic or basic characteristics. The bound hydrogen atom is then capable of interacting with other acidic or basic groups in a type of hydrogen bond in what is known as dihydrogen bonding.[53] Early theoretical analysis of such interactions by Liu and Hoffmann showed that they are attractive and are mainly electrostatic in character.[54]

Dihydrogen bonds may play an important role in proton transfer reactions[55] and consequently there has been a great deal of interest, both experimental and theoretical, in recent years. This gives a broad range of different metal centres and interactions that can be used to test how the PIXEL method compares to higher levels of theory. Additionally, this presents an interesting example because it concerns 2nd and 3rd row transition metals, and since sublimation enthalpy data are scarce for transition metal complexes containing these metals, comparison with other computational methods provides a further test to the proposed new PIXEL parameters for these elements.

In dihydrogen bonding, large electron rich transition metals are required to promote greater electron density in the bound hydrogen atoms. However, due to the large number of electrons present in such transition metals, many theoretical approaches such as *ab initio* methods are not used regularly due to the high cost of these computations.[55] DFT methods are, however, considered to be within "chemical accuracy" (that is, within ~5 kJ mol^{-1}) of any available experimental data, and all of the results compared below have been obtained in such a manner.

Models of the complexes listed below in Table 2.7 were generated using Materials Studio 5.5[43] and were then optimised using Gaussian09[31] at the same level of theory described in the original papers.[39-41]

Complex	Coul	Disp	Rep	Pol	Tot	DFT	Ref.
$CpRu(CO)(PH_3)H\ldots HOOCCF_3$	-53.0	-22.4	63.6	-36.6	-48.4	-35.1	25
$CpRu(CO)(PH_3)H\ldots HOC(CF_3)_3$	-50.7	-27.3	65.0	-35.4	-48.4	-40.6	25
$CpMo(dpe)H_2H\ldots HOCH(CF_3)_2$	-62.3	-35.1	81.3	-30.3	-46.4	-41.6	26
$CpW(dpe)H_2H\ldots HOCH(CF_3)_2$	-69.6	-36.6	85.6	-32.9	-53.5	-45.3	26
$PP_3RuHH^{ax}\ldots HOCH_3$	-54.8	-15.4	57.1	-22.3	-35.4	-40.6	27
$PP_3RuHH^{eq}\ldots HOCH_3$	-51.8	-18.8	52.8	-23.1	-40.9	-40.5	27
$PP_3RuHH^{ax}\ldots HOCF_3$	-103.6	-20.9	92.6	-61.0	-92.9	-86.9	27
$PP_3RuHH^{eq}\ldots HOCF_3$	-92.6	-23.7	117.1	-77.4	-76.6	-72.6	27

Table 2.7: Breakdown of PIXEL values into component energy terms along with total values and reference DFT energies. dpe is $PH_2CH_2CH_2PH_2$. All values are in kJ mol^{-1}.

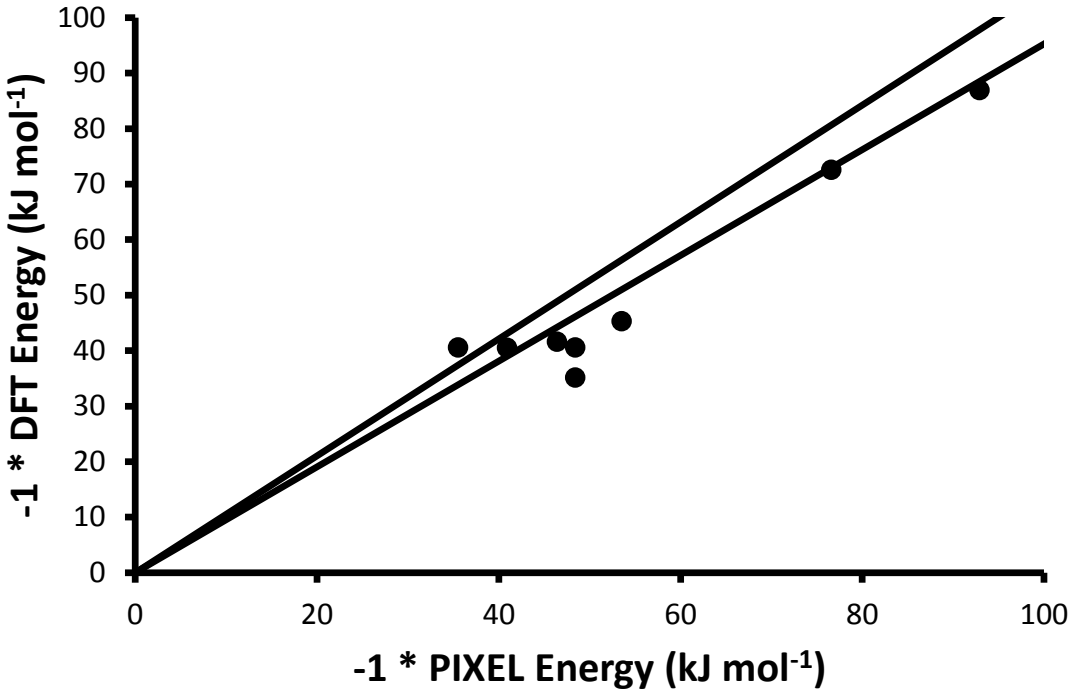

Figure 2.7: Comparison of PIXEL calculated energies with DFT reference energies for a selection of dihydrogen bonded complexes. The black lines are ±5% of the DFT calculated interaction energy.

As Figure 2.7 shows, the PIXEL method agrees well with the different DFT studies ($y = 0.91x$, $R = 0.96$), most differences in values being around 5 kJ mol^{-1}. Additionally, Table 2.7 shows that the interactions are predominantly electrostatic in character, in accordance to observations made by Liu and Hoffmann, and that the Coulombic term increases with increasing fluorination. This is to be expected, as the electronegativity of the fluorine will increase the positive charge on the hydroxyl hydrogen atom. Consequently, this hydrogen atom becomes more acidic, strengthening the dihydrogen bond. The dispersion interaction also increases with the degree of fluorination (see Table 2.7). This is a result from the change in the disposition of the alcohol upon fluorination, best illustrated by the overlay of the PP_3RuHH system shown in Figure 2.8. The change in geometry is due to a secondary dispersion interaction between the fluorine atoms on the alcohol and the hydrogen atoms of the Ru complex, as discussed by Jacobsen.[56]

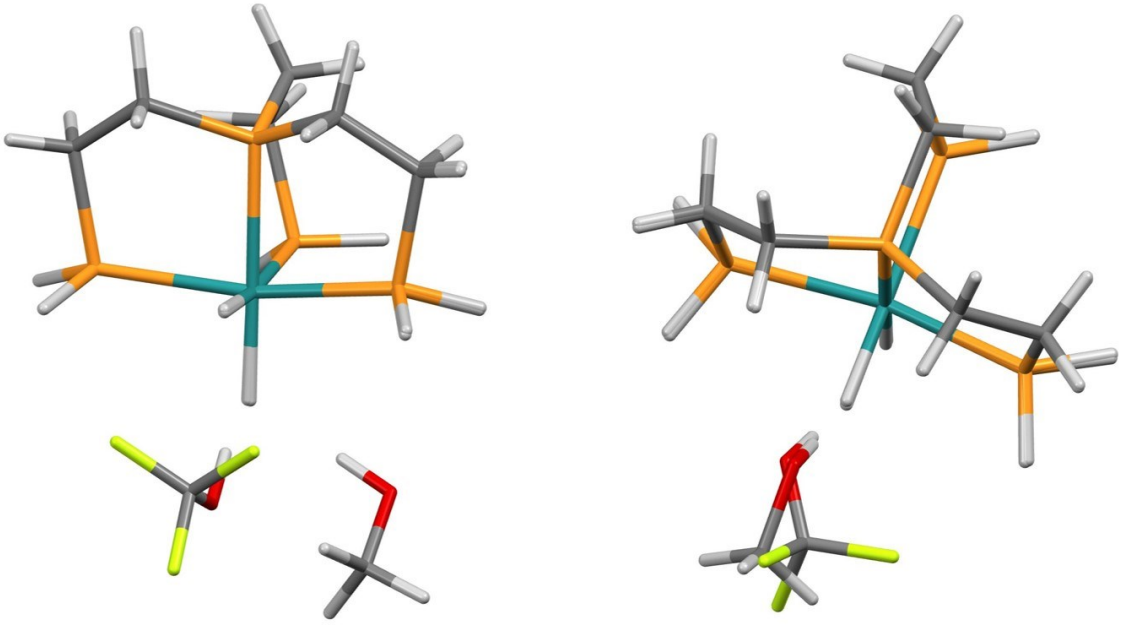

Figure 2.8: Binding geometries to the axial hydride (left) and equatorial hydride (right) in PP_3RuHH. Changes in the disposition of the alcohol upon fluorination are shown by an overlay in each case.

2.5.4 Intermolecular Embraces

Intermolecular embraces occur between complexes containing aromatic ligands, and consist of edge-to-face (EF) and offset-face-to-face (OFF) interactions between the aromatic groups.[57] Due to the arrangement of the ligands around the transition metal centre, these EF and OFF interactions can occur in concert, creating multiple embrace motifs such as a parallel fourfold aryl embrace (P4AE), as illustrated in Figure 2.9.

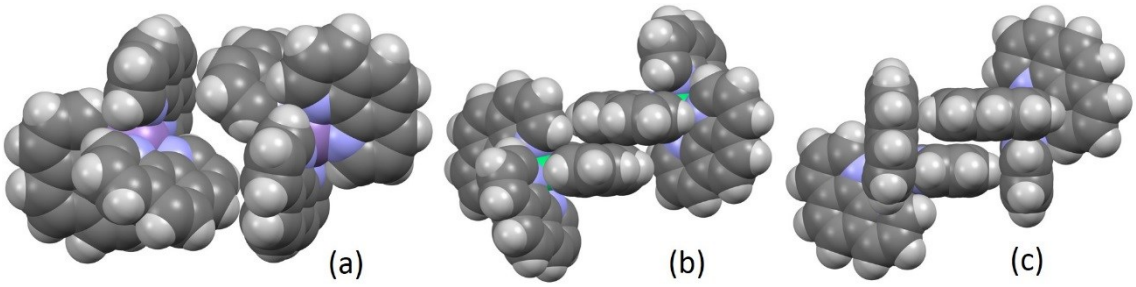

Figure 2.9: Intermolecular embraces in transition metal complexes: (a) EF embrace in $Mn(phen)_3$ (CSD refcode SOMZOJ); (b) OFF embrace in $Ni(phen)_3$ (ZELJOP); (c) P4AE embrace in $Ni(phen)_3$ (PNIMNC10).

Since 1995 Dance and colleagues have been investigating embrace motifs between molecules in the solid state.[58] While the CSD is an excellent tool for geometrical analysis of such interactions, there is a lack of experimental thermodynamic data, and so once again comparisons between different computational methods must be

made. The majority of Dance's work has been performed using DMol[3],[59] a computational chemistry program that is often used for transition metal containing species. Figure 2.10 shows the sixfold aryl embrace of a pair of $[Ru(bipy)_3]^0$ complexes, made up of 6 EF interactions, and compares the intermolecular potential calculated by DMol to the results obtained from PIXEL calculations at various condensation levels.

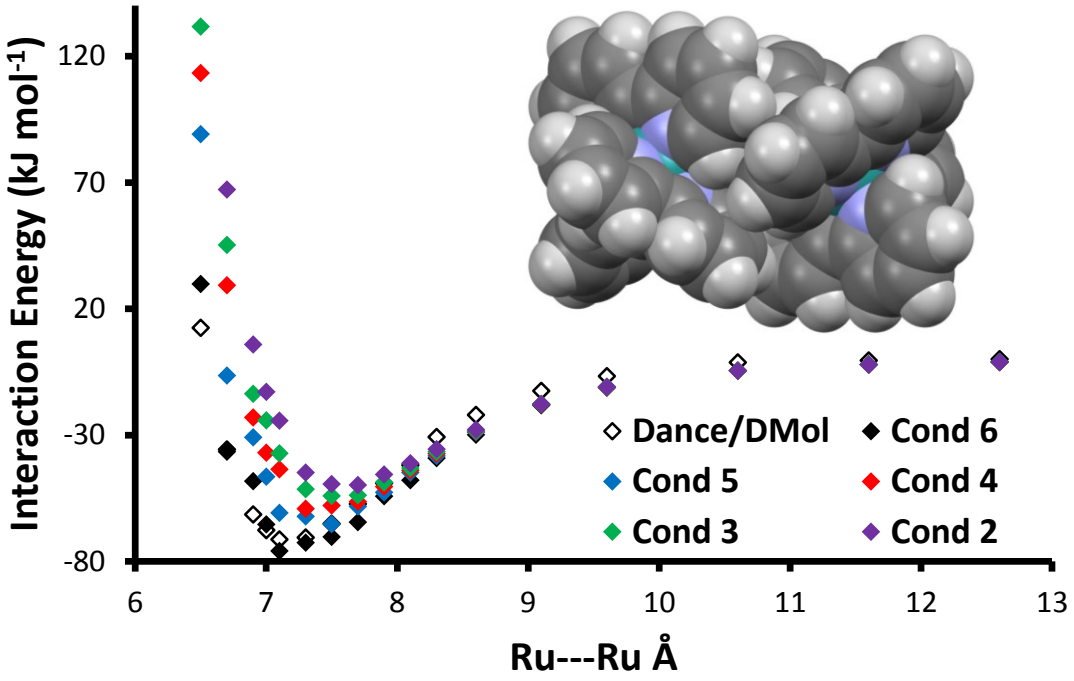

Figure 2.10: The potential curve for the intermolecular embrace between two $[Ru(bipy)_3]^0$ complexes (insert) as calculated by Dance using DMol and by PIXEL at a range of different condensation levels.

Calculations by Dance[42] report the bottom of the energy well at a Ru-Ru distance of 7.2 Å and an energy of around -70 kJ mol^{-1}. At condensation level 6, PIXEL analysis gives an optimum distance of 7.1 Å with an energy of -75.9 kJ mol^{-1}.

With each decrease in condensation level the depth of the energy well is reduced. The interaction has large Coulombic and polarisation components, which are affected by the condensation level much more than the dispersion or the repulsion terms.

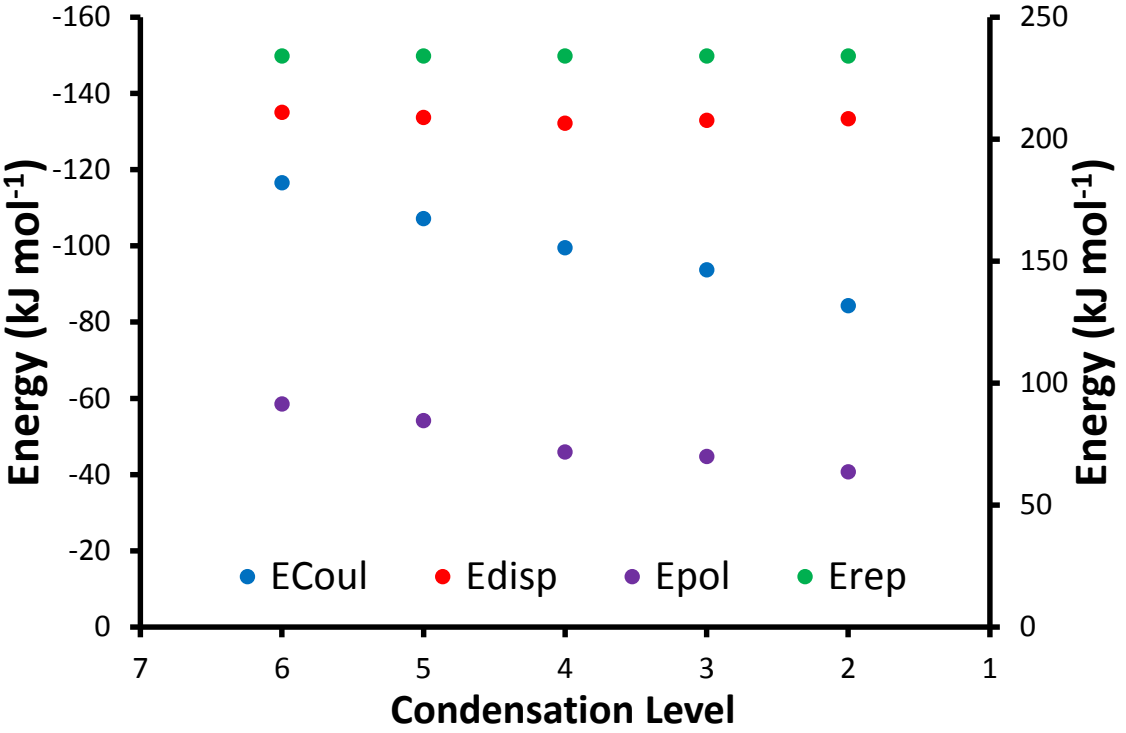

Figure 2.11: Variation in the individual PIXEL terms with condensation level. E_{rep} is shown on the right hand axis, other terms are on the left hand axis.

Figure 2.11 shows how the individual energy terms vary with respect to the condensation level at an embrace separation of 7.1 Å. The dispersion and repulsion terms remain effectively constant, while the Coulombic and polarisation terms decrease as the pixel size is reduced. This explains why the depth of the wells and the position of the minima change with condensation level. The lower Coulombic and polarisation terms resulting from the condensation level are unable to compensate for the increased repulsion at small separations. As the $[Ru(bipy)_3]^0$ complexes move apart, the repulsion will decrease, but so will the Coulombic interaction as this is highly dependent on the distance between the molecules. The embrace separation in crystalline $[Ru(bipy)_3]^0$ is 7.7 Å,[60] and with decreasing condensation level, the PIXEL result seems to move closer to this value (the minimum of the condensation level 2 well occurring at this point).

The curves calculated using the PIXEL method are not as smooth as that obtained using DMol, but this is likely due to the fact that no optimisations were performed at each step during the PIXEL calculation, whereas this was the case with the higher level method.

2.6 Conclusions

The PIXEL method has been adapted to incorporate 1st, 2nd and 3rd row transition metal species. For 1st row transition metal complexes the agreement observed between PIXEL lattice energies and experimental sublimation enthalpies (straight line parameters $y = 0.99(1)x$ and $R = 0.92$) is comparable with those obtained by Gavezzotti for organic crystals. Using the results of such PIXEL calculations, the nature of the interactions in the crystal structures of chromium hexacarbonyl and *bis*(acetylacetonato)-oxo-vanadium(IV) have been rationalised. For 2nd and 3rd row transition metals, a range of dimer interactions involving dihydrogen bonding and intermolecular embraces calculated using the PIXEL method compare favourably with those obtained from higher level computational methods.

The successful incorporation of 1st row transition metals into the PIXEL method, evidenced by the excellent agreement of calculated lattice energies with experimental sublimation enthalpies, means that the benefits of the PIXEL formulation can be applied to a wider range of chemical species. This is expanded upon in the following Chapter as an investigation of the adsorption of small gas molecules in metal-organic frameworks. Regarding 2nd and 3rd row transition metals, the scarcity of experimental sublimation enthalpies for complexes containing these elements means that thorough validation of the parameters is not currently possible. The initial results ($y = 1.02(3)x$ and $R = 0.92$) are promising, however, and the agreement of PIXEL energies with dimer interactions calculated at higher levels of computational theory is reassuring.

The PIXEL formulation is intended as a method of calculating intermolecular interactions, and as such it is unsuitable for calculation of energies where there is any covalent character to the interaction. For example, an attempt to apply PIXEL calculations to aurophilic interactions was unsuccessful (see this Chapter's supplementary information for further details), with dimer energies calculated as being between -2.4 and 63.8 kJ mol^{-1} (indicating a repulsion between the monomers) compared to reference energies of -10.5 to -45.1 kJ mol^{-1}. Symmetry adapted perturbation theory calculations have also been noted to fail for these systems,[61] which are of remarkable complexity, and where instantaneous charge transfer is important.[62] Consequently, these interactions are not fully closed-shell interactions in nature.[63] Since such interactions can often occur in inorganic chemistry, care should be taken to ensure

that the PIXEL method is applied only to systems governed by the purely intermolecular interactions it was designed to calculate.‡

‡ Many thanks are due to Nik Kaltsoyannis for fruitful discussions concerning the nature of aurophilicity, and to Andrew Bond for his assistance using processPIXEL with transition metal complexes.

2.7 References

1. A. Gavezzotti, *Zeitschrift für Kristallographie*, 2005, **220**, 499-510.
2. A. Gavezzotti, *Molecular Aggregation - Structure Analysis and Molecular Simulation of Crystals and Liquids*, 1st edn., Oxford University Press, New York, 2007.
3. A. Gavezzotti, *Journal of Chemical Theory and Computation*, 2005, **1**, 834-840.
4. C. J. Eckhardt and A. Gavezzotti, *Journal of Physical Chemistry B*, 2007, **111**, 3430-3437.
5. W. B. Schweizer and J. D. Dunitz, *Journal of Chemical Theory and Computation*, 2006, **2**, 288-291.
6. S. Aldridge, A. J. Downs, C. Y. Tang, S. Parsons, M. C. Clarke, R. D. L. Johnstone, H. E. Robertson, D. W. H. Rankin and D. A. Wann, *Journal of the American Chemical Society*, 2009, **131**, 2231-2243.
7. C. J. Adams, A. Angeloni, A. G. Orpen, T. J. Podesta and B. Shore, *Crystal Growth & Design*, 2006, **6**, 411-422.
8. C. J. Adams, P. C. Crawford, A. G. Orpen and T. J. Podesta, *Dalton Transactions*, 2006, 4078-4092.
9. A. Perez Paz, L. A. Espinosa Leal, M.-R. Azani, A. Guijarro, P. J. Sanz Miguel, G. Givaja, O. Castillo, R. Mas-Balleste, F. Zamora and A. Rubio, *Chemistry - A European Journal*, 2012, **18**, 13787-13799.
10. J. Muniz, C. Wang and P. Pyykko, *Chemistry - A European Journal*, 2011, **17**, 368-377.
11. H. Schmidbaur and A. Schier, *Chemical Society Reviews*, 2012, **41**, 370-412.
12. D. Di Tommaso, S. A. French and C. R. A. Catlow, *Journal of Molecular Structure: THEOCHEM*, 2007, **812**, 39-49.
13. D. Di Tommaso, S. A. French, A. Zanotti-Gerosa, F. Hancock, E. J. Palin and C. R. A. Catlow, *Inorganic Chemistry*, 2008, **47**, 2674-2687.
14. S. A. French, D. Di Tommaso, A. Zanotti-Gerosa, F. Hancock and C. R. A. Catlow, *Chemical Communications*, 2007, **23**, 2381-2383.
15. H. Li, E. N. Brothers and M. B. Hall, *Inorganic Chemistry*, 2014, **53**, 9679-9691.
16. T. Dudev and C. Lim, in *Annual Review of Biophysics*, 2008, vol. 37, pp. 97-116.
17. D. P. Martin, Z. S. Hann and S. M. Cohen, *Inorganic Chemistry*, 2013, **52**, 12207-12215.
18. I. Yruela, *Metallomics*, 2013, **5**, 1090-1109.
19. A. de Almeida, B. L. Oliveira, J. D. G. Correia, G. Soveral and A. Casini, *Coordination Chemistry Reviews*, 2013, **257**, 2689-2704.
20. H. Chiniforoshan, L. Tabrizi, M. Hadizade, M. R. Sabzalian, A. N. Chermahini and M. Rezapour, *Spectrochimica Acta Part A - Molecular and Biomolecular Spectroscopy*, 2014, **128**, 183-190.
21. R. Q. Snurr, A. O. Yazaydin, D. Dubbeldam and H. Frost, in *Metal-Organic Frameworks: Design and Application*, ed. L. R. MacGillivray, John Wiley & Sons, Inc., Hoboken, New Jersey, 2010, pp. 313-339.
22. S. Keskin, J. Liu, R. B. Rankin, J. K. Johnson and D. S. Sholl, *Industrial & Engineering Chemistry Research*, 2009, **48**, 2355-2371.
23. T. Duren, Y.-S. Bae and R. Q. Snurr, *Chemical Society Reviews*, 2009, **38**, 1237-1247.
24. A. Gavezzotti, *Journal of Physical Chemistry B*, 2002, **106**, 4145-4154.
25. A. Gavezzotti, *Journal of Physical Chemistry B*, 2003, **107**, 2344-2353.
26. RSC, 2013, p. RSC Visual Elements Periodic Table.
27. J. Emsley, *The Elements*, Oxford University Press, New York, 1989.
28. J. S. Chickos and W. E. Acree, *Journal of Physical and Chemical Reference Data*, 2002, **31**, 537-698.
29. S. Nag, K. Banerjee and D. Datta, *New Journal of Chemistry*, 2007, **31**, 832-834.
30. S. S. Batsanov, *Inorganic Materials*, 2001, **37**, 871-885.
31. G. W. T. M. J. Frisch, H. B. Schlegel, G. E. Scuseria, M. A. Robb, J. R. Cheeseman, G. Scalmani, V. Barone, B. Mennucci, G. A. Petersson, H. Nakatsuji, M. Caricato, X. Li, H. P. Hratchian, A. F. Izmaylov, J. Bloino, G. Zheng, J. L. Sonnenberg, M. Hada, M. Ehara, K. Toyota, R. Fukuda, J. Hasegawa, M. Ishida, T. Nakajima, Y. Honda, O. Kitao, H. Nakai, T. Vreven, J. A. Montgomery, Jr., J. E. Peralta, F. Ogliaro, M. Bearpark, J. J. Heyd, E. Brothers, K. N. Kudin, V. N. Staroverov, R. Kobayashi, J. Normand, K. Raghavachari, A. Rendell, J. C. Burant, S. S. Iyengar, J. Tomasi, M. Cossi, N. Rega, J. M. Millam, M. Klene, J. E. Knox, J. B.

Cross, V. Bakken, C. Adamo, J. Jaramillo, R. Gomperts, R. E. Stratmann, O. Yazyev, A. J. Austin, R. Cammi, C. Pomelli, J. W. Ochterski, R. L. Martin, K. Morokuma, V. G. Zakrzewski, G. A. Voth, P. Salvador, J. J. Dannenberg, S. Dapprich, A. D. Daniels, Ö. Farkas, J. B. Foresman, J. V. Ortiz, J. Cioslowski, and D. J. Fox, *Gaussian 09*, (2009) Gaussian Inc., Wallingford.

32. A. Gavezzotti, *OPiX*, (2003), Milan.
33. A. Gavezzotti, *Acta Crystallographica Section B - Structural Science*, 2010, **66**, 396-406.
34. R. F. W. Bader, *Atoms in Molecules: A Quantum Theory*, Oxford University Press, Oxford, 1990.
35. T. A. Keith, *AIMAll*, (2012) TK Gristmill Software, Overland Park, KS, USA.
36. I. J. Bruno, J. C. Cole, P. R. Edgington, M. Kessler, C. F. Macrae, P. McCabe, J. Pearson and R. Taylor, *Acta Crystallographica Section B - Structural Science*, 2002, **58**, 389-397.
37. R. M. Stephenson and S. Malanowski, *Handbook of the Thermodynamics of Organic Compounds*, Elsevier, New York, 1987.
38. G. Beech and R. Lintonbon, *Thermochimica Acta*, 1971, **2**, 86-88.
39. N. V. Belkova, M. Besora, L. M. Epstein, A. Lledos, F. Maseras and E. S. Shubina, *Journal of the American Chemical Society*, 2003, **125**, 7715-7725.
40. I. Andrieu, N. V. Belkova, M. Besora, E. Collange, L. M. Epstein, A. Lledos, R. Poli, P. O. Revin, E. S. Shubina and A. V. Vorontsov, *Russian Chemical Bulletin*, 2003, **52**, 2679-2682.
41. E. I. Gutsul, N. V. Belkova, M. S. Sverdlov, L. M. Epstein, E. S. Shubina, V. I. Bakhmutov, T. N. Gribanova, R. M. Minyaev, C. Bianchini, M. Peruzzini and F. Zanobini, *Chemistry - A European Journal*, 2003, **9**, 2219-2228.
42. I. Dance, *Molecular Crystals and Liquid Crystals*, 2005, **440**, 265-293.
43. *Materials Studio Release Notes*, (2010) Accelrys Software Inc., Cambridge, UK.
44. S. K. Wolff, D. J. Grimwood, J. J. McKinnon, M. J. Turner, D. Jayatilaka and M. A. Spackman, *CrystalExplorer (Version 3.1)*, (2012) University of Western Australia.
45. D. Jayatilaka and D. J. Grimwood, in *Computational Science - ICCS 2003, Pt IV, Proceedings*, eds. P. M. A. Sloot, D. Abramson, A. V. Bogdanov, J. J. Dongarra, A. Y. Zomaya and Y. E. Gorbachev, 2003, vol. 2660, pp. 142-151.
46. L. Maschio, B. Civalleri, P. Ugliengo and A. Gavezzotti, *Journal of Physical Chemistry A*, 2011, **115**, 11179-11186.
47. A. D. Bond, *Journal of Applied Crystallography*, 2014, **47**, 1777-1780.
48. A. Whitaker and J. W. Jeffery, *Acta Crystallographica*, 1967, **23**, 977-984.
49. M. Hoshino, A. Sekine, H. Uekusa and Y. Ohashi, *Chemistry Letters*, 2005, **34**, 1228-1229.
50. D. I. Arnold, F. A. Cotton, J. H. Matonic and C. A. Murillo, *Chemical Communications*, 1996, **18**, 2113-2114.
51. P. K. Hon, R. L. Belford and C. E. Pfluger, *Journal of Chemical Physics*, 1965, **43**, 3111-3115.
52. U. Schilde, W. Bansse, E. Ludwig and E. Uhlemann, *Zeitschrift für Kristallographie*, 1995, **210**, 627-628.
53. V. I. Bakhmutov, *Dihydrogen Bonds: Principles, Experiments and Applications*, John Wiley & Sons, Inc., Hoboken, NJ, 2008.
54. Q. Liu and R. Hoffmann, *Journal of the American Chemical Society*, 1995, **117**, 10108-10112.
55. G. Orlova and S. Scheiner, *Journal of Physical Chemistry A*, 1998, **102**, 260-269.
56. H. Jacobsen, *Physical Chemistry Chemical Physics*, 2009, **11**, 7231-7240.
57. I. Dance, *CrystEngComm*, 2003, **5**, 208-221.
58. I. Dance and M. Scudder, *CrystEngComm*, 2009, **11**, 2233-2247.
59. B. Delley, *Journal of Chemical Physics*, 1990, **92**, 508-517.
60. E. E. Perez Cordero, C. Campana and L. Echegoyen, *Angewandte Chemie - International Edition*, 1997, **36**, 137-140.
61. R.-F. Liu, C. A. Franzese, R. Malek, P. S. Zuchowski, J. G. Angyan, M. M. Szczesniak and G. Chalasinski, *Journal of Chemical Theory and Computation*, 2011, **7**, 2399-2407.
62. L. Magnko, M. Schweizer, G. Rauhut, M. Schutz, H. Stoll and H. J. Werner, *Physical Chemistry Chemical Physics*, 2002, **4**, 1006-1013.
63. Z.-F. Li, X.-P. Yang, H.-X. Li and Z. Guo, *Organometallics*, 2014, **33**, 5101-5110.

Chapter 3

Use of the PIXEL Method to Investigate Gas Adsorption in Metal-Organic Frameworks

3.1 Synopsis

PIXEL has been used to perform calculations of adsorbate-adsorbent interaction energies between a range of metal-organic frameworks (MOFs) and gas molecules. Interactions have been calculated for adsorption between MOF-5 and Ar, H_2, and N_2, $Zn_2(BDC)_2(TED)$ (BDC = 1,4-benzenedicarboxylic acid, TED = triethylenediamine) and H_2 and HKUST-1 and CO_2. The locations of the adsorption sites and the calculated energies, which show differences in the Coulombic or dispersion characteristic of the interaction, are compared to experimental data and literature energy values calculated using standard computational methods of analysis for adsorption in metal-organic frameworks.

3.2 Introduction

Over the last decade, the study of metal-organic frameworks (MOFs) has become a very popular avenue of research, with particular focus on their potential uses for gas storage and separation. Structurally, MOFs are made up of metal-ligand nodes that are connected by organic bridging ligands to form 3-dimensional porous frameworks. Synthesis of such frameworks can be achieved by combinations of these nodes and linkers to give a variety of structures with different pore sizes, topologies and chemical functionalities.[1] This so-called "modular synthesis" means that it is theoretically possible to create a vast catalogue of metal-organic frameworks for specific applications that is not possible for other porous materials such as zeolites.[2]

To date, there are over 10,000 MOF structures recorded in the Cambridge Structural Database (CSD).[3] However, comparatively little work has been done to investigate the precise locations of adsorption sites in these structures since such experiments can be difficult to carry out and require specialist equipment.[4] Additionally, the time taken to determine these positions for such a large number of structures experimentally renders such methods impractical. Consequently, computational modelling of gas adsorption in metal-organic frameworks is a very appealing alternative, as calculations can be performed under a range of different simulated conditions, and additionally theoretical MOFs can be tested for suitability before any synthetic work is undertaken.

Common simulation techniques for modelling adsorbate-adsorbent interactions in MOFs are molecular dynamics (MD), Monte Carlo simulations (MC) and quantum mechanical methods (QM). Each of these methods has various advantages and disadvantages as discussed below.

3.2.1 Molecular Dynamics Simulations

Molecular dynamics calculations commonly involve the use of classical force fields which define interactions between pairs of atoms, although it is also possible to perform such calculations using density functional theory. Normally the MOF atoms are fixed at positions which are determined through X-ray diffraction experiments before a suitable force field is chosen,[5] although some studies have investigated structural changes upon gas adsorption.[6] Interactions between the MOF and adsorbate molecules are then calculated using a combination of partial charges and Lennard-Jones or Buckingham potentials to account for the mixture of Coulombic and dispersion forces that comprise such interactions.

While the speed of such calculations makes molecular dynamics appealing to study such systems, the development of dedicated force fields requires accurate experimental measurements of adsorption obtained at a range of temperatures and pressures. Yang and Zhong[7] used experimental data for H_2 adsorption in MOF-5 at 77 K and pressures of up to 1 bar to fit interaction potential parameters before using their purpose-built force field to predict the adsorption behaviour at pressures up to 100 bar. When this behaviour is compared to experimental data at these higher pressures however,[8-10] the simulated adsorption was found to be more than double the experimental results.

Furthermore, since experimental adsorption isotherms are commonly used to create tailored force fields for MOF adsorption calculations,[11] the purity of the sample used to obtain the experimental isotherms is a critical factor. For instance, Liu *et al.*[12] compared a range of experimental adsorption isotherms for H_2 adsorption in HKUST-1 and found that the maximum uptake at 77 K and 1 bar ranged from 1.33 – 2.6 wt % when measured by different groups. This range results from the purity of the different samples, where any defects or residual solvent molecules from the synthesis of the MOF affect the adsorption capabilities of each sample. Since such experimental

considerations can lead to errors in tailored force fields, generic force fields such as DREIDING or UFF are commonly used instead. This can also overcome the chemical diversity of metal-organic frameworks. However, such force fields do not account for polarisation which can lead to the Coulombic interactions being underestimated.[13]

3.2.2 Monte Carlo Simulations

Monte Carlo simulations calculate interactions between the framework and adsorbate molecules using similar methods to molecular dynamics. Monte Carlo simulations consist of millions of random steps which are accepted or rejected according to initial specification criteria, and the results are averaged over the whole simulation.[14] As the potential energies are known at all steps of the simulation, the positions and energies of different binding sites in the MOF structure are accessible. Since they also rely on force fields to perform calculations, Monte Carlo simulations suffer from the same drawbacks as discussed for molecular dynamics.

3.2.3 Quantum Mechanical Methods

Quantum mechanical (QM) methods involve various different approximations to the solution of the Schrödinger equation in order to calculate different properties, such as interactions between adsorbent and adsorbate molecules. While such simulations do not require the use of empirically parameterised force fields to calculate interaction energies, many QM methods, particularly density functional theory (DFT), do not accurately model dispersion interactions, which are often extremely important in molecular adsorption.[11] For instance, an *ab initio* study of H_2 adsorption in MOF-5 by Sillar *et al.*[15] highlighted the dangers of neglecting dispersion. Periodic DFT calculations using the PBE exchange-correlation functional found the interaction energy at one site in MOF-5 to be -1.8 kJ mol^{-1}. When the dispersion correction of Grimme was used, this interaction increased to -6.3 kJ mol^{-1}, indicating how important such corrections are to studying hydrogen adsorption.

Perturbation methods, such as MP2, can be used instead of DFT to overcome the shortcomings of the calculation of dispersion energies, but such methods are extremely computationally expensive. MP2 calculations on periodic systems are possible,[16] but to date no such studies have been performed on metal-organic frameworks, and as such

MP2 calculations are normally carried out on small fragments representing the chemistry of the MOF.[11] The choice of fragment used is very important as well. Sillar also calculated the hydrogen adsorption energy of site I in MOF 5 (see Figure 3.2 below) at the MP2 level of theory,[15] obtaining energies of -4.4 kJ mol^{-1} for a model not including the aromatic linkers, and -6.0 kJ mol^{-1} for a model when the linkers were included.

3.2.4 The Potential Advantages of PIXEL for Adsorption Calculations

While the methods described above are useful for predicting various physical properties of MOFs and MOF adsorption, the PIXEL methods presents itself as a feasible alternative for calculating adsorption energies and predicting adsorption sites across a wide range of MOFs and adsorbate molecules. Although it requires discrete molecules for its calculations, as long as a model fragment is chosen judiciously, practically any MOF, either experimentally determined or theoretical, can be investigated. However, since PIXEL can only calculate interaction energies between two independent fragments, cooperative adsorption between two or more molecules and secondary adsorption cannot be investigated using this method.

Calculation of the electron densities of the adsorbent and adsorbate fragments is the only computationally expensive step, with adsorption interactions taking very little time to calculate on a desktop PC. The transferability of the PIXEL method means that it can be applied across a range of systems and that in all such cases the same parameters are being used so that calculations are comparable. Furthermore, since the method gives energies broken down into a range of chemically meaningful terms, it can be used to ascertain the character of different interactions.

This work aims to test the suitability of the PIXEL method for calculating adsorption sites in metal-organic frameworks. Calculations have been performed on a selection of different MOFs and adsorbates for systems where structural and energetic information for adsorption was available. Three different MOFs have been chosen on the basis that they displayed various chemical functionalities, experimental and theoretical data for adsorption for a range of gases were available, and the chemistry of the MOFs could be represented with small models. These three frameworks are MOF-5, $Zn_2(BDC)_2(TED)$ and HKUST-1, and are described in the following section.

3.3 Description of Metal-Organic Frameworks Studied

3.3.1 MOF-5

MOF-5 (also known as IRMOF-1) is one of the most widely studied metal-organic frameworks. Often considered to be the "archetypal" MOF, the original paper describing MOF-5[17] has been cited nearly 3000 times. Consequently, its applications to gas storage have been extensively studied. There is a wealth of information available regarding adsorption in this system, with both experimental and theoretical studies of the uptake of many gases such as H_2,[18] methane,[19] CO_2,[20] N_2,[21] and Ar.[21]

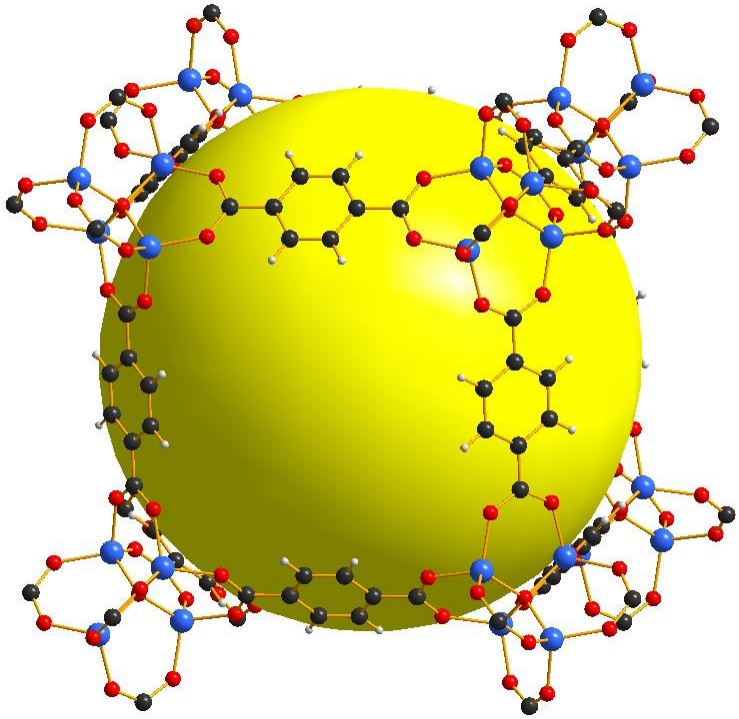

Figure 3.1: A section of the structure of MOF-5. Carbon atoms are shown in grey, hydrogen in white, oxygen in red and zinc in light blue. The yellow sphere indicates the large pores that exist throughout the framework.

MOF-5 consists of Zn_4O_{13} clusters connected by benzene dicarboxylate linkers (Figure 3.1). The framework structure leads to large pores throughout MOF-5, the largest of which is around 15 Å in diameter (shown as the yellow sphere in Figure 3.1), and it is within such pores that gas molecules can be adsorbed. Single crystal X-ray diffraction studies between 30 and 293 K by Rowsell *et al.*[22] found eight symmetry independent adsorption sites in the structure of MOF-5, using argon as the adsorbate. Three of these sites are associated with the metal cluster, two are associated with the organic linker, and the remaining three are located towards the centre of the pores, and

are the result of secondary adsorption. Figure 3.2 shows the locations of the five sites that are primarily associated with the framework structure.

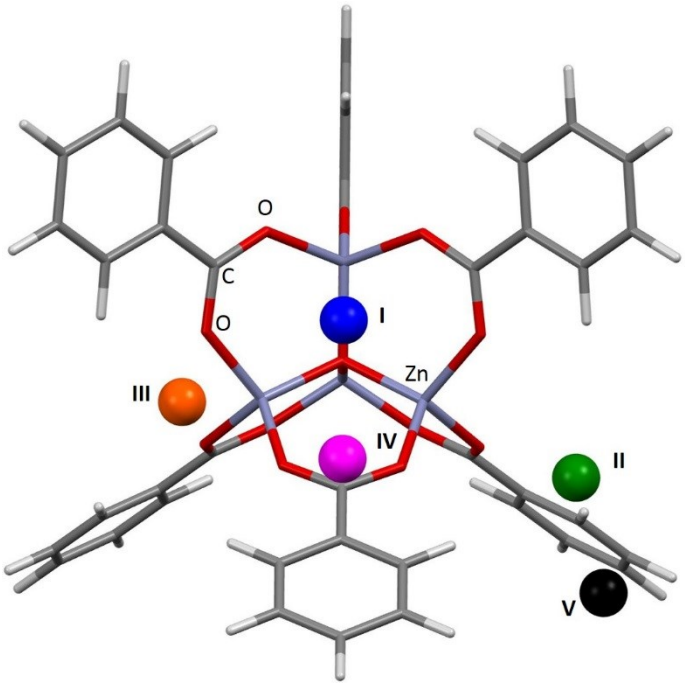

Figure 3.2: The five adsorption sites primarily associated with the framework structure of MOF-5. The locations of these sites were obtained from single crystal diffraction data (CSD Refcode LAWFUL).[22]

Site I sits directly above the central oxygen atom of the $Zn_4O(CO_2)_6$ unit, site II lies above the zinc atom in the ZnO_3 unit, site III lies above the ZnO_2 unit of the metal cluster, site IV lies above the phenyl ring, and site V lies to the edge of the phenyl ring. Distances from the adsorption sites to selected framework atoms are shown in Table 3.1.

Site	Framework Atom	Expt. Distance (Å)
I	C (carboxylate)	3.572
II	O (carboxylate)	3.492
III	O (carboxylate)	3.792
IV	C (aromatic)	3.637
V	H (aromatic)	3.288

Table 3.1: Distances of adsorption sites from selected framework atoms corresponding to the model in Figure 3.2.

The fragment of MOF-5 shown in Figure 3.2, with the benzene dicarboxylate linkers capped with hydrogen atoms, captures the chemistry of the framework sufficiently to model the pore around the areas where adsorption takes place. As such, this fragment is

suitable for PIXEL calculations, and was the fragment chosen for all calculations based on the MOF-5 system that are discussed in this Chapter.

3.3.2 $Zn_2(BDC)_2(TED)$

$Zn_2(BDC)_2(TED)$ (BDC = 1,4-benzenedicarboxylic acid, TED = triethylenediamine), first reported by Lee *et al.*,[23] consists of $Zn_2(DBC)_4$ paddlewheels connected by triethylenediamine molecules [Figure 3.3(a)]. This metal-organic framework has a 3-dimensional porous structure consisting of intersecting channels with two different sized pore windows [Figure 3.3(b) & (c)].

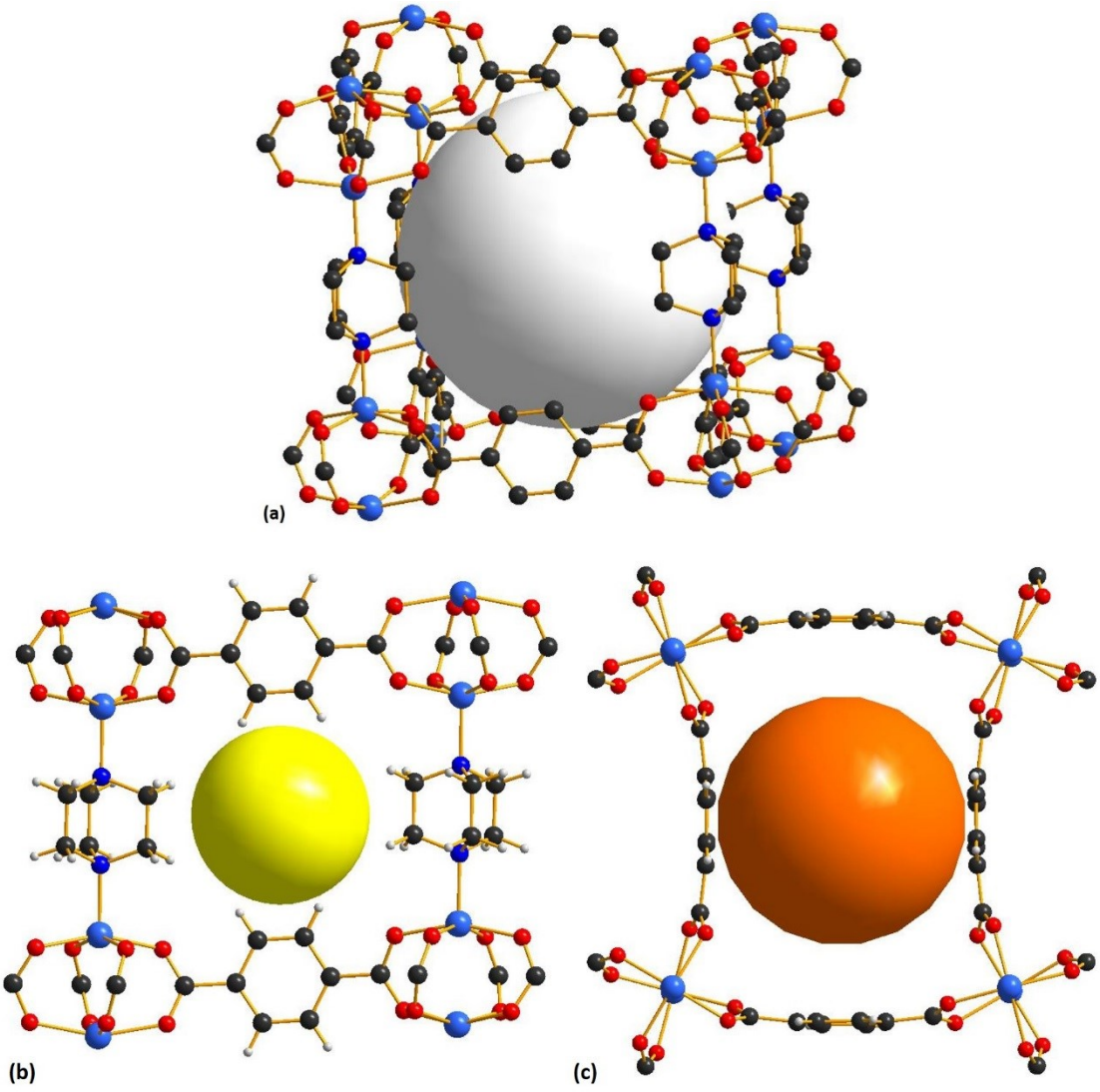

Figure 3.3: (a) A section of the structure of $Zn_2(BDC)_2(TED)$ (hydrogen atoms omitted for clarity). Carbon atoms are shown in grey, nitrogen in dark blue, oxygen in red and zinc in light blue. Also shown are the two different channels viewed along the crystallographic *a*-axis (b) and the *c*-axis (c).

The small channel [represented by the yellow sphere in Figure 3.3(b)] has a cross section of 4.8 x 3.2 Å and the larger pore [orange sphere in Figure 3.3(c)] has a maximum diameter of 7.5 Å.[23] Several experimental and theoretical studies of adsorption in these channels exist for hydrogen,[24, 25] methane,[26] nitrogen,[27] CO,[27] and CO_2,[27] as well as the separation of liquid mixtures such as methanol/water.[28]

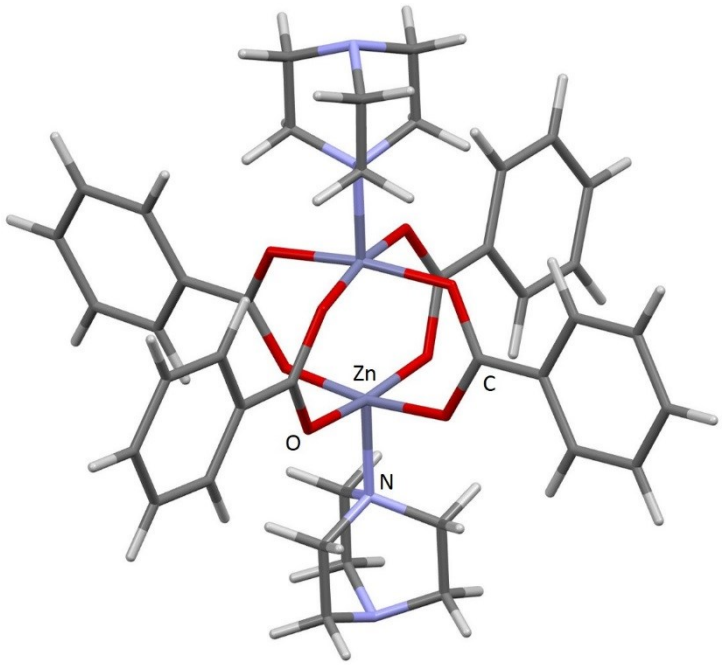

Figure 3.4: The fragment model of $Zn_2(BDC)_2(TED)$ used for PIXEL studies in this Chapter.

The effective structure of these two channels can be captured by capping the BDC linkers of the paddlewheel motif with hydrogen atoms (Figure 3.4), and this fragment was the structure chosen for PIXEL studies of the $Zn_2(BDC)_2(TED)$ framework.

3.3.3 HKUST-1

HKUST-1 [also known as Cu(BTC), where BTC is benzene-1,3,5-tricarboxylate] is a highly porous metal-organic framework. First synthesized by Chui *et al.*,[29] it consists of $Cu_2(BTC)_4$ paddlewheel building blocks (Figure 3.5) connected to make a 3-dimensional porous structure.

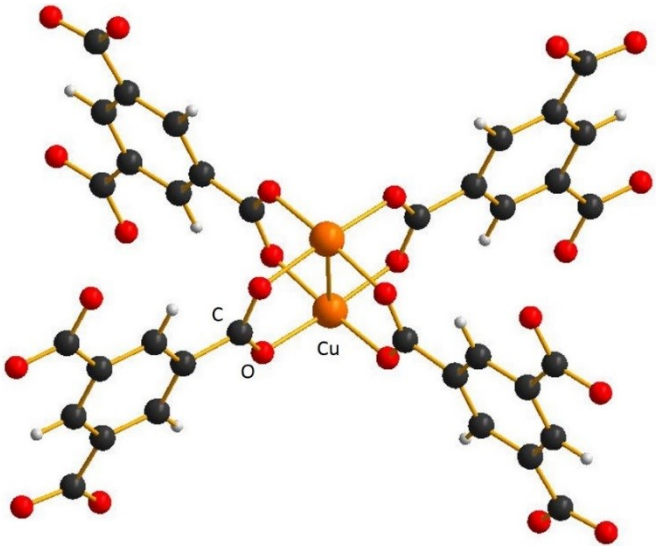

Figure 3.5: The copper paddlewheel motif that is the building block of HKUST-1. Carbon atoms are shown in grey, hydrogen in white, oxygen in red and copper in orange.

The nature of the copper paddlewheel building blocks leads to a large and complex structure where there are three distinct interconnected pores (Figure 3.6). The smallest of these pores has a diameter of around 5 Å, the medium pore 11 Å and the large pore around 13.5 Å.

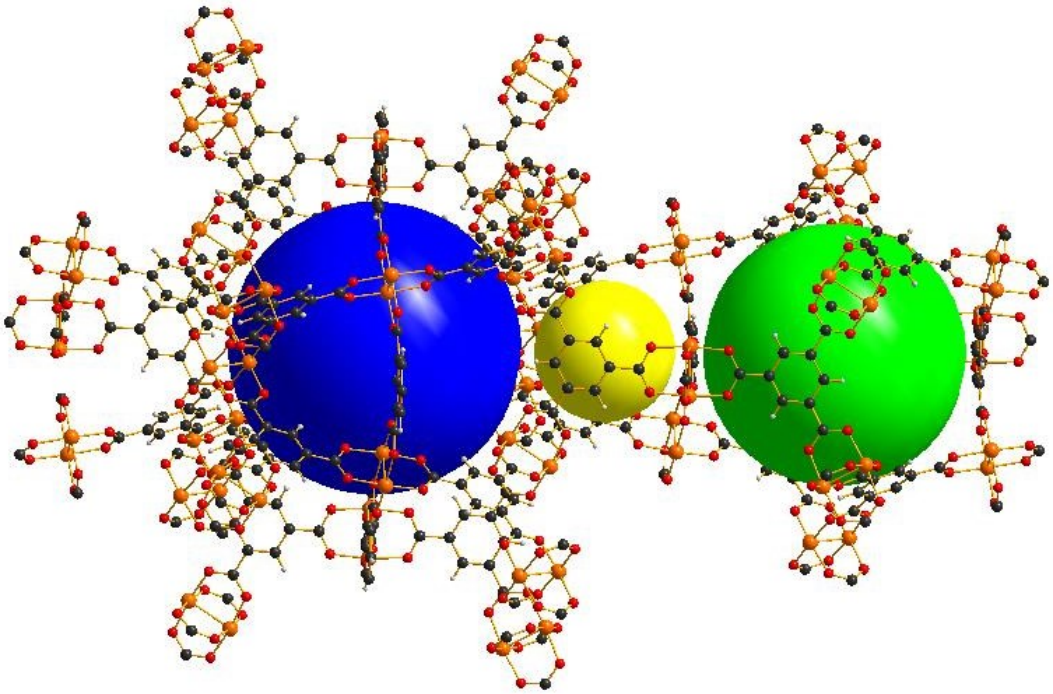

Figure 3.6: The three pores in HKUST-1. The small pore is shown as the yellow sphere, medium as green and large as blue.

The large pore volumes in HKUST-1 have made it the subject of a number of experimental and theoretical studies of gas adsorption, in particular the adsorption of hydrogen,[30] nitrogen,[31] CO,[31] CO_2,[31, 32] and NO.[33] In this Chapter, the nature of the adsorption of CO_2 by HKUST-1 is investigated in the small pore, as in the study of Grajciar and co-workers.[32] This region was chosen as it allowed for a smaller, computationally less demanding, fragment model to be chosen, than for either of the two larger pores. This model was obtained by capping three of the copper paddlewheel motifs as well as three of the carboxylate groups as shown in Figure 3.7.

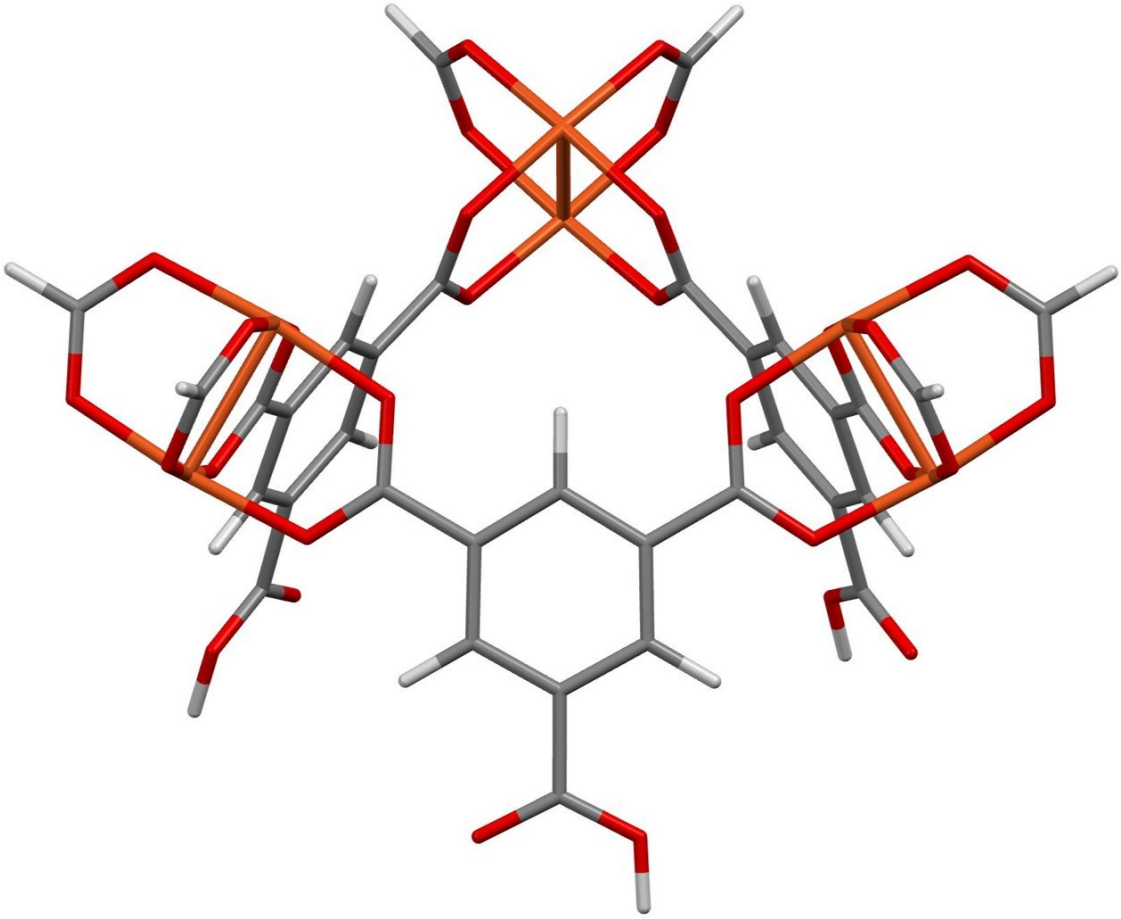

Figure 3.7: The small fragment chosen to model the small pore in HKUST-1 used for the PIXEL studies in this Chapter.

3.4 Experimental

MOF fragments were generated from crystal structures obtained from the Cambridge Structural Database[3] which were then modified using Materials Studio[34] and Mercury.[35] Fragments were chosen to create a model that represented the key structural features of the MOFs whilst keeping the total number of atoms below 100 (required because of array size limits imposed by the implementation of the PIXEL code with a Windows operating system). Figures in Section 3.3 show the fragments used in each case and how they are related to the actual structures of the MOFs. Structural coordinates for the fragments used are contained within the Supplementary Information. Bond lengths for H_2 and N_2 adsorbate molecules were obtained from reference 36, while those for CO_2 were obtained from its crystal structure.[37]

Fortran programs were written to automate the following procedure, and the source codes are contained in the Supplementary Information for this Chapter. Systems were set up such that the MOF fragments were positioned in the centre of a 20 x 20 x 20 Å grid. The adsorbate molecule was put at the grid origin and then moved in 1 Å steps systematically along the *x*, *y*, and *z* axes of the grid (with the exception of MOF-5/Ar, where the step size was 0.5 Å). A PIXEL calculation was performed at each of these grid points unless the position of the adsorbate molecule would lead to overlap of the covalent radii of any atoms. This was performed by calculating the distances between the atoms in the adsorbate molecule to those in the fragment and comparing these distances to the sum of the covalent radii for each atomic species.

Except in the case of Ar, the orientation of the adsorbate molecule was varied at each grid point. Thirteen orientations were used to sample each search point, with the molecules aligned along the following *x,y,z* vectors: 1,0,0; 0,1,0: 0,0,1: 1,1,0; 1,0,1: 0,1,1; -1,1,0; -1,0,1; 0,-1,1; 1,1,1; -1,1,1; 1,-1,1; -1,-1,1. This allowed a reasonable number of orientations to be investigated without becoming too numerous as to be excessively computationally demanding.

The symmetry of the MOF-5 and HKUST-1 fragments allowed a reduced search to be performed, and as such only the search space corresponding to the asymmetric unit of -43*m* for MOF-5 ($0 \leq x \leq 1$; $y \leq \min(x, 1 - x)$; $z \leq y$) and that of a 3-fold axis along the [1,1,1] direction ($0 \leq x \leq 1$; $y \leq x$; $z \leq x$) for the HKUST-1 fragment were used.

Electron densities were obtained using Gaussian09[38] at the B3LYP/6-31G** level of theory. PIXEL calculations were carried out at condensation level five (a pixel size of 0.2 x 0.2 x 0.2 Å) and the atomic parameters for metal and non-metal atoms are the same as those used in Chapter 2 (Table 3.2).

Atom	*DIFA*	*RAVDW*	*RINTER*	*ZTOT*	*ZVAL*	*POLZE*	*ELNEG*	*POTIO*	*WEIGHT*
H	0.40	1.10	1.10	1	1	0.39	2.10	0.500	1.0079
C	0.90	1.77	1.77	6	4	1.35	2.50	0.414	12.011
N	0.50	1.64	1.64	7	5	0.95	3.00	0.534	14.007
O	0.40	1.58	1.58	8	6	0.75	3.50	0.500	16.000
F	0.00	1.46	1.46	9	7	0.40	4.00	0.640	19.000
Cl	0.25	1.76	1.76	17	7	2.30	3.00	0.477	35.453
Br	0.10	1.87	1.87	35	7	3.27	2.80	0.434	79.904
Ar	0.40	1.80	1.80	18	8	1.75	2.50	0.579	39.948
Cu	0.40	2.00	1.35	29	11	2.81	1.75	0.284	63.550
Zn	0.40	2.10	1.31	30	12	3.63	1.66	0.345	65.380

Table 3.2: Atomic parameters used for PIXEL calculations in this Chapter.

Upon completion, the energies at each gridpoint were ranked from highest to lowest, and the 200 strongest interactions were visualised around the fragment using Mercury. This allowed the independent adsorption sites to be located visually, with any points arising from favourable interactions in locations between these independent adsorption sites being omitted. For the MOF-5/Ar, MOF-5/N_2 and MOF-5/H_2 systems, once located, the positions of the independent sites were refined by performing a 0.2 Å grid search around a reduced space (searching in the region $x/y/z$ – 1 Å to $x/y/z$ + 1 Å, where $x/y/z$ are the coordinates of the independent adsorption site). All RMS fits were calculated using Mercury, and are based on the centres of mass of the adsorbate molecules.

3.5 Results and Discussion

Gas adsorption sites and energies for different systems calculated using PIXEL are compared to literature values in the following order: MOF-5/Ar; MOF-5/N_2; MOF-5/H_2; $Zn_2(BDC)_2(TED)/H_2$; HKUST-1/CO_2.

3.5.1 Gas Adsorption between MOF-5 and Ar

Figure 3.8 shows the results of the PIXEL calculations performed on this system for the locations of the five highest energy symmetrically independent adsorption sites (red) overlaid with those obtained experimentally by Rowsell (black).[22]

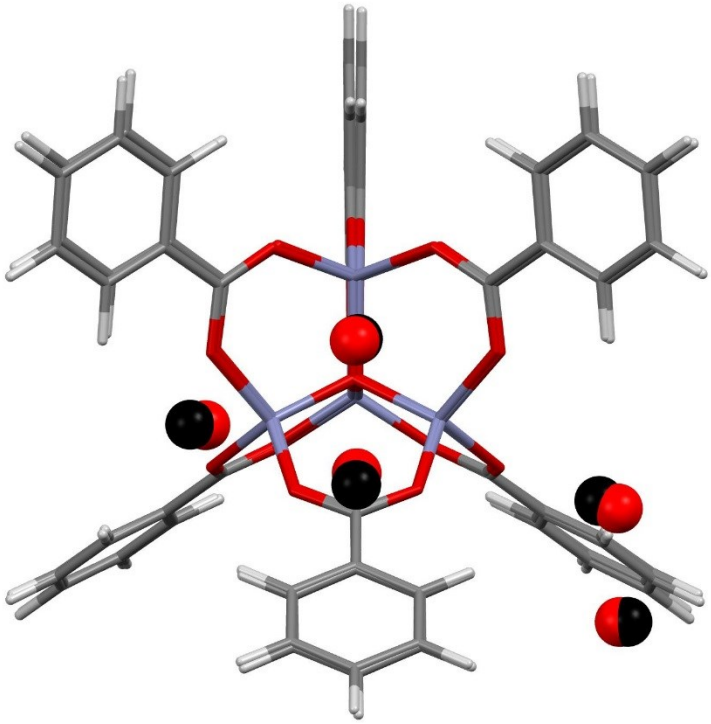

Figure 3.8: Overlay of Ar adsorption sites in MOF-5 located using PIXEL (red) with those obtained experimentally (black).

The RMS fit of the overlay between the central Zn_4O and the Ar atoms of each fragment as calculated in Mercury is 0.251 Å when a 1 x 1 x 1 Å grid was used, indicating that the locations of the sites obtained from PIXEL lie in the positions corresponding to sites I-V. Using a smaller grid step of 0.2 x 0.2 x 0.2 Å for these sites leads to a slightly improved RMS fit of 0.195 Å. Table 3.3 shows the distances from selected framework atoms of the adsorption sites obtained experimentally compared to those found using PIXEL with the finer grid search.

Site	Framework Atom	Expt. Distance (Å)	PIXEL Distance (Å)
I	C (carboxylate)	3.572	3.697
II	O (carboxylate)	3.492	3.527
III	O (carboxylate)	3.792	3.442
IV	C (aromatic)	3.637	3.672
V	H (aromatic)	3.288	3.199

Table 3.3: Average distances of Ar adsorption sites from particular framework atoms corresponding to the model in Figure 3.8.

In a theoretical study, Monte Carlo methods were used by Dubbeldam *et al.*[39] to probe the energies of the adsorption sites of argon in MOF-5 found by the X-ray diffraction study of Rowsell.[22] Energy minimizations of a single argon atom at a temperature of 30 K (one of the temperatures at which crystallographic data were obtained) found preferential adsorption at sites I, II and IV. Upon higher loading, site III is filled preferentially over site II, although the binding energies for these sites are found to be almost equal. Adsorption energies are reported at these four sites, although it should be noted that Dubbeldam *et al.* were unable to identify site V, and consequently no energy data were available for this site. Since the experimental data of Rowsell *et al.* shows that site V is only occupied at a lower temperature than site IV, it would be expected that site V has a correspondingly lower adsorption energy.

Site	$E_{classical}$	E_{PIXEL}	E_{Coul}	E_{disp}	E_{rep}	E_{pol}
I	-11.52	-11.4	-2.7	-15.6	7.7	-0.7
II	-8.42	-9.8	-3.4	-13.5	8.6	-1.4
III	-8.44	-8.2	-3.0	-12.9	8.8	-1.0
IV	-6.99	-3.7	-1.7	-8.2	6.8	-0.6
V	–	-3.2	-0.5	-4.3	1.9	-0.2

Table 3.4: Adsorption energies for Ar in MOF-5 obtained from classical Monte Carlo simulations and from the PIXEL method. No experimental occupancy data is available. All values are in kJ mol^{-1}.

Table 3.4 shows the PIXEL calculated adsorption energies corresponding to the geometric data in Table 3.3 compared to those obtained through Monte Carlo methods. All values lie within around 3 kJ mol^{-1} or less of each other, and the trend in the order of site energy observed is similar in both cases. These discrepancies can likely be accounted for by the slight differences in the locations of the sites as described above.

The interactions are clearly dominated by the dispersion term in each case, and it seems that the preferential ordering of the different adsorption sites is determined by the number of short contacts that can be made between the adsorbing argon atoms and the atoms of the framework. Since an argon atom at site I interacts with the central oxygen as well as three zinc atoms and three CO_2 moieties, this site will have the highest dispersion interaction, as is observed. Argon atoms at sites II and III will interact with one zinc atom and three and two oxygen atoms respectively, explaining the decreasing dispersion interactions for these sites. Since sites IV and V interact only with the aromatic ring of the organic linker, they have the lowest interaction energy, as is observed from both PIXEL and the classical studies.

3.5.2 Gas Adsorption between MOF-5 and N_2

Figure 3.9 shows the locations of the adsorption sites obtained from PIXEL, and Table 3.5 shows the average distances between the N_2 centres of mass and particular framework atoms.

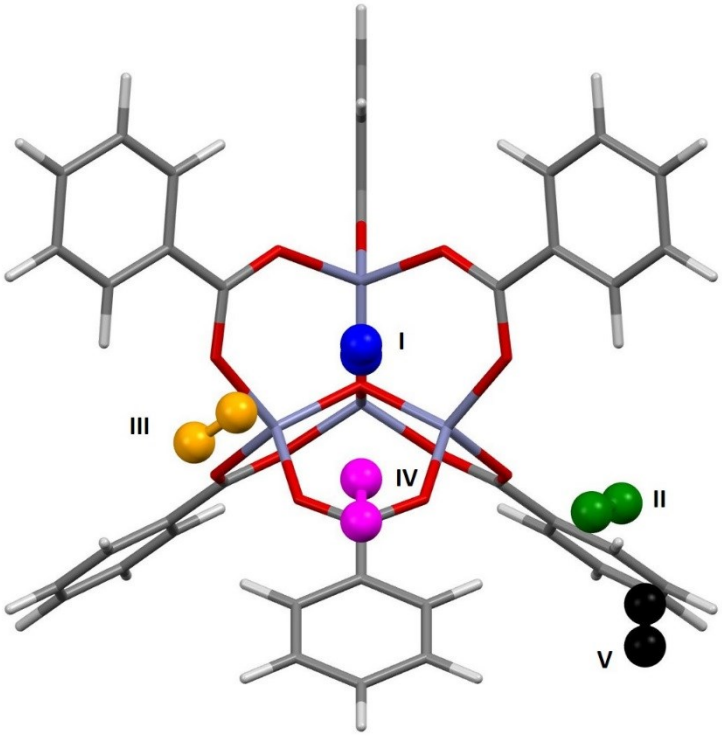

Figure 3.9: N_2 adsorption sites in MOF-5 located using PIXEL.

Site	Framework Atom	Expt. Distance (Å)	PIXEL Distance (Å)
I	C (carboxylate)	3.655	3.404
II	O (carboxylate)	3.518	3.379
III	O (carboxylate)	3.967	3.442
IV	C (aromatic)	3.770	3.664
V	H (aromatic)	3.610	3.329

Table 3.5: Average distances of N_2 adsorption sites from particular framework atoms corresponding to the model in Figure 3.9.

The same studies as mentioned above for adsorption with argon also report adsorption between MOF-5 and N_2.[22, 39] Experimental measurements show that at 30 K sites I, II and V are occupied. It was found that site IV becomes occupied preferentially to site V at 50 K, and at 90 K site II is occupied instead of site III. The RMS fit between the centres of mass of the independent adsorption sites found using the PIXEL method is 0.549 Å, which is reduced to 0.295 Å upon a search over a finer grid spacing (0.2 Å step). PIXEL calculated adsorption energies corresponding to the geometries in Table 3.5 are shown in Table 3.6 along with those obtained from Monte Carlo studies. Also shown are the component energy terms from each PIXEL calculation. Once again, no energetic data were reported for site V, so no comparison can be made.

Site	$E_{classical}$	E_{PIXEL}	E_{Coul}	E_{disp}	E_{rep}	E_{pol}
I	-12.13	-17.0	-18.7	-33.2	40.5	-5.6
II	-8.70	-10.7	-6.7	-16.9	15.3	-2.4
III	-10.65	-10.1	-4.4	-14.0	9.9	-1.6
IV	-7.57	-5.2	-1.5	-7.6	4.3	-0.5
V	–	-3.8	-1.6	-4.4	2.6	-0.4

Table 3.6: Adsorption energies for N_2 in the different adsorption sites of MOF-5. No data were available for the interaction with Site V. All values are in kJ mol^{-1}.

As Table 3.6 shows, while site I is significantly higher in energy than the other sites, and sites IV and V are the lowest in energy, the magnitudes of the PIXEL calculated energies for sites II and III are swapped with regards to the energies obtained from Monte Carlo methods. However, the results of the PIXEL calculations agree with qualitative analysis from Rowsell based on variable temperature studies,[22] where site II was found to have a higher energy of adsorption than site III. Since no energetic data were available for site V it is impossible to compare values, however PIXEL calculates this site as being of a similar energy to site IV, which agrees with what is observed in

the experimental study by Rowsell, since both sites IV and V are occupied only at low temperatures (50 K and 30 K respectively).[22] Once again, the interactions are dominated by the dispersion term, and this is likely due to the proximity of close contacts in each case. In the case of site I, the Coulombic interaction is around three times larger than those of the other sites. This likely arises from the proximity of the N_2 molecule to the metal cluster; the nitrogen atom closest to the cluster sits 3.188 Å from three Zn^{2+} ions. While the charge on a nitrogen atom in N_2 is formally zero, the proximity of the lone pair, and the corresponding electron density, to the three cations will result in a favourable electrostatic interaction.

3.5.3 Gas Adsorption between MOF-5 and H_2

Figure 3.11 shows the most favourable orientations of the H_2 molecules at sites I-IV as calculated by PIXEL, and Table 3.7 shows the distances of the centres of mass of these sites to selected framework atoms.

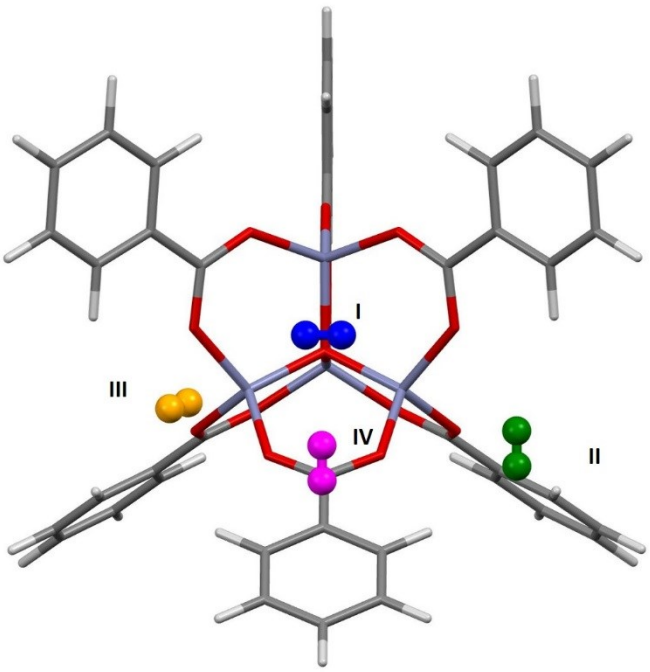

Figure 3.11: The most favourable orientations of the H_2 molecules found using PIXEL at sites I-IV in MOF-5.

Site	Framework Atom	Expt. Distance (Å)	PIXEL Distance (Å)
I	C (carboxylate)	3.373	3.150
II	O (carboxylate)	3.316	2.812
III	O (carboxylate)	3.409	2.860
IV	C (aromatic)	3.476	3.410

Table 3.7: Average distances of H_2 molecules from particular framework atoms corresponding to the model in Figure 3.11.

The initial RMS fit from the 1.0 Å grid search was 0.359 Å, which was improved slightly to 0.328 Å with a finer 0.2 Å grid space. The distances of the PIXEL calculated adsorption sites from selected framework atoms are shown in Table 3.7. In this case, sites II and III are found significantly closer to the framework than those observed experimentally. However, if sites II and III as found by PIXEL are occupied simultaneously, a short H…H distance of 2.149 Å exists, which is smaller than the sum of the van der Waals radii (2.2 Å). The distances for sites II and III obtained from PIXEL are consistent with those calculated for single H_2 molecule adsorption at the MP2 level by Sillar, where H…O distances of 2.988 Å and 2.969 Å were obtained for sites II and III respectively, indicating that it is the interactions between the adsorbate molecules at these sites affecting their locations, and this is not accounted for by PIXEL.

Neutron powder diffraction studies at 3.5 K by Yildirim and Hartman[40] of hydrogen adsorption in MOF-5 at various concentrations of D_2 (4 – 46 D_2 molecules per 4 Zn) found four independent adsorption sites consistent with sites I-IV as described above. Once located, periodic DFT calculations using plane-waves (local density approximation[41]) were used to calculate the binding energies of H_2 molecules at these sites. Two different orientations of the gas molecules were simulated, one where the H_2 molecule lay parallel to the 3-fold axis near the adsorption site (E_{par}), and the other where it lay perpendicular to this axis (E_{perp}), the most favourable interactions occurring for the perpendicular orientation of the H_2 molecules. Table 3.8 shows the energies of the interactions at sites I-IV as calculated by PIXEL, along with the breakdown of individual terms, compared to the literature DFT energies.

Site	$E_{DFT(par)}$	$E_{DFT(perp)}$	E_{PIXEL}	E_{Coul}	E_{disp}	E_{rep}	E_{pol}
I	-12.8	-15.4	-13.1	-9.7	-22.6	24.0	-4.7
II	-8.3	-11.1	-8.1	-7.8	-15.3	19.3	-4.3
III	-5.4	-10.4	-7.5	-6.4	-11.5	12.7	-2.3
IV	-8.9	-10.2	-3.1	-1.6	-5.3	4.5	-0.6

Table 3.8: Adsorption energies for H_2 in the different adsorption sites of MOF-5. All values are in kJ mol^{-1}.

With the exception of Site IV, while the PIXEL energies are around 4 kJ mol^{-1} lower than the DFT energies, the correct trend is observed compared to the DFT E_{perp} energies, which are the more favourable in each case. However, since the coordinates used for the DFT calculations are not available, it is difficult to compare the effect of the orientation of the H_2 molecule using the two methods.

Importantly, the order of the site energies calculated with PIXEL corresponds to the experimental observations of the adsorption mechanism in this system.[40] While the interaction energy for site IV calculated with PIXEL is significantly lower than that from DFT, the binding energy for a similar interaction was calculated as -3.78 kJ mol^{-1} by Dubbeldam,[39] a result close to the PIXEL energy of -3.1 kJ mol^{-1}. Consequently, this discrepancy could arise from cooperative stabilisation of site IV by loadings in the other sites, an effect not accounted for by PIXEL.

3.5.4 Gas Adsorption between $Zn_2(BDC)_2(TED)$ and H_2

A study by Kong *et al.*[25] investigated hydrogen adsorption in $Zn_2(BDC)_2(TED)$ (where BDC is benzenedicarboxylate and TED is triethylenediamine) using both experimental and theoretical techniques found that in this system there are no specific adsorption sites, but rather two channels, denoted A and B, that run through the structure through which the binding energies are almost equal. Channel A runs parallel to the Zn(TED) axis and Channel B runs perpendicular to this (Figure 3.12, black and blue lines respectively).

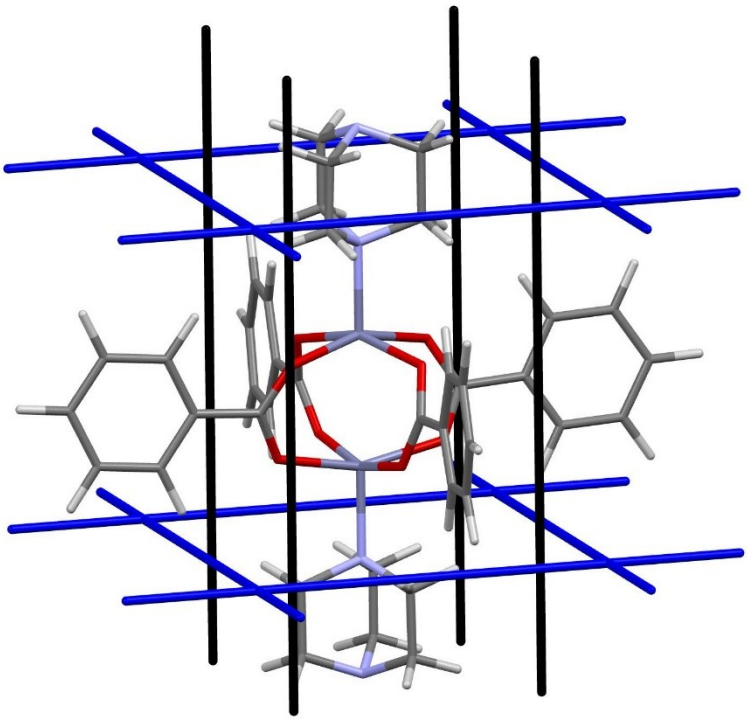

Figure 3.12: Adsorption channels in $Zn_2(BDC)_2(TED)$. The black lines show the A channels, and the blue lines show the B channels.

Using a recently developed non-empirical van der Waals density functional,[42, 43] it was found that throughout both channels the hydrogen binding energy was around -10 kJ mol^{-1}, with a variation of only around 1 kJ mol^{-1} depending on channel and H_2 orientation. This was found to be consistent with experimental data, where a single Langmuir isotherm was used to fit the uptake data, and from which binding energies of around -7 kJ mol^{-1} were obtained.

Figure 3.13 shows the results of the PIXEL calculation for the 100 highest energy H_2 interactions, and Figure 3.14 shows the frequencies of these energies.

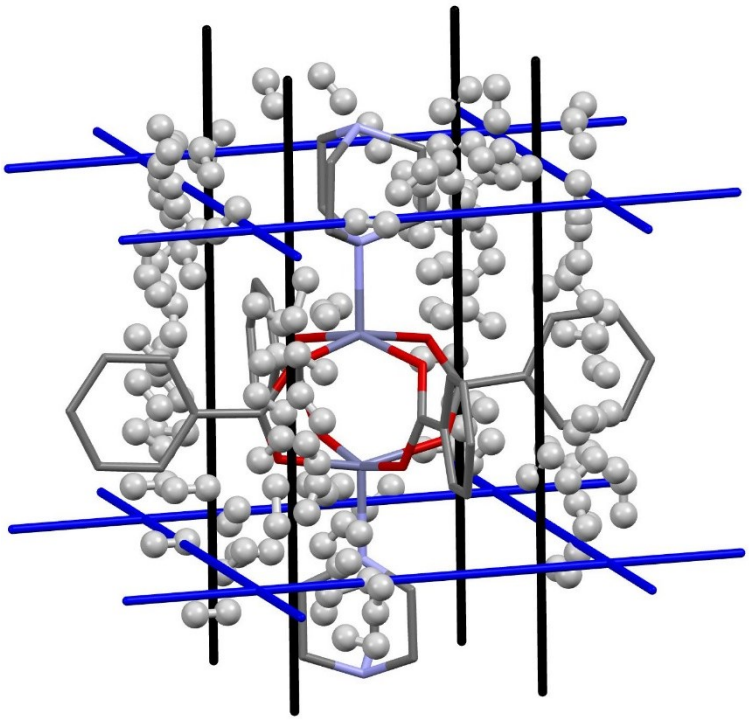

Figure 3.13: H_2 adsorption in $Zn_2(BDC)_2(TED)$ for the first 100 binding sites. Hydrogen atoms are omitted from the framework structure for clarity.

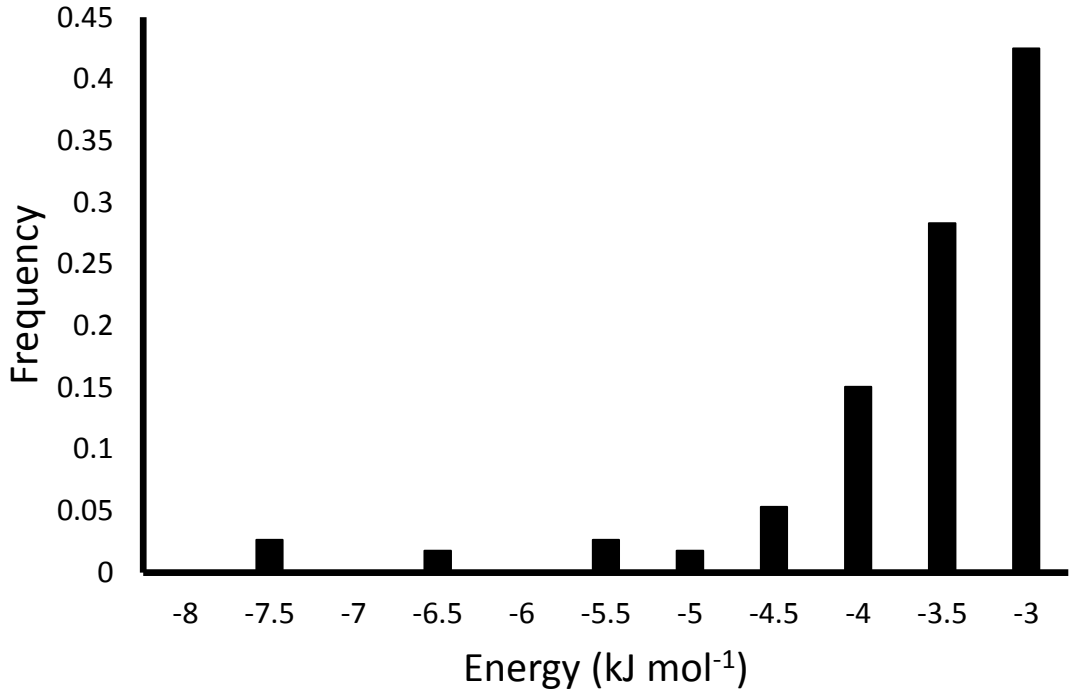

Figure 3.14: Energy frequency for the first 100 binding sites of H_2 in $Zn_2(BDC)_2(TED)$ as calculated by PIXEL.

The PIXEL calculated adsorption energies of the H_2 binding sites shown in Figure 3.13 and 3.14 all lie in the range of -7.6 kJ mol^{-1} to -3.1 kJ mol^{-1}, with an average interaction of -3.9 kJ mol^{-1}. Additionally, the orientation of the H_2 molecule seems to have very little impact on the energy calculated at each point. This indicates that in this system the H_2 molecules simply condense in the channels of the framework, and as such it does not present a strong candidate for a hydrogen storage material under the criteria of Bhatia and Myers.[44]

3.5.5 Gas Adsorption between HKUST-1 and CO_2

Figure 3.15 shows the location of the three independent sites found by PIXEL analysis, and Table 3.9 shows the energies of these interactions compared to DFT/CC energies.

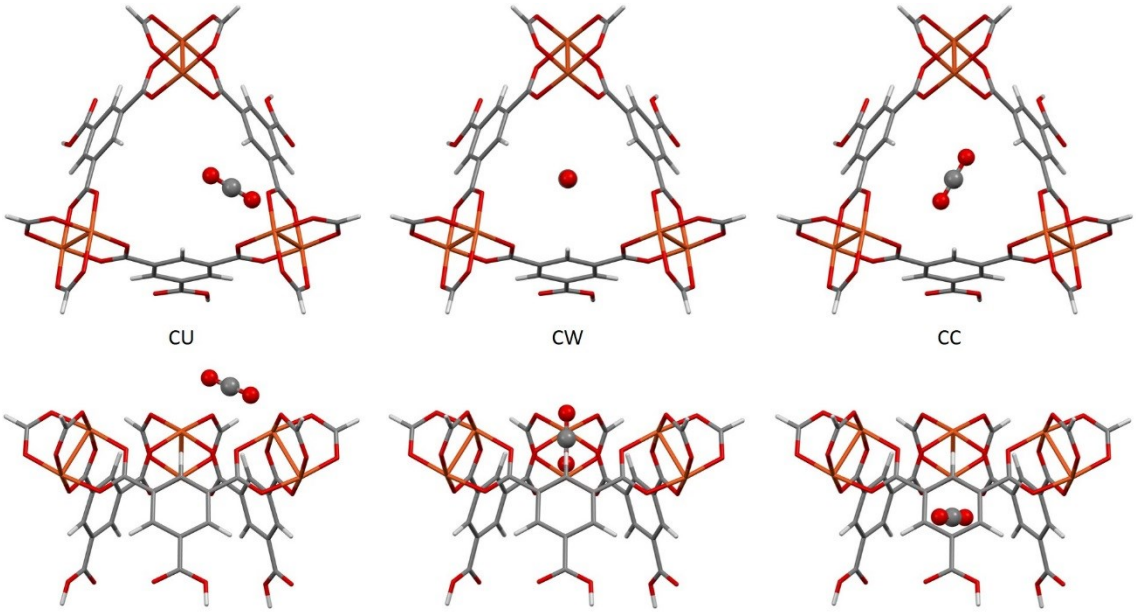

Figure 3.15: The three independent CO_2 adsorption sites found in HKUST-1 viewed perpendicular (top) and parallel (bottom) to the small cage opening.

Site	$E_{DFT/CC}$	E_{PIXEL}	E_{Coul}	E_{disp}	E_{rep}	E_{pol}
CU	-28.2	-42.7	-48.1	-29.5	61.0	-26.1
CW	-23.1	-23.2	-6.9	-19.9	5.1	-1.5
CC	-23.2	-20.3	-9.0	-24.1	15.6	-2.9

Table 3.9: Adsorption energies for CO_2 in HKUST-1 as calculated by DFT/CC and PIXEL methods, including a breakdown of the interaction terms from PIXEL. All values are in kJ mol^{-1}. See text below for definitions of CU, CW and CC sites.

Grajciar *et al.* used DFT/CC[45] calculations (a combination of DFT and coupled-cluster) along with microcalorimetry experiments to find CO_2 adsorption sites in the metal-organic framework HKUST-1 (also known as CuBTC).[32] This study shows that at low CO_2 coverage (up to 15 bar pressure of CO_2 at 300 K) there are three distinct adsorption sites situated around the window of the small cage: one at the open copper site (denoted CU); one at the window of the small cage (denoted CW); and one in the centre of the cage (denoted CC).

The DFT/CC calculations find the CU site to be located close to the copper paddlewheel with a Cu-O distance of 2.39 Å and a Cu-O-C angle of 123°. PIXEL calculations find this site with a Cu-O distance of 2.337 Å and a Cu-O-C angle of 148.87°. It should be noted that during the PIXEL calculations, the orientation of the adsorbate molecule is not optimised as it is in the DFT/CC calculations, but rather a range of different orientations are sampled. As such, some differences in the orientation are to be expected. The angle of the CO_2 molecule points it along the edge of the small window, and as a result the adsorbate will interact with the neighbouring paddlewheel as well as the aromatic hydrogen of the organic linker. This explains the domination of the Coulombic term for this interaction, as shown in Table 3.9. The total energy of this site obtained from PIXEL calculations is -42.7 kJ mol^{-1}, some 14.5 kJ mol^{-1} higher than the DFT/CC energy. Since this site lies near an open metal centre, further calculations were performed to check whether this discrepancy was the result of poor parameterisation for copper in PIXEL. The interaction of a CO_2 molecule with a small model consisting of one copper paddlewheel motif where the carboxylates had been capped with hydrogen atoms gave an energy of -17.7 kJ mol^{-1}. The magnitude of this value suggests that, rather than poor parameterisation resulting in the abnormally high energy for the CU site, the large value is a result of the small fragment model not being large enough to properly model the interaction site.

The locations of the CW and CC sites are defined with respect to a plane defined by the upper Cu^{2+} ions of the three paddlewheel motifs. DFT/CC methods calculate the carbon atom of the CW site to be 1.19 Å below this plane, and the angle the CO_2 molecular axis makes with the plane is 84.5°. For the CC site, the carbon atom is 3.47 Å below the plane and the angle is 23.5°. PIXEL calculations find the distances and angles of the CW site to be 0.3464 Å and 90° respectively, while those for the CC site are

3.8105 Å and 0°. Again, as mentioned above, orientations are not optimised during the PIXEL calculations, but the agreement with the DFT/CC results is good, with the exception of the distance of the CW site from the defined plane. The PIXEL search was carried out at a grid spacing of 1.0 Å, and there is another site located at 2.0785 Å below the plane, but this site is of lower energy than that which is reported in Table 3.9 (-21.8 kJ mol^{-1}). A finer grid spacing of 0.5 Å finds a CW site which lies 1.2124 Å below the plane (a distance which compares well with the DFT/CC value of 1.19 Å), the energy of which is -26.0 kJ mol^{-1}, making this the most favourable location of this site. These values are summarised in Table 3.10.

Site	C…Plane (Å)	∠ CO_2-Plane
CW_{DFT}	1.19	84.5
CW_{PIXEL}	1.21	90.0
CC_{DFT}	3.47	23.5
CC_{PIXEL}	3.81	0.0

Table 3.10: Geometric data for the CW and CC CO_2 adsorption sites in HKUST-1 with respect to the plane defined by the upper Cu^{2+} ions in the three paddlewheel motifs.

CW and CC interactions are dominated by the dispersion term, which is to be expected since they predominantly interact with the aromatic linkers rather than the open copper paddlewheel sites.

3.6 Investigations of "Novel" Frameworks

One of the advantages to using a fragment to represent a MOF structure is that no knowledge of the space group is necessary. As such, "novel" metal-organic frameworks can be modelled simply by making modifications to the fragment, be it functionalising the organic linkers or changing the metal used in the clusters. This means that screening of the adsorption capabilities of a number of possible target structures can be carried out relatively easily.

Lofti and Saboohi used DFT-D calculations to explore the effects of functionalising the benzene-dicarboxylate linkers in MOF-5 with different halogens.[46] They found that, while no improvements are observed upon replacing all four aromatic hydrogen atoms with fluorine, adsorption energies increase by an order of magnitude

upon functionalization with chlorine and bromine, with adsorption energies ranging from around 3.8 to 38 kJ mol^{-1} upon functionalisation.

PIXEL calculations were performed on three modified versions of the model used to investigate the adsorption of H_2 with MOF-5 as described in Section 3.4.3, with four aromatic hydrogen atoms on each linker being replaced by fluorine, chlorine and bromine. The same sites as were located in MOF-5 were found in each case, and Table 3.11 shows the relative energies of these sites for the functionalised structures. Figure 3.16 shows the variation in the different energy terms from the PIXEL calculations.

Site	MOF-5	F-MOF-5	Cl-MOF-5	Br-MOF-5
I	-11.9	-11.8	-13.2	-13.7
II	-7.1	-8.1	-7.0	-8.6
III	-6.4	-5.9	-5.5	-3.9
IV	-2.2	-3.1	-4.5	-5.0

Table 3.11: Comparison of the PIXEL calculated energies of the four H_2 binding sites in MOF-5 and halogen functionalised MOF-5. All energies are in kJ mol^{-1}.

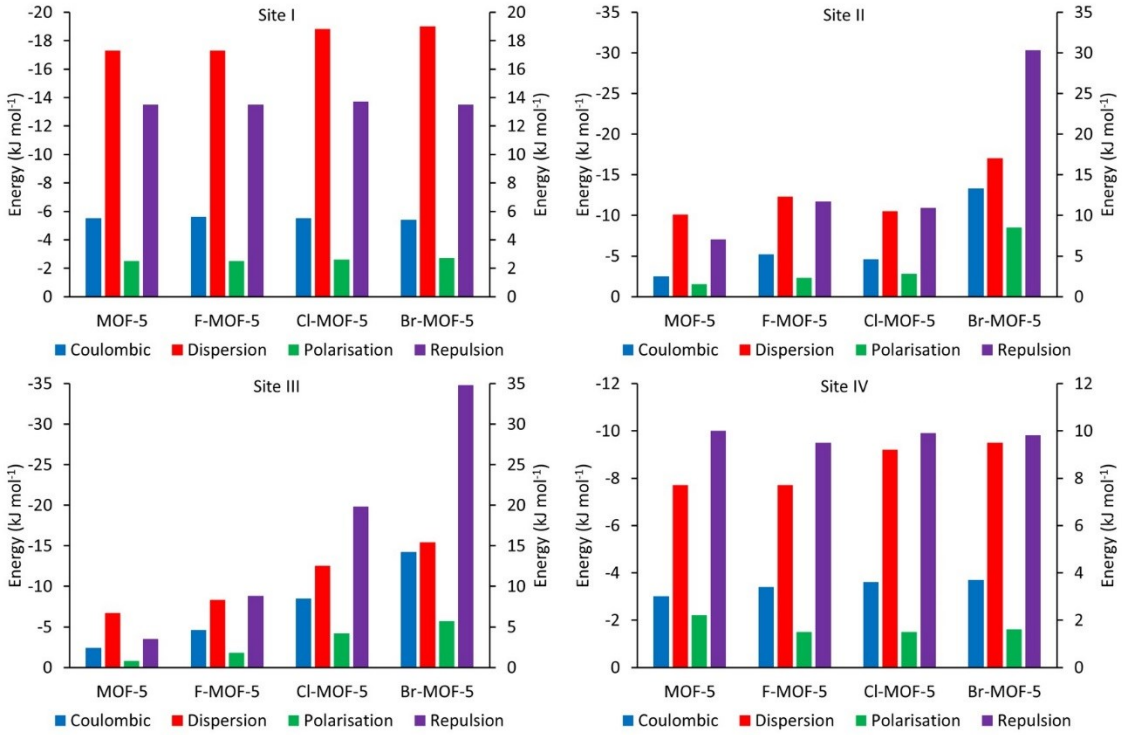

Figure 3.16: PIXEL component energies for the four adsorption sites in MOF-5 and its halogen functionalised analogues. Repulsion bars correspond to the right hand axis, others to the left axis.

Table 3.11 shows that, while there is little difference observed upon functionalization of the linker with fluorine, adsorption energies generally increase over sites I, II and IV for chlorine and bromine, while the binding becomes weaker at site III upon halogenation. Figure 3.16 shows the reasons for these differences. The terms for site I remain almost constant upon functionalization, except for the dispersion term which increases slightly. Since site I is the furthest removed from the linkers, interacting predominantly with the zinc oxide cluster, halogenation will have little effect on this site, with the exception of the observed increase in dispersion caused by the additional electron density of the halogens. Sites II and III are located at the edge and face of the metal cluster respectively, and as such will be much more sensitive to the halogenation. This can be seen from Figure 3.16, where there is a general increase in the magnitude of all the terms. While this is somewhat compensated for with site II by the increase in the Coulombic and dispersion terms, the proximity of site III to the halogen atoms means that it becomes increasingly less favourable. In site IV, the terms again remain relatively constant, except from the dispersion term which increases with the size of the halogen used for functionalization. As the interaction at this site is dominated by the dispersion term, this is to be expected as such an interaction will become more favourable with increasing electron density.

While the improvement in binding energies observed with PIXEL are much more modest than those seen using DFT-D, the trend of increasing adsorption upon functionalization of MOF-5 with heavier halogens is consistent. Since sites II and III are seldom occupied simultaneously,[39] the loss in binding energy observed at site III is compensated for by the increase in the three other sites. Consequently, functionalization by halogenation of the linker molecules in MOF-5 presents itself as a valid route for improvements in H_2 adsorption in this system.

3.7 Conclusions

Understanding adsorption interactions between various molecular species and metal-organic frameworks is extremely important to the advancement of various technologies, particularly in the fields of gas storage and separation. While several different methods of calculating such interactions exist, the PIXEL method presents itself as a valuable tool in such analysis. The short computing times mean that screening

of different MOFs can be performed rapidly, and almost any MOF can be studied through careful modelling of a fragment structure. Additionally, the large number of atomic species covered by PIXEL means that theoretical MOFs can be studied.

The adsorption sites calculated using the PIXEL method reproduce those observed experimentally, with RMS values between 0.195 Å and 0.328 Å. The trends of the PIXEL adsorption energies correlate reasonably well with experimental and theoretical data, except in cases where cooperativity arises between adsorption sites, where the PIXEL method is unable to reproduce many body interactions.

PIXEL has many advantages over other methods of calculating adsorption energies in metal-organic frameworks. The fact that it is general across all elements means that force fields specific to each individual structure are not necessary. This means that all calculations use the same sets of parameters and are therefore comparable. Furthermore, the simplicity of modifying the fragment means that the adsorption characteristics of almost any conceivable metal-organic framework can be investigated easily and quickly.

PIXEL calculations are also very quick to perform. All calculations were performed over 13 processors of two desktop computers, and taking symmetry into account, full screening of the interactions between a simple adsorbate such as argon and MOF-5 can be accomplished in around 30 minutes. This calculation time is orders of magnitude faster than corresponding quantum mechanical calculations, which can take hours, if not days, per calculation. For comparison, a single point energy calculation for MOF-5 (using CSD refcode SAHYIK) with the CASTEP simulation package[47*] using 12 processors, the computing time was around nine hours per calculation.

The results of these studies show PIXEL as a promising tool for investigating gas adsorption in metal-organic frameworks. Since analysis of a system can be achieved so quickly, particularly for highly symmetric cases, PIXEL can be used for rapid screening of structures to find areas of interest before more focussed calculations are performed.

[*] Symmetry reduced to *P*1, PBE exchange correlation functional, "on-the-fly" pseudopotentials, 550 eV basis set cut-off (giving energy convergence of 0.02 meV per atom), gamma point only, energy per atom 0.02 meV.

3.8 References

1. S. L. James, *Chemical Society Reviews*, 2003, **32**, 276-288.
2. U. Mueller, M. Schubert, F. Teich, H. Puetter, K. Schierle-Arndt and J. Pastre, *Journal of Materials Chemistry*, 2006, **16**, 626-636.
3. I. J. Bruno, J. C. Cole, P. R. Edgington, M. Kessler, C. F. Macrae, P. McCabe, J. Pearson and R. Taylor, *Acta Crystallographica Section B - Structural Science*, 2002, **58**, 389-397.
4. N. Nijem, J.-F. Veyan, L. Kong, K. Li, S. Pramanik, Y. Zhao, J. Li, D. Langreth and Y. J. Chabal, *Journal of the American Chemical Society*, 2010, **132**, 1654-1664.
5. R. Q. Snurr, A. O. Yazaydin, D. Dubbeldam and F. H., in *Metal-Organic Frameworks: Design and Application*, ed. L. R. MacGillivray, John Wiley & Sons, Inc., Hoboken, New Jersey, 2010, pp. 313-339.
6. N. A. Ramsahye, G. Maurin, S. Bourrelly, P. L. Llewellyn, T. Devic, C. Serre, T. Loiseau and G. Ferey, *Adsorption - Journal of the International Adsorption Society*, 2007, **13**, 461-467.
7. Q. Y. Yang and C. L. Zhong, *Journal of Physical Chemistry B*, 2005, **109**, 11862-11864.
8. A. G. Wong-Foy, A. J. Matzger and O. M. Yaghi, *Journal of the American Chemical Society*, 2006, **128**, 3494-3495.
9. B. Panella, M. Hirscher, H. Putter and U. Muller, *Advanced Functional Materials*, 2006, **16**, 520-524.
10. A. Dailly, J. J. Vajo and C. C. Ahn, *Journal of Physical Chemistry B*, 2006, **110**, 1099-1101.
11. S. Keskin, J. Liu, R. B. Rankin, J. K. Johnson and D. S. Sholl, *Industrial & Engineering Chemistry Research*, 2009, **48**, 2355-2371.
12. J. Liu, J. T. Culp, S. Natesakhawat, B. C. Bockrath, B. Zande, S. G. Sankar, G. Garberoglio and J. K. Johnson, *Journal of Physical Chemistry C*, 2007, **111**, 9305-9313.
13. W. Xie and J. Gao, *Journal of Chemical Theory and Computation*, 2007, **3**, 1890-1900.
14. T. Duren, Y.-S. Bae and R. Q. Snurr, *Chemical Society Reviews*, 2009, **38**, 1237-1247.
15. K. Sillar, A. Hofmann and J. Sauer, *Journal of the American Chemical Society*, 2009, **131**, 4143-4150.
16. P. Y. Ayala, K. N. Kudin and G. E. Scuseria, *Journal of Chemical Physics*, 2001, **115**, 9698-9707.
17. H. Li, M. Eddaoudi, M. O'Keeffe and O. M. Yaghi, *Nature*, 1999, **402**, 276-279.
18. J. L. C. Rowsell and O. M. Yaghi, *Angewandte Chemie - International Edition*, 2005, **44**, 4670-4679.
19. T. Duren, L. Sarkisov, O. M. Yaghi and R. Q. Snurr, *Langmuir*, 2004, **20**, 2683-2689.
20. A. R. Millward and O. M. Yaghi, *Journal of the American Chemical Society*, 2005, **127**, 17998-17999.
21. M. Eddaoudi, H. L. Li and O. M. Yaghi, *Journal of the American Chemical Society*, 2000, **122**, 1391-1397.
22. J. L. C. Rowsell, E. C. Spencer, J. Eckert, J. A. K. Howard and O. M. Yaghi, *Science*, 2005, **309**, 1350-1354.
23. J. Y. Lee, D. H. Olson, L. Pan, T. J. Emge and J. Li, *Advanced Functional Materials*, 2007, **17**, 1255-1262.
24. J. Liu, J. Y. Lee, L. Pan, R. T. Obermyer, S. Simizu, B. Zande, J. Li, S. G. Sankar and J. K. Johnson, *Journal of Physical Chemistry C*, 2008, **112**, 2911-2917.
25. L. Kong, V. R. Cooper, N. Nijem, K. Li, J. Li, Y. J. Chabal and D. C. Langreth, *Physical Review B*, 2009, **79**, 081407.
26. V. Krungleviciute, S. Pramanik, A. D. Migone and J. Li, *Microporous and Mesoporous Materials*, 2012, **161**, 134-138.
27. J. R. Karra and K. S. Walton, *Journal of Physical Chemistry C*, 2010, **114**, 15735-15740.
28. Y. F. Chen, J. Y. Lee, R. Babarao, J. Li and J. W. Jiang, *Journal of Physical Chemistry C*, 2010, **114**, 6602-6609.
29. S. S. Y. Chui, S. M. F. Lo, J. P. H. Charmant, A. G. Orpen and I. D. Williams, *Science*, 1999, **283**, 1148-1150.
30. Y. Liu, C. M. Brown, D. A. Neumann, V. K. Peterson and C. J. Kepert, *Journal of Alloys and Compounds*, 2007, **446**, 385-388.
31. S. Bordiga, L. Regli, F. Bonino, E. Groppo, C. Lamberti, B. Xiao, P. S. Wheatley, R. E. Morris and A. Zecchina, *Physical Chemistry Chemical Physics*, 2007, **9**, 2676-2685.

32. L. Grajciar, A. D. Wiersum, P. L. Llewellyn, J.-S. Chang and P. Nachtigall, *Journal of Physical Chemistry C*, 2011, **115**, 17925-17933.
33. B. Xiao, P. S. Wheatley, X. Zhao, A. J. Fletcher, S. Fox, A. G. Rossi, I. L. Megson, S. Bordiga, L. Regli, K. M. Thomas and R. E. Morris, *Journal of the American Chemical Society*, 2007, **129**, 1203-1209.
34. *Materials Studio Release Notes*, (2010) Accelrys Software Inc., Cambridge, UK.
35. C. F. Macrae, I. J. Bruno, J. A. Chisholm, P. R. Edgington, P. McCabe, E. Pidcock, L. Rodriguez-Monge, R. Taylor, J. van de Streek and P. A. Wood, *Journal of Applied Crystallography*, 2008, **41**, 466-470.
36. H. Lipson, *Endeavour*, 1966, **25**, 53.
37. A. Simon and K. Peters, *Acta Crystallographica Section B - Structural Science*, 1980, **36**, 2750-2751.
38. G. W. T. M. J. Frisch, H. B. Schlegel, G. E. Scuseria, M. A. Robb, J. R. Cheeseman, G. Scalmani, V. Barone, B. Mennucci, G. A. Petersson, H. Nakatsuji, M. Caricato, X. Li, H. P. Hratchian, A. F. Izmaylov, J. Bloino, G. Zheng, J. L. Sonnenberg, M. Hada, M. Ehara, K. Toyota, R. Fukuda, J. Hasegawa, M. Ishida, T. Nakajima, Y. Honda, O. Kitao, H. Nakai, T. Vreven, J. A. Montgomery, Jr., J. E. Peralta, F. Ogliaro, M. Bearpark, J. J. Heyd, E. Brothers, K. N. Kudin, V. N. Staroverov, R. Kobayashi, J. Normand, K. Raghavachari, A. Rendell, J. C. Burant, S. S. Iyengar, J. Tomasi, M. Cossi, N. Rega, J. M. Millam, M. Klene, J. E. Knox, J. B. Cross, V. Bakken, C. Adamo, J. Jaramillo, R. Gomperts, R. E. Stratmann, O. Yazyev, A. J. Austin, R. Cammi, C. Pomelli, J. W. Ochterski, R. L. Martin, K. Morokuma, V. G. Zakrzewski, G. A. Voth, P. Salvador, J. J. Dannenberg, S. Dapprich, A. D. Daniels, Ö. Farkas, J. B. Foresman, J. V. Ortiz, J. Cioslowski, and D. J. Fox, *Gaussian 09*, (2009) Gaussian Inc., Wallingford.
39. D. Dubbeldam, H. Frost, K. S. Walton and R. Q. Snurr, *Fluid Phase Equilibria*, 2007, **261**, 152-161.
40. T. Yildirim and M. R. Hartman, *Physical Review Letters*, 2005, **95**, 215504.
41. M. C. Payne, M. P. Teter, D. C. Allan, T. A. Arias and J. D. Joannopoulos, *Reviews of Modern Physics*, 1992, **64**, 1045-1097.
42. M. Dion, H. Rydberg, E. Schroder, D. C. Langreth and B. I. Lundqvist, *Physical Review Letters*, 2004, **92**, 246401.
43. T. Thonhauser, V. R. Cooper, S. Li, A. Puzder, P. Hyldgaard and D. C. Langreth, *Physical Review B*, 2007, **76**, 125112.
44. S. K. Bhatia and A. L. Myers, *Langmuir*, 2006, **22**, 1688-1700.
45. O. Bludsky, M. Rubes, P. Soldan and P. Nachtigall, *Journal of Chemical Physics*, 2008, **128**, 114102.
46. R. Lotfi and Y. Saboohi, *Computational and Theoretical Chemistry*, 2014, **1044**, 36-43.
47. S. J. Clark, M. D. Segall, C. J. Pickard, P. J. Hasnip, M. J. Probert, K. Refson and M. C. Payne, *Zeitschrift Fur Kristallographie*, 2005, **220**, 567-570.

Chapter 4

Calculation of Atomic Polarisabilities

4.1 Synopsis

Atomic polarisabilities have been calculated for a range of 60 different organic compounds using the Atoms in Molecules (AIM) approach, and for a subset of five of these compounds using the Hirshfeld volumes method. Once obtained, these polarisabilities were used in PIXEL calculations, and the resulting lattice energies were compared to literature sublimation enthalpies as well as to PIXEL results using the standard atomic polarisability values contained within the program.

4.2 Introduction

For many years the PIXEL method[1] has been used to calculate lattice energies and intermolecular interactions between molecules in the solid state. The results are in good agreement with experimental values, and give results comparable with other computational methods but with a much smaller requirement in computational resources.[2] One of PIXEL's most attractive features is its basis in simple physical principles which allows for a semi-empirical approach to the energy calculations.[3, 4] Aside from four empirical parameters, PIXEL requires only fundamental atomic properties such as ionisation potentials, electronegativities and van der Waals radii. For the most part, these values are obtained from standard reference tables and texts, with the exception of atomic polarisabilities. This parameter is of great importance as it is used during the calculation of the dispersion term, an interaction which has a major influence on crystal packing. For instance, in acridine the dispersion energy accounts for -124.5 kJ mol^{-1} of the total lattice energy of the system (-95.5 kJ mol^{-1}),[2] an interaction which dwarfs the energies of many hydrogen bonding networks.

The PIXEL formulation[5] uses values of atomic polarisabilities (α) calculated using the Slater-Kirkwood approximation (discussed in Chapter 2),[6] a method where the magnitude of α is related to the van der Waals radius of the atomic species in question. This results in a series of standard values that are fixed for each atomic species in the PIXEL program. An example of these values are shown in Table 1.

Atomic Species	Atomic Polarisability (Å^3)
H	0.39
C (aliphatic)	1.05
C (aromatic)	1.35
N	0.95
O	0.75

Table 4.1: Examples of the atomic polarisabilities used in the PIXEL method.[7]

While this approach allows for atomic polarisabilities to be calculated quickly and easily, it can be considered as an oversimplification. With the exception of carbon, there is no differentiation between the chemical environments of the atomic species involved in the program. Since carbon is the most abundant element in organic chemistry, in most cases it will outweigh the contributions of other atomic species and as such the lack of diversity in α will not significantly affect the overall energy calculated. However, there are many situations where carbon is not the most abundant element in the molecule, particularly when inorganic complexes are considered. It seems reasonable to expect that an oxygen atom in a carboxyl group will have a different polarisability to an oxygen atom in an ether. A much preferred option would be to have some variation in the standard values of α to allow for different chemical environments in different functional groups as is the case with carbon as discussed above. Empirically changing the polarisabilities for all scenarios is not satisfactory, and a standard method for calculating these values is required. Two methods of calculating atomic polarisabilities are tested in this work: the Atoms in Molecules (AIM) approach, and through the use of Hirshfeld volumes.

4.1.1 Atoms in Molecules

Quantum theory of atoms in molecules (QTAIM or AIM)[8] is a method in which the molecular electron density is partitioned into mononuclear sites to give "atomic basins".[9] This partitioning in turn allows for the calculation of electronic properties on a per atom basis. As such, calculating the change in dipole moment of an atom upon application of an external field to the molecule will allow for the atomic polarisability of an atom to be obtained.

4.1.2 Hirshfeld Volumes

Given that there exists a linear relationship between polarisability and volume,[10] it is possible to obtain effective atomic polarisabilities using Equation 4.1:

$$\alpha_i = \alpha_i^{free}\left(\frac{V_{atom}}{V_{atom}^{free}}\right) \qquad (4.1)$$

where α_i is the effective atomic polarisability, α_i^{free} is the polarisability of the free atom and the term in the bracket is the ratio of the Hirshfeld atomic volume and the free atomic volume as defined by the Hirshfeld partitioning scheme.[11] This allows individual polarisabilities to be obtained for each atom in a molecule by performing a full Hirshfeld population analysis and applying the partitioning ratio to atomic static dipole polarisabilities for each element (Table 4.2).[12-15]

Element	Static Dipole Polarisability (Å^3)	Reference
H	0.667	12
C	1.630	13
N	1.101	14
O	0.895	14
Cl	2.178	15

Table 4.2: Static dipole polarisabilities in Å^3 for a range of atoms used to test Hirshfeld calculated atomic polarisabilities for use in the PIXEL method.

4.2 Experimental

4.2.1 AIM Calculations

Initial calculations were performed on a set of 24 organic compounds with known molecular polarisabilities (Table 4.3)[16] to ascertain whether atomic polarisabilities obtained by the AIM approach reproduced molecular polarisabilities comparable to literature values.

Compound	Exp.	B3LYP	HCTH	PBE0
1-butanol	8.88	8.27	8.49	8.14
acetaldehyde	4.60	4.26	4.44	4.19
acetamide	5.67	5.50	5.73	5.38
acetic acid	5.10	4.76	4.91	4.66
bromoethane	8.05	6.67	6.77	6.50
crotonaldehyde	8.50	8.03	8.32	7.90
cyclohexanol	11.56	10.96	11.22	10.79
diethyl ketone	9.93	9.43	9.73	9.31

ethyl cyclohexane	15.90	13.98	14.35	13.85
ethyl ether	10.20	8.44	8.74	8.31
ethyl propyl ether	10.68	10.25	10.59	10.10
isoprene	9.99	9.74	9.92	9.60
methyl ethyl ketone	8.13	8.28	8.54	8.18
o-anisidine	14.20	14.33	14.72	14.09
p-benzoquinone	14.50	11.12	11.33	10.92
paraldehyde	17.90	12.52	13.00	12.28
phenazine	23.43	24.99	25.53	24.53
phenol	11.10	10.64	10.81	10.47
propionic acid	6.90	6.50	6.69	6.38
propyl ether	12.80	12.06	12.47	11.89
quinoline	15.70	16.48	16.75	16.21
styrene	15.00	14.35	14.73	14.10
thiophene	9.67	8.99	9.05	8.82
trichloroethylene	10.03	8.94	8.98	8.69

Table 4.3: The organic compounds used for initial testing of the AIM method. Also listed are experimental molecular polarisabilities taken from ref. 16, and those obtained from AIM calculations using the indicated functionals. Values are in Å^3.

The method used to calculate atomic polarisabilities was that of Laidig and Bader,[17] and calculations were performed as outlined by Keith.[9, 18] Geometry optimisations of each molecule were performed using Gaussian09 using a B3LYP[19] functional with a 6-311++G** basis set. Wavefunctions of the optimised structures were then calculated with and without applied electric fields (field magnitudes of ±0.0010 a.u., ±0.0025 a.u. and ±0.0050 a.u. were used) along the *x*-, *y*- and *z*-axes using B3LYP, HCTH[20] and PBE0[21] functionals, again with 6-311++G** basis sets. These functionals were chosen as they have been previously used to calculate atomic and molecular polarisabilities, and a large basis set with diffuse functions is recommended for this procedure.[22-24] The wavefunction at zero-field was then processed with AIMAll[18] to obtain atomic dipole moments at zero-field. A wavefunction with an electric field applied along the *x*-axis was then used as above to obtain the atomic dipole moments in the presence of the applied field. The change in the *x*, *y* and *z* components of the atomic dipole moments were then calculated as the difference between these moments with the field applied and without. These changes in dipole moment were then divided by the change in applied field to obtain the XX, YX and ZX components of the atomic polarisability tensors. This process was repeated with fields applied along the *y*- and *z*- axes to construct full nine component polarisability tensors for each atom in the

structure. The diagonal terms (XX, YY and ZZ) of these tensors were then averaged to give the individual atomic polarisabilities.* The sum of the individual atomic polarisabilities in a molecule gives the molecular polarisability. Fields of ±0.0010 a.u., ±0.0025 a.u. and ±0.0050 a.u. were used with each functional. The results obtained were independent of the field applied; for example, the molecular polarisability of acetic acid was calculated as 4.75 $Å^3$ regardless of field magnitude or direction. This process was automated using the program POLAR, the source code of which is included in the Supplementary Material for this Chapter. Figure 4.1 shows the molecular polarisabilities calculated in this way to the experimental polarisabilities for the molecules listed in Table 4.3.

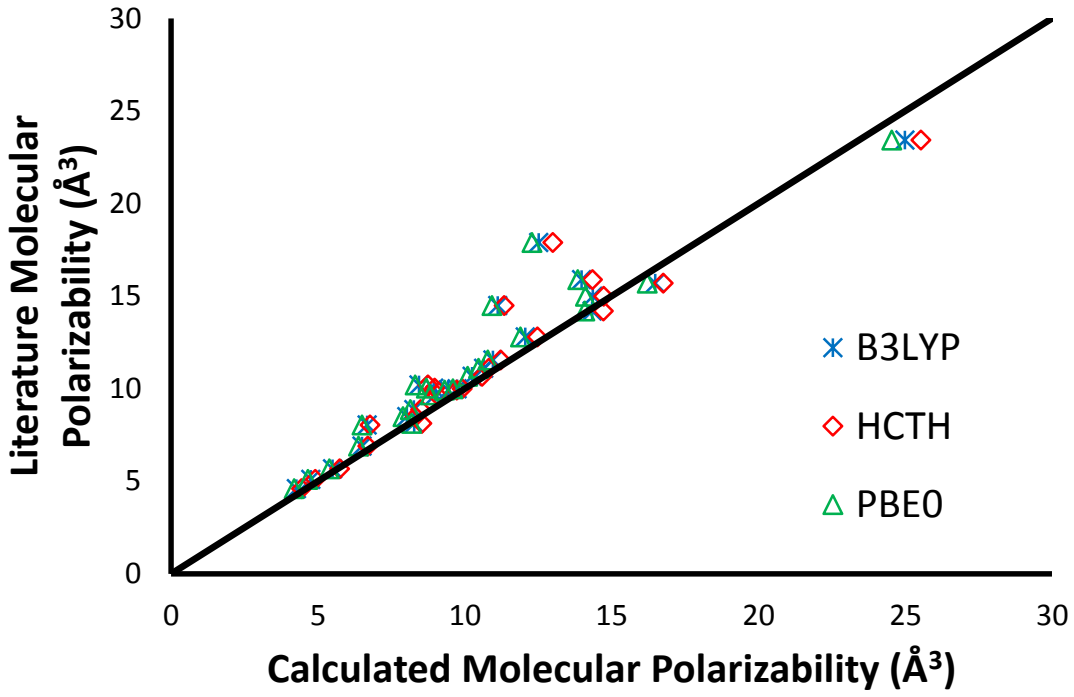

Figure 4.1: Molecular polarisabilities calculated using AIMAll compared with reference values. The black line is $y = x$.

The straight line parameters for the three functionals tested are as follows: B3LYP $y = 1.06(3)x$, $R = 0.95$; HCTH $y = 1.03(2)x$, $R = 0.95$; PBE0 $y = 1.07(3)x$, $R = 0.95$. As these parameters show, the agreement between the calculated polarisabilities and the literature values is excellent. There are two noticeable outliers, however, that occur for paraldehyde and for *p*-benzoquinone, where the calculated molecular

* An example calculation for the atomic polarisability of the carboxylic acid carbon atom in acetic acid is given in the Supplementary Information, Section S.4.1.

polarisabilities are significantly lower than the literature values regardless of the functional used. The literature molecular polarisabilities for these two compounds are derived from a tabulation of data collected between 1910 and 1952,[25] since no more recent results were available. Consequently, the age of these data may mean that they are somewhat less reliable than more recent determinations. Additionally, given that molecular polarisabilities for compounds containing similar functional groups to those in paraldehyde and *p*-benzoquinone are successfully reproduced using the AIM method, these outliers are likely to result from inaccuracies in the original literature values.

Since the HCTH functional shows the best agreement between calculated and literature molecular polarisabilities, it was chosen as the method to be used for further calculations. A set of 60 organic compounds displaying a range of chemical functionalities which had been previously investigated by PIXEL calculations[2] was used to test the performance of the atomic polarisabilities calculated from AIM methods (Table 4.4).

Compound	PIXEL Energy	CSD Refcode
acetic acid	-62.4	ACETAC01
acridine	-95.9	ACRDIN01
anthracene	-104.2	ANTCEN14
anthraquinone	-96.8	ANTQUO08
teophyllin	-121.5	BAPLOT01
1,3-phthalic acid	-132.1	BENZDC01
benzene	-49.9	BENZEN07
fumaronitrile	-65.4	BISJIW
benzamide	-100.9	BZAMID01
coumarin	-80.9	COUMAR10
trinitro-triazacyclohexane	-121.2	CTMTNA
2,3-diazanaphthalene	-89.4	DAZNAP
2,8-dichlorodioxin	-102.1	DCBDOX10
1,4-dichlorobenzene	-68.7	DCLBEN01
dichlorobenzoquinone	-71.6	DCLBQN
dimethylnitroaniline	-91	DIMNAN01
9,10-dihydroanthracene	-85.4	DITBOX
dimethylbenzoic acid	-97.8	DMBZAC01
dimethylnaphthalene	-82.4	DMNAPH05
1,3-dinitrobenzene	-83.1	DNBENZ15
1,4-dinitrobenzene	-91.3	DNITBZ11
1,2,3,4-tetrachlorodioxin	-114.8	FELSEU
formic acid	-56.2	FORMAC01
formamide	-73	FORMAM02

hexachlorobenzene	-93.5	HCLBNZ11
imidazole	-84.6	IMAZOL13
malonic acid	-105.8	MALNAC06
melamine	-153	MELAMI04
dimethylnitramine	-73.9	METNAM04
maleic anhydride	-66.5	MLEICA
N,N-dimethyl-4-nitroaniline	-83.4	MNTDMA01
trinitromethylaniline	-123.3	MTNANL
naphthoquinone	-82.9	NAPHQU
naphthalene	-75	NAPHTA10
2-naphthoic acid	-104.8	NAPOAC01
nitrotoluene	-73.9	NITOLU
nitrophenol	-94.6	NITPOL02
nitroguanidine	-157.8	NTRGUA03
tetranitro-tetraazacyclooctane	-163.2	OCHTET12
n-octane	-59.5	OCTANE01
oxalic acid	-106.3	OXALAC04
parabanic acid	-96.2	PARBAC11
phenanthrene	-96.6	PHENAN08
pyromellitic dianhydride	-94.5	PYMDAN
pyrene	-107.9	PYRENE02
succinic anhydride	-77.5	SUCANH15
triamino-trinitrobenzene	-73.9	TATNBZ
1,3,5-trichlorobenzene	-111.8	TCHLBZ
tetracyanoquinodimethane	-84.2	TCYQME
1,4-dicyanobenzene	-86	TEPNIT11
1,3,5-trinitrobenzene	-95.5	TNBENZ10
trinitroaniline	-105.9	TNIOAN
trinitroxylene	-109.5	TNOXYL
trinitrophenetole	-83.4	TNPHNT
tetroxocane	-107.8	TOXOCN
urea	-94.6	UREAXX09
N,N-dimethylurea	-88.2	WIFKEB
1,2-dinitrobenzene	-100.7	ZZZFYW01
2,4,6-trinitrotoluene	-91	ZZZMUC01
2,6-dinitrotoluene	-170.5	ZZZQSC01

Table 4.4: The 60 organic compounds used for validation along with CSD refcodes, and PIXEL lattice energies. All values are in kJ mol^{-1}.

4.2.2 Hirshfeld Volume Calculations

A subset of five compounds from the 60 listed in Table 4.4 was used to investigate the use of polarisabilities calculated using the Hirshfeld partitioning scheme for use in PIXEL calculations. The five compounds were acetic acid, formamide, hexachlorobenzene, imidazole and octane, selected as they show a range of chemical

functionalities. Calculations were performed using CASTEP v.7.01.[26] Initially, a suitable plane wave basis set cut-off was obtained by repeating single-point energy calculations on each molecule with an increasing cut-off value until an energy difference of less than 0.1 meV/atom was obtained. Input files were prepared using Materials Studio v.5.5.3,[27] the PBE functional[21] was used with native pseudopotentials ("on the fly"). The separation between *k*-points was chosen to be no more than 0.07 $Å^{-1}$ to ensure thorough sampling of reciprocal space.[28] Geometry optimisations were then performed using the PBE functional with either the TS dispersion correction scheme[29] or the TS-SCS scheme.[30] The keywords "calculate_hirshfeld : true" and "iprint : 2" were used in the CASTEP "param" file to perform a Hirshfeld volume analysis. The results from this analysis were used with the values in Table 4.2, as described in Equation 4.1, to generate atomic polarisabilities for use with PIXEL. Electron densities for use with PIXEL were calculated using Gaussian09 at the MP2[31]/6-31G**, MP2/6-311++G** and PBE1PBE/6-31G** levels of theory.

4.3 Results and Discussion

4.3.1 AIM Polarisabilities

Figure 4.2 shows the lattice energies obtained from PIXEL calculations performed using atomic polarisabilities calculated with AIMAll using the HCTH functional as well as those using the standard polarisabilities included in the PIXEL code.

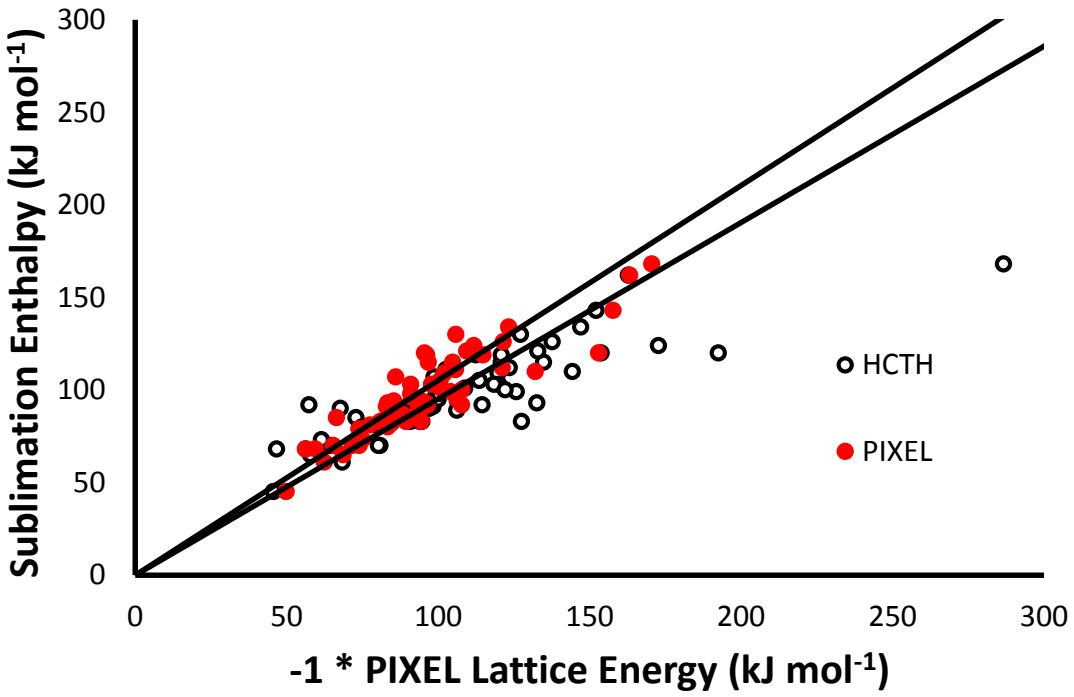

Figure 4.2: Comparison of literature sublimation enthalpies to calculated lattice energies for the 60 compounds outlined in Table 4.4. Red circles are energies calculated using standard PIXEL polarisabilities. Open circles are energies where AIM polarisabilities calculated using the HCTH functional were used. Black lines correspond to ±5% of the literature values.

The straight line parameters for the standard polarisabilities are $y = 1.01(1)\,x$ and $R = 0.89$. The parameters for when AIM polarisabilities were used are $y = 0.86(2)\,x$ and $R = 0.60$ representing a substantially poorer performance. This is a somewhat surprising result, as it would be expected that polarisabilities tailored to the chemical environments of the atomic species would yield a better agreement to experimental sublimation enthalpies. The lattice energies calculated using AIM polarisabilities are generally too large, indicating that these polarisabilities are being overestimated. It was reasoned that the HCTH functional may be optimised for a set of molecules with different

functionalities to those in the set of 60 molecules being used for validation. Indeed, the training set used for validation of the HCTH functional[20] contains no aromatics, acids or nitro- groups. In initial testing (Section 4.2.1), the B3LYP functional performed well and it was decided to return to this more general functional to investigate whether it would result in any improvement to the PIXEL energies calculated with AIM polarisabilities, the results of which are shown in Figure 4.3.

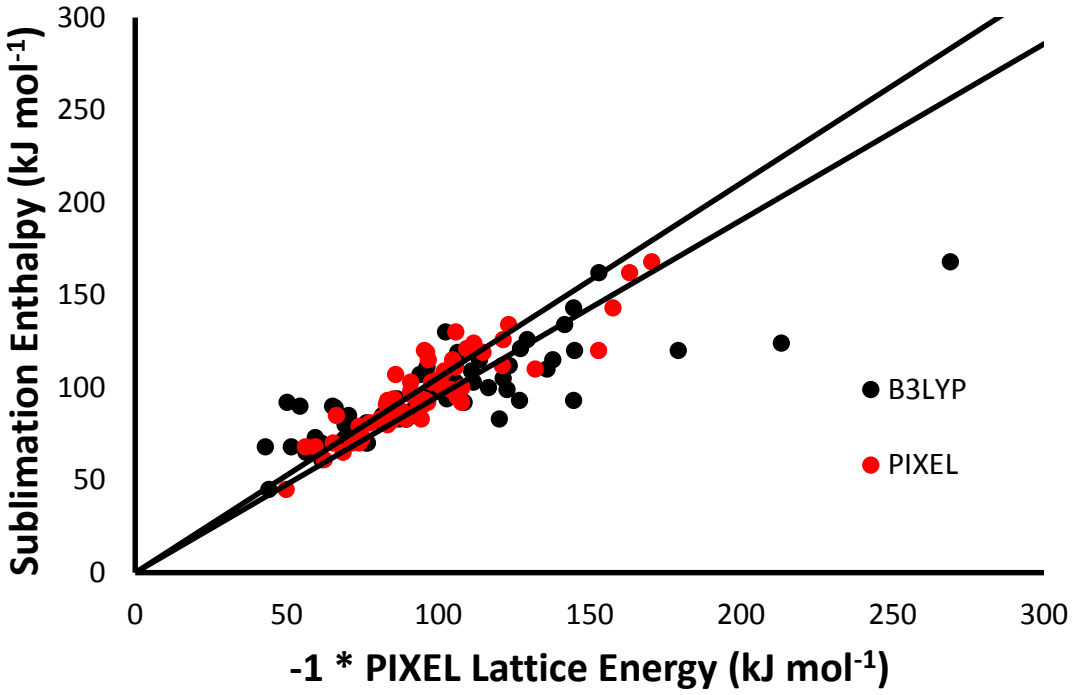

Figure 4.3: Comparison of literature sublimation enthalpies to calculated lattice energies for the 60 compounds outlined in Table 4.4. Red circles are energies calculated using standard PIXEL polarisabilities. Black circles are energies where AIM polarisabilities calculated using the B3LYP functional were used. Black lines correspond to ±5% of the literature values.

The straight line parameters for energies calculated with AIM polarisabilities using the B3LYP functional are $y = 0.89(3)\ x$ and $R = 0.32$. These parameters are even worse than those obtained from the HCTH functional ($y = 0.86(2)\ x$ and $R = 0.60$), showing that no improvement is obtained from the use of B3LYP to calculate polarisabilities using the AIM method. Table 4.5 shows the calculated lattice energies for each method, along with the deviations of these values from the experimental sublimation enthalpies.

Compound	Exp.	HCTH	HCTH Dev.	B3LYP	B3LYP Dev.
acetic acid	61	68.3	7.3	61.6	0.6
acridine	93	132.6	39.6	126.9	33.9
anthracene	99	125.8	26.8	122.8	23.8
anthraquinone	115	120.9	5.9	113.7	-1.3
teophyllin	126	137.7	11.7	129.4	3.4
1,3-phthalic acid	110	144.3	34.3	136	26
benzene	45	45.6	0.6	44.2	-0.8
fumaronitrile	70	80.8	10.8	76.7	6.7
benzamide	101	108.8	7.8	103.1	2.1
coumarin	83	93.9	10.9	89.4	6.4
trinitro-triazacyclohexane	112	123.5	11.5	123.5	11.5
2,3-diazanaphthalene	83	90.9	7.9	87.3	4.3
2,8-dichlorodioxin	109	119.8	10.8	111	2
1,4-dichlorobenzene	65	57.9	-7.1	56.4	-8.6
dichlorobenzoquinone	70	80.3	10.3	76.3	6.3
dimethylnitroaniline	103	120	17	105.8	2.8
9,10-dihydroanthracene	94	91.1	-2.9	86.4	-7.6
dimethylbenzoic acid	103	118.4	15.4	111.7	8.7
dimethylnaphthalene	83	94.7	11.7	89.6	6.6
1,3-dinitrobenzene	85	85	0	81.7	-3.3
1,4-dinitrobenzene	96	99	3	96.3	0.3
1,2,3,4-tetrachlorodioxin	119	120.9	1.9	114.6	-4.4
formic acid	68	46.7	-21.3	43	-25
formamide	72	74.2	2.2	68.9	-3.1
hexachlorobenzene	90	67.7	-22.3	65.2	-24.8
imidazole	82	84.5	2.5	80.9	-1.1
malonic acid	111	102.6	-8.4	96.3	-14.7
melamine	120	192.5	72.5	179.3	59.3
dimethylnitramine	70	64.3	-5.7	61.4	-8.6
maleic anhydride	85	72.9	-12.1	70.5	-14.5
N,N-dimethyl-4-nitroaniline	93	93.8	0.8	144.8	51.8
trinitromethylaniline	134	147.1	13.1	141.8	7.8
naphthoquinone	91	98.4	7.4	93.2	2.2
naphthalene	73	74.3	1.3	71.3	-1.7
2-naphthoic acid	115	134.8	19.8	137.9	22.9
nitrotoluene	79	73.9	-5.1	71.2	-7.8
nitrophenol	94	106.4	12.4	102.9	8.9
nitroguanidine	143	152.2	9.2	144.8	1.8
tetranitro-tetraazacyclooctane	162	162.8	0.8	153.1	-8.9
n-octane	68	56.3	-11.7	51.6	-16.4
oxalic acid	95	100.1	5.1	94.7	-0.3
parabanic acid	119	112.4	-6.6	106.5	-12.5
phenanthrene	92	114.5	22.5	108.6	16.6
pyromellitic dianhydride	83	127.5	44.5	120.2	37.2
pyrene	100	122.1	22.1	116.6	16.6

succinic anhydride	81	79.5	-1.5	76.4	-4.6
triamino-trinitrobenzene	168	286.7	118.7	269.1	101.1
1,3,5-trichlorobenzene	73	61.5	-11.5	59.5	-13.5
tetracyanoquinodimethane	124	172.8	48.8	213.3	89.3
1,4-dicyanobenzene	89	106.2	17.2	66	-23
1,3,5-trinitrobenzene	107	98.7	-8.3	94	-13
trinitroaniline	120	153.8	33.8	145.1	25.1
trinitroxylene	130	127.2	-2.8	102.5	-27.5
trinitrophenetole	121	132.9	11.9	127.2	6.2
tetroxocane	80	74.9	-5.1	69.3	-10.7
urea	92	57.4	-34.6	50.2	-41.8
N,N-dimethylurea	90	97.1	7.1	54.4	-35.6
1,2-dinitrobenzene	87	89.6	2.6	90.9	3.9
2,4,6-trinitrotoluene	105	113.6	8.6	121.5	16.5
2,6-dinitrotoluene	98	100.4	2.4	99.4	1.4

Table 4.5: PIXEL lattice energies calculated using AIM polarisabilities and their deviations from experimental sublimation enthalpies. All values are in kJ mol^{-1}.

As Table 4.5 shows, there are many large deviations between experimental sublimation enthalpies and the calculated lattice energies. Considering both HCTH and B3LYP give rise to several deviations, many of which are for different compounds, it seems that it is not simply the functional used to calculate the polarisabilities that gives rise to these errors, but rather the process itself. To further investigate the source of these deviations, the individual polarisabilities of atoms in different functional groups were inspected. It was found that for some apparently chemically similar atoms, the calculated polarisabilities were considerably larger than expected, and the standard deviations on these values were very high. Table 4.6 shows the OPiX and average calculated polarisabilities (from the HCTH results) for a selection of atoms in different functional groups that are very common in organic chemistry, along with the standard deviations of these values.

Atomic Species	OPiX Polarisability[5]	Average Polarisability	Standard Deviation
C (quaternary)	1.05	1.996799	1.00416942
C (aromatic)	1.35	1.451147	0.1829547
N (tertiary)	0.95	1.912422	0.54016028
O (carbonyl)	0.75	1.119464	0.25335394

Table 4.6: OPiX and average values and standard deviations of atomic polarisabilities for atoms in different functional groups of molecules from the set of 60 described above. Values are in $Å^3$.

As Table 4.6 shows, there seems to be very little consistency in the calculated polarisabilities, and considering how common these functional groups are to organic chemistry, these discrepancies are likely the source of the significant deviations described above. In particular, the calculated polarisabilities of quaternary carbon atoms are extremely high, and the standard deviation is approximately 50% of the total value. The failure to consistently produce a polarisability for an atomic species that is of such critical importance to organic chemistry is very troubling. This outcome, as well as the deviations seen in Table 4.5 and the fact that the atomic polarisabilities included in the PIXEL program give results that correspond much better with experimental values of sublimation enthalpies, indicates that polarisabilities calculated through the Atoms in Molecules approach are not suitable for PIXEL calculations.

4.3.2 Hirshfeld Volumes

Figure 4.4 shows the PIXEL lattice energies calculated with polarisabilities obtained from applying the results of the Hirshfeld volume analysis with the TS dispersion correction scheme to the static dipole polarisabilities in Table 4.2 for the five compounds acetic acid, formamide, hexachlorobenzene, imidazole and octane. Also shown are lattice energies calculated using the standard atomic polarisabilities included in the OPiX package.

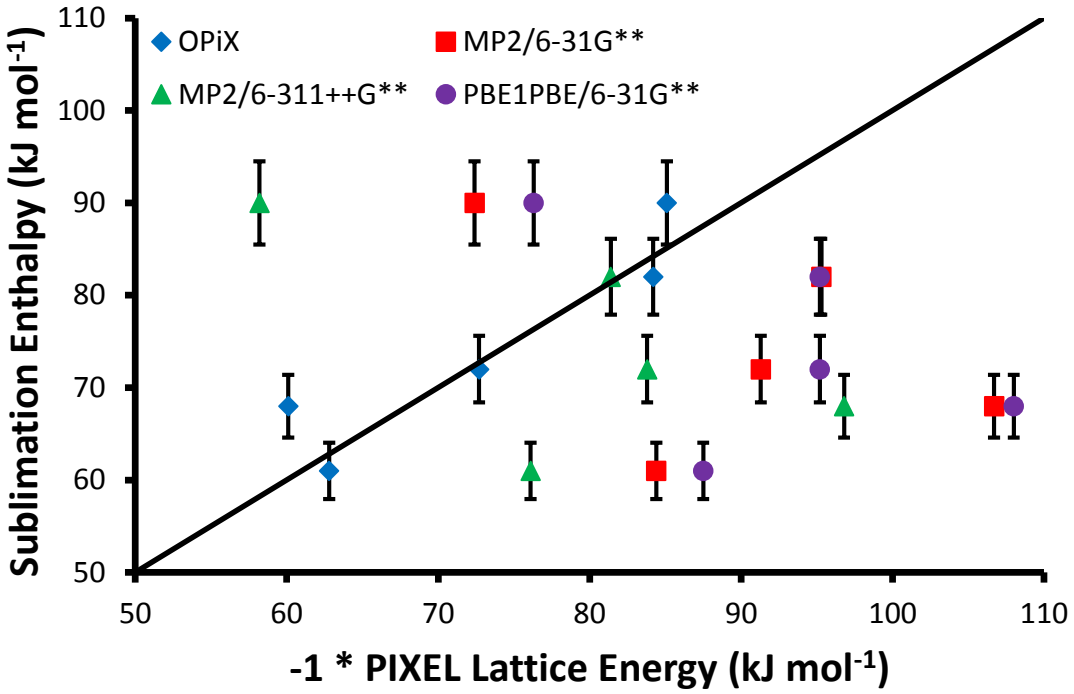

Figure 4.4: Comparison of literature sublimation enthalpies to PIXEL calculated lattice energies for the subset of five compounds. Blue diamonds close to the line are energies calculated using the standard atomic polarisabilities contained within the OPiX package with electron densities calculated at the MP2/6-31G** level. The remaining points use polarisabilities calculated using Hirshfeld volume analysis with the TS dispersion correction scheme, with electron densities calculated at the levels of theory indicated in the legend. Error bars are ±5% of experimental values, and the black line is $y = x$.

From the scatter of the data points in Figure 4.4, it is evident that atomic polarisabilities obtained in this way are not suitable for PIXEL calculations; there is no correlation with experimental sublimation enthalpies whatsoever, regardless of the electron density used.

In an attempt to improve on the performance of the TS scheme to obtain atomic polarisabilities, Hirshfeld analysis was performed using the TS-SCS dispersion correction scheme, which has been previously used to improve polarisabilities calculated using the TS scheme.[30] Figure 4.5 shows the results of the calculations using these polarisabilities.

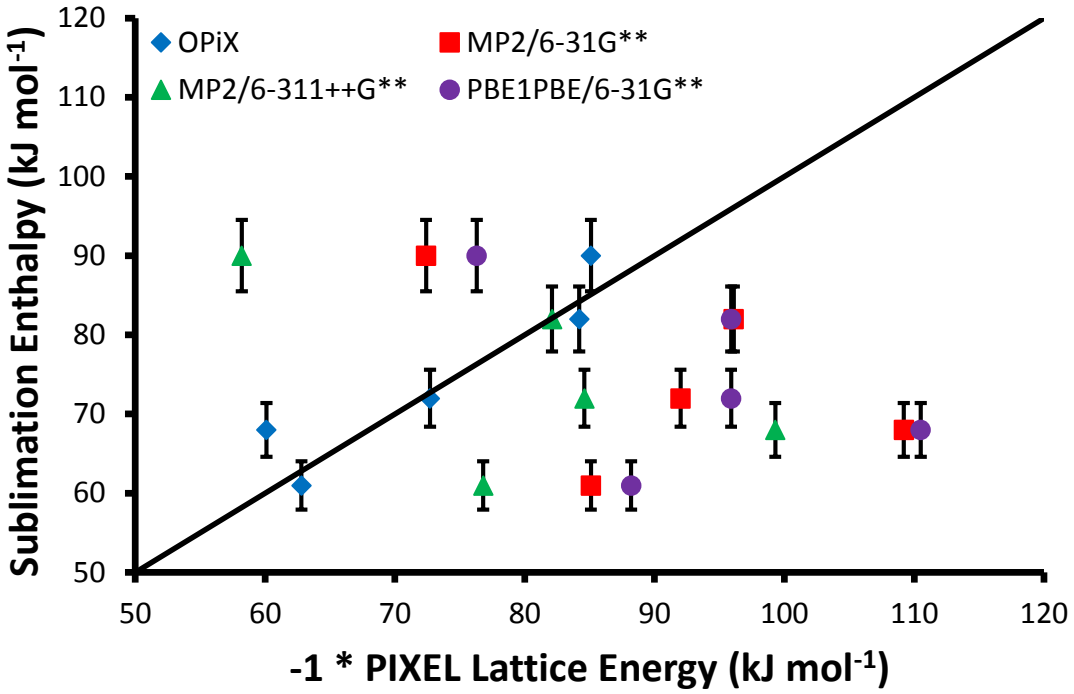

Figure 4.5: A similar comparison to that in Figure 4.4, this time using polarisabilities calculated using Hirshfeld volume analysis with the TS-SCS dispersion correction scheme. Error bars are ±5% of experimental values, and the black line is $y = x$.

Once again, the lattice energies calculated using atomic polarisabilities obtained from Hirshfeld volume analysis do not correlate with experimental sublimation enthalpies. There is no improvement observed from the use of the TS-SCS scheme over the results obtained from the TS scheme. In fact, some energies are calculated even further from the literature sublimation enthalpies for this method. This is a surprising result, considering the TS-SCS scheme was expected to improve the calculated polarisabilities.

During the analysis of the Hirshfeld volumes, it was noticed that values of the ratio described in Equation 4.1 were somewhat counterintuitive. Table 4.6 shows the averaged results of the Hirshfeld analysis for hexachlorobenzene, and the corresponding calculated atomic polarisabilities, along with the standard PIXEL values from OPiX.

Atom	$(V/V_{free})_{TS}$	α_{TS} (Å^3)	$(V/V_{free})_{TS\text{-}SCS}$	$\alpha_{TS\text{-}SCS}$ (Å^3)	α_{OPiX} (Å^3)
C	0.917	1.495	0.917	1.494	1.35
Cl	0.958	2.086	0.957	2.085	2.30

Table 4.6: Average results of the Hirshfeld analysis for hexachlorobenzene.

A similar analysis of Cl_2 yields a Hirshfeld ratio of 0.985 for each chlorine atom, which is larger than those calculated for the chlorine atoms in hexachlorobenzene. Due to the differences in electronegativity between carbon and chlorine, the carbon atoms in the aromatic ring would carry a partial positive charge and the chlorine atoms a partial negative charge. In this case, it would be expected that the electron density around the chlorine atoms in hexachlorobenzene would be increased, giving them a greater effective electron density than the chlorine atoms in Cl_2, and consequently a higher Hirshfeld ratio. However, the opposite is observed here, which seems to suggest that these calculated Hirshfeld volumes may be unsuitable for this application.

When the atomic polarisabilities calculated through Hirshfeld volume analysis are used in the PIXEL formulation, the calculated lattice energies do not correlate at all with experimental sublimation enthalpies. Once again, the standard atomic polarisabilities contained in the OPiX package perform better than the polarisabilities calculated in this way, and as such, the Hirshfeld volume method is not suitable for obtaining PIXEL parameters.

4.4 Conclusions

Attempts have been made to generate tailored atomic polarisabilities for use in the PIXEL method through the Atoms in Molecules approach and the Hirshfeld volumes method. Using AIM, the straight line parameters obtained for fits of calculated lattice energies to experimental sublimation enthalpies for polarisabilities calculated at the HCTH/6-311++G** level are $y = 0.86(2)\,x$ and $R = 0.60$, while those obtained at the B3LYP/6-311++G** level are $y = 0.89(3)\,x$ and $R = 0.32$. This indicates a poorer agreement when using calculated atomic polarisabilities than for lattice energies calculated using the standard polarisability values contained within the OPiX package, where the straight line parameters are $y = 1.01(1)\,x$ and $R = 0.89$. For polarisabilities obtained through Hirshfeld volume analysis, no correlation between calculated lattice energies and literature values was observed, regardless of the scheme used. Consequently, neither method is suitable for the calculation of atomic polarisabilities for use in the PIXEL method.[†]

[†] Many thanks are due to Anthony Reilly for helpful discussions concerning Hirshfeld analysis, and contributions to the AIM calculations by Claudio Putzu are gratefully acknowledged.

4.5 References

1. A. Gavezzotti, *Zeitschrift Fur Kristallographie*, 2005, **220**, 499-510.
2. L. Maschio, B. Civalleri, P. Ugliengo and A. Gavezzotti, *Journal of Physical Chemistry A*, 2011, **115**, 11179-11186.
3. A. Gavezzotti, *Journal of Physical Chemistry B*, 2002, **106**, 4145-4154.
4. A. Gavezzotti, *Journal of Physical Chemistry B*, 2003, **107**, 2344-2353.
5. A. Gavezzotti, *OPiX*, (2003), Milan.
6. K. J. Miller, *Journal of the American Chemical Society*, 1990, **112**, 8533-8542.
7. A. Gavezzotti, *Molecular Aggregation - Structure Analysis and Molecular Simulation of Crystals and Liquids*, 1st edn., Oxford University Press, New York, 2007.
8. R. F. W. Bader, *Atoms in Molecules: A Quantum Theory*, Oxford University Press, Oxford, 1990.
9. C. F. B. R. J. Matta, ed., *The Quantum Theory of Atoms in Molecules: From Solid State to DNA and Drug Design*, WILEY-VCH Verlag GmbH & Co., Weinheim, 2007.
10. T. Brinck, J. S. Murray and P. Politzer, *Journal of Chemical Physics*, 1993, **98**, 4305-4306.
11. F. L. Hirshfeld, *Theoretica Chimica Acta*, 1977, **44**, 129-138.
12. S. P. Goldman, *Physical Review A*, 1989, **39**, 976-980.
13. K. Anderson and A. J. Sadlej, *Physical Review A*, 1992, **46**, 2356-2362.
14. H. J. Werner and W. Meyer, *Physical Review A*, 1976, **13**, 13-16.
15. E. A. Reinsch and W. Meyer, *Physical Review A*, 1976, **14**, 915-918.
16. W. M. Haynes, ed., *CRC Handbook of Chemistry and Physics*, 93rd Edition edn., CRC Press/Taylor and Francis, Boca Raton, FL., 2013.
17. K. E. Laidig and R. F. W. Bader, *Journal of Chemical Physics*, 1990, **93**, 7213-7224.
18. T. A. Keith, *AIMAll*, (2012) TK Gristmill Software, Overland Park, KS, USA.
19. A. D. Becke, *Journal of Chemical Physics*, 1996, **104**, 1040-1046.
20. F. A. Hamprecht, A. J. Cohen, D. J. Tozer and N. C. Handy, *Journal of Chemical Physics*, 1998, **109**, 6264-6271.
21. J. P. Perdew, K. Burke and M. Ernzerhof, *Physical Review Letters*, 1996, **77**, 3865-3868.
22. C. Adamo, M. Cossi, G. Scalmani and V. Barone, *Chemical Physics Letters*, 1999, **307**, 265-271.
23. C. Adamo, G. E. Scuseria and V. Barone, *Journal of Chemical Physics*, 1999, **111**, 2889-2899.
24. C. Van Caillie and R. D. Amos, *Chemical Physics Letters*, 2000, **328**, 446-452.
25. A. A. Marycott and F. Buckley, *U.S. National Bureau of Standards Circular No. 537*, 1953.
26. S. J. Clark, M. D. Segall, C. J. Pickard, P. J. Hasnip, M. J. Probert, K. Refson and M. C. Payne, *Zeitschrift Fur Kristallographie*, 2005, **220**, 567-570.
27. *Materials Studio Release Notes*, (2010) Accelrys Software Inc., Cambridge, UK.
28. J. Binns, M. R. Healy, S. Parsons and C. A. Morrison, *Acta Crystallographica Section B - Structural Science, Crystal Engineering and Materials*, 2014, **70**, 259-267.
29. A. Tkatchenko and M. Scheffler, *Physical Review Letters*, 2009, **102**, 073005.
30. A. Tkatchenko, R. A. DiStasio, Jr., R. Car and M. Scheffler, *Physical Review Letters*, 2012, **108**, 236402.
31. M. Headgordon, J. A. Pople and M. J. Frisch, *Chemical Physics Letters*, 1988, **153**, 503-506.

Chapter 5

Alternative Methods for Calculating the PIXEL Electron Density

5.1 Synopsis

Electron densities for PIXEL calculations have been calculated using semi-empirical methods for 60 organic compounds. The semi-empirical methods tested were MNDO, AM1 and PM3. The lattice energies subsequently calculated using these electron densities were then compared to experimental sublimation enthalpies, giving straight line parameters of $y = 0.92(2)x$ (where y are the experimental sublimation enthalpies and x are the calculated lattice energies, both in kJ mol^{-1}) and a correlation coefficient $R = 0.74$ for MNDO densities, $y = 0.87(2)x$ and $R = 0.60$ for AM1 densities, and $y = 0.83(2)x$ and $R = 0.75$ for PM3 densities. Additionally, the lattice energies and component PIXEL energy terms calculated from semi-empirical electron densities are compared to those obtained at the MP2/6-31G** level of theory.

5.2 Introduction

In its current implementation, PIXEL makes use of *ab initio* (or DFT) electron densities that are normally obtained at the MP2/6-31G** level of theory. This can, however, be computationally demanding, and the calculation of electron densities in this manner can be both time consuming and expensive, particularly for large molecules. While lower quality basis sets can be used for larger systems, full quantum mechanical calculation of the electron density remains expensive.

In order to interface the PIXEL method with programs such as Mercury,[1] improvements in the speed of the electron density calculation are necessary. To this end, semi-empirical calculations, which can be performed extremely quickly, represent a faster and cheaper method for obtaining the electron densities. This would allow for much more rapid screening of intermolecular interactions, particularly in large systems.

Semi-empirical methods are set up in a similar fashion to Hartree-Fock calculations, but with certain factors such as two-electron integrals being approximated by empirical parameters. This greatly simplifies the calculations, resulting in computing times that are a fraction of those for Hartree-Fock and post Hartree-Fock methods.

5.3 Experimental

The trial set of 60 organic complexes used was obtained from previous work carried out by Maschio *et al.*[2] and crystal structures were obtained from the CSD[3] using Mercury.[1] For each structure OH, NH and CH distances were changed to 0.993, 1.015 and 1.089 Å, respectively, normalising these distances to "standard" neutron values. A list of the compounds investigated along with their CSD Refcodes is given in Table 5.1.

Electron densities were calculated using Gaussian03[4] at the MNDO,[5, 6] AM1[7] and PM3[8, 9] levels of theory and were used to perform PIXEL calculations. Gaussian03 was used instead of the more recent Gaussian09 in this instance as Gaussian09 no longer has the facility to produce density files with semi-empirical methods. MNDO, AM1 and PM3 were chosen as they were the semi-empirical methods available. In order to carry out the semi-empirical calculations, modification of the route section in the Gaussian Job File produced by OPiX[10] must be made to include an internal operations keyword. For example, at the MNDO level, the route section for the electron density calculation is as follows:

#MNDO nosym pop=esp cube=cards cube=frozenc IOp(4/24=1)

where IOp(4/24=1) updates the orbitals and eigenvalues by multiplying them by $S^{-1/2}$. Otherwise, calculations proceed as indicated in the OPiX manual.

Experimental sublimation enthalpies were obtained from Ref. 2, and PIXEL energies were recalculated with MP2/6-31G** densities to ensure that the only variation of the PIXEL input was the electron densities used in each calulation.

Compound	Refcode	Exptl.	MP2	MNDO	AM1	PM3
acetic acid	ACETAC01	61	62.3	42.6	46.9	56.5
acridine	ACRDIN01	93	95.5	117.4	128.2	124.8
anthracene	ANTCEN14	99	103.4	126	148.5	142.7
anthraquinone	ANTQUO08	115	96.3	116.3	116.4	120.9
teophyllin	BAPLOT01	126	121.3	128.4	134.9	125.6
1,3-phthalic acid	BENZDC01	110	131.6	106.3	111.1	127
benzene	BENZEN07	45	49.9	60.5	73.5	70.3
fumaronitrile	BISJIW	70	65.3	48.9	47.9	56.7
benzamide	BZAMID01	101	100.9	98.8	106.5	99.7
coumarin	COUMAR10	83	80.9	93.5	102.3	102.1
trinitro-triazacyclohexane	CTMTNA	112	110	129.9	133.9	172.8
2,3-diazanaphthalene	DAZNAP	83	89.1	96.1	106.1	104.2

2,8-dichlorodioxin	DCBDOX10	109	99.6	126.6	143.7	137
1,4-dichlorobenzene	DCLBEN01	65	67.5	81.4	80.1	76.6
dichlorobenzoquinone	DCLBQN	70	74.9	83.2	76.7	79.3
dimethylnitroaniline	DIMNAN01	103	89.1	116.1	124.1	125.3
9,10-dihydroanthracene	DITBOX	94	85.3	105	120.7	117.6
dimethylbenzoic acid	DMBZAC01	103	96.8	91.5	93.4	102.1
dimethylnaphthalene	DMNAPH05	83	81.3	99.4	115.7	111.6
1,3-dinitrobenzene	DNBENZ15	85	73.6	97	101.1	110.4
1,4-dinitrobenzene	DNITBZ11	96	85.2	104.5	104.2	131
1,2,3,4-tetrachlorodioxin	FELSEU	119	110.4	147.2	147.2	146.3
formic acid	FORMAC01	68	59.6	49.1	52.3	61.2
formamide	FORMAM02	72	72.2	63.9	69.3	59.6
hexachlorobenzene	HCLBNZ11	90	85.3	125.8	124.8	121.3
imidazole	IMAZOL13	82	83.5	77.5	86	73.7
malonic acid	MALNAC06	111	105.5	79.5	86	100
melamine	MELAMI04	120	154.1	169.5	188.6	144.4
dimethylnitramine	METNAM04	70	69.1	70	76.2	82.4
maleic anhydride	MLEICA	85	66.4	65.7	59.7	69.7
N,N-dimethyl-4-nitroaniline	MNTDMA01	93	81.9	107.4	114	116.9
trinitromethylaniline	MTNANL	134	116.9	147.5	145.3	176.9
naphthoquinone	NAPHQU	91	89.1	99.4	103.7	107.4
naphthalene	NAPHTA10	73	74.1	91	105.2	101.7
2-naphthoic acid	NAPOAC01	115	104.3	103.2	100.9	110.1
nitrotoluene	NITOLU	79	66.4	82	89.5	91.2
nitrophenol	NITPOL02	94	95.9	108.9	115.6	123.4
nitroguanidine	NTRGUA03	143	126.8	141.1	147.7	144.4
tetranitro-tetraazacyclooctane	OCHTET12	162	147.9	160	168.4	215
n-octane	OCTANE01	68	59	75.1	73.4	73.9
oxalic acid	OXALAC04	95	105.8	73.3	73.9	95.5
parabanic acid	PARBAC11	119	96.5	80.9	77.5	86
phenanthrene	PHENAN08	92	95.1	115.8	135.8	131.5
pyromellitic dianhydride	PYMDAN	83	94.3	103.4	84.2	107.6
pyrene	PYRENE02	100	107.1	129.5	148.9	143.7
succinic anhydride	SUCANH15	81	76.5	77.1	72.3	83.1
triamino-trinitrobenzene	TATNBZ	168	155.6	208.3	217.2	211.6
1,3,5-trichlorobenzene	TCHLBZ	73	70.4	91.7	90.8	88.1
tetracyanoquinodimethane	TCYQME	124	118.3	105.7	103.8	117.3
1,4-dicyanobenzene	TEPNIT11	89	82.2	74.7	72.5	82.9
1,3,5-trinitrobenzene	TNBENZ10	107	78.8	107.3	99.9	126.8
trinitroaniline	TNIOAN	120	95.5	135	133.7	149.6
trinitroxylene	TNOXYL	130	98.9	127.9	125.5	165.5
trinitrophenetole	TNPHNT	121	98.4	128.8	122.8	155.5
tetroxocane	TOXOCN	80	82.8	87.7	96.1	90.4
urea	UREAXX09	92	114.5	99.5	106.5	93.8
N,N-dimethylurea	WIFKEB	90	98.3	94.6	101	92.8
1,2-dinitrobenzene	ZZZFYW01	87	81.1	102.7	106.4	116.1

2,4,6-trinitrotoluene	ZZZMUC01	105	90.6	123.7	118.1	154.4
2,6-dinitrotoluene	ZZZQSC01	98	82.7	106.3	109	129.6

Table 5.1: The 60 organic compounds investigated along with the CSD Refcodes and energetic data. Exptl. is the experimental sublimation enthalpy, and MP2, MNDO, AM1 and PM3 are PIXEL lattice energies obtained from electron densities calculated at the corresponding levels of theory. Values are in kJ mol^{-1}.

5.4 Results and Discussion

5.4.1 Computing Times

Electron density calculations using semi-empirical methods are indeed significantly faster than those carried out at the MP2/6-31G** level. For instance, taking acetic acid and triamino-trinitrobenzene as examples of small and large organic molecules, the computing times as calculated using 8 processors of the University of Edinburgh computing cluster EDDIE are shown in Table 5.2.

Compound	**AM1**	**MNDO**	**PM3**	**MP2**
acetic acid	2.4 s	2.5 s	2.5 s	13.3 s
triamino-trinitrobenzene	11.6 s	11.3 s	11.7 s	1208.6 s

Table 5.2: Computing times, measured in seconds, for the calculation of electron densities using semi-empirical and MP2 methods for acetic acid and triamino-trinitrobenzene.

As Table 5.2 shows, the computing times for the semi-empirical methods are a fraction of those required by MP2. These fast computing times mean that such calculations could conceivably be performed in the order of minutes on a desktop computer. Such speeds of calculation mean that for interfacing with a program such as Mercury, in the interests of calculation time at least, semi-empirical methods are suitable candidates for the calculation of electron densities for PIXEL calculations.

5.4.2 Comparison of PIXEL Results

Table 5.1 shows the literature sublimation enthalpies and PIXEL calculated lattice energies for the 60 organic compounds investigated. Figure 5.1 shows this data graphically for energies calculated with MP2 densities (a), MNDO densities (b), AM1 densities (c) and PM3 densities (d).

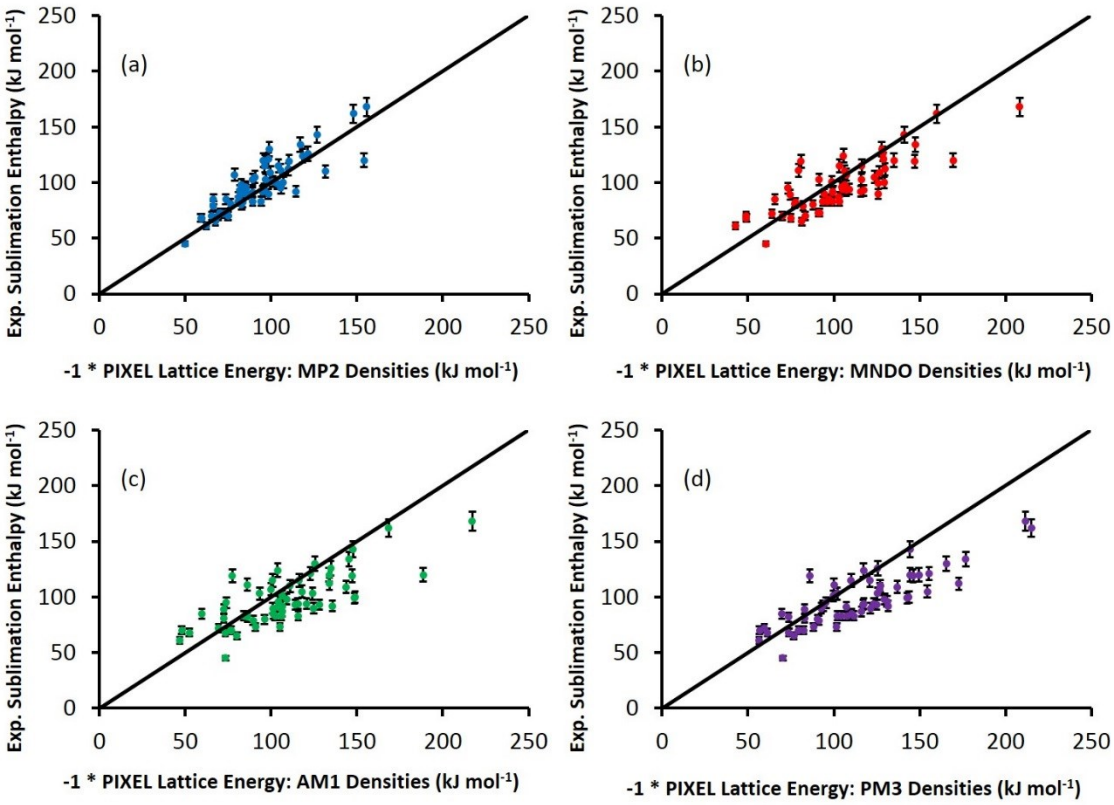

Figure 5.1: PIXEL lattice energies calculated using MP2 densities (a) MNDO densities (b), AM1 densities (c) and PM3 densities (d) versus experimental sublimation enthalpies for the 60 compounds listed in Table 5.1. The solid black lines are $y = x$. Error bars are ±5% of the literature sublimation enthalpies.

The agreement between PIXEL energies calculated using MP2 densities with experimental sublimation enthalpies is consistent with that in Ref. 2 [$y = 1.04(2)x$, $R = 0.86$]. However, the agreement when using semi-empirical densities is substantially poorer [MNDO: $y = 0.92(2)x$, $R = 0.74$; AM1: $y = 0.87(2)x$, $R = 0.60$; PM3: $y = 0.83(2)x$, $R = 0.75$]. This is likely due to the incorrect modelling of the individual PIXEL terms calculated using semi-empirical electron densities.

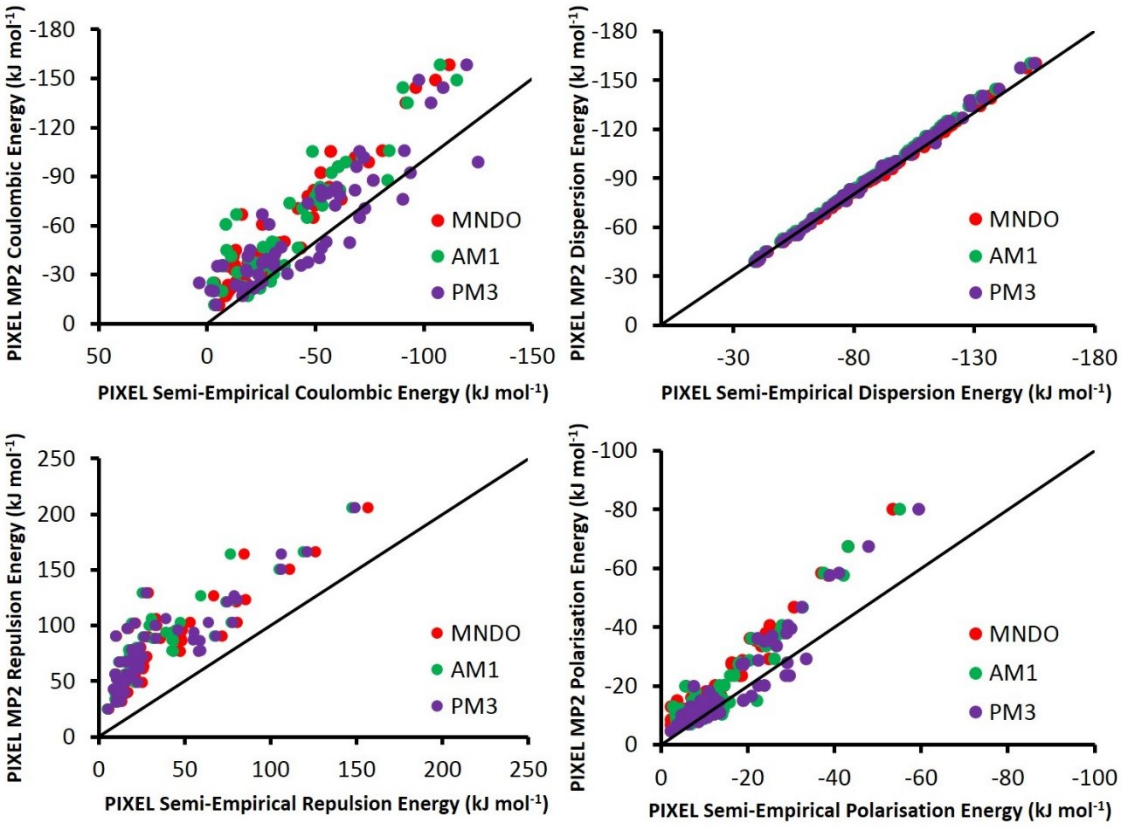

Figure 5.2: The four different PIXEL terms calculated using semi-empirical electron densities compared to those for MP2 densities for the 60 compounds listed in Table 5.1. Black lines are $y = x$.

Figure 5.2 shows the breakdown of the energies obtained from semi-empirical densities into the different PIXEL component terms compared to those from densities calculated at the MP2/6-31G** level. Tables containing the numerical data for the individual terms are contained within the supplementary information for this chapter. While the agreement between the dispersion terms calculated using semi-empirical electron densities and those calculated at the MP2/6-31G** level is excellent (Table 5.3), the agreement for the other terms is much poorer, particularly in the case of the Coulombic and repulsion terms.

Term	m_{MNDO}	R_{MNDO}	m_{AM1}	R_{AM1}	m_{PM3}	R_{PM3}
Dispersion	1.022(2)	1.00	1.047(1)	1.00	1.035(2)	1.00
Polarisation	1.55(3)	0.97	1.42(3)	0.96	1.26(3)	0.94

Table 5.3: Straight line parameters, where y are the energies from MP2 densities and x are the energies from semi-empirical densities, for the dispersion and polarisation terms.

The agreement between the dispersion energies calculated using semi-empirical electron densities with those obtained using MP2 densities is likely due to the method of calculating this term, where the calculated electron densities are only used to scale the atomic polarisabilities on a per-pixel basis, and the empirical approach of this calculation seems to be robust to the nature of the electron density. Similarly, while the polarisation energies calculated using semi-empirical electron densities are numerically too small, the spread of the data is modest, particularly for the MNDO densities. Again, this is likely due to the similar treatment of the calculated electron densities for the polarisation term as for the dispersion term.

Visual inspection of the agreement of the Coulombic and repulsion terms shows that there is little point in attempting to calculate a linear fit to these data. The values obtained from the semi-empirical densities are again numerically too small compared to the values from MP2 densities, and there seems to be no correlation between the two methods. In the case of the Coulombic terms, some interactions that are calculated as attractive using MP2 densities are found to be repulsive with semi-empirical densities, a result that is simply incorrect. This discrepancy is likely due to the way in which these terms are calculated, where the nature of the electron density plays a more crucial role than in the calculation of the dispersion and polarisation terms.

Given the poor agreement between the lattice energies calculated using semi-empirical electron densities with experimental sublimation enthalpies, and the lack of correlation between the majority of the component PIXEL terms calculated with such densities and those obtained at the MP2/6-31G** level, it is clear that semi-empirical electron densities are not suitable for use in PIXEL calculations.

5.5 Conclusions

In an effort to improve the overall speed of performing a PIXEL calculation, lattice energies calculated with electron densities obtained through the use of semi-empirical methods were compared to the experimental sublimation enthalpies, and the results were also compared to PIXEL calculations performed with *ab initio* densities. While electron densities calculated with semi-empirical methods can be obtained in a fraction of the time of those calculated at the MP2/6-31G** level, it is clear that the

agreement of the lattice energies calculated with semi-empirical electron densities compare poorly with experimental sublimation enthalpies.

Although electron densities calculated with MNDO, AM1 and PM3 are not suitable for use with PIXEL calculations, it is possible, however unlikely, that improved semi-empirical methods such as PM6 would result in lattice energies that more closely correspond to experimental values. However, since it is not currently possible to implement PM6 electron densities in Gaussian, other computational programs would be necessary to investigate this method.

5.6 References

1. C. F. Macrae, I. J. Bruno, J. A. Chisholm, P. R. Edgington, P. McCabe, E. Pidcock, L. Rodriguez-Monge, R. Taylor, J. van de Streek and P. A. Wood, *Journal of Applied Crystallography*, 2008, **41**, 466-470.
2. L. Maschio, B. Civalleri, P. Ugliengo and A. Gavezzotti, *Journal of Physical Chemistry A*, 2011, **115**, 11179-11186.
3. I. J. Bruno, J. C. Cole, P. R. Edgington, M. Kessler, C. F. Macrae, P. McCabe, J. Pearson and R. Taylor, *Acta Crystallographica Section B - Structural Science*, 2002, **58**, 389-397.
4. G. W. T. M. J. Frisch, H. B. Schlegel, G. E. Scuseria, M. A. Robb, J. R. Cheeseman, J. A. Montgomery, Jr., T. Vreven, K. N. Kudin, J. C. Burant, J. M. Millam, S. S. Iyengar, J. Tomasi, V. Barone, B. Mennucci, M. Cossi, G. Scalmani, N. Rega, G. A. Petersson, H. Nakatsuji, M. Hada, M. Ehara, K. Toyota, R. Fukuda, J. Hasegawa, M. Ishida, T. Nakajima, Y. Honda, O. Kitao, H. Nakai, M. Klene, X. Li, J. E. Knox, H. P. Hratchian, J. B. Cross, V. Bakken, C. Adamo, J. Jaramillo, R. Gomperts, R. E. Stratmann, O. Yazyev, A. J. Austin, R. Cammi, C. Pomelli, J. W. Ochterski, P. Y. Ayala, K. Morokuma, G. A. Voth, P. Salvador, J. J. Dannenberg, V. G. Zakrzewski, S. Dapprich, A. D. Daniels, M. C. Strain, O. Farkas, D. K. Malick, A. D. Rabuck, K. Raghavachari, J. B. Foresman, J. V. Ortiz, Q. Cui, A. G. Baboul, S. Clifford, J. Cioslowski, B. B. Stefanov, G. Liu, A. Liashenko, P. Piskorz, I. Komaromi, R. L. Martin, D. J. Fox, T. Keith, M. A. Al-Laham, C. Y. Peng, A. Nanayakkara, M. Challacombe, P. M. W. Gill, B. Johnson, W. Chen, M. W. Wong, C. Gonzalez, and J. A. Pople, *Gaussian 03*, (2004) Gaussian Inc., Wallingford, CT.
5. M. J. S. Dewar and W. Thiel, *Journal of the American Chemical Society*, 1977, **99**, 4899-4907.
6. M. J. S. Dewar and W. Thiel, *Journal of the American Chemical Society*, 1977, **99**, 4907-4917.
7. M. J. S. Dewar, E. G. Zoebisch, E. F. Healy and J. J. P. Stewart, *Journal of the American Chemical Society*, 1985, **107**, 3902-3909.
8. J. J. P. Stewart, *Journal of Computational Chemistry*, 1989, **10**, 209-220.
9. J. J. P. Stewart, *Journal of Computational Chemistry*, 1989, **10**, 221-264.
10. A. Gavezzotti, *OPiX*, (2003), Milan.

Chapter 6

Melting Point Alternation in the Primary Amines*

* Maloney, A.G.P.; Wood, P.A.; Parsons, S., (2014) *CrystEngComm*

DOI: 10.1039/c3ce42639d

6.1 Synopsis

The crystal structures of the primary amines from ethylamine to decylamine have been determined by X-ray diffraction following in situ crystallisation from the liquids. In the series from propylamine to decylamine structures remain in the same phase on cooling from the melting point to 150 K, and the structures of these compounds were determined by single-crystal methods. By contrast, ethylamine undergoes a slow reconstructive phase transition on cooling to 150 K. The structure of the high-temperature form was determined by single-crystal methods at 180 K, while that of the low-temperature form was determined by powder diffraction at 150 K. The stability of the low-temperature form can be ascribed in part to more energetic hydrogen bond formation. PIXEL calculations indicate that hydrogen bonding and methyl–methyl interactions at the chain ends are optimised in the early members of the series, with particularly inefficient inter-chain interactions observed for propylamine and pentylamine. In the later members of the series dispersion interactions become the principal structure-directing interaction and the energies of the hydrogen bonds and methyl–methyl interactions become weaker to accommodate more efficient inter-chain packing. The weakest methyl–methyl interactions occur in heptyl- and nonyl-amines. Overall, intermolecular interactions in the even membered amines are stronger and the packing more efficient than in the odd members, leading to an alternation in melting points along the series, an effect reminiscent of results obtained for the alkanes, carboxylic acids and several α–ω alkyl derivatives.

6.2 Introduction

Provided suitable functional groups are present, crystal packing in molecular materials is often considered to be directed by hydrogen bond formation. The predictability and robustness of hydrogen bonds make them natural choices for synthons in crystal engineering: a recent survey[1] of the most important and reproducible supramolecular synthons was dominated by hydrogen-bonded dimers with energies of up to 70 kJ mol^{-1}. When interpreting crystal structures, too, hydrogen bonds are easily recognised because they are both short and highly directional, and their formation provides convincing explanation for why a particular structure has formed.

While the directionality of H-bonds makes them very useful in design of strategies for crystal engineering, it is possible to over-emphasise their importance when interpreting crystal structures, for example when identifying which contacts might be amenable to modification by changing temperature or pressure or formation of a co-crystal. The point has recently been made by Gavezzotti[2] that this can lead us to ignore other significant, but less easily recognised, intermolecular interactions. The crystal structure of serine hydrate is an illustrative example.[3] It consists of layers of serine molecules connected together by layers of water molecules, which form hydrogen bonds to serine molecules in the layers above and below. But this interpretation of the structure completely neglects the importance of interlayer electrostatic interactions between the NH_3^+ and CO_2^- moieties of zwitterionic serine molecules. The energies of these interactions are 48 kJ mol^{-1} for a centroid-centroid distance of over 6 Å compared to energies of 49 and just 2 kJ mol^{-1} for the water…serine interactions in which the H…O distances are *ca.* 1.9 Å.

The serine hydrate example shows that electrostatic interactions have substantial energies over much longer distances than are usually considered for intermolecular interactions, and this makes them difficult to recognise. Likewise, significant dispersion (or van der Waals) interactions are also hard to identify from geometrical data alone because they contain no distinctive interatomic contacts. Stacking interactions might be considered to be an exception, but even here the range of possible geometries seen in crystal structures is substantial, and interactions with large ring off-sets may still be stabilising. In aniline,[4] for example, π…π stacking interactions with a centroid-centroid distance of 5.8 Å have the same interaction energies (12 kJ mol^{-1}) as the NH…N hydrogen bonds. Indeed, the NH…N hydrogen bonds are not the strongest intermolecular interactions in aniline at all, being about half the strength of NH…π contacts. They even become destabilising at elevated pressure.

A complete view of the relative importance of different intermolecular interactions in the examples cited above was only obtained by evaluating intermolecular energies rather than relying on geometrical analysis alone. Though a number of methods are available for calculating intermolecular interaction energies, the PIXEL method is becoming established as a rapid and accurate method for this application.[5-10] In the PIXEL method an intermolecular energy is evaluated by summing energy contributions

arising from all pairs of volume elements ('pixels') contained in the electron density distributions of the two molecules in question. The electron densities can be obtained using conventional quantum mechanical methods, such as MP2 or DFT. The calculations yield a lattice energy broken down into contributions from individual intermolecular interactions for a crystal structure. The lattice energies show good agreement with experimental sublimation energies and individual contact energies are as accurate as those from high-level quantum mechanical methods.[1, 11, 12] Moreover, the contact energies are broken down into chemically meaningful electrostatic, polarisation, dispersion and repulsion terms. These calculations, which take only a few hours on a desk-top computer, are having a transformative effect on the analysis of crystal structures.

In this chapter, the crystal structures of the primary amines from ethylamine to decylamine are described, and PIXEL calculations are used to identify the point at which inter-chain dispersion interactions become the dominant intermolecular contacts. Also described is the effect that this dominance has on the hydrogen bonds. Amines were chosen for this study because NH…N interactions are amongst the weakest conventional H-bonds, having energies of 10-20 kJ mol^{-1}; for comparison OH…O energies are 20-40 kJ mol^{-1} in phenols and carboxylic acids.[9] The primary amines are therefore an ideal system to investigate the extent of stabilisation provided by H-bonding relative to dispersion interactions as the latter increase with chain length.

Improvements in *in-situ* crystallisation instrumentation and techniques have allowed for studies of *n*-alkanes and their derivatives to become much more practical in the last twenty years. The structures of the alkanes themselves are described in a classic paper by Boese,[13] who also studied the α,ω-alkanediols and α,ω-alkanediamines,[14] α,ω-alkanedithiols,[15] and α,ω-alkanedicarboxylic acids.[16] Bond has investigated the structures of the *n*-alkyl carboxylic acids.[17] Topological analysis of the alkane structures showed that the shapes of the odd numbered alkanes lead to inefficient packing in the regions of the crystal where methyl groups are positioned next to each other. This resolved the long-standing question of the source of the alternation of melting points along the series, in which the odd alkanes have lower melting points than their neighbouring even-membered homologues. The melting points of the primary amines also alternate, with odd members of the series having lower melting points than the even

members (Figure 6.1). This appears counter-intuitive in the context of Boese's results since an even amine has an odd chain length (e.g. butylamine has a five-membered chain containing 4C + 1N), and this study will also reveal how hydrogen bonding modifies the packing of the alkyl chains.

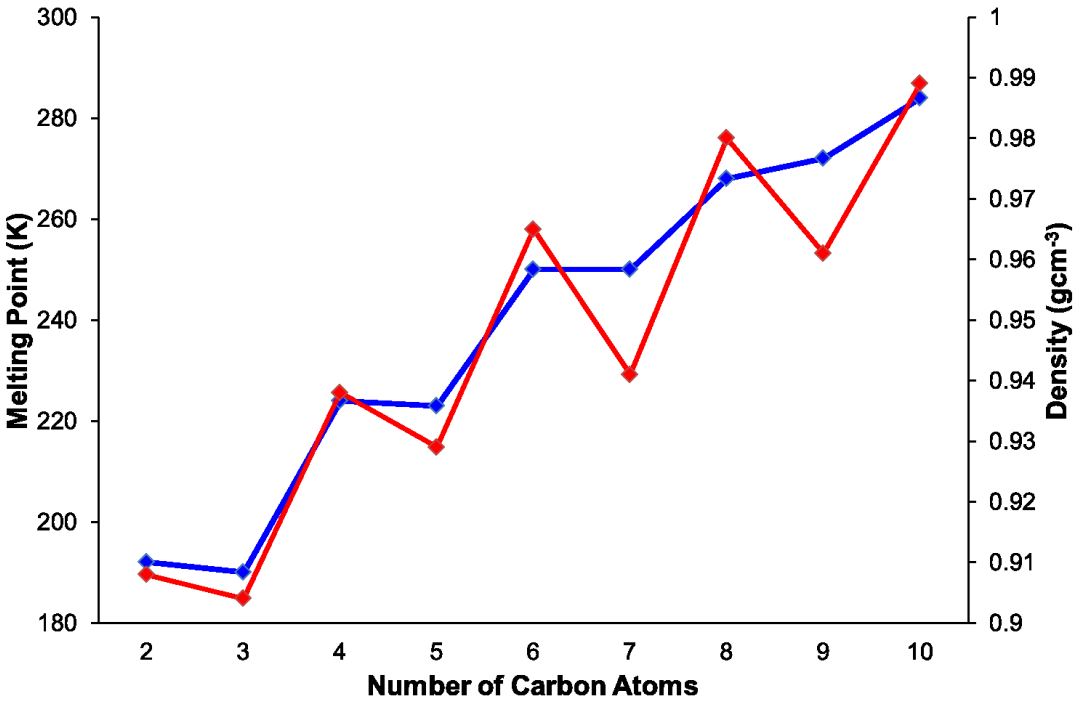

Figure 6.1: The melting point (blue) and density alternation (red) in short chain primary monoamines.

6.3 Experimental

6.3.1 General Procedure

All compounds were obtained from Sigma Aldrich or Acros Organics and used as received; all are liquid at room temperature. In a typical experiment the sample was drawn into a thin glass capillary (o.d. 0.2 – 0.3 mm) and sealed before being cooled to 10 K below the literature melting point, to form a polycrystalline solid. An OHCD (Optical Heating and Crystallization Device) Laser Assisted Crystal Growth Device was then used to crystallize the sample for X-ray analysis by way of zone melting procedures outlined by Boese[18] and Guru Row.[19] Crystal growth was effected by running the laser up the capillary over the course of between five and ten three minute cycles, with the starting point moved further up the capillary for each cycle. This

process yielded oriented "oligocrystalline" samples containing a number of individual needle-like crystals. The diffraction pattern of one crystallite was extracted and indexed using RLATT.[20]

X-ray data were collected at 150 K on a Bruker three-circle Apex II diffractometer equipped with an Oxford Cryosystems low-temperature device.[21] Following integration by SAINT,[22] a multi-scan absorption correction was applied (SADABS).[23] The structures were solved by direct methods (SIR92)[24] and refined against $|F|^2$ using all data (CRYSTALS).[25] Hydrogen atoms were located in difference maps and refined subject to restraints placed on bond distances, angles and isotropic displacement parameters. Carbon and nitrogen atoms were refined freely with anisotropic displacement parameters. Crystal and refinement parameters for all structures are listed in Table 6.1.

	ethylamine 1	ethylamine 2	propylamine	butylamine	pentylamine
Chemical formula	C_2H_7N	C_2H_7N	C_3H_9N	$C_4H_{11}N$	$C_5H_{13}N$
M_r	45.08	45.09	59.11	73.14	87.16
Crystal system, space group	Monoclinic, $P2_1/c$	Monoclinic, $P2_1/c$	Orthorhombic, *Pbcn*	Orthorhombic, *Pbcn*	Orthorhombic, *Pbcn*
Temperature (K)	180	150	150	150	150
a, b, c (Å)	8.2633 (3), 7.3098 (3), 5.5317 (2)	8.97420 (18), 5.21927 (8), 7.40243 (16)	23.2870 (13), 6.2354 (4), 5.9794 (4)	26.7852 (8), 6.8166 (2), 5.6703 (2)	33.546 (4), 6.4878 (8), 5.7295 (7)
α, β, γ (°)	90, 99.088 (3), 90	90, 112.9722 (13), 90	90, 90, 90	90, 90, 90	90, 90, 90
V (Å^3)	329.94 (2)	319.22 (1)	868.23 (9)	1035.31 (6)	1247.0 (3)
Z	4	4	8	8	8
T_{min}, T_{max}	0.79, 0.99	–	0.80, 0.98	0.82, 0.98	0.75, 0.98
No. of measured, independent and observed reflections	3375, 679, 614	–	9836, 890, 690	7989, 1572, 1327	7311, 1275, 547
R_{int}	0.027	–	0.059	0.026	0.075
θ values (°)	θ_{max} = 26.4, θ_{min} = 2.5	$2\theta_{min}$ = 4 $2\theta_{max}$ = 65	θ_{max} = 26.4, θ_{min} = 1.8	θ_{max} = 30.5, θ_{min} = 1.5	θ_{max} = 26.4, θ_{min} = 1.2
$(\sin\theta/\lambda)_{max}$ (Å^{-1})	0.625	–	0.626	0.714	0.626
***R* factors and goodness of fit**	$R[F^2 > 2\sigma(F^2)]$ = 0.038, $wR(F^2)$ = 0.085, S = 0.93	R_p = 0.032, R_{wp} = 0.049, R_{exp} = 0.024, χ^2 = 4.347	$R[F^2 > 2\sigma(F^2)]$ = 0.060, $wR(F^2)$ = 0.149, S = 0.99	$R[F^2 > 2\sigma(F^2)]$ = 0.047, $wR(F^2)$ = 0.142, S = 1.11	$R[F^2 > 2\sigma(F^2)]$ = 0.061, $wR(F^2)$ = 0.196, S = 0.96
No. of reflections/data points	679	6694	883	1572	1274
No. of parameters	56	-	73	90	107
No. of restraints	27	-	36	45	54
H-atom treatment	Restrained refall	Rigid body	Restrained refall	Restrained refall	Restrained refall
$\Delta\rho_{max}$, $\Delta\rho_{min}$ (e Å^{-3})	0.18, -0.12	–	0.29, -0.29	0.26, -0.11	0.18, -0.20

	hexylamine	**heptylamine**	**octylamine**	**nonylamine**	**decylamine**
Chemical formula	$C_6H_{15}N$	$C_7H_{17}N$	$C_8H_{19}N$	$C_9H_{21}N$	$C_{10}H_{23}N$
M_r	101.19	115.22	129.25	143.27	157.30
Crystal system, space group	Orthorhombic, $Pca2_1$	Monoclinic, $P2_1/c$	Orthorhombic, $Pca2_1$	Monoclinic, $P2_1/c$	Orthorhombic, $Pca2_1$
Temperature (K)	150	150	150	150	150
a, b, c (Å)	6.9725 (3), 17.7977 (6), 5.6105 (2)	5.5669 (5), 41.700 (4), 6.9982 (7)	7.0309 (5), 22.3077 (15), 5.5826 (4)	5.5458 (2), 50.6527 (17), 7.0521 (2)	7.0660 (4), 26.8352 (15), 5.5730 (3)
α, β, γ (°)	90, 90, 90	90, 90, 90	90, 90, 90	90, 90.040 (2), 90	90, 90, 90
V (Å^3)	696.23 (5)	1624.6 (3)	875.59 (11)	1981.00 (11)	1056.74 (10)
Z	4	8	4	8	4
T_{min}, T_{max}	0.83, 0.98	0.67, 0.98	0.65, 0.99	0.86, 0.98	0.81, 0.99
No. of measured, independent and observed reflections	8013, 913, 794	2893, 2893, 1116	16559, 998, 980	3641, 3641, 1162	9645, 1286, 1182
R_{int}	0.033	0.097	0.075	0.078	0.048
θ values (°)	θ_{max} = 28.7, θ_{min} = 1.1	θ_{max} = 26.4, θ_{min} = 2.0	θ_{max} = 26.5, θ_{min} = 1.8	θ_{max} = 25.4, θ_{min} = 1.6	θ_{max} = 27.1, θ_{min} = 1.5
$(\sin\theta/\lambda)_{max}$ (Å^{-1})	0.675	0.626	0.627	0.602	0.641
***R* factors and goodness of fit**	$R[F^2 > 2\sigma(F^2)]$ = 0.042, $wR(F^2)$ = 0.108, S = 1.01	$R[F^2 > 2\sigma(F^2)]$ = 0.075, $wR(F^2)$ = 0.313, S = 1.09	$R[F^2 > 2\sigma(F^2)]$ = 0.054, $wR(F^2)$ = 0.108, S = 1.00	$R[F^2 > 2\sigma(F^2)]$ = 0.037, $wR(F^2)$ = 0.143, S = 0.88	$R[F^2 > 2\sigma(F^2)]$ = 0.054, $wR(F^2)$ = 0.123, S = 0.98
No. of reflections/data points	910	2893	998	2585	1281
No. of parameters	124	282	158	350	192
No. of restraints	64	144	82	180	100
H-atom treatment	Restrained refall	Mixture of ind. and const. refinement	Restrained refall	Restrained refall	Restrained refall
$\Delta\rho_{max}$, $\Delta\rho_{min}$ (e Å^{-3})	0.26, -0.13	0.54, -0.50	0.17, -0.17	0.09, -0.13	0.30, -0.16

Table 6.1: Crystallographic data for the primary monoamines.

6.3.2 Heptylamine, Octylamine and Nonylamine

The structures of heptylamine, octylamine and nonylamine were found to form twinned crystals. Heptylamine and nonylamine are monoclinic but with β close to 90°. A two-fold axis about **a** was used to model pseudomerohedral twinning in both cases. The twin scale factors were found to be 0.227(6) and 0.205(2) for heptylamine and nonylamine, respectively.

The crystal of octylamine was a non-merohedral twin with the following twin law:

$$\begin{pmatrix} 0.993 & -0.054 & 0.024 \\ -0.061 & -0.980 & -0.060 \\ 0.430 & 0.590 & -0.977 \end{pmatrix}$$

Overlap of reflections from the different domains was modest and only data from the more intense domain was used for refinement.

6.3.3 Ethylamine

A crystal of ethylamine grown at 180 K underwent a phase transition upon cooling to 150 K, becoming polycrystalline. Single crystal diffraction data collected at 180 K were used to determine the structure of the high-temperature phase as described above; that of the low-temperature phase was investigated using powder methods.

A sample of ethylamine in a glass capillary was mounted onto a Bruker D8 Advance powder diffractometer equipped with a Lynxeye position-sensitive detector and an Oxford Cryosystems low-temperature device. The radiation source was Ge-monochromated CuKα_1. The sample froze immediately to a polycrystalline powder on mounting at 180 K. Powder diffraction data were collected in 2 hour scans between 2θ = 5 – 65°. Successive patterns showed that a phase transition was occurring slowly, but even after 12 hours the pattern consisted of a mixture of phase 1 (which had been identified previously by single-crystal diffraction) and a new phase 2.

The temperature was cycled between 100 and 150 K, monitoring a characteristic phase 1 peak at 2θ = 16°. After three cycles this peak was no longer present. Data were then collected at 150 K in eight 2 hour scans; the patterns were summed to give a single data set for further analysis.

The first 2 hour pattern collected at 180 K could be modelled (Topas-Academic)[26] as pure phase 1 using the coordinates determined by single crystal diffraction. The instrument contribution to the line shape was modelled using fundamental parameters, with a pseudo-Voigt convolution to account for sample broadening. A nine-term Chebychev polynomial was used for the background. The coordinates were held fixed at the values obtained from the single crystal study. Amines form needle-like crystals, and preferred orientation was severe; it was modelled with a spherical harmonic expansion to *eighth* order. R_{wp} = 7.44%, S = 1.33. The final Rietveld fit is shown in Figure 6.2a.

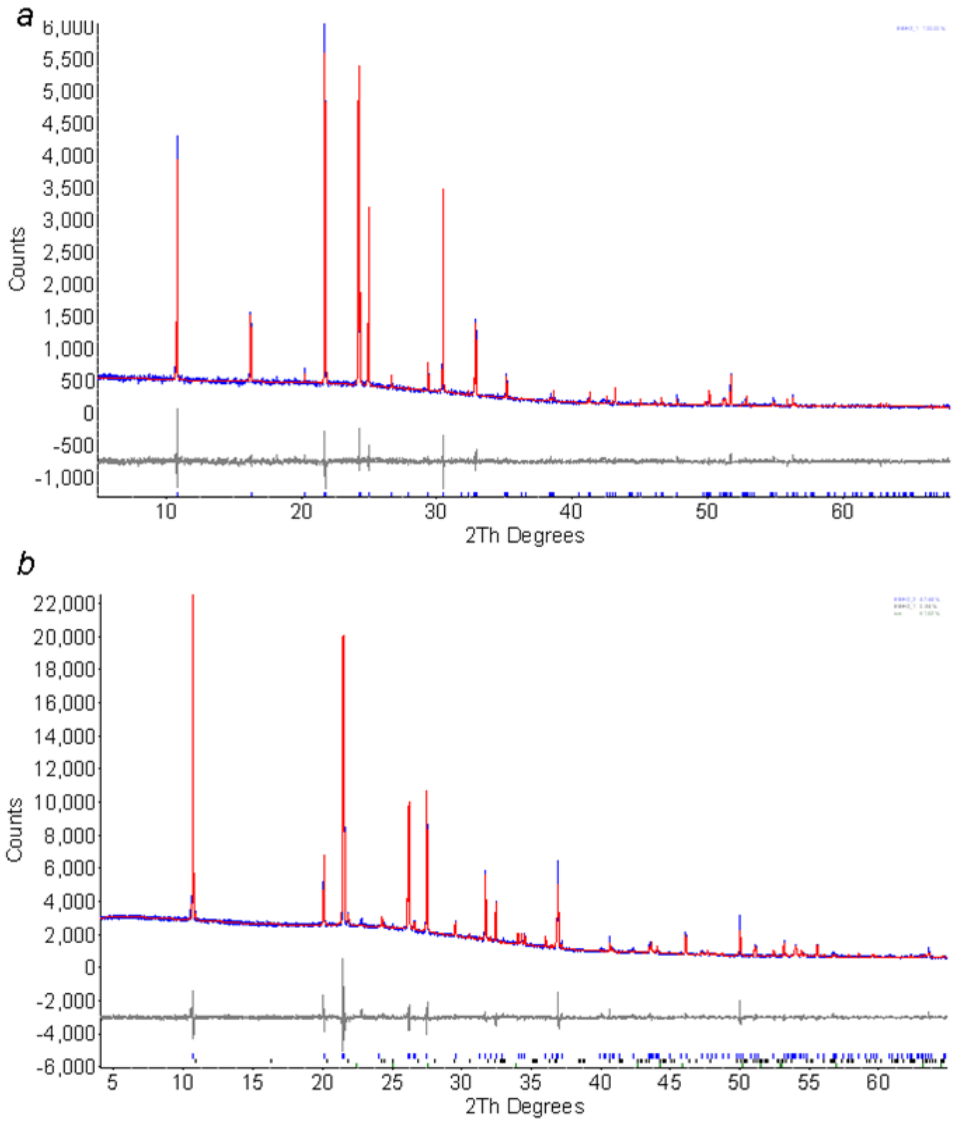

Figure 6.2: Final fits obtained after Rietveld refinement of ethylamine phase 1 at 180 K (a) and phase 2 at 150 K (b). The colour scheme is blue (observed), red (calculated) and grey (difference).

The powder pattern of phase 2 was indexed using DICVOL[27] as incorporated into DASH Version 3.2[28] on the basis of 16 reflections. The *M*(16) parameter for the indexing was 73.0. Attempts to solve the structure by simulated annealing in DASH were not successful, presumably because of the extreme preferred orientation present in the sample. Instead the structure was solved in Topas, treating the ethylamine molecule as a rigid body, but allowing spherical harmonic preferred orientation parameters to optimise as well. The structure was solved in a few minutes by this procedure. The positions of the NH_2 hydrogen atoms were confirmed by carrying out geometry optimisations using periodic DFT-D calculations (DMOL^3 code[29] as implemented in Materials Studio).[30] The PBE exchange correlation functional[31] was used with the DNP basis set,[32] a cut-off of 3.7 Å and a correction for dispersion as described by Grimme.[33] Integrations were carried out on a 2 x 3 x 2 **k**-point grid. The cell parameters were held fixed at values from a Pawley refinement. Three calculations were performed, starting from different values of the H-N-C-C torsion angle. An initial torsion angle of 60° yielded the lowest energy optimised structure, with an amino conformation which is similar those in the rest of the series. Optimisation starting from torsion angles of 180° and -60° gave structures which were 12.2 and 65.0 kJ mol^{-1} higher in energy, the latter because of unfavourable H…H intermolecular interactions. The model was refined, restraining the orientation and position of the molecule to the DMOL^3 values in the manner described in ref. 4. Internal geometry (i.e. the distances, angles and torsions) were constrained to values derived from the DFT-optimisations, allowing them to vary had negligible effect on the data fitting parameters. Also included in the model was a single peak to model ice (which had begun to accumulate on the sample tube) and a small amount of phase 1. R_{wp} = 4.943%, S = 2.085. The final Rietveld fit is shown in Figure 6.2b.

The total energy of phase 2 was found to be 2.9 kJ mol^{-1} lower than that of phase 1. The fact that it is lower inspires some confidence in the solution of this phase obtained from the powder diffraction study.

6.3.4 PIXEL Calculations

Electron densities were calculated using Gaussian09[34] at the MP2[35] level of theory with the 6-31G** basis set using molecular geometries derived from the crystal structures with NH and CH distances extended to 1.015 and 1.089 Å.[36] This "normalization" corrects approximately for the effects of asphericity of H-atom electron densities which lead to systematic shortening of distances involving hydrogen atoms when determined by X-ray diffraction. The PIXEL method, as implemented in the program suite OPiX,[37] was then used to calculate the intermolecular interaction energies. The principal intermolecular contact energies are listed in the Supplementary Information. The sublimation enthalpies of the primary monoamines have apparently not been determined, so the lattice energies obtained cannot be compared with experimental data.

6.3.5 Molecular Modeling

Optimization of model structures of propylamine, butylamine and pentylamine was carried out in Materials Studio. For example, the structure of propylamine was optimized starting from a model consisting of propylamine molecules occupying the molecular positions in the crystal structure of butylamine. To create this model, space group symmetry was removed from the crystal structure of butylamine to leave a single molecule. The terminal methyl group was changed into a hydrogen atom, and molecular geometry optimization was performed by DFT (DMOL^3). The PBE exchange correlation functional was used with the DNP basis set. The original space group symmetry and lattice translations of the butylamine crystal structure were then re-imposed to obtain a model of propylamine molecules on butylamine positions. The Forcite module of Materials Studio was then used to perform a geometry optimization, using the Conjugate Gradient algorithm with the COMPASS force-field[38] and Hirshfeld charges calculated in the DFT optimization. The same method was used to optimize the crystal structures of propyl-, butyl- and pentylamine from different starting geometries.

6.3.6 Void calculations

Void calculations were performed using OLEX2 v.1.2.2.[39] This program allows control of void searches through specification of the distance from the molecular surface

used to define the boundary of interstitial voids. Void analysis at a distance of 0.5 Å from the molecular surface yielded an overall view of void space in the structures. It was found to be possible to quantify void space in the Me…Me region only by carrying out the analysis using a distance of 0.7 Å, enabling differences in packing efficiency in this region of the structures to be quantified.

6.3.7 Other Programs Used

Crystal structures were visualized in MERCURY.[40] Searches of the Cambridge Structural Database utilized the program CONQUEST[41] with database updates up to November 2012. Geometric calculations were carried out using PLATON.[42] Hirshfeld surface analysis was accomplished with CrystalExplorer version 3.[43]

6.4 Results and Discussion

6.4.1 Melting Point and Density Alternation

The melting points and densities (calculated from crystal structures) of the primary amines are plotted in Figure 6.1. The melting points alternate, with the odd members of the series having a systematically lower melting point than their even neighbours. The densities also alternate in a way that matches the trend of the melting points.

6.4.2 Crystal Structures and Intermolecular Energy Calculations

Table 6.1 lists the unit cell parameters of the primary monoamines from ethylamine to decylamine. With the exception of ethylamine all structures are orthorhombic or, in the case of heptylamine and nonylamine, pseudo-orthorhombic. The unit cells have one dimension of ~5.7 Å and another of ~7.0 Å; the third axis is much longer. The identities of the short, medium and long axes vary according to the space group setting used. The alkyl chains are oriented along the long axis which generally increases in length with chain length, though from hexylamine to decylamine it should be noted that the length of the long axis alternates between even and odd numbered carbon chains. This is a result of the number of molecules in the unit cell varying from 4 for even numbered carbon chains to 8 for odd numbered chains. Propylamine, butylamine and pentylamine can be seen to pack in a different space group to the

longer-chain compounds. However, *Pca2₁* (in its *Pbc*2₁ setting) is related to *Pbcn* by removal of an inversion centre.

In the series of compounds investigated, N-C bond distances range from 1.451(4) Å to 1.465(1) Å and the C-C bond distances from 1.508(8) Å to 1.529(3) Å, while the N-C-C-C and C-C-C-C torsion angles along the chains lie between 176.5(18)° and 184.5(3)°. This shows that the C-N skeleton of all of the molecules is approximately planar. When viewed along the N-C bond, the orientation of the amino group is such that the two N-H bonds lie either side of the first C-C bond of the alkyl chain.

Figure 6.3 shows Hirshfeld fingerprint plots[44] which summarise similarities and differences in packing. The two spikes present for all compounds in the series are characteristic of hydrogen bonding interactions. The collection of points between the spikes in the propylamine and pentylamine plots distinguishes these from the other members of the series. The red area down the diagonal of the plots arises from the interactions between carbon chains. The higher incidence of red points on the plot for the even amines indicates that there are more short contacts present between the carbon chains and thus more efficient packing, consistent with the melting point and density alternation discussed in Section 6.4.1.

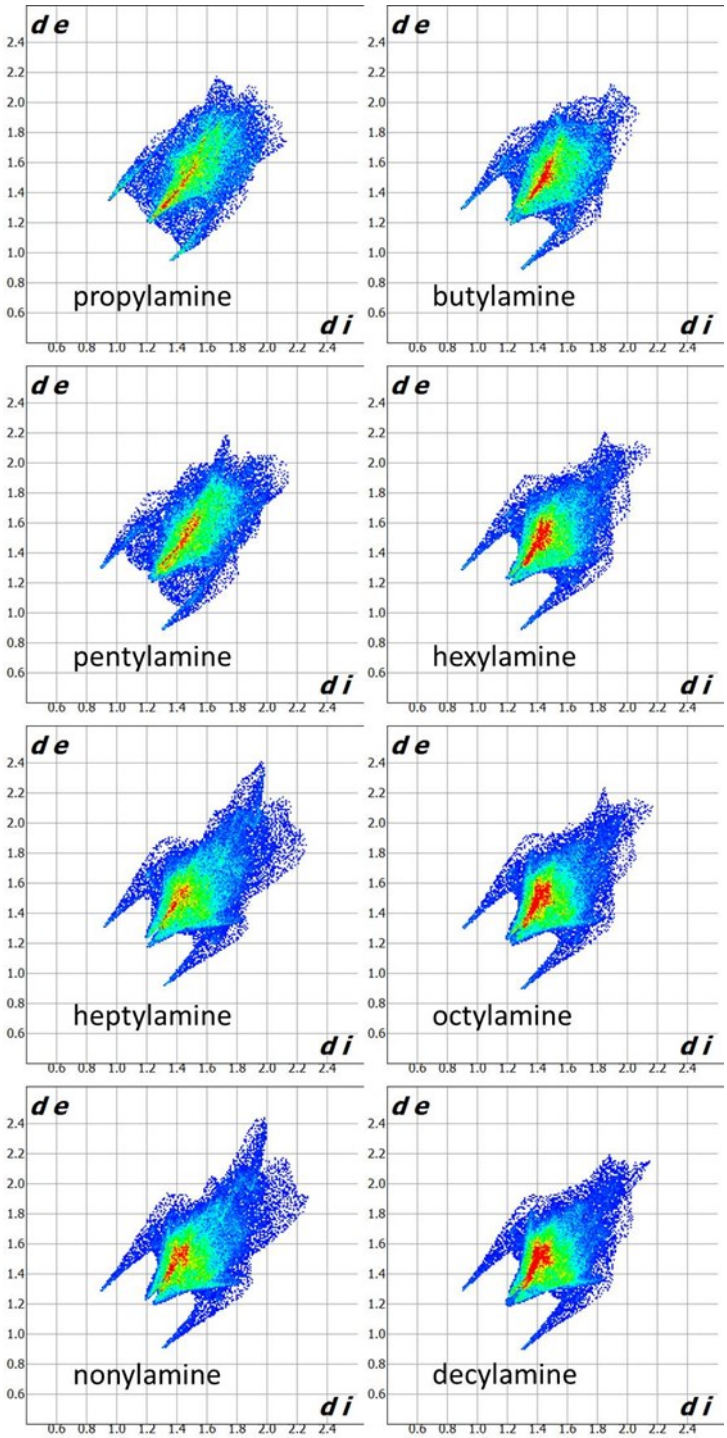

Figure 6.3: Hirshfeld fingerprint plots for the primary amines. *de* is the distance from the surface to the nearest nucleus outside the surface. *di* is the corresponding distance to the nearest nucleus inside the surface.

Lattice energies, calculated using the PIXEL method, alternate between odd and even members of the series in correlation with the melting points (Figure 6.4a). The constituent energy terms (Figure 6.4b) show that while the Coulombic and polarisation

interactions remain relatively constant, dispersion and repulsion energies vary significantly. The dispersion interaction increases with the length of the carbon chain but not monotonically: there is an alternation between odd and even membered carbon chains which reflects the alternation in packing efficiency discussed above.

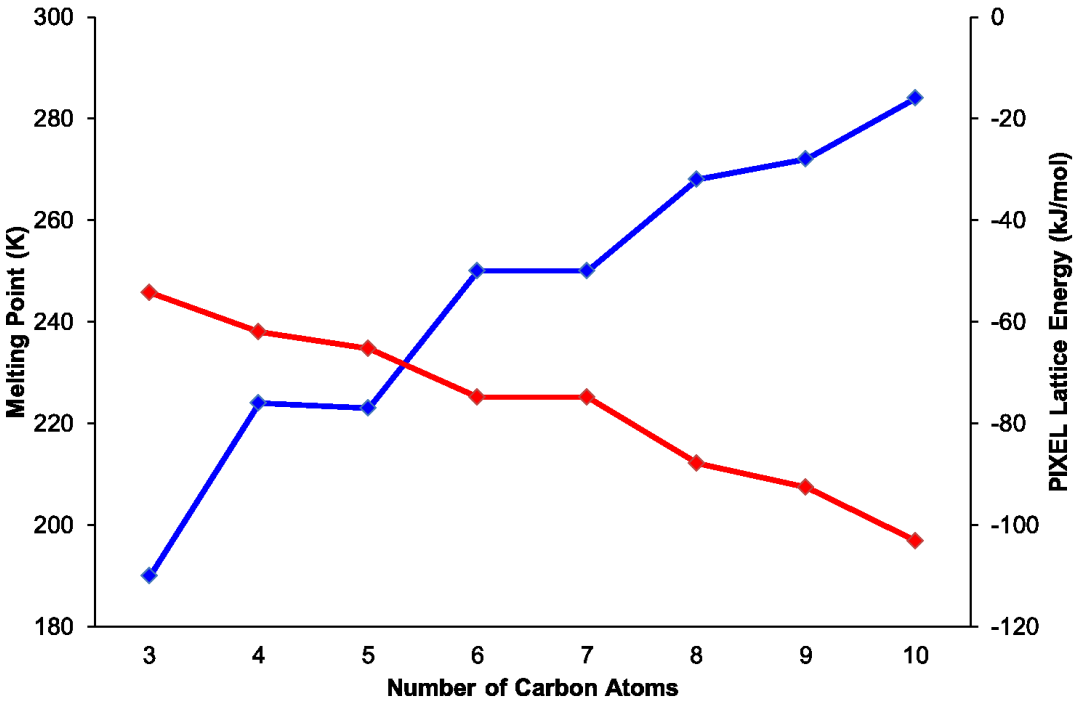

Figure 6.4a: The calculated lattice energies of the primary amines (red). Melting points (blue) are shown for reference.

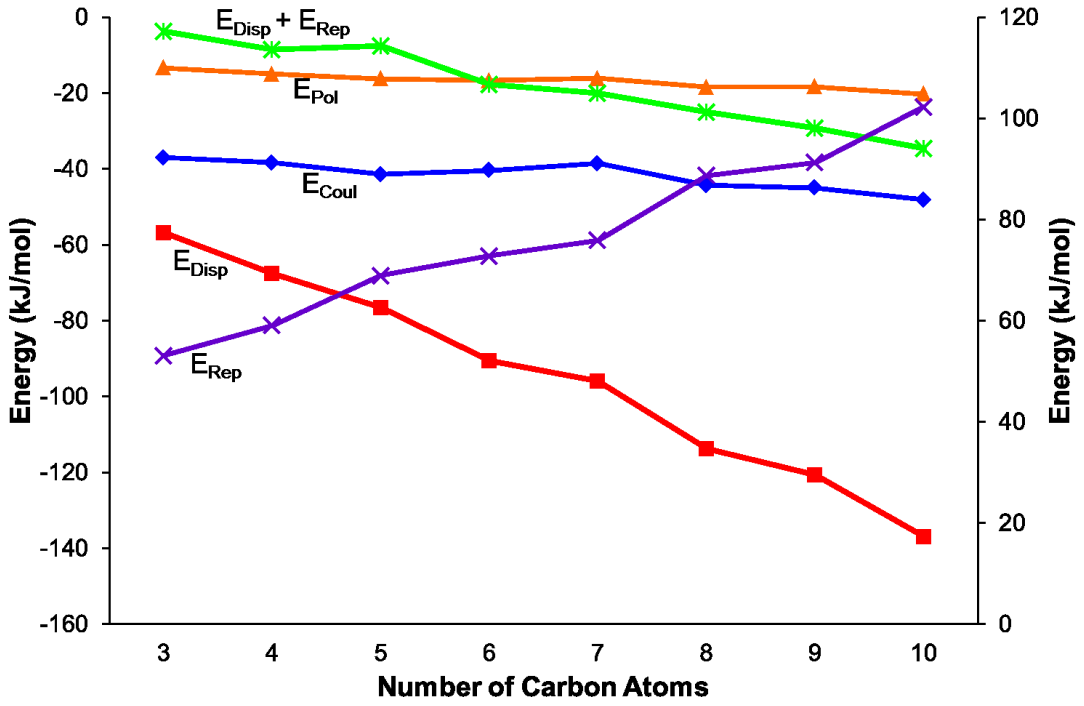

Figure 6.4b: The component Coulombic, dispersion, repulsion and polarisation energies. The right-hand vertical axis refers to the (positive) repulsion term only, all other terms are negative and are referred to the left axis.

The energy calculations identify the five principal intermolecular contacts as two hydrogen bonding and three dispersion interactions formed parallel to long axes of the molecules (see Supplementary Information section S.6.1). Figure 6.5 shows the sums of the energies of the hydrogen bonds and the dispersion interactions and the total energies of these contacts for each compound. For the early primary amines (propylamine to pentylamine) the hydrogen bonding interaction is dominant, while for the later compounds (hexylamine to decylamine) the dispersion interactions dominate.

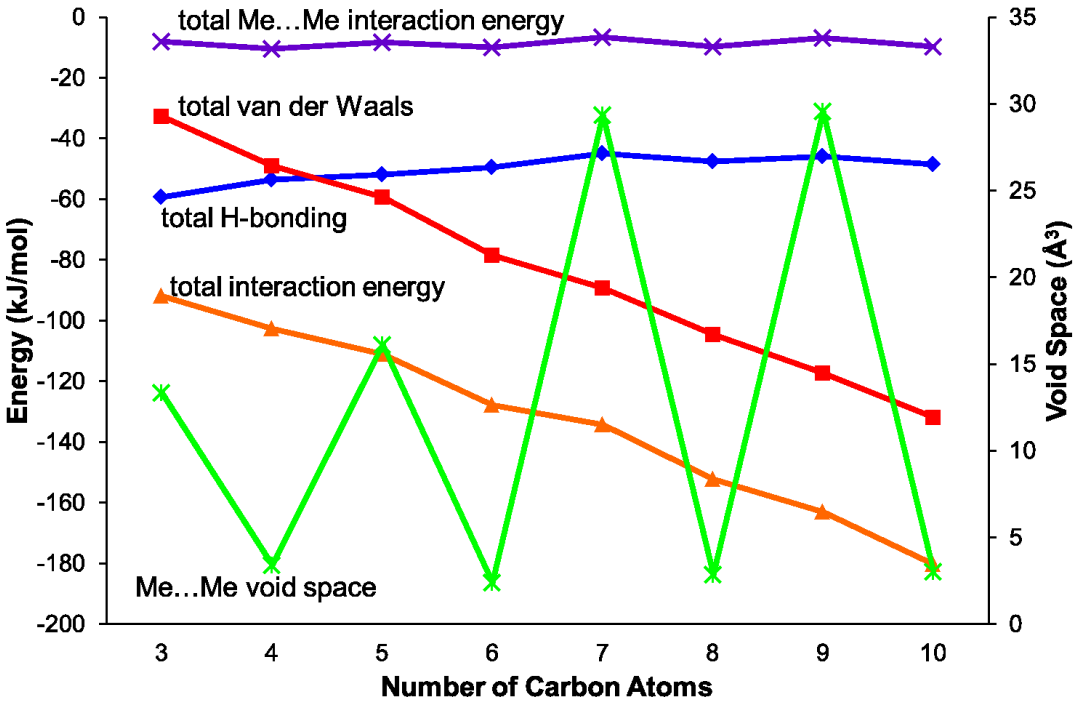

Figure 6.5: The principal interaction energies for the primary amines along with methyl-methyl void space. Interaction energies use the left-hand axis, Me…Me void space to the right-hand axis.

6.4.3 Hydrogen Bonds

Hydrogen bonding interactions are shown for butylamine in Figure 6.6, with the geometric parameters and energies for all members of the series listed in Table 6.2. In all cases a hydrogen bond is formed by each NH donor. For all of the even monoamines and the later odd compounds (heptylamine and nonylamine), one of these interactions is significantly shorter than the other, with differences in H…N distances between 0.53 and 0.67 Å. The PIXEL interaction energies (Table 6.2) reflect these geometric differences, with the longer interaction having about half to two-thirds of the energy of the shorter one. The H-bond distances and energies are more similar in propylamine and pentylamine (differences in length are 0.10 and 0.32 Å), recalling a distinction which had been evident in the fingerprint plots of Figure 6.3.

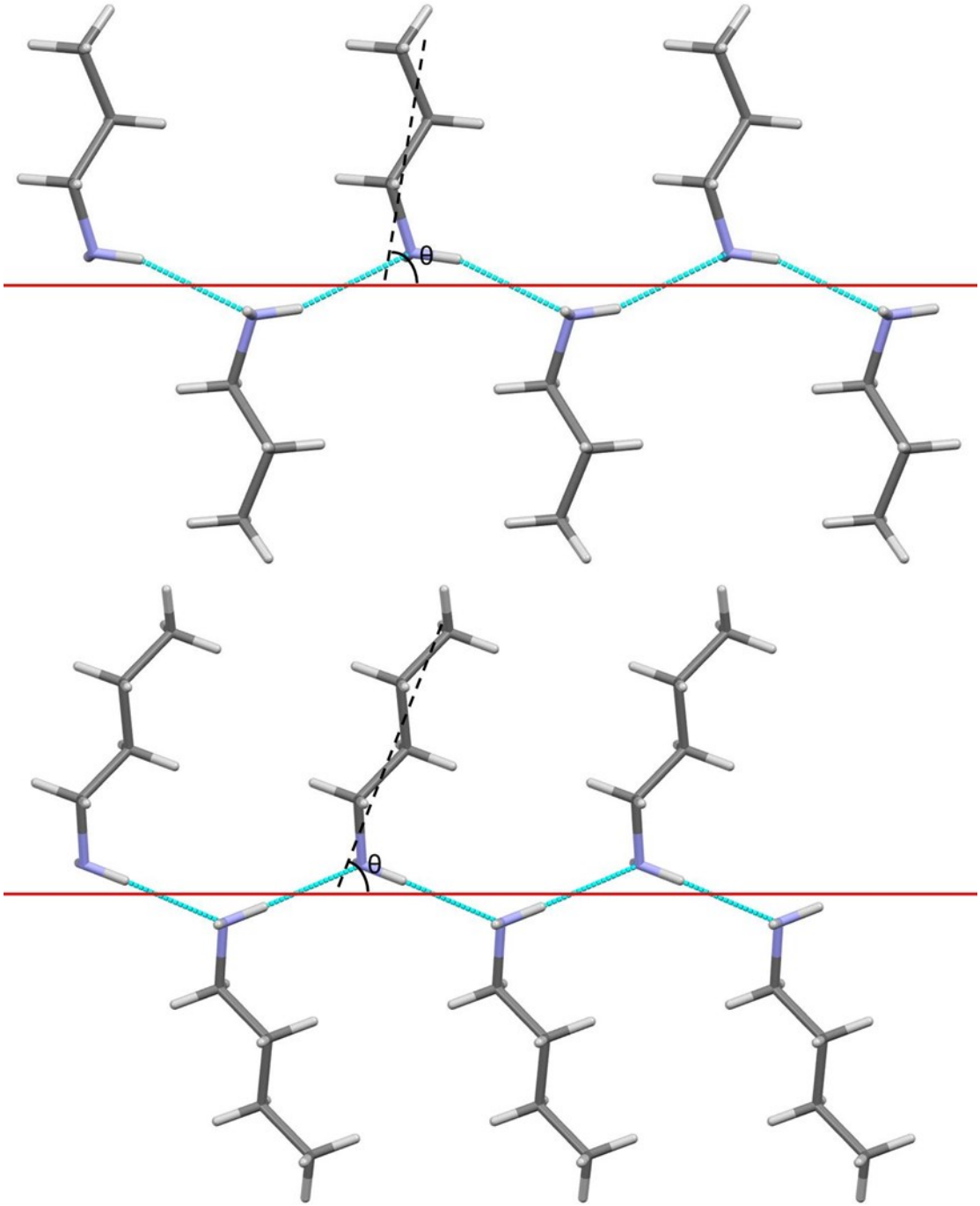

Figure 6.6a: Short hydrogen bonds form infinite chains, shown for propylamine (top) and butylamine (bottom). The differences in hydrogen bonding motifs can be quantified by the angle, θ, between the average position of the molecular chain (dashed black line) and the direction of the hydrogen bonding chain (solid red line).

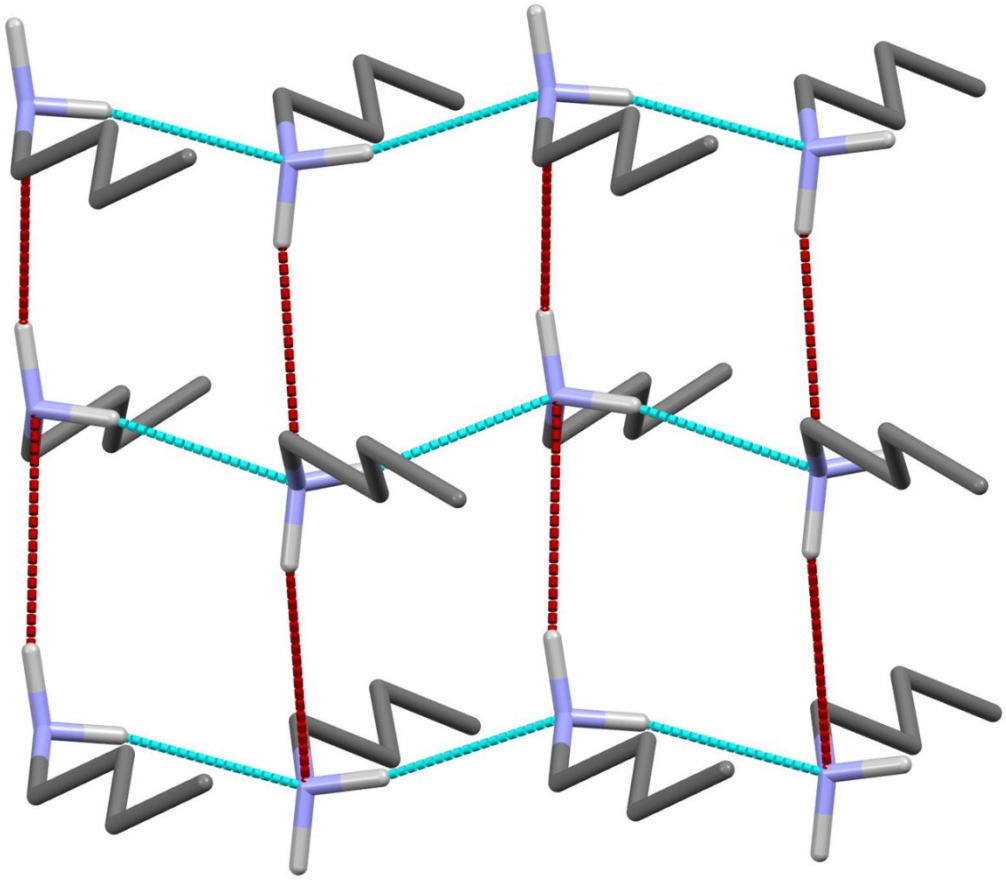

Figure 6.6b: Chains of butylamine molecules built by short hydrogen bonds (blue contacts) interact by a longer hydrogen bond interaction (red contacts) to form layers of molecules. Hydrogen atoms on the carbon skeletons are omitted for clarity.

Compound	N-H…N Distance (Å)	N…N Distance (Å)	N-H…N Angle (Deg)	Energy ($kJmol^{-1}$)
Propylamine	2.42(1)	3.259(2)	162(1)	-16.3
	2.52(1)	3.334(2)	157(1)	-13.2
Butylamine	2.30(1)	3.173(1)	169(1)	-17.1
	2.83(1)	3.608(1)	150(1)	-9.5
Pentylamine	2.34(2)	3.182(3)	173(2)	-15.6
	2.66(2)	3.464(4)	157(2)	-10.3
Hexylamine	2.30(2)	3.162(4)	166(2)	-16.4
	2.93(1)	3.702(2)	150(2)	-8.2
Heptylamine	2.35(3)	3.164(8)	158(5)	-13.7
	2.94(3)	3.730(7)	154(5)	-8.8
Octylamine	2.303(19)	3.159(4)	164(2)	-15.7
	2.96(2)	3.738(3)	152(2)	-8.1
Nonylamine	2.31(2)	3.153(4)	164(2)	-15.9
	2.98(2)	3.764(4)	150(2)	-7.7
Decylamine	2.317(18)	3.158(4)	165(2)	-16.7
	2.99(2)	3.756(3)	151(2)	-7.5

Table 6.2: The hydrogen bonding parameters of the primary mono-amines

The shorter hydrogen bonding interactions build *C*(2) chains[45] of molecules that run along the ~5.7 Å axis (Figure 6.6a and b, blue contacts). The chains interact with each other through the longer H-bonds, which also form *C*(2) chains along the ~7.0 Å axis (Figure 6.6b, red contacts). The combination of the two chains gives rise to layers. In the cases of propylamine and pentylamine, short NH…HN contacts (2.53 – 2.56 Å) are present between hydrogen atoms along the longer C(2) chain; it is these contacts that are responsible for the diffuse region between the hydrogen bond spikes that is observed in the fingerprint plots for these molecules. Similar features are seen in the fingerprint plots of carboxylic acid $R_2^2(8)$ dimers.[46]

6.4.4 Interactions between carbon chains and their influence on H-bonding

The formation of long and short hydrogen bonds arises as the result of differences in the orientations of the molecules with respect to the direction of the hydrogen bonded chains. The solid red lines in Figure 6.6a show the direction of the chains while the black dashed lines show the long molecular axis. The angles between these two lines (θ) are listed in Table 6.3.

No. Carbon Atoms	Average θ	Void Volume as % of Unit Cell
3	87.366(232)	7.48
4	69.925(359)	4.51
5	85.697(235)	7.16
6	65.105(223)	3.83
7	65.162(125)	6.44
8	64.413(180)	3.45
9	64.436(27)	5.63
10	63.849(291)	3.28

Table 6.3: Average values of θ, the angle between the hydrogen bonding chain and the long molecular axis, and the void volume as percentage of unit cell (calculated at a resolution of 0.1 Å at 0.5 Å from the molecular surface) for the primary monoamines.

The values of θ for propylamine and pentylamine are much closer to 90° (hereafter referred to as the 'perpendicular' motif) than those for the even numbered and longer chain odd numbered amines, which lie in the range 63 - 70° (the 'oblique' motif). As the molecules tilt (decreasing the value of θ), the hydrogen bonds along the first *C*(2) chain become shorter and the N-H…N angle becomes more linear, while those along the other *C*(2) chain become longer with a decreased N-H…N angle. The H-bond

energies in Table 6.2 follow the same parabolic trend with N-H…N angle as shown in Figure 6 of Ref. 47, which means that while the energies of the shorter, more linear H-bonds (Table 6.2) remain fairly constant at ~16 kJ mol^{-1} the energy of the longer H-bond diminishes rapidly as it becomes less linear. Overall, the perpendicular motif of propyl- and pentyl- amines results in a stronger hydrogen bonding network than is generated in the other amines by the oblique motif.

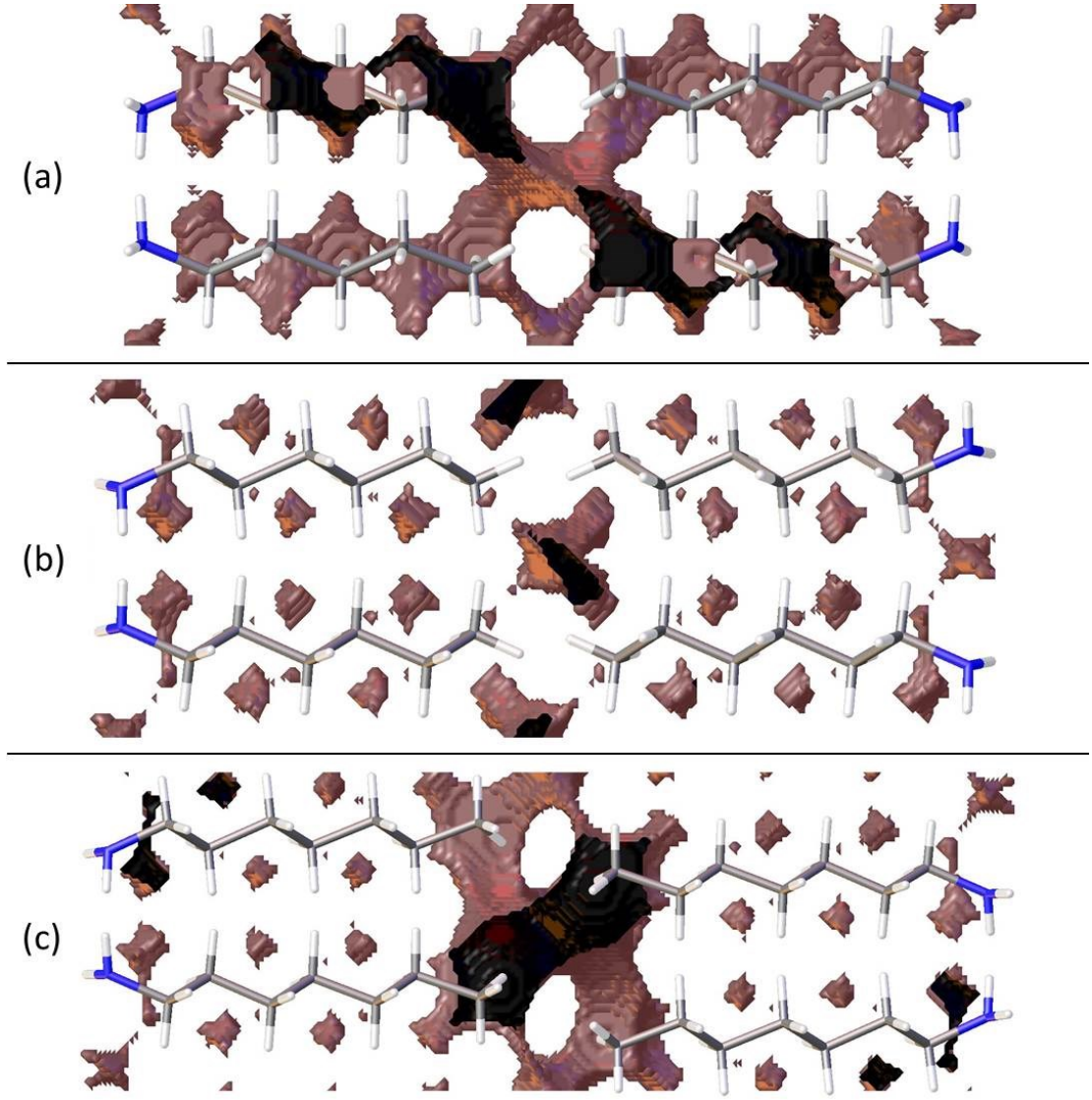

Figure 6.7: Void analysis at a distance of 0.5 Å from the molecular surface for (a) pentylamine, (b) hexylamine and (c) heptylamine. Differences in hydrogen bonding motif lead to bigger gaps between carbon chains.

Though the perpendicular chain-packing motif facilitates H-bond formation in propyl and pentyl amine, the finger-print analysis of Figure 6.3 shows that chain-packing is less efficient in these structures than in the even and later odd members of the

amine series. Calculation of the void spaces (Figure 6.7) and volumes (Table 6.3) demonstrates that more efficient interleaving of CH_2 groups in neighbouring chains is promoted by the oblique motif. The interleaving is less effective in propylamine and pentylamine, which have larger voids between the carbon chains (cf Figures 6.7 a and b), but stronger hydrogen bonds.

These geometric considerations, along with the energetic analysis depicted in Figure 6.5, suggests that in the longer chain (C_6 and above) compounds hydrogen bonding (promoted by the perpendicular motif) is "sacrificed" in the interests of stronger dispersion inter-chain interactions (promoted by the oblique motif). Butylamine appears to be a kind of "transition" structure, its relatively short carbon chain packing in the oblique motif; this point is discussed further below.

6.4.5 Methyl-Methyl Interactions

Contacts between terminal methyl groups have a decisive effect on the crystal structures of the alkanes and carboxylic acids.[13, 17] Even-membered alkanes pack in such a way as to allow equally short methyl-methyl interactions at both ends of the carbon chain. For odd alkanes, the methyl-methyl interaction at one end of the carbon chain is longer than those that are observed for the even molecules, resulting in a lower density and weakening of all three classes of intermolecular interaction. While the even amines have an odd number of atoms in the chain, differences in the packing of the methyl groups between odd and even members of the series similar to those in the alkanes are observed.

In the amines the layers of molecules built-up by the hydrogen bonding motifs stack along the long unit cell axes, and the layers interact with each other by methyl-methyl contacts (Figures 6.7 – 6.9). PIXEL calculations indicate that Me…Me interaction energies are in the range 1.7 to 4.1 kJ mol^{-1}, and though these are individually weak, their combined energies range from 6.5 to 10.5 kJ mol^{-1} (Table 6.4), *i.e.* rather similar values to the weaker H-bonds. A "Crystal Packing Feature" search in Mercury* focussing on methyl-methyl interactions shows that in the series from hexyl- to decyl-amine the even and odd structures fall into two separate classes (Table 6.5).

*This is not a common use of this search type, and instructions for performing the search are provided in the Supplementary Information, section S.6.2.

The structures of propyl- and pentylamine form a third class, with butylamine in a class on its own, consistent with its status as a 'transition' structure (see above).

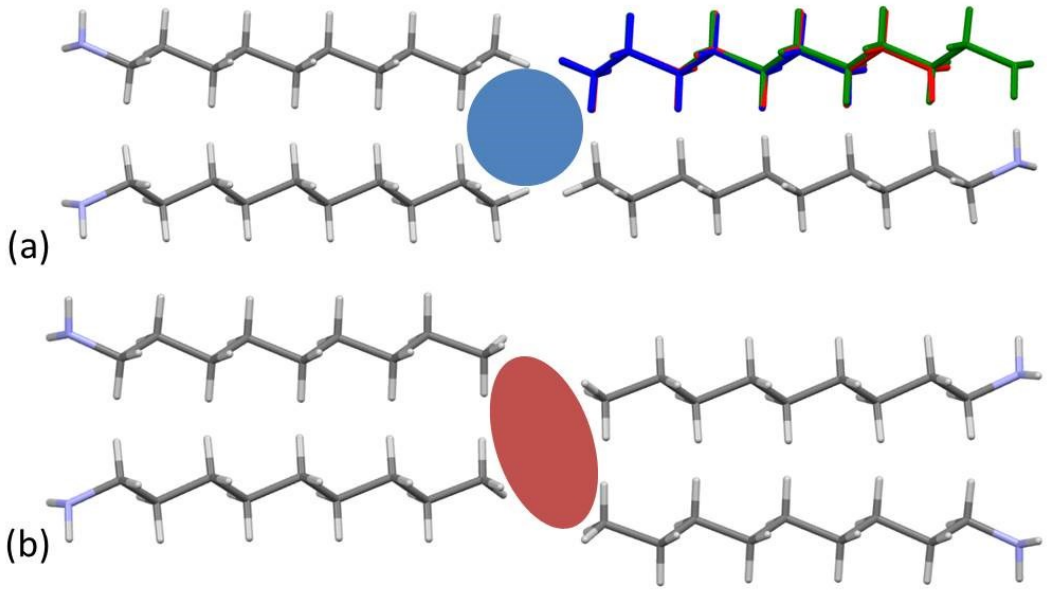

Figure 6.8: The methyl-methyl interactions for (a) even monoamines and (b) odd monoamines. Additionally, Figure 6.8a shows the overlay of hexyl- (blue), octyl- (red) and decylamine (green). The coloured shapes indicate the differences between chain ends for odd and even molecules.

Compound	Total Methyl-Methyl Interaction Energy ($kJmol^{-1}$)	Methyl-Methyl Void Space ($Å^3$)
Propylamine	-8.1	13.349
Butylamine	-10.3	3.393
Pentylamine	-8.2	16.124
Hexylamine	-9.6	2.411
Heptylamine	-6.5	29.371
Octylamine	-10.0	2.866
Nonylamine	-6.8	29.573
Decylamine	-9.8	3.011

Table 6.4: Energetic analysis of the methyl-methyl interaction energies.

Compound	RMS Packing Agreement (c.f. hexylamine)	RMS Packing Agreement (c.f. heptylamine)
Hexylamine	N/A	No Match
Heptylamine	No Match	N/A
Octylamine	0.07	No Match
Nonylamine	No Match	0.065
Decylamine	0.097	No Match

Table 6.5: Results of the Crystal Packing Feature analysis of methyl-methyl interactions. The molecules are compared to a cluster of hexylamine or heptylamine molecules.

In the odd monoamines, the methyl group is on the opposite side of the long molecular axis to the amine group, whereas in even monoamines they are on the same side. Figure 6.8 shows that this leads to a less efficient juxtaposition of opposing methyl groups for the odd amines. There is therefore a pronounced alternation in void volume along the series which correlates with the interaction energies (Figure 6.5, Table 6.4). This result is strongly reminiscent of the packing effects described using a topological model by Boese in the alkanes.

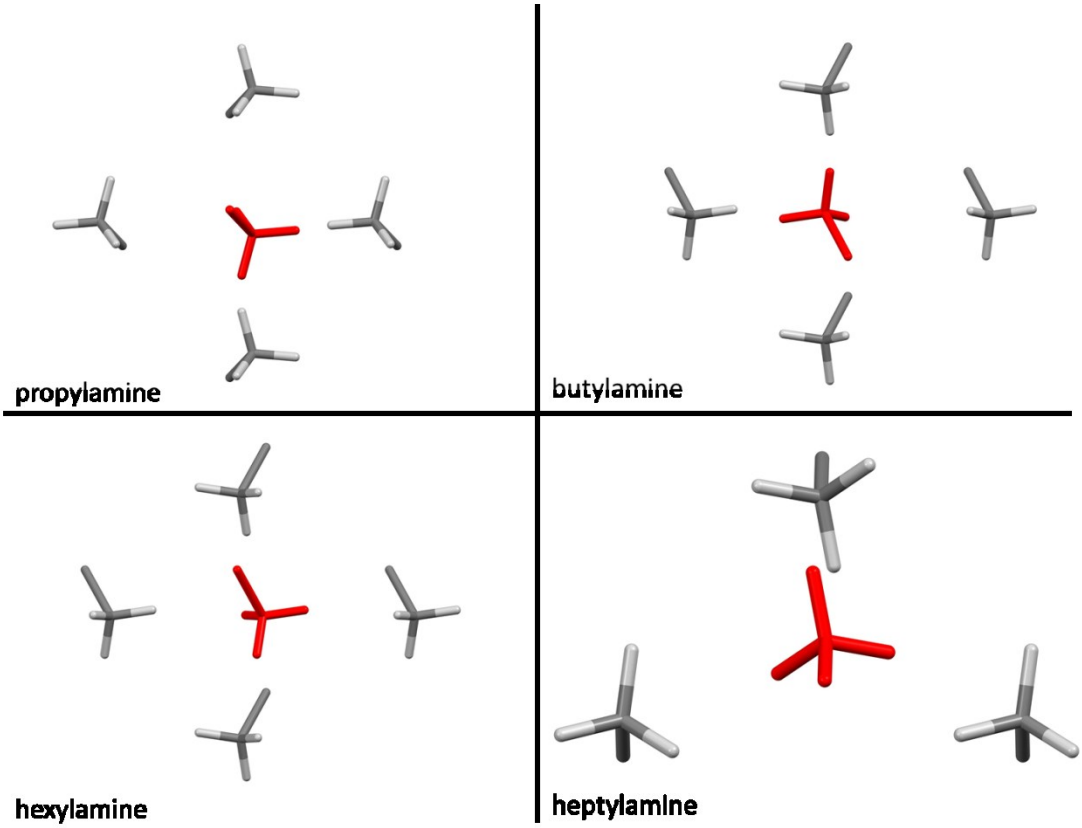

Figure 6.9: Inter-layer methyl-methyl interactions viewed along the long unit cell axis. Only methyl groups and their neighbouring carbon atoms are shown for clarity. The red molecule in each case sits in the upper layer.

Four Me…Me interactions are formed in hexyl-, octyl- and decyl- amines, but only three in heptyl- and nonyl- amines, reflecting the identification of different classes for these compounds in the Mercury Packing Feature analysis (Figure 6.9). The perpendicular motif of propyl- and pentyl- amines leads to formation of four Me…Me contacts, distinguishing them from the longer-chain odd homologues. The result is that heptyl- and nonyl- amines have markedly higher void volumes and lower energies than

in propyl- and pentyl- amines. As in the longer chain even amines, butylamine forms four Me…Me interactions, but the relatively high value of θ changes the relative orientations of the methyl groups. The total Me…Me energy for buytlamine is the highest in the series at 10.5 kJ mol^{-1}.

Overall, the methyl…methyl interactions are more efficient for the even members of the series and short chain amines than for the longer chain odd compounds. This trend in the odd compounds reflects the one seen for the H-bonds: as the chains become longer the end-of-chain interactions are forced to adopt less than optimal geometries in order to accommodate the energetically dominant dispersion interactions formed between chains.

6.4.6 Butylamine as a transition structure

It was noted in Sections 6.4.4 and 6.4.5 that the structure of butylamine appeared to be anomalous in adopting an oblique motif, and in Section 6.4.5 that its methyl groups interact in a motif that is different to the other even amines. It has $\theta \approx 70°$, higher than the other oblique structures. Additionally, it exhibits the strongest individual hydrogen bonding interaction (-17.3 kJ mol^{-1}) which occurs at an N-H…N angle of 169(1)°, a more linear angle that any observed for the other even amines, and a strong total methyl-methyl interaction energy (-10.5 kJ mol^{-1}). Butylamine can therefore be considered as a transition structure between the oblique and perpendicular motifs, where the lower dispersion interactions that result from its relatively short chain are compensated for by optimisation of the interactions that occur at the chain ends.

Molecular modelling was used to explore the behaviour of the short-chained primary amines further by optimising model structures consisting of molecules of one amine placed on the sites occupied in a different amine structure. The results are shown in Table 6.6. In the case of propylamine, regardless of whether the starting structure adopted the oblique or perpendicular motif, the optimisation always yielded the perpendicular structure seen experimentally. This is consistent with the data shown in Figure 6.5: propylamine is dominated by hydrogen bonding, and this favours the perpendicular motif. For butyl- and pentylamine, the optimised structure depends on the starting model: perpendicular and oblique motifs are both preserved on optimisation. This also seems to agree with the energies shown in Figure 6.5 for these compounds;

the dispersion and hydrogen bonding interactions are nearly balanced. An inspection of the energies calculated from the optimisations shows that in each case the different forms only differ by around 2 kJ mol^{-1}, though the lower energy form in each case is that which is observed experimentally.

Compound	Unit Cell/Molecular Positions Used	Input θ (°)	Output θ (°)	Energy ($kJmol^{-1}$)
Propylamine	Propylamine	87.366	81.31	-31.29
	Butylamine	69.925	81.318	-31.30
Butylamine	Butylamine	69.925	61.337	-40.92
	Pentylamine	85.697	86.517	-39.80
Pentylamine	Pentylamine	85.697	85.193	-47.03
	Hexylamine*	65.105	64.09	-44.95

Table 6.6: Results of the molecular modelling optimisations. * Indicates that a modified version of the hexylamine cell was used to ensure 8 molecules in the unit cell.

6.4.7 Ethylamine

While all of the other primary amines investigated showed no differences (other than a small amount of thermal contraction) in structure between the temperature of crystal growth and 150 K, ethylamine undergoes a phase transition (Figure 6.10).

In phase 1 the strongest intermolecular interaction is formed through H-bonding interactions N1H12…N1 in which the N…H distance is 2.387(11) Å and the angle <NH…N is 166.8(11)°. These H-bonds propagate along **c** to build chains (Figure 6.10a). A chain motif occurs along **b** in phase 2 with the N1H12…N1 distance measuring 2.356(11) Å and <NH…N = 169.2(11)°, though the orientations of the molecules with respect to the chain direction are different in the two phases (Figure 6.10b). While the primary H-bonds in phase 1 are slightly shorter and less linear than in phase 2, energetic analysis indicates that they are stronger; −18.4 kJ mol^{-1} in phase 1 and −17.0 kJ mol^{-1} in phase 2. These calculations are based on molecule-molecule energies however, and in phase 1 this interaction is enhanced by a favourable interaction between the carbon chain of one molecule and the NH_2 group of the other.

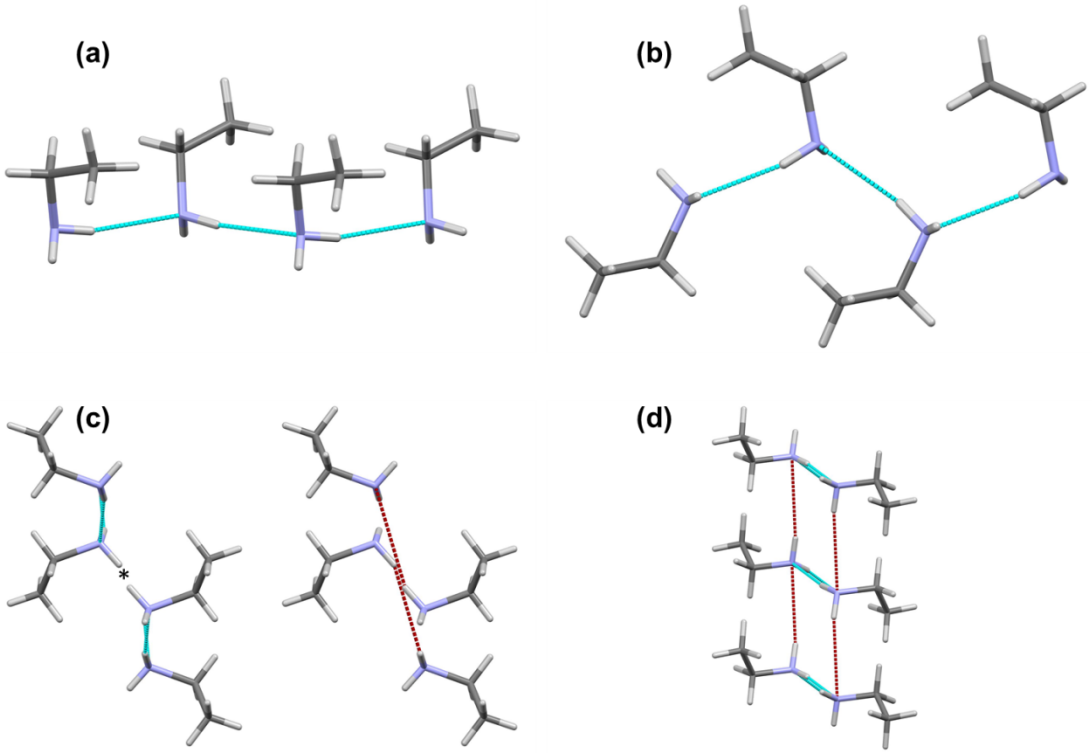

Figure 6.10: The two phases of ethylamine: (a) the H-bonded chain in phase 1; (b) the H-bond chain in phase 2; (c) interacting chains in phase 1 viewed along the **c** axis; (d) interacting chains in phase 2 viewed along the **b** axis. Short hydrogen bonds are shown in blue and long hydrogen bonds are shown in red. The * indicates the position of the NH…HN dipole-dipole interaction.

In phase 2 the interactions between chains take the form of N1H11…N1 H-bonds with H…N = 2.868(10) Å, <NH…N = 167.0(9)° and energy −11.4 kJ mol^{-1}. The distance is similar to the longer contact seen in the other even-membered amines, but the angle is more linear and it is therefore somewhat stronger (cf Table 6.2).

While N1H11…N1 H-bonding interactions are formed in phase 1, they are long (NH…N = 3.167(12) Å, <NH…N = 154.1(10)°) and less than half the strength (−8.3 kJ mol^{-1}) of the primary H-bond described above. Also formed are side-on dipole-dipole interactions between pairs of N-H bonds opposed across inversion centres, in which the N…H distance is 2.971(11) Å, and the interaction energy −12.7 kJ mol^{-1}. A similar contact is formed in phase 2, but it is much longer (3.679(10) Å) and weaker (−5.3 kJ mol^{-1}). The two interactions are compared in Figure 6.11 which shows the Hirshfeld surfaces coloured according to electrostatic potential.

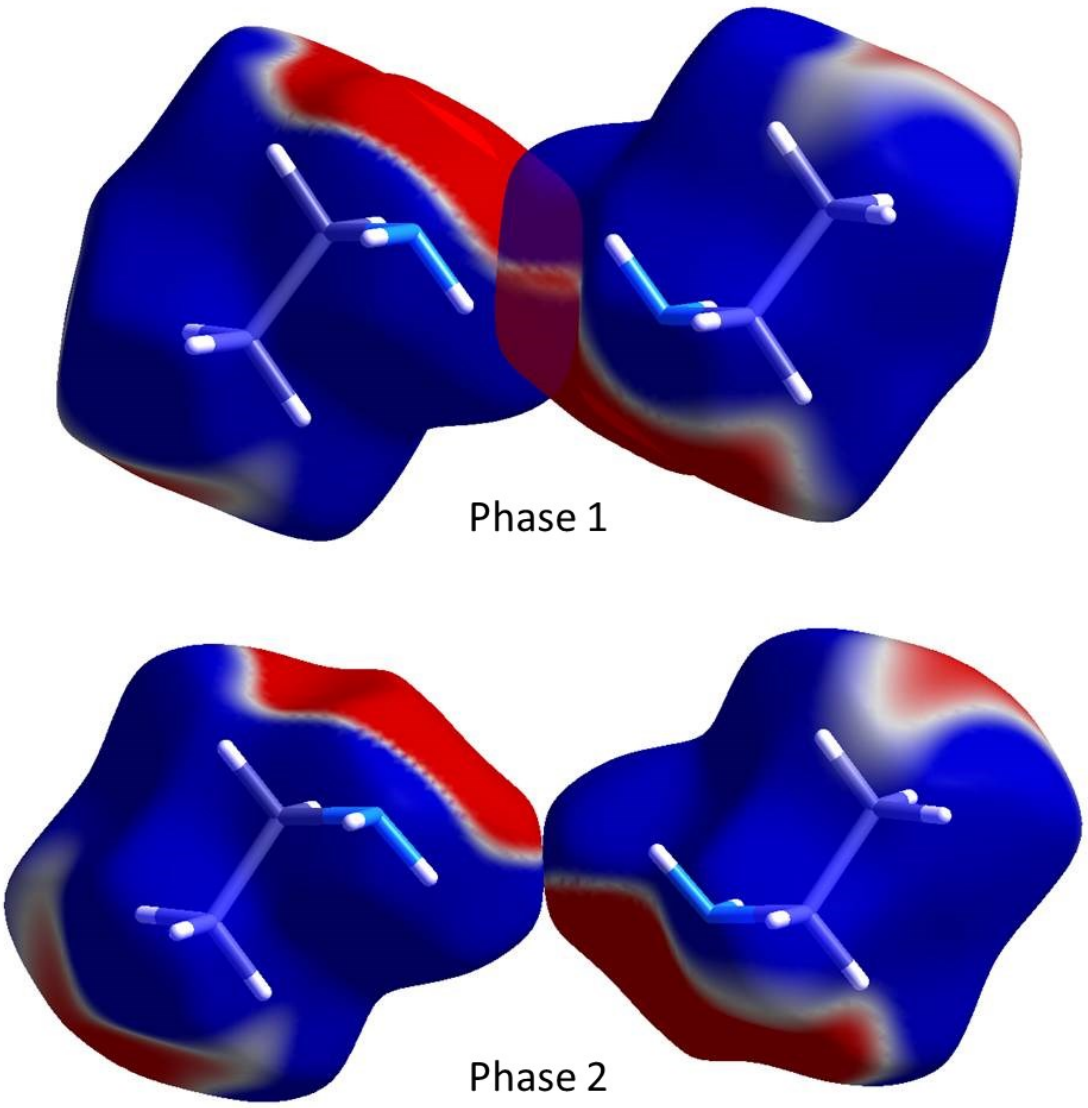

Figure 6.11: The dipole-dipole interaction in ethylamine shown using the electrostatic potential (ESP) mapped onto Hirshfeld surfaces. *Ab initio* wavefunctions were obtained at the Hartree-Fock level with a MIDI! basis set.[48] The ESP is mapped from -0.005 au (red) to 0.005 au (blue).

While the phase change results in a significant reduction of energy of the dipole-dipole interaction, phase 2 of ethylamine has a higher density (0.935 versus 0.908 g cm^{-3}) and has stronger dispersion interactions than phase 1 (11 interactions with a dispersion term > 5 kJ mol^{-1} for phase 2 compared to 9 for phase 1).

Overall, PIXEL analysis indicates that the lattice energy of phase 2 (−51.0 kJ mol^{-1}) is 1.6 kJ mol^{-1} more negative than that of phase 1 (−49.4 kJ mol^{-1}), a result in reasonable agreement with the DFT optimisations above (2.9 kJ mol^{-1}). The difference in H-bonding contributes 1.7 kJ mol^{-1} in favour of phase 2, and rearrangement into a

more efficient H-bonding network is an important component of the driving force of the transition, though the energetics of other contacts are also affected.

6.5 Conclusions

Though H-bonding is frequently identified as a structure-directing interaction, the role of other interactions can often be missed because they lack the characteristic interatomic features of hydrogen bonds, and they are therefore less easy to identify on the basis of geometric features alone. However, if a crystal structure is interpreted in the light of packing-energy calculations it becomes straight-forward to identify all intermolecular interactions and to rank them in the order of their importance. Tools such as Hirshfeld surface analysis and multivariate analysis enable similar structures to be grouped into classes; the transition from one class to another can also be interpreted in the light of the energy calculations. The aim of this work is to illustrate this approach to packing analysis by determining the change in the hierarchy of intermolecular interactions which occurs along a homologous series of compounds exhibiting relatively weak H-bonding. The series chosen was the primary amines from ethylamine to decylamine, the structures of which have been determined for the first time.

The crystal structures of the primary amines consist of layers in which molecules interact though NH…N H-bonding and dispersion interactions between alkyl chains. The layers stack with dispersion interactions between methyl groups in opposing layers. In the early members of the series H-bonding is the strongest intermolecular interaction, and both amine H-atoms act as donors in H-bonds with energies of ~10 kJ mol^{-1} or higher. As the alkyl chains become longer the dispersion interactions between the chains become more stabilising than the H-bonds. The interactions are balanced for butylamine and pentylamine, but dispersion becomes dominant at hexylamine and beyond. In these later structures, while the energy of one NH…N H-bond is similar to those in the short-chain compounds, the energy of the other drops to ~8 kJ mol^{-1} or lower. At the same time packing of the chains becomes more efficient, with less free space between the chains promoted by a change in orientation of the molecules relative to the direction of chains formed by NH…N H-bonds.

The competition between optimisation of the packing at the ends of the alkyl chains versus packing along the lengths of the chains is also seen in the interlayer

methyl-methyl interactions of the odd membered amines. Methyl-methyl interactions are consistently weaker for the odd members of the series because of the different positions of the terminal methyl and amine groups relative to the chain axis. The change in the molecular orientation that occurs between pentyl- and heptyl-amine, which improves dispersion contacts between chains, changes the number of methyl-methyl interactions from four to three at the layer interface, resulting in a drop in the total interaction energy of about 25%. By contrast the layer stacking in the even amines is fairly consistent along the series.

The principal classes of intermolecular interaction in the primary amines are thus NH…N H-bonding and the interchain and interlayer dispersion interactions. There is an alternation in the energy of all three between odd and even members of the series. As described above, and just as in the alkanes, the interlayer packing of methyl groups is less efficient for the odd-membered amines. The energy calculations show that the effect propagates to the H-bonds and the interchain dispersion contacts, and the combined effect is the source of the alternation of melting points along the series.

In addition to revealing the subtle energy balances which exist in crystal structures, the use of energy calculations also suggests which structures in the series may be susceptible to phase modification. Molecular mechanics simulations support the conclusion based on geometrical and energy analysis that butylamine is something of a transition structure between the regimes dominated by H-bonding and dispersion interactions. It may be therefore possible to modify its packing, for example by applying pressure. Similarly the large interlayer void spaces in heptyl- and nonyl-amines will be strongly disfavoured at high pressure, so that these too may be modified under extreme conditions. Finally, in the presence of stronger hydrogen bonds the transition between H-bonded and dispersion dominated regimes is likely to occur at longer chain lengths than in the amines, and this presents an interesting future study of the simple alcohols.

6.6 References

1. J. D. Dunitz and A. Gavezzotti, *Crystal Growth & Design*, 2012, **12**, 5873-5877.
2. A. Gavezzotti, *CrystEngComm*, 2013, **15**, 4027-4035.
3. R. D. L. Johnstone, D. Francis, A. R. Lennie, W. G. Marshall, S. A. Moggach, S. Parsons, E. Pidcock and J. E. Warren, *CrystEngComm*, 2008, **10**, 1758-1769.
4. N. P. Funnell, A. Dawson, W. G. Marshall and S. Parsons, *CrystEngComm*, 2013, **15**, 1047-1060.
5. A. Gavezzotti, *Journal of Physical Chemistry B*, 2002, **106**, 4145-4154.
6. A. Gavezzotti, *Journal of Physical Chemistry B*, 2003, **107**, 2344-2353.
7. A. Gavezzotti, *Zeitschrift Fur Kristallographie*, 2005, **220**, 499-510.
8. A. Gavezzotti, *Journal of Chemical Theory and Computation*, 2005, **1**, 834-840.
9. A. Gavezzotti, *Molecular Aggregation - Structure Analysis and Molecular Simulation of Crystals and Liquids*, 1st edn., Oxford University Press, New York, 2007.
10. J. D. Dunitz and A. Gavezzotti, *Angewandte Chemie - International Edition*, 2005, **44**, 1766-1787.
11. L. Maschio, B. Civalleri, P. Ugliengo and A. Gavezzotti, *Journal of Physical Chemistry A*, 2011, **115**, 11179-11186.
12. W. B. Schweizer and J. D. Dunitz, *Journal of Chemical Theory and Computation*, 2006, **2**, 288-291.
13. R. Boese, H. C. Weiss and D. Blaser, *Angewandte Chemie - International Edition*, 1999, **38**, 988-992.
14. V. R. Thalladi, R. Boese and H. C. Weiss, *Angewandte Chemie - International Edition*, 2000, **39**, 918-922.
15. V. R. Thalladi, R. Boese and H. C. Weiss, *Journal of the American Chemical Society*, 2000, **122**, 1186-1190.
16. V. R. Thalladi, M. Nusse and R. Boese, *Journal of the American Chemical Society*, 2000, **122**, 9227-9236.
17. A. D. Bond, *New Journal of Chemistry*, 2004, **28**, 104-114.
18. R. Boese and M. Nussbaumer, *In Situ Crystallisation Techniques*, Oxford University Press, 1994.
19. D. Chopra and T. N. Guru Row, *Journal of the Indian Institute of Science*, 2007, **87**, 167-211.
20. *RLATT*, (2000) Bruker AXS, Madison WI.
21. J. Cosier and A. M. Glazer, *Journal of Applied Crystallography*, 1986, **19**, 105-107.
22. *SAINT*, (2006) Bruker-AXS, Madison, WI.
23. G. M. Sheldrick, *SADABS*, (2008) University of Gottingen, Gottingen, Germany.
24. A. Altomare, G. Cascarano, C. Giacovazzo and A. Guagliardi, *Journal of Applied Crystallography*, 1993, **26**, 343-350.
25. P. W. Betteridge, J. R. Carruthers, R. I. Cooper, K. Prout and D. J. Watkin, *Journal of Applied Crystallography*, 2003, **36**, 1487.
26. A. Coelho, *TOPAS-Academic: General Profile and Structure Analysis Software for Powder Diffraction Data*, (2007), Brisbane, Australia.
27. A. Boultif and D. Louer, *Journal of Applied Crystallography*, 1991, **24**, 987-993.
28. W. I. F. David, K. Shankland, J. van de Streek, E. Pidcock, W. D. S. Motherwell and J. C. Cole, *Journal of Applied Crystallography*, 2006, **39**, 910-915.
29. B. Delley, *Journal of Chemical Physics*, 2000, **113**, 7756-7764.
30. *Materials Studio Release Notes*, (2010) Accelrys Software Inc., Cambridge, UK.
31. J. P. Perdew, K. Burke and M. Ernzerhof, *Physical Review Letters*, 1996, **77**, 3865-3868.
32. B. Delley, *Journal of Chemical Physics*, 1990, **92**, 508-517.
33. S. Grimme, *Journal of Computational Chemistry*, 2006, **27**, 1787-1799.
34. G. W. T. M. J. Frisch, H. B. Schlegel, G. E. Scuseria, M. A. Robb, J. R. Cheeseman, G. Scalmani, V. Barone, B. Mennucci, G. A. Petersson, H. Nakatsuji, M. Caricato, X. Li, H. P. Hratchian, A. F. Izmaylov, J. Bloino, G. Zheng, J. L. Sonnenberg, M. Hada, M. Ehara, K. Toyota, R. Fukuda, J. Hasegawa, M. Ishida, T. Nakajima, Y. Honda, O. Kitao, H. Nakai, T. Vreven, J. A. Montgomery, Jr., J. E. Peralta, F. Ogliaro, M. Bearpark, J. J. Heyd, E. Brothers, K. N. Kudin, V. N. Staroverov, R. Kobayashi, J. Normand, K. Raghavachari, A. Rendell, J. C. Burant, S. S. Iyengar, J. Tomasi, M. Cossi, N. Rega, J. M. Millam, M. Klene, J. E. Knox, J. B.

Cross, V. Bakken, C. Adamo, J. Jaramillo, R. Gomperts, R. E. Stratmann, O. Yazyev, A. J. Austin, R. Cammi, C. Pomelli, J. W. Ochterski, R. L. Martin, K. Morokuma, V. G. Zakrzewski, G. A. Voth, P. Salvador, J. J. Dannenberg, S. Dapprich, A. D. Daniels, Ö. Farkas, J. B. Foresman, J. V. Ortiz, J. Cioslowski, and D. J. Fox, *Gaussian 09*, (2009) Gaussian Inc., Wallingford.

35. M. Headgordon, J. A. Pople and M. J. Frisch, *Chemical Physics Letters*, 1988, **153**, 503-506.
36. F. H. Allen and I. J. Bruno, *Acta Crystallographica Section B - Structural Science*, 2010, **66**, 380-386.
37. A. Gavezzotti, *OPiX*, (2003), Milan.
38. H. Sun, *Journal of Physical Chemistry B*, 1998, **102**, 7338-7364.
39. O. V. Dolomanov, L. J. Bourhis, R. J. Gildea, J. A. K. Howard and H. Puschmann, *Journal of Applied Crystallography*, 2009, **42**, 339-341.
40. C. F. Macrae, I. J. Bruno, J. A. Chisholm, P. R. Edgington, P. McCabe, E. Pidcock, L. Rodriguez-Monge, R. Taylor, J. van de Streek and P. A. Wood, *Journal of Applied Crystallography*, 2008, **41**, 466-470.
41. I. J. Bruno, J. C. Cole, P. R. Edgington, M. Kessler, C. F. Macrae, P. McCabe, J. Pearson and R. Taylor, *Acta Crystallographica Section B - Structural Science*, 2002, **58**, 389-397.
42. A. L. Spek, *Acta Crystallographica Section D - Biological Crystallography*, 2009, **65**, 148-155.
43. D. J. G. S.K. Wolff, J.J. McKinnon, M.J. Turner, D. Jayatilaka, M.A. Spackman, *Crystal Explorer*, (2012) University of Western Australia.
44. M. A. Spackman and J. J. McKinnon, *CrystEngComm*, 2002, 378-392.
45. M. C. Etter, J. C. Macdonald and J. Bernstein, *Acta Crystallographica Section B - Structural Science*, 1990, **46**, 256-262.
46. J. J. McKinnon, M. A. Spackman and A. S. Mitchell, *Acta Crystallographica Section B - Structural Science*, 2004, **60**, 627-668.
47. P. A. Wood, F. H. Allen and E. Pidcock, *CrystEngComm*, 2009, **11**, 1563-1571.
48. R. E. Easton, D. J. Giesen, A. Welch, C. J. Cramer and D. G. Truhlar, *Theoretica Chimica Acta*, 1996, **93**, 281-301.

Chapter 7

Conclusion

7.1 Conclusion

The PIXEL method, with its computational speed and conceptual simplicity, is a powerful tool for understanding the interactions that govern the solid state. The breakdown of interaction energies into chemically meaningful terms allows the nature of such interactions to be inferred at a level of accuracy comparable to higher level computational methods. Studies of the competing interactions in the crystal structures of the primary amines have further demonstrated that geometric considerations alone are not enough to rationalise the balances of different interactions. It was shown that, as the length of the carbon chain increased, hydrogen bonding interactions were sacrificed to enable more efficient interchain interactions, and methyl-methyl interactions were found to have a considerable effect on the alternation in melting point, results not entirely obvious from geometrical analysis alone. PIXEL parameters for the atoms common to organic chemistry are transferrable between such systems, however over 50% of the entries in the Cambridge Structural Database are metal containing species.

With the successful parameterisation of the 1st row transition metals, the PIXEL method can now be used to analyse almost any organic or molecular based inorganic structure, although further experimental sublimation data are required to validate the parameterisation for 2nd and 3rd row transition metals. The reproduction of experimental sublimation enthalpies shows that the parameters are robust, and the agreement between PIXEL dimer energies to those obtained through quantum mechanical methods for dihydrogen bonding interactions and intermolecular embraces demonstrates that accurate intermolecular energies can be obtained quickly and cheaply. The application of the PIXEL method to the calculation of adsorption sites in metal-organic frameworks to reproduce qualitatively experimental observations promotes its use in the computational modelling of more complex systems, where the initial results of PIXEL studies can be subsequently refined by higher level methods.

Using different methods to improve upon the atomic polarisabilities required for the calculation of dispersion and polarisation energies have been unsuccessful, as have attempts to use electron densities obtained through semi-empirical calculations. Other methods of calculating polarisabilities and densities are available, however, and future advances in these fields could result in further improvements to the PIXEL method and

its eventual incorporation into a program such as Mercury so that the calculation of intermolecular interactions becomes a standard step in crystal structure analysis.